Lecture Notes in Mechanical Engineering

Chander Prakash
Grzegorz Krolczyk
Sunpreet Singh
Alokesh Pramanik *Editors*

Advances in Metrology and Measurement of Engineering Surfaces

Select Proceedings of ICFMMP 2019

Springer

Lecture Notes in Mechanical Engineering

Series Editors

Fakher Chaari, National School of Engineers, University of Sfax, Sfax, Tunisia

Mohamed Haddar, National School of Engineers of Sfax (ENIS), Sfax, Tunisia

Young W. Kwon, Department of Manufacturing Engineering and Aerospace Engineering, Graduate School of Engineering and Applied Science, Monterey, CA, USA

Francesco Gherardini, Dipartimento Di Ingegneria, Edificio 25, Università Di Modena E Reggio Emilia, Modena, Modena, Italy

Vitalii Ivanov, Department of Manufacturing Engineering Machine and Tools, Sumy State University, Sumy, Ukraine

Lecture Notes in Mechanical Engineering (LNME) publishes the latest developments in Mechanical Engineering—quickly, informally and with high quality. Original research reported in proceedings and post-proceedings represents the core of LNME. Volumes published in LNME embrace all aspects, subfields and new challenges of mechanical engineering. Topics in the series include:

- Engineering Design
- Machinery and Machine Elements
- Mechanical Structures and Stress Analysis
- Automotive Engineering
- Engine Technology
- Aerospace Technology and Astronautics
- Nanotechnology and Microengineering
- Control, Robotics, Mechatronics
- MEMS
- Theoretical and Applied Mechanics
- Dynamical Systems, Control
- Fluid Mechanics
- Engineering Thermodynamics, Heat and Mass Transfer
- Manufacturing
- Precision Engineering, Instrumentation, Measurement
- Materials Engineering
- Tribology and Surface Technology

To submit a proposal or request further information, please contact the Springer Editor of your location:

China: Dr. Mengchu Huang at mengchu.huang@springer.com
India: Priya Vyas at priya.vyas@springer.com
Rest of Asia, Australia, New Zealand: Swati Meherishi at swati.meherishi@springer.com
All other countries: Dr. Leontina Di Cecco at Leontina.dicecco@springer.com

To submit a proposal for a monograph, please check our Springer Tracts in Mechanical Engineering at http://www.springer.com/series/11693 or contact Leontina.dicecco@springer.com

Indexed by SCOPUS. The books of the series are submitted for indexing to Web of Science.

More information about this series at http://www.springer.com/series/11236

Chander Prakash · Grzegorz Krolczyk ·
Sunpreet Singh · Alokesh Pramanik
Editors

Advances in Metrology and Measurement of Engineering Surfaces

Select Proceedings of ICFMMP 2019

Springer

Editors
Chander Prakash
School of Mechanical Engineering
Lovely Professional University
Phagwara, India

Sunpreet Singh
Centre for Nanofibers
and Nanotechnology
National University of Singapore
Singapore, Singapore

Grzegorz Krolczyk
Department of Mechanical Engineering
Opole University of Technology
Opole, Poland

Alokesh Pramanik
Curtin University
Perth, WA, Australia

ISSN 2195-4356 ISSN 2195-4364 (electronic)
Lecture Notes in Mechanical Engineering
ISBN 978-981-15-5150-5 ISBN 978-981-15-5151-2 (eBook)
https://doi.org/10.1007/978-981-15-5151-2

© Springer Nature Singapore Pte Ltd. 2021
This work is subject to copyright. All rights are reserved by the Publisher, whether the whole or part of the material is concerned, specifically the rights of translation, reprinting, reuse of illustrations, recitation, broadcasting, reproduction on microfilms or in any other physical way, and transmission or information storage and retrieval, electronic adaptation, computer software, or by similar or dissimilar methodology now known or hereafter developed.
The use of general descriptive names, registered names, trademarks, service marks, etc. in this publication does not imply, even in the absence of a specific statement, that such names are exempt from the relevant protective laws and regulations and therefore free for general use.
The publisher, the authors and the editors are safe to assume that the advice and information in this book are believed to be true and accurate at the date of publication. Neither the publisher nor the authors or the editors give a warranty, expressed or implied, with respect to the material contained herein or for any errors or omissions that may have been made. The publisher remains neutral with regard to jurisdictional claims in published maps and institutional affiliations.

This Springer imprint is published by the registered company Springer Nature Singapore Pte Ltd.
The registered company address is: 152 Beach Road, #21-01/04 Gateway East, Singapore 189721, Singapore

Contents

On Study of Stress Intensity Factors for Different FGM Plates Having Inclined Edge Crack Using Extended Finite Element Method 1
Vikas Goyat, Suresh Verma, and Ramesh Kumar Garg

Analysis of Sensitization in Austenitic Stainless Steel-Welded Joint 13
Hitesh Arora, Viranshu Kumar, Chander Prakash, Danil Pimenov, Mandeep Singh, Hitesh Vasudev, and Vishaldeep Singh

Comparative Analysis on Mechanical Properties of Al 6061 and Al 7075 Cross Matrix Composites 25
R. Balaji, J. V. Muruga Lal Jeyan, A. Basithrahman, Talasila Estheru Rani, and S. Abirami

Tensile and Flexural Behaviour of Areca Husk Fibre Reinforced Epoxy Composite 35
Sakshi S. Kamath, D. N. Punith, S. Preetham, S. N. Gautham, Janardhan, K. Lalith Yashwanth, and Basavaraju Bennehalli

Control Techniques and Failure Mode of Active Magnetic Bearing in Machine Tool System 45
Shishir Bisht, Nitin Kumar Gupta, and G. D. Thakre

A Technological Review on Temperature Measurement Techniques in Various Machining Processes 55
Vineet Dubey, Anuj Kumar Sharma, and Rabesh Kumar Singh

Development of a Model for the Number of Bends During Stirrup Making Process 69
S. N. Waghmare, Sagar D. Shelare, C. K. Tembhurkar, and S. B. Jawalekar

Numerical Analysis of Heat Transfer in Ferrofluid Under Constant External Magnetic Field 79
Jaswinder Singh Mehta, Rajesh Kumar, Harmesh Kumar, and Harry Garg

Formulation of a Mathematical Model for Quantity of Deshelled Nut in Charoli Nut Deshelling Machine 89
Sagar D. Shelare, Ravinder Kumar, and Pravin B. Khope

On Investigation of Dimensional Deviation for Hybrid Composite Matrix of PLA 99
Sudhir Kumar, Rupinder Singh, T. P. Singh, and Ajay Batish

Performance Evaluation of Graphene-Gear Oil Nanolubricants in Rayleigh Step Bearing 109
Gaurab Kumar Ghosh, Ankit Kotia, Niranjan Kumar, and Subrata Kumar Ghosh

The Effect of Two-Step Austempering on Abrasion Wear Characteristics of the Ductile Cast Iron 119
C. S. Wadageri, R. V. Kurahatti, Dayanand M. Goudar, Vijaykumar Hiremath, and V. Auradi

Effect of Particle Content and Temperature on Steady-State Creep in Thick Composite Cylinder 127
Gagandeep Singh Kohli, Tejeet Singh, and Harwinder Singh

Comparative Study on Wind Tunnel Calibrating Instruments 139
Akhila Rupesh, J. V. Muruga lal Jeyan, V. M. Ram Mohan, K. Praveen Kumar, T. Abhishek, T. Ashish, K. V. V. M. Reddy, and Greeshma Maddireddy

Wear and Friction Study of the Coated Piston Rings Material 149
Vinayak Goel, Mudit Shukla, and Vipin Kumar Sharma

Thermal Conductivity Analysis of Graphene Oxide Nanofluid Using Three-Level Factorial Design 161
Munish Gupta, Jodh Singh, Harmesh Kumar, and Rajesh Kumar

Design Optimization of Go-Kart Chassis Frame Using Modal Analysis 171
A. A. Dere, Manpreet Singh, A. Thakan, Rajeev Kumar, and Harpreet Singh

Effect of Process Parameters on Water Absorption and Impact Strength of Hybrid PLA Composites 187
Guravtar Singh Mann, Lakhwinder Pal Singh, Pramod Kumar, and Sunpreet Singh

Comparative Investigation of Different Types of Cutting Fluid in Minimum Quantity Lubrication Machining Using CFD 199
Payal Chauhan, Anjali Gupta, Amit Kumar Thakur, and Rajesh Kumar

To Study the Effect of Loading on Defect Signature by Using Statistical Parameters 209
Rajeev Kumar, Manpreet Singh, Jaiinder Preet Singh, Piyush Gulati, and Harpreet Singh

Vibration Analysis of Carbon Fiber and Glass Fiber Composite Beam 223
Ajay Kumar Kaviti and Amit Kumar Thakur

Analysis of Transient Thermal Temperature Distribution Over Service Life of Taper Roller Bearing Using FEA 231
Rajeev Kumar, Manpreet Singh, Jujhar Singh, and Siddique Khan

Incipient Fault Detection in Roller Bearing Using Ultrasonic Diagnostic Technique 243
Shashikant Pandey, P. Sateesh Kumar, M. Amarnath, Teki Tanay Kumar, and Paladugu Rakesh

Comparative Analysis of Imaging and Novel Markerless Approach for Measurement of Postural Parameters in Dental Seating Tasks 253
Vibha Bhatia, Jagjit Singh Randhawa, Ashish Jain, and Vishakha Grover

About the Editors

Dr. Chander Prakash is Associate Professor in the School of Mechanical Engineering, Lovely Professional University, Jalandhar, India. He has received Ph.D in mechanical engineering from Panjab University, Chandigarh, India. His area of research is biomaterials, rapid prototyping & 3-D printing, advanced manufacturing, modeling, simulation, and optimization. He has more than 11 years of teaching experience and 6 years' of research experience. He has contributed extensively to the world in the titanium and magnesium based implant literature with publications appearing in *Surface and Coating Technology*, *Materials and Manufacturing Processes*, *Journal of Materials Engineering and Performance*, *Journal of Mechanical Science and Technology, Nanoscience and Nanotechnology Letters*, *Proceedings of the Institution of Mechanical Engineers*, *Part B: Journal of Engineering Manufacture*. He has authored 60 research papers and 10 book chapters. He is also editor of 3 books: "Current Trends in Bio-manufacturing"; "3D Printing in Biomedical Engineering"; and "Biomaterials in Orthopaedics and Bone Regeneration - Design and Synthesis". He is also guest editor of 3 journals: special issue of "Functional Materials and Advanced Manufacturing", Facta Universitatis, Series: Mechanical Engineering (Scopus Indexed), Materials Science Forum (Scopus Indexed), and special issue on "Metrology in Materials and Advanced Manufacturing", Measurement and Control (SCI indexed).

Prof. Grzegorz Krolczyk is Professor in the Opole University of Technology. He is an originator and a Project Manager of OUTech's new Surface Integrity Laboratory. In his career he has held positions such as: head of unit design and technology, product engineer, production manager, product development engineer and production director. He is the co-author and project leader of a project Innovative, energy-efficient diaphragm flow device of a new generation. His industrial engineering experience was gained while working in a European holding company involved in machining of construction materials and plastic injection, where he was responsible for contacts with companies on technical issues such as quotation and implementation of new products. In professional career he was responsible from the implementation to production of products such as peristaltic

pumps, ecological sprayers to spray organic pesticides and many pressure equipment operating e.g. in chemical plants. As a production manager, he was responsible from implementation to production and launching the assembly line for innovative sprayer ultra-low volume spraying system. He is author and co-author of over 80 scientific publications and nearly 20 studies and implementation of industry. The main directions of scientific activity are surface metrology, optimization of geometrical and physical parameters of surface integrity, optimization of production and cutting tool wear analysis in dry machining process of difficult-to-cut materials. He is also editor of various Journals and Books.

Dr. Sunpreet Singh is researcher in NUS Nanoscience & Nanotechnology Initiative (NUSNNI). He has received Ph.D in Mechanical Engineering from Guru Nanak Dev Engineering College, Ludhiana, India. His area of research is additive manufacturing and application of 3D printing for development of new biomaterials for clinical applications. He has contributed extensively in additive manufacturing literature with publications appearing in Journal of Manufacturing Processes, Composite Part: B, Rapid Prototyping Journal, Journal of Mechanical Science and Technology, Measurement, International Journal of Advance Manufacturing Technology, and Journal of Cleaner Production. He has authored 10 book chapters and monographs. He is working in joint collaboration with Prof. Seeram Ramakrishna, NUS Nanoscience & Nanotechnology Initiative and Prof. Rupinder Singh, manufacturing research lab, GNDEC, Ludhiana. He is also editor of 3 books- "Current Trends in Bio-manufacturing"; "3D Printing in Biomedical Engineering"; and "Biomaterials in Orthopaedics and Bone Regeneration - Design and Synthesis". He is also guest editor of 3 journals- special issue of "Functional Materials and Advanced Manufacturing", Facta Universitatis, series: Mechanical Engineering (Scopus Indexed), Materials Science Forum (Scopus Indexed), and special issue on "Metrology in Materials and Advanced Manufacturing", Measurement and Control (SCI indexed).

Dr. Alokesh Pramanik is currently a lecturer in the School of Civil and Mechanical Engineering, Faculty of Science and Engineering, Curtin University. He received his Ph.D in Mechanical Engineering from The University of Sydney and Masters form National University of Singapore. His area of research is biomaterials, rapid prototyping & 3-D printing, advanced manufacturing, modeling, simulation, and optimization. He has more than 15 years of teaching experience and 6 years research experience. He has contributed extensively to the world in the materials and manufacturing by publishing more than 80 research articles.

On Study of Stress Intensity Factors for Different FGM Plates Having Inclined Edge Crack Using Extended Finite Element Method

Vikas Goyat, Suresh Verma, and Ramesh Kumar Garg

Abstract The aim of the present work is to provide a parametric analysis of stress intensity factor (SIF) in different functionally graded material (FGM) plates using the extended finite element method (XFEM). Exponential, power laws and sigmoid functions have been used for the material gradation of FGM plates. The relations of SIF have been presented with crack length and FGM material properties such as material modulus ratio, FGM layer thickness and power-law index. The present work reveals that the FGM material properties considerably affect the SIF values. Out of four FGM material models considered in this study, the sigmoid FGM model shows the least value of SIF.

Keywords Functionally graded material (FGM) · Extended finite element method (XFEM) · Stress intensity factor (SIF) · Crack

1 Introduction

Irwin introduced SIF in 1957, and it is a theoretical factor to analyze the stress state in fracture mechanics. The stress concentration-based failure criteria are not suitable for fractured solids as the value of stress concentration factor reaches infinity at the crack tip [1]. SIF depends on the geometry of solid, geometry of crack and load conditions. This factor is independent of material properties for a homogeneous material solid but, when solid is made of non-homogeneous material, the non-homogeneity of material will affect the value of SIF. FGM is a kind of non-homogeneous material whose properties vary continuously along with the dimension of solid. The early SIF analysis for FGMs was found in the work of Eischen [2]. The eigenfunction expression was used to calculate the stress field of the crack tip. Knoda and Erdogan [3] confirmed the result obtained by Eischen [2]. Gu et al. [4] reported a simple

V. Goyat (✉)
SRM Institute of Science and Technology, Delhi NCR Campus, Modinagar, UP 201204, India
e-mail: viky.goyat@gmail.com

S. Verma · R. K. Garg
Deenbandhu Chhotu Ram University of Science & Technology, Murthal, Haryana 1310027, India

© Springer Nature Singapore Pte Ltd. 2021

C. Prakash et al. (eds.), *Advances in Metrology and Measurement of Engineering Surfaces* , Lecture Notes in Mechanical Engineering,
https://doi.org/10.1007/978-981-15-5151-2_1

scheme of conventional J-integral to calculate SIF in FGM for finite element method (FEM) and also reported that the conventional J-integral loses its path independent property in FGMs. Kim and Paulino [5] presented a detailed review of all modified interaction integral formulations used to evaluate the mix mode SIF in FGM solids. Goli and Kazemi [6] reported the behavior of cracked FGM solid using XFEM. Khazal et al. [7] solved the edge crack problem in FGM solid using the extended element-free Galerkin method. Goyat et al. [8, 9] presented XFEM methodology for FGM plates having a hole as a discontinuity. Kanua et al. [10] presented a systematic review on fracture analysis of FGM solids in the aspect of the type of fracture problem and method used in the analysis. They suggested that the analytical and standard numerical method faces difficulties in the modeling of fracture problem in FGM solids, whereas advanced numerical methods like XFEM can easily model such problems.

The present work consists of the parametric analysis of SIF in FGM plane stress solid plates having inclined edge crack and subjected to uniaxial tensile load. The FGM is considered to be grade along the width of the plate with different functions such as exponential, power laws and sigmoid. The parametric analysis presented in this work may provide insight to model, analyze and reduction in SIF in FGM solids of different gradation functions.

2 Materials and Method

2.1 FGM Material Models

Four FGM material models graded along the x-direction (along width) of the plate are used in this work as follows:

Exponential FGM (EFGM):

$$E(x) = E_1 \mathrm{e}^{\left(\left(\frac{1}{W} \ln E^*\right)x\right)} \tag{1}$$

Power-law FGM (PFGM-A):

$$E(x) = E_1\left[1 + \left(E^* - 1\right)\left(\frac{x}{W}\right)^n\right] \tag{2}$$

Sigmoid FGM (SFGM):

$$\begin{aligned} E(x) &= E_1\left[1 + \frac{(E^* - 1)}{2}\left(\frac{x}{\frac{W}{2}}\right)^n\right] \text{ for } 0 \le x \le \frac{W}{2} \\ E(x) &= E_1\left[E^* - \frac{(E^* - 1)}{2}\left(\frac{W - x}{\frac{W}{2}}\right)^n\right] \text{ for } \frac{W}{2} \le x \le W \end{aligned} \tag{3}$$

Another parametric form of power-law FGM (PFGM-B) [11]

$$E(x) = E_1\left[E^* - \left(E^* - 1\right)\left(1 - \frac{x}{W}\right)^n\right] \tag{4}$$

Poisson's ratio for all the FGM models plate has been considered constant as:

$$v(x) = v = 0.3 \tag{5}$$

where $E(x)$ is Young's modulus of FGM, E_2 is Young's modulus at $(x = W)$, E_1 is Young's modulus of material at $(x = 0)$, H is height of plate, W is width of plate, material modulus ratio $E^* = E_2/E_1$ and $v(x)$ is Poisson's ratio of FGM.

2.2 Extended Finite Element Method (XFEM)

In XFEM, the displacement field variable for a domain having a crack in it has been represented as follows:

$$u = \sum_{i=I} N_i u_i + \sum_{i=HEN} N_i a_i H(x) + \sum_{i=CTN} N_i \left(\sum_{l=1}^{4} b_i^l F^l(x)\right) \tag{6}$$

where the first term of displacement field variable (u) is the classical FEM term, the second term denoted as the Heaviside enrichment term which provides the ability to handle crack faces within finite element and last term is crack tip enrichment term, it enables the finite element space to approximate the crack tip behavior without conformal FEM mesh. In Eq. 6, I represents the set of classical FEM nodes, u_i is the classical nodal displacement or classical degrees of freedom, *HEN* represents the set of the Heaviside enriched nodes, a_i is the additional degrees of freedom for *HEN*, $H(x)$ represents the Heaviside enrichment function, *CTN* is the set of crack tip enriched nodes, b_i^l is the degrees of freedom (additional) for *CTN*, $F^l(x)$ is the crack tip enrichment function and N_i is the shape function. To model the crack face behavior, the value of the Heaviside enrichment function is taken as +1 for adjacent nodes above the crack face and-1 for adjacent nodes below the crack face. To model the crack tip, the following crack tip enrichment functions are used in crack tip polar coordinate system r and are θ as:

$$\left\{F^l(r,\theta)\right\}_{l=1}^{4} = \left\{\sqrt{r}\cos\left(\theta/2\right),\ \sqrt{r}\sin\left(\theta/2\right),\ \sqrt{r}\sin\left(\theta/2\right)\sin\theta,\ \sqrt{r}\cos\left(\theta/2\right)\sin\theta\right\} \tag{7}$$

The standard FEM form can be obtained by using displacement function as:

$$\left[k_{ij}\right]\left\{d_j\right\} = \left\{f_i\right\} \tag{8}$$

where d is nodal displacement vector, f represents the nodal force vector and k is stiffness matrix which can be obtained as:

$$k_{ij}^{\alpha\beta} = \int_{\Omega} \left(B_i^{\alpha}\right)^T D(x)\left(B_j^{\beta}\right)\mathrm{d}\Omega \tag{9}$$

where $\alpha = \beta = \{u, a, b\}$

Further,u :Standard DOF, a :Heaviside DOF, b : Crack Tip DOF

The numerical integration in XFEM for enriched elements is different from the standard elements that utilize standard Gauss quadrature. These enriched elements are first subdivided into triangles, and afterward, fourth- and sixth-order triangular Gauss quadrature has been used for Heaviside and crack tip enriched elements, respectively.

2.3 Interaction Integral

The SIF has been calculated using J-integral in FEM as well as XFEM for homogeneous materials. It is very efficient method as it is path independent and can be calculated away from the crack tip, which enhances the capability of this method. In non-homogeneous materials such as FGM conventional J-integral loses its path independence property. This can be re-established in the new interaction integral approach, i.e., non-equilibrium interaction integral presented by Paulino and Kim [5]. In this formulation, the auxiliary displacement $\left(u_i^2\right)$ and strain field (ε_{ij}^2) are considered same as of homogeneous materials having Young's modulus (E_{tip}) and Poisson's ratio (v_{tip}) of crack tip and the auxiliary stress field (σ_{ij}^2) is calculated using FGM constitutive relation matrix $(D_{ijkl}(x))$ as:

$$\sigma_{ij}^2 = D_{ijkl}(x)\varepsilon_{kl}^2 \tag{10}$$

By using this scheme, the mix mode interaction integral (M) will be represented as:

$$\begin{aligned} M = &\int_A \left\{\sigma_{ij}^1 u_{i,1}^2 + \sigma_{ij}^2 u_{i,1}^1 - \frac{1}{2}\left(\sigma_{ij}^1\varepsilon_{ij}^2 + \sigma_{ij}^2\varepsilon_{ij}^1\right)\delta_{1j}\right\} q_{,j}\mathrm{d}A \\ &+ \int_A \left\{\sigma_{ij,j}^2 u_{i,1}^1 - D_{ijkl,1}\varepsilon_{kl}^1\varepsilon_{ij}^2\right\} q\mathrm{d}A \end{aligned} \tag{11}$$

where

$$\sigma_{ij,j}^2 = \left(D_{ijkl}\right)_{tip}\varepsilon_{kl,j}^2 + D_{ijkl,j}(x)\varepsilon_{kl}^2 + \left(D_{ijkl}(x) - \left(D_{ijkl}\right)_{tip}\right)\varepsilon_{kl,j}^2 \tag{12}$$

The actual and auxiliary fields are represented by superscript (1 and 2), respectively. Subscript $(,_1)$ denotes the derivative term with respect to dimension x_1. The q is a weight function whose value is zero for path segment near to the crack tip and one for the path segment far to the crack tip. The mix mode SIFs can be obtained by comparing Eq. 11 with following Eq. 13.

$$M = \frac{2}{E'}\left[\left(K_I^1\right)\left(K_I^2\right) + \left(K_{II}^1\right)\left(K_{II}^2\right)\right] \tag{13}$$

where $E' = E_{\text{tip}}/(1 - \upsilon_{\text{tip}}^2)$ for plane strain condition and $E' = E_{\text{tip}}$ for plane stress condition case.

3 Results and Discussion

The SIF values have been computed by a MATLAB computer code that has been developed using XFEM model with quadrilateral eight node (Q8) elements. The SIF values presented in this work are normalized by a factor (πa), where a is the crack length.

3.1 Validation of Computer Code

The validation has been done to check the accuracy of the developed computer code. The problem geometry and material model for validation of computer code are shown in Fig. 1. The obtained results of the present work are compared with the work of Erdogan and Wu [12], and comparison is presented in Fig. 2. From this comparison, it is noted that the results of the present work have a good agreement with the results of Erdogan and Wu [12] with an error of less than 1.5%. From Fig. 2, it is clear that $E^* > 1$ has lower values of SIF of mode-I (*KI*) than homogeneous material case ($E^* = 1$). Further, $E^* < 1$ cases show higher values of *KI* for *a/W* > 0.2 when compared with the homogeneous material case ($E^* = 1$). Thus, the range of material modulus ratio $E^* = 1$–10 is suitable for the further analysis of edge crack.

3.2 Parametric Analysis of Edge Crack

The edge crack in different FGM plates under uniaxial tensile load has been analyzed for SIF of mode-I (*KI*). The geometrical model for the analysis is shown in Fig. 3.

The variation of SIF with normalized crack length (*a/W*) for EFGM is depicted in Fig. 4. It is observed from Fig. 4 that the EFGM is capable to reduce SIF from the

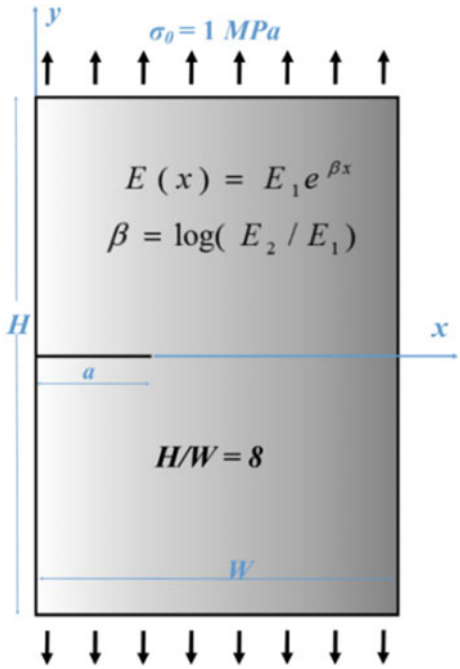

Fig. 1 Geometric model for validation of edge crack in FGM plate

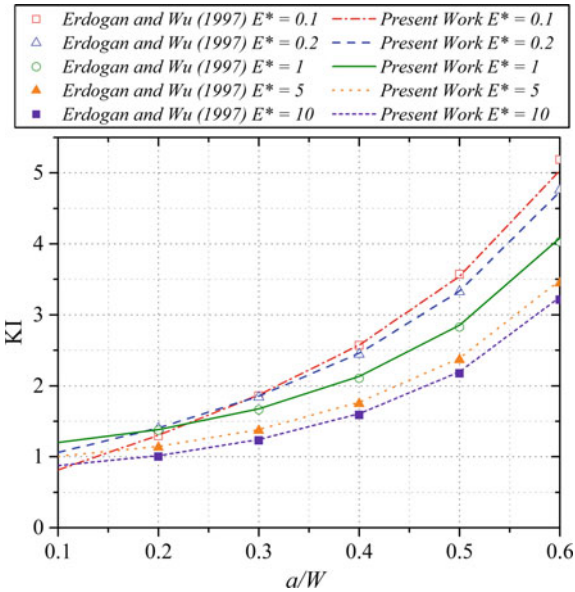

Fig. 2 Comparison of present work with Erdogan and Wu [12] for SIF of mode-I (*KI*) in EFGM plate

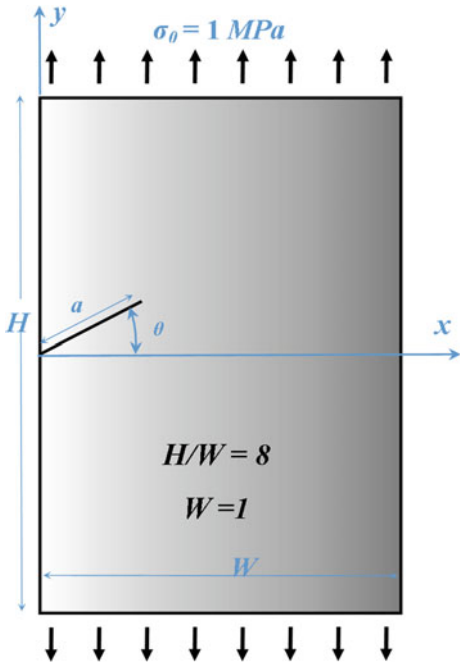

Fig. 3 Problem geometry for parametric analysis of edge crack in FGM plate

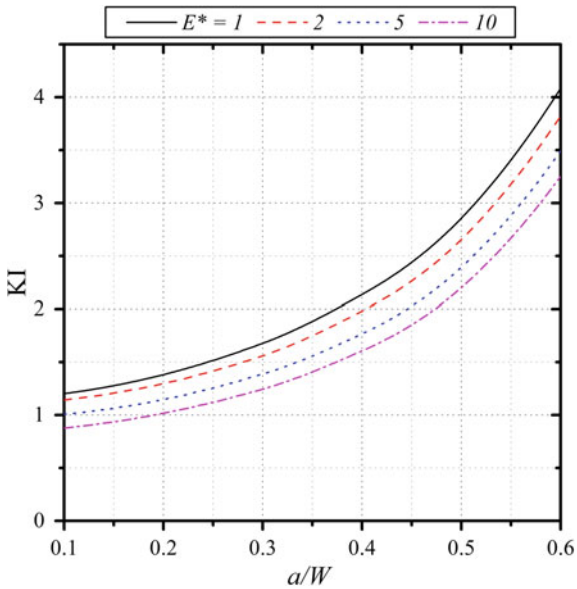

Fig. 4 Variation of SIF of mode-I (*KI*) for straight edge crack along with normalized crack length (*a/W*) in EFGM plate

reference values of the homogeneous material case, i.e., $E^* = 1$ and the amount of reduction in the values of *KI* is proportional to material modulus ratio.

Figures 5, 6 and 7 represent the variation of SIF *KI* with normalized crack length (*a/W*) for PFGM-A, PFGM-B and SFGM 5, respectively, with material modulus

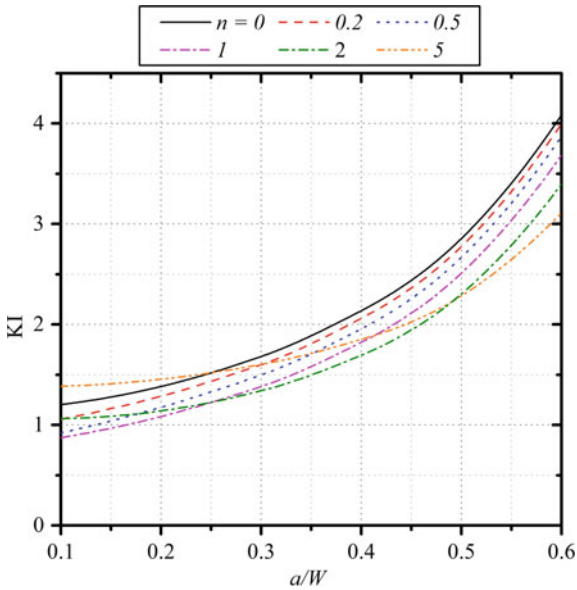

Fig. 5 Variation of SIF of mode-I (*KI*) for straight edge crack along with normalized crack length (*a/W*) in PFGM-A plate

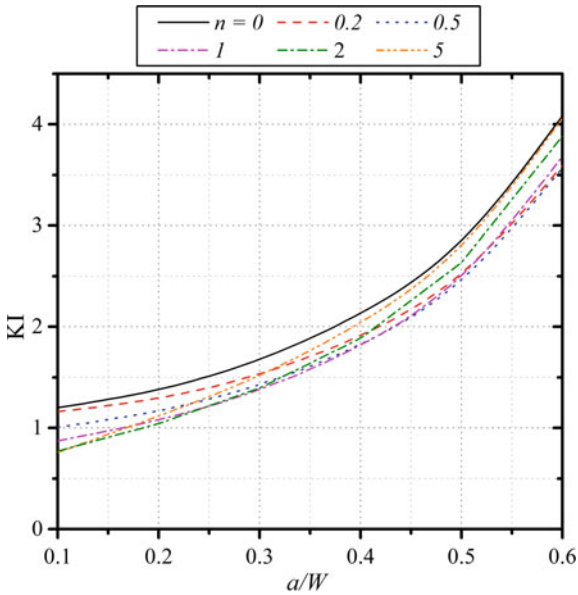

Fig. 6 Variation of SIF of mode-I (*KI*) for straight edge crack along with normalized crack length (*a/W*) in PFGM-B Plate

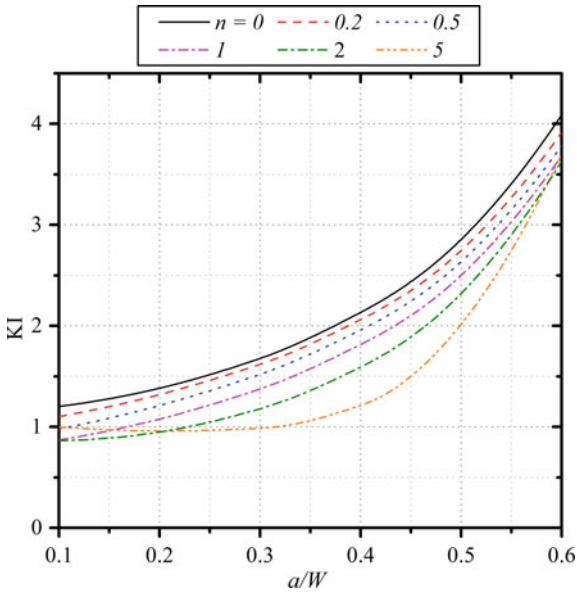

Fig. 7 Variation of SIF of mode-I (*KI*) for straight edge crack along with normalized crack length (*a/W*) in SFGM plate

ratio $E^* = 1$. .From Figs. 5, 6 and 7, it has been noticed that the application of FGM (except PFGM-A ($n = 5$)) reduces SIF in comparison with homogeneous case ($n = 0$) for the full range of normalized crack length (*a/W*). While PFGM-A with $n = 5$ shows higher values of SIF *KI* for $a/W < 0.3$ and it has lower values of *KI* for $a/W \geq 0.3$, when compared with the homogeneous case ($n = 0$). In PFGM-A, no power-law index (n) assured the lowest values of SIF (*KI*) for the whole range of *a/W* but, one can choose $n = 2$ for better results. Similarly, for PFGM-B, $n = 1$ and SFGM, $n = 5$ have been found best in their class. If the comparison is made between EFGM, PFGM-A ($n = 2$), PFGM-B ($n = 1$) and SFGM ($n = 5$), it is observed that SFGM with $n = 5$ is the best one in terms of least SIF.

Figure 8 shows the effect of E^* on SIF along with normalized crack length (*a/W*) for SFGM ($n = 5$). It is observed that the increase in the value of E^* shows a significant decrease in SIF (*KI*) values.

Figures 9 and 10 show the variation of SIFs (*KI* and *KII*) with crack inclination angle θ and different material modulus ratio E^* for SFGM ($n = 5$) along with $a/W = 0.2$. It is noted that SIF of mode-I (*KI*) decreases with increases in the inclination angle for all values of E^*. SIF of mode-II (*KII*) first increases until θ reach 45° and then starts decreasing with a further increase in crack inclination angle θ. Further, it is again observed that higher material modulus ratio assures the least value of SIF of mode-I as well as mode-II.

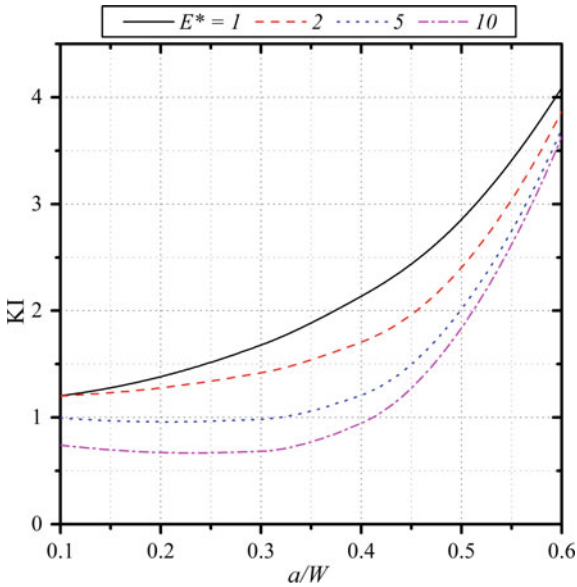

Fig. 8 Effect of material modulus ratio on SIF (*KI*) of straight edge crack in SFGM plate of $n = 5$

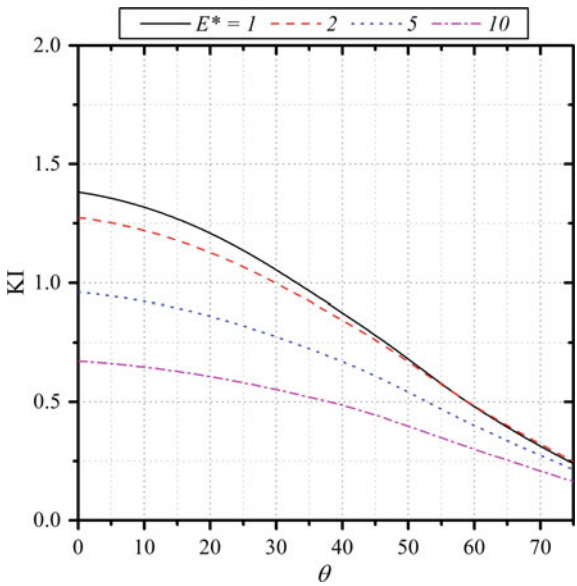

Fig. 9 Effect of crack inclination on SIF (*KI*) for SFGM ($n = 5$ and $a/W = 0.2$) plate

4 Conclusion

From the present work, the analysis of SIF in FGM (plane stress) plates having inclined edge crack and subjected to uniaxial tensile load, it has been concluded that

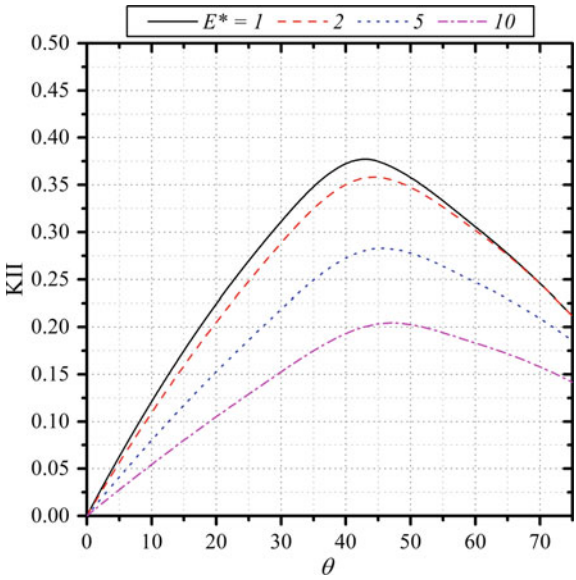

Fig. 10 Effect of crack inclination on SIF (*KII*) for SFGM ($n = 5$ and $a/W = 0.2$) plate

the SIF of edge crack is significantly affected by FGM properties. The lower values of SIF have been observed in the FGM plates as compared to the homogeneous material plate. The amount of reduction in SIF can be regulated by the function of FGM, power-law index and material modulus ratio. Out of four FGM material models considered in this analysis, the SFGM model provides the least value of SIF, and further, power-law index $n = 5$ has been suggested for SFGM. It has been also noted that the higher value of the material modulus ratio promises the least value of SIF.

References

1. Inglis, C. E. (1913). Stresses in a plate due to the presence of cracks and sharp corners. *Transactions Institute Naval Architecture, 55,* 219–241.
2. Eischen, J. W. (1987). Fracture of nonhomogeneous materials. *International Journal of Fracture, 34*(1), 3–22.
3. Konda, N., & Erdogan, F. (1994). The mixed mode crack problem in a nonhomogeneous elastic medium. *Engineering Fracture Mechanics, 47*(4), 533–545.
4. Gu, P., Dao, M., & Asaro, R. J. (1999). A simplified method for calculating the crack-tip field of functionally graded materials using the domain integral. *Journal of Applied Mechanics, 66*(1), 101–108.
5. Kim, J. H., & Paulino, G. H. (2005). Consistent formulations of the interaction integral method for fracture of functionally graded materials. *Journal of Applied Mechanics, 72*(3), 351–364.
6. Goli, E., & Kazemi, M. T. (2014). XFEM modeling of fracture mechanics in transversely isotropic FGMs via interaction integral method. *Procedia Materials Science, 3,* 1257–1262.

7. Khazal H., Bayesteh H., Mohammadi S., Ghorashi S. S., & Ahmed, A. (2016). An extended element free Galerkin method for fracture analysis of functionally graded materials. *Mechanics of Advanced Materials and Structures, 23*(5), 513–528.
8. Goyat, V., Verma, S., & Garg, R. K. (2017). Reduction of stress concentration for a rounded rectangular hole by using a functionally graded material layer. *Acta Mechanica, 228*(10), 3695–3707.
9. Goyat, V., Verma, S., & Garg, R. K. (2018). Reduction in stress concentration around a pair of circular holes with functionally graded material layer. *Acta Mechanica, 229*(3), 1045–1060.
10. Kanu N., Vates U. K., Singh G. K., & Chavan S. (2018). Fracture problems, vibration, buckling, and bending analyses of functionally graded materials: A state-of-the-art review including smart FGMS. *Particulate Science and Technology,* 1–26. https://doi.org/10.1080/02726351.2017.1410265.
11. Goyat, V., Verma, S., & Garg, R. K. (2018). On the reduction of stress concentration factor in an infinite panel using different radial functionally graded materials. *International Journal of Materials and Product Technology, 57*(1–3), 109–131.
12. Erdogan, F., & Wu, B. H. (1997). The surface crack problem for a plate with functionally graded properties. *Journal of Applied Mechanics, 64*(3), 449–456.

Analysis of Sensitization in Austenitic Stainless Steel-Welded Joint

Hitesh Arora, Viranshu Kumar, Chander Prakash, Danil Pimenov, Mandeep Singh, Hitesh Vasudev, and Vishaldeep Singh

Abstract The main aim of this paper is to study the mechanical properties of the weld also the microstructure of the weld joints were analyzed. The effects of sensitization of gas tungsten arc (GTA) welded 304L stainless steel (SS) joints were observed. 304L stainless steel was heated to 450–950 °C, soaked for 0.5–2 h, and was observed. The three heat groups were chosen from the operative window of tungsten inert gas welding; these heat groups are low heat -2200 J/mm, medium heat–3320 J/mm, and high heat 3800 J/mm. Using these heat groups, weld joints were made which were normalized at 750 °C, 850 °C, and 1000 °C for 0.5 h, 1 h, and 2 h, respectively. These specimens were used to perform tensile test, impact strength test, microstructure, and microhardness for welded joint. The effect of sensitization was observed for these joints for stated mechanical properties. The outcomes of this study indicate that the tensile strength is maximum at weld joints normalized at 750 °C but remarkably decreased as the temperature was increased while the yield strength did not notably change with increasing of the temperature. The Charpy impact energy and micro-harness showed higher value at weld joints normalized at 750 °C but remarkably decreased as the temperature was increased. The major reason for Charpy impact energy decrease was compound of manganese–silicon–Sulfur formed in the weld pool during solidification. The microstructures of sensitized samples have been observed by optical microscope. The sensitization was found to be more for heat-treated welded joints and parent metal as compared to unprocessed weld joints and parent metal. Precisely, welded joints were normalized at 850 °C with soaking time 2 h and allowed to cool in a furnace was observed to be more sensitized.

H. Arora · C. Prakash · M. Singh · H. Vasudev · V. Singh (✉)
Department of Mechanical Engineering, Lovely Professional University, Phagwara, Punjab, India
e-mail: vishaldeep.18537@lpu.co.in

V. Kumar
National Institute of Foundry & Forge Technology, Ranchi, India

D. Pimenov
Department of Automated Mechanical Engineering, South Ural State University, Chelyabinsk, Russia

© Springer Nature Singapore Pte Ltd. 2021

C. Prakash et al. (eds.), *Advances in Metrology and Measurement of Engineering Surfaces* , Lecture Notes in Mechanical Engineering,
https://doi.org/10.1007/978-981-15-5151-2_2

Keywords Microstructure · Sensitization · Microhardness · Tensile strength · Impact strength

1 Introduction

Austenitic stainless steel has excellent corrosion resistance as well as mechanical properties but when the temperature is raised between 450 and 950 °C, the chromium rich carbides ($M_{23}C_6$) are formed near the grain boundaries which result in the corrosion. The chromium-depleted zone is formed near to the carbides. In this zone, the chromium concentration decreases to 12 wt% [1]. Austenitic stainless steel is sensitized when it is heat treated (normalized) in between 450 °C to 900 °C and soaked for 0.5–2 h. Sensitization reduces the chromium rich carbides which results improving corrosion resistance. With the diminution of chromium from chromium-enriched carbide at temperature between 450 and 950 °C encounters by the steel, in the Heat Affected Zone of a weld normally, Cr-enriched Cr carbide, M represents Cr and some minute quantity of Fe in $M_{23}C_6$. The carbon atom diffuses to grain boundaries where carbon atom combines with chromium atom to form chromium carbide at sensitization temperature. The chromium carbide precipitates from areas contiguous to the grain boundaries which result in depletion of chromium. These areas are anodic as compared to the rest of the grains and therefore results in intergranular corrosion, which are favorably attacked by corrosive media [2].

Sensitization results in dilapidation of corrosion resistance over and above the mechanical properties [3, 4]. Many researchers have analyzed the welding of austenitic stainless steel with the gas tungsten arc welding process and the mechanical properties of austenitic stainless steel [5–9] The welding techniques used and the sensitization situations are changed in every case. The mechanical properties and consequence of microstructure of welded 316L joints were studied by [10]. The best results were observed when the weld joint was prepared using shielded metal arc welding (SMAW). For preparing the weld joint, E316L-16 electrode was used at low heat input conditions along with 5% of ferrite.

2 Experimental Details

2.1 Base and Filler Material

For the present study, the base material used was AISI 304L austenitic stainless steel. Nine plates were formed of 25 cm (length) × 10 cm (width) × 0.6 cm (thickness). These samples were used for the gas tungsten arc welding and the filler material used was 304L stainless steel solid electrode of 0.315 cm diameter. The chemical composition of the material used for the experimentation is shown in Table 1.

Table 1 Composition of 304 L and the filler wire (in wt%)

Composition	Carbon	Manganese	Silicon	Chromium	Nickel	Phosphorus	Sulfur	Molybdenum
Base material (304L)	0.021	1.05	0.55	18.10	9.10	–	–	–
Filler wire (304L)	0.045	1.50	1.00	20.00	9.00	0.04	0.03	0.75

Table 2 Welding parameters used for butt welded joints

Welding current (A)	Voltage (V)	Pass	Welding velocity (mm/min)	Heat input (J/mm)	Total heat input (J/mm)
130	23	1st	98	1430	3320
		2nd	75	1890	
180	23	1st	105	1700	3800
		2nd	85	2100	
210	25	1st	215	1020	2200
		2nd	187	1180	

2.2 Welding Procedure

For the preparation of the specimen to be analyzed, the parent metal was cleaned with the 1500 grit sand paper. The contaminated particles like rust were removed from the parent metal before the welding process which will avoid the defects during welding. After cleaning the parent metal plate, it was held so as to perform the welding [11]. For the different heat input values, the current was changed from 130A to 210A at the constant voltage of 25 V along with the varying welding speed while preparing specimen.

There were no welding defects like blow holes and porosity while preparing the weld bead and also the weld geometry was good. The parameters selected for welding are given in Table 2. For the analysis of mechanical properties and the microstructure, the measurements were occupied from the section which is transverse to direction of flow of weld bead. The analysis of microstructures was detected with an optical microscope. Figure 1 shows the weld samples taken for the tests.

2.3 Sensitization Treatment

The welded samples were prepared at low heat input 2.2 kJ/mm (210A). The performances of these welds were found to be the best when compared to the welds with different heat input conditions for various mechanical properties like microhardness, tensile and impact strength, and microstructure. Therefore, 210 A current was chosen for the said analysis. Another test sample was prepared of SS 304 L which was 250 mm long, 500 mm wide, and 6 mm thick. The same procedure was followed and the same parameters were used as mentioned for last study. The nine samples were made from the welded plate and were normalized at different temperatures and different time of soaking. After that, various properties were examined for the prepared samples. The temperatures used for sensitization were 750, 850 and 1000 °C and the soaking time was 30, 60, and 120 min. Six different time and temperature conditions were selected for sensitization of samples.

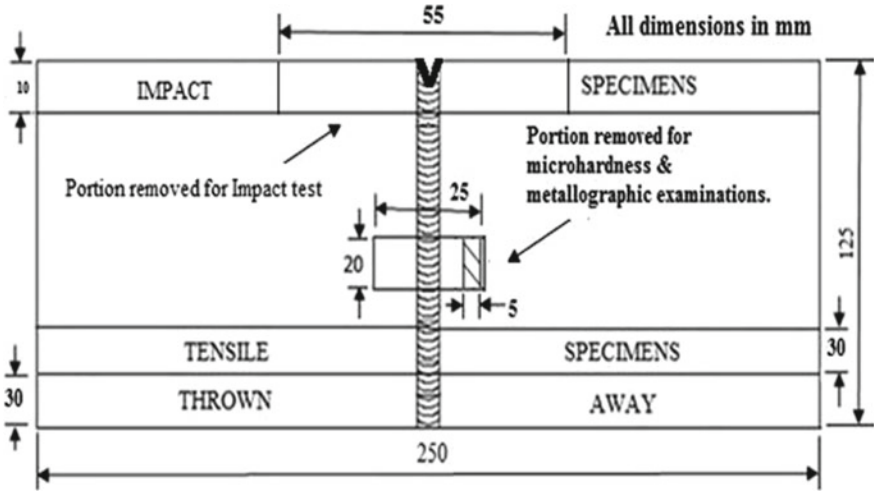

Fig. 1 Pattern of samples prepared from the welded plate

Heat treatment was done in muffle furnace. The nine specimens prepared from welded plate at 210 A were normalized and air cooled at above-stated temperature and time. For these samples, tensile strength, impact strength, microstructure, and microhardness were analyzed [12]. For example, three specimens were prepared at 750 °C with soaking time of 30 min and air cooled, and out of these three samples, one sample is used for tensile strength, second for impact strength, and third for microstructure and microhardness. Similarly, the next three samples were heated at 750 °C with soaking time of 60 min and air cooled. In the same way, all the specimens were prepared and the same properties were analyzed for these specimens.

2.4 Sampling of Specimen

Figure 1 shows the schematic diagram of the specimens prepared from the welded plate and their mechanical properties like tensile strength, impact strength, hardness, and microstructure were analyzed.

2.5 Tensile, Microhardness, and Impact Test

The weld pad was machined to prepare three specimens as shown in Fig. 2. The specimen prepared for analysis of tensile test, impact strength, and microhardness was taken according to ASTM E08 standards [9] as shown in Fig. 2. To perform the test on the various specimens, the hydraulically operated digital tensile test machine

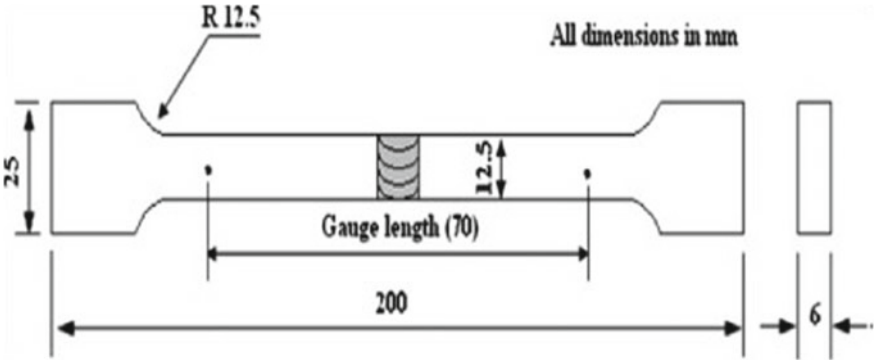

Fig. 2 Tensile specimen specifications

Fig. 3 Tensile-, microhardness-, and impact-tested specimens viewing the place of fracture at different normalization temperature

was used of capacity 400 kN. The Vickers's microhardness testing machine was used to check the microhardness. The load capacity of the machine is 0.5 kg. Impact strength was measured using Charpy impact testing machine. Figure 3 shows the photograph of the specimens after performing the above-mentioned tests [13–17].

2.6 Metallographic

The weld pad was machined to prepare the specimen as shown in Fig. 1. These specimens were analyzed for the change in microstructure of welding. The specimens were ground and cleaned with different grades of emery paper (800, 1000, 1500, and 2000 grit). Subsequent to cleaning the example with emery papers, every one of the examples was cleaned with velvet fabric utilizing alumina slurry. The last cleaning of the example was finished by precious stone glue (1 μm) utilizing Hiffin chloride as ointment. These cleaned examples were profound carved with Kalling's reagent (5 g copper (II) chloride, 100 ml hydrochloric acid and 100 ml ethanol) [10]. These specimens were finally observed using optical microscope.

3 Results and Discussion

3.1 Metallographic Studies of Specimen Welded at Different Welding Conditions

The micrographs of the specimen were analyzed and the presence of delta ferrite was observed in the matrix of austenite. Whereas the equiaxed grains of austenite are present in the parent metal. The dark bands observed are stringers of ferrite. These ferrite bands are least in weld at minimum heat input of 2.20 kJ/mm. The photomicrographs of the specimen are shown in Fig. 4. The currents selected for preparing specimen weld (130, 180, and 210 A) were cracked inside the weld bead. The strength of all the joints observed was good. When the specimen was polished, the lack of fusion was found which was prepared at 130 A. The tensile strength of 94.28% of the base metal was observed at low heat input of 2.2 kJ/mm. This tensile strength is the highest at given heat input. Hardness is maximum at 220 A and minimum because of arc formed by weak current at 130 A in the sample. Table 3 shows the macrostructural and microstructural details of the weld joints.

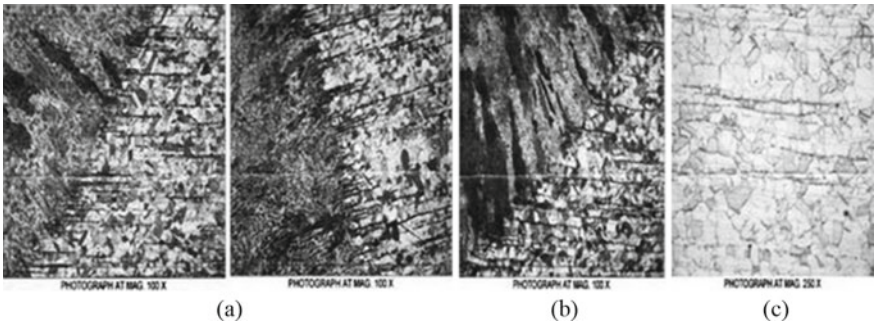

Fig. 4 Photographs of base material and welded joints at different heat inputs **a** 2.2 (kJ/mm), **b** 3.32 (kJ/mm), **c** 3.8 (kJ/mm), and **d** Base metal (at 100x)

Table 3 Mechanical properties details of the weld joints

Depiction	Tensile strength (GPa)	Yield strength (GPa)	Microhardness (HV)	Impact strength (J/mm^2)
Base material	0.7874	0.4535	253	1600
2200 (J/mm) (210A)	0.7477	0.2884	250	1560
3800 (J/mm) (180A)	0.4716	0.3049	250	1480
3320 (J/mm) (130A)	0.6300	0.2964	240	1400

Fig. 5 **a** Optical micrograph showing the microstructure of sample heated to 750 °C held for 30 min, **b** Sample heated to 750 °C held for 1 h, **c** Sample heated to 750 °C held for 2 h

Table 4 Mechanical properties details of the weld joints normalizing at 750 °C

Description	Tensile strength (GPa)	Yield strength (GPa)	Microhardness (HV)	Impact strength (J/mm^2)
750 °C for 30 min	0.7507	0.4434	246	1400
750 °C for 1 h	0.7367	0.4770	235	1280
750 °C for 2 h	0.7321	0.4971	232	1200

3.2 Metallographic Studies of Specimen Normalizing at 750 °C

Figure 5 shows the photomicrographs of the specimen which were normalized at a temperature of 750 °C with soaking time of 30 min, 1 h, and 2 h, respectively. While analyzing the samples, the chromium-depleted zones were observed. These zones are negligible for the specimen with soaking time of 30 min. These chromium-depleted zones increase with the increase in soaking time. Table 4 shows the macrostructural and microstructural details of the weld joints normalizing at 750 °C. With the increase in normalization temperature and soaking time, the tensile strength, impact strength, and micro hardness decrease.

3.3 Metallographic Studies of Specimen Normalizing at 850 °C

Figure 6 shows the photomicrographs of the specimen which were normalized at a temperature of 850 °C with soaking time of 30 min, 1 h, and 2 h, respectively. The chromium depleted zones were also observed in these specimens also. These zones also increase with increase in soaking time. When the comparison of mechanical properties was done for samples sensitized at 850 and 750 °C, it has been found that the two samples resemble with each other. With the increase in normalization temperature and soaking time, the tensile strength, impact strength, and microhardness

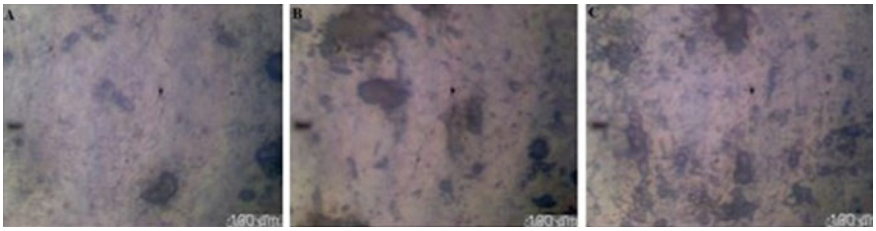

Fig. 6 **a** Optical micrograph showing the microstructure of sample heated to 850 °C held for 30 min, **b** Sample heated to 850 °C held for 1 h, and **c** Sample heated to 850 °C held for 2 h

Table 5 Mechanical properties details of the weld joints are normalizing at 850 °C

Description	Tensile strength (GPa)	Yield strength (GPa)	Microhardness (HV)	Impact strength (J/mm^2)
850 °C for 30 min	0.7426	0.4635	234	2600
850 °C for 1 h	0.7367	0.4526	260	2500
850 °C for 2 h	0.7220	0.4621	242	1900

decrease. Table 5 illustrates the mechanical properties of the weld joints which were normalized at 850 °C.

3.4 Metallographic Studies of Specimen Normalizing at 1000 °C

Figure 7 shows the photomicrographs of samples which were heat treated at 1000 °C. At high temperature, the carbide precipitates were observed which are negligible for sample whose soaking time is 30 min and minimum precipitates were observed for sample with soaking time 120 min. These precipitates are negligible with increase in temperature and expose time. Figure 7c clearly shows the desensitization. Table 6

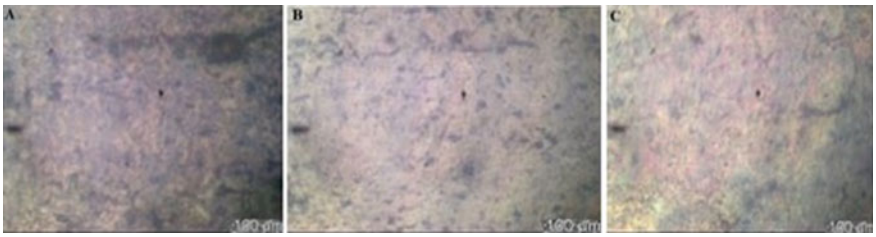

Fig. 7 **a** Optical micrograph showing the microstructure of sample heated to 1000 °C held for 30 min, **b** 1000 °C held for 1 h, and **c** 1000 °Cheld for 2 h

Table 6 Mechanical properties details of the weld joints normalizing at 1000 °C

Description	Tensile strength (GPa)	Yield strength (GPa)	Microhardness (HV)	Impact strength (J/mm^2)
1000 °C for 30 min	0.6168	0.4312	235	1.84
1000 °C for 1 h	0.6296	0.3765	227	2.00
1000°C for 2 h	0.6859	0.3710	225	2.20

shows the mechanical properties of weld. At 1000 °C, with soaking time 30 min, sensitization was observed for sample and desensitization was observed for sample with soaking time 1 h and 2 h. Tensile strength and impact strength were analyzed for 304L stainless steel which was normalized. The analysis shows that the tensile and impact strength increase with increase in temperature and time for soaking but the hardness decreases due to desensitization.

4 Conclusions

- The sensitization was observed for SS 304L when the samples were heated to a temperature of 750 and 850 °C with soaking time of 30, 60, and 120 min.
- The joint strength was observed to be good for all the three welds. But at minimum heat input 2200 (J/mm), the best result was observed. The microhardness and tensile strength of the sample are 250 HV and 0.7477 (GPa), respectively, as compared to 253 (HV) and 0.7874 (GPa) for the base metal.
- Tensile strength, impact strength, and hardness for 304L stainless steel decrease with increase in normalizing temperature and soaking time for the sample.
- At 1000 °C with soaking time 30 min, sensitization was observed for sample and desensitization was observed at 1 and 2 h soaking time.

References

1. Davis, J. R. (1994). *ASM specialty handbook*. ASM International: Stainless Steels.
2. Kumar, V., Arora, H., Pandey, P. K., & Rathore, V. (2015). Analysis of sensitization of austenitic stainless steel by different welding processes: a review. *International journal of applied engineering research, 17837–17848,* 10.
3. Wasnik, D. N., Kain, V., Samajdar, I., Verlinden, B., & De, P. K. (2002). Controlling grain boundary energy to make austenitic stainless steel resistance to intergranular stress corrosion cracking. *ASM Int., 402–407,* 12.
4. Unnikrishnan, R., Satish Idury K. S. N., Ismail, T. P., Bhadauria, A., Shekhawat, S. K., Khatirkar, R. K., & Sapate, S. G. (2014). Effect of heat input on the microstructure, residual stresses and corrosion resistance of 304L austenitic stainless steel weldments. *Material Characterization, 93*, 10–23.

5. Arora, H., Singh, R., & Brar, G. (2019). Thermal and structural modelling of arc welding processes: a literature review, *Measurement and Control.*
6. Prakash, C., Singh, S., Singh, M., Gupta, M. K., Mia, M., & Dhanda, A. (2019). Multi-objective parametric appraisal of pulsed current gas tungsten arc welding process by using hybrid optimization algorithms. *The International Journal of Advanced Manufacturing Technology*, *101*(1–4), 1107–1123.
7. Arora, H., Singh, R., & Brar, G. (2018). Finite element simulation of weld-induced residual stress in GTA welded thin cylinders. *Reference Module in Materials Science and Materials Engineering*, 1–14.
8. Atanda, P., Fatudimu, A., & Oluwole, O. (2010). Sensitization study of Normalized 316L Stainless Steel. *Journal Minerals and Materials Characterization and Engineering, 13–23,* 9.
9. Lo, K. H., Zeng, D., & Kwok, C. T. (2011). Effects of sensitisation-induced martensitic transformation on the tensile behaviour of 304 austenitic stainless steel. *Materials Science and Engineering A, 1003–1007,* 528.
10. Abigail Rodríguez, N., Packer, S., Steel, R., Rodrigo Muñiz, C., de Jesús Pérez, M., & Almanza, E. (2010). Analysis of sensitization phenomenon in friction stir welded 304 stainless steel. *Frontiers of Materials Science in China, 415–419,* 4.
11. Baek, J. H., Kim, Y. P., Kim, W. S., & Tai, Y. K. (2001). Fracture toughness And fatigue crack growth properties of the base metal and weld metal of a type 304 stainless steel pipeline for LNG transmission. *International Journal of Pressure Vessels and Piping, 351–357,* 78.
12. Prakash, C., Singh, S., Verma, K., Sidhu, S. S., & Singh, S. (2018). Synthesis and characterization of Mg-Zn-Mn-HA composite by spark plasma sintering process for orthopedic applications. *Vacuum, 155*, 578–584.
13. Prakash, C., Singh, S., Pruncu, C. I., Mishra, V., Królczyk, G., Pimenov, D. Y., & Pramanik, A. (2019). Surface modification of Ti-6Al-4V alloy by electrical discharge coating process using partially sintered Ti-Nb electrode. *Materials*, *12*(7), 1006.
14. Singh, S., Singh, G., Prakash, C., & Kumar, R. (2020). On the mechanical characteristics of friction stir welded dissimilar polymers: statistical analysis of the processing parameters and morphological investigations of the weld joint. *Journal of the Brazilian Society of Mechanical Sciences and Engineering, 42*(4), 1–12.
15. Singh, S., Prakash, C., & Gupta, M. K. (2020). On friction-stir welding of 3D printed thermoplastics. In *Materials Forming, Machining and Post Processing* (pp. 75–91). Cham: Springer.
16. Prakash, C., Singh, S., Singh, M., Gupta, M. K., Mia, M., & Dhanda, A. (2019). Multi-objective parametric appraisal of pulsed current gas tungsten arc welding process by using hybrid optimization algorithms. *The International Journal of Advanced Manufacturing Technology, 101*(1–4), 1107–1123.
17. Dhanda, A., Kansal, H. K., & Prakash, C. (2016). Experimental investigation and optimization of dissimilar joints of Aisi 304 and Aisi 4140 using pulsed current gas tungsten arc welding process. In *IVth International Conference on Production and Industrial Engineering (CPIE-2016)* (pp. 1–10). Jalandhar.

Comparative Analysis on Mechanical Properties of Al 6061 and Al 7075 Cross Matrix Composites

R. Balaji, J. V. Muruga Lal Jeyan, A. Basithrahman, Talasila Estheru Rani, and S. Abirami

Abstract Aluminum alloy 6061 and aluminum alloy 7075 (or simply denoted as Al 6061 and Al 7075, respectively) are widely used in the field of aviation, automobiles, and marine due to their exceptional properties such as good strength, lightweight, and better corrosion. In this paper, Al 6061 and Al 7075 are used as base materials for reinforcement to further enhance their mechanical properties. Alumina, silicon carbide, boron carbide, and titanium oxide are used as reinforcement particles. The cross matrix composites of Al 6061 and Al 7075 are produced by the widely used stir casting method. The different weight percentages of reinforcement particles are used to prepare different composition of cross composites. The resultant composites are heat-treated in T6 condition and machined in the suitable dimension for testing. The mechanical characterization was carried out by performing hardness, tensile, and impact tests, and their results have been presented. Moreover, the comparison of mechanical properties of alloys Al 6061 and Al 7075 is also given; specifically, the tensile stress and impact value of Al 6061 are shown to be increased when the reinforcement particles are added comparing to Al 7075 cross composites.

Keywords Cross matrix composites · Aluminum alloys · Stir casting · Mechanical properties · And heat treatment

R. Balaji · J. V. Muruga Lal Jeyan · T. Estheru Rani
Department of Aerospace Engineering, School of Mechanical Engineering, Lovely Professional University, Phagwara, Punjab 600099, India
e-mail: balaaero07@gmail.com

J. V. Muruga Lal Jeyan
e-mail: Muruga.22724@lpu.co.in

T. Estheru Rani
e-mail: chowdaryammulu999@gmail.com

A. Basithrahman (✉) · S. Abirami
Department of Aeronautical Engineering, Nehru Institute of Engineering and Technology, Thirumalayampalayam, Coimbatore, Tamil Nadu 641105, India
e-mail: basithabbas93@gmail.com

S. Abirami
e-mail: nietabirami.s@nehrucolleges.com

© Springer Nature Singapore Pte Ltd. 2021

C. Prakash et al. (eds.), *Advances in Metrology and Measurement of Engineering Surfaces* , Lecture Notes in Mechanical Engineering,
https://doi.org/10.1007/978-981-15-5151-2_3

1 Introduction

The use of the aluminum alloys in various industries because of its lightweight, and strength. In the virtual, role of hard ceramic in industry is quit high, but the soft matrix alloy, generally aluminum, improves the mechanical properties of the materials and increases the performance of the composites [1]. Aluminum alloy is used in various industries in line for to its good mechanical properties, and it can be able to withstand different atmospheric conditions without getting cored. But, it displays substandard tribological possessions in extensive application [2, 3]. To increase the brittleness of the aluminum-based materials, we were having plenty of ways, but reinforcing the materials could be the best option among all, reinforcements such as SiC and Al_2O_3 ceramic particles [4]. Many methods normally used to prepare the composites like powder metallurgy [5], but all are not simplest one; complicity range is higher. Stir casting [6] is one of the easiest way to manufacture the composites economically. Squeeze casting [7] is are often used rarely. Comparing to all the above-listed methods, stir casting is way better and simplest one for fabricating particulate reinforced composites [8]. Pre-aging is one of the best ways to increase the tensile properties of the material at various retrogression temperatures; in addition, it will increase the electrical resistivity and hardness of the AA7075 aluminum alloy [9]. The hardness of aged AA7075 alloy increases [10]. Boron carbide reinforced with aluminum alloys at 10% of its weight to increase the hardness and wear resistance. AA 7075 produces higher wear resistance comparing to AA 6061 alloy. The AA 7075/B_4C/graphite cross matrix attains better results [11]. Superior mechanical and tribological properties increased by reinforcing Sic with Alloys [12]. There is an increment in the mechanical and thermal properties using this substance of the materials. The wear resistance of the Al 7075-SiC-b4c composites is improved by aggregating the SiC ceramic particles. The coefficient of friction is indirectly proportional to the volume content of reinforcements [13]. Comparative analysis of the mechanical behavior of cold-worked and annealed 7075 aluminum alloy. In above 265 °C temperature, the rearrangement of the molecules inside the sample specimens at the same time yield and tensile strength gradually decreased [14]. Reinforcement of alloys with Sic increases the tensile strength and lowers the ductility of the alloys [15]. The propagation of 0–8 wt% of the Al_2O_3 and 5 wt% of graphite particles in AA7075 will increase the behavior of the material with various loads. Due to the reinforcement, ultimate strength of the materials increases. The mechanical strength is improved by toting Al_2O_3 particle and sinking due to toting of graphite particle [16].

In this work, the two different types of cross composites were produced by stir casting method using Al 6061 and Al 7075 aluminum alloys. Three different compositions of the cross composites are produced by using reinforcement particles. The comparative results of mechanical properties of two cross composites are analyzed.

Table 1 Composition of Al 6061

Element	Si	Fe	Cu	Mn	Mg
Weight (%)	0.514	0.23	0.161	0.071	0.96
Element	Ni	Zn	Ti	Cr	Al
Weight (%)	0.010	0.015	0.031	0.103	Bal.

Table 2 Composition of Al 7075

Element	Si	Fe	Cu	Mn	Mg
Weight (%)	0.219	0.219	1.582	0.043	2.036
Element	Ni	Zn	Ti	Cr	Al
Weight (%)	0.037	5.403	0.045	0.205	Bal.

2 Experimental Procedure

2.1 Material Composition

TiO_2, Al_2O_3, B_4C, and SiC are cast off as the strengthening particles, and Al 6061 and Al 7075 are used as base material. The composition of Al 6061 and Al 7075 is shown in Tables 1 and 2. Al 6061 and Al 7075 are used because they have virtuous mechanical properties and reveal good wettability. The most collective alloys of aluminum for broad purpose practice.

2.2 Preparation of Composites

Widely used casting technique to manufacture a cross metal matrix composites is stir casting technique because of its uniform reinforcement distribution. The metal matrix which has the uniform distribution will increase the quality of the materials. In this comparative study, the base material was Al 6061 and Al 7075 followed by the reinforcement particles Al_2O_3, SiC, TiO_2, and B_4C. For this comparative analysis, initially Al 6061 was taken followed by Al 7075. In the first casting process, reinforcement particles were Al_2O_3, SiC, and B_4C. For each casting, the reinforcement particles added at the equal amount to validate the result. Graphite crucible electric furnace is used here to heat the aluminum alloys at high temperature. The heat treatment was carried out for one hour in the electric furnaces with the temperature of 650°–800° which is high comparing to the melting temperature. To eliminate dusty particles, preheating is conducted at the temperature range of 450–550 °C. Semisolid molten material was cast off using mechanical stirrer. At the operating speed of 550 to 1100 rpm, the mild steel mechanical stirrer is used for stirring. Preheated reinforcement materials are slowly added during the vortex materialization stage. Magnesium

alloy of 1% is added to molten alloy in the second cross composite. Stirring speed is increased after adding the reinforcement, and the duration is maintained 5 min. The casting materials are obtained after preheated mold in a solid form. Using the base materials with different has been manufactures.

3 Compositions

The two types of cross composites with different type of compositions are shown in the table with compositions code. In the first cross composite Al 6061 is used as a base material, and B_4C, Al_2O_3, and SiC are cast off as reinforcement particles. The Al_2O_3 reinforcement weight proportion is varied, and B_4C and SiC weight percentages are maintained as constant (Table 3).

Al_2O_3, B_4C, and TiO_2 were casted as strengthening particles in the second cross composite Al 7075 weight are varied and the rest of the composition is kept constant.

Table shows the composition code of the different composition of cross metal matrix composites (Table 4).

3.1 Heat Treatment Process

The heat treatment process for cast and composite bars was carried out. Muffles were used to heat-treat the materials at T6 condition to an accuracy of ±1 °C for 8 h at 529 °C, followed by water quenching and then aged at 159 °C for 8 h. The casted materials are machined after heat treatment process for testing process with necessary dimension.

Table 3 Composition code of Al 6061

S. No.	Composition	Code
1	Al 6061-3%Al_2O_3-5%B_4C-5%SiC	A-1
2	Al 6061-6%Al_2O_3-5%B_4C-5%SiC	A-2
3	Al 6061-9%Al_2O_3-5%B_4C-5%SiC	A-3

Table 4 Composition code of Al 7075

S. No.	Composition	Code
1	Al 7075-3%Al_2O_3-5%B_4C-5%TiO_2	B-1
2	Al 7075-6%Al_2O_3-5%B_4C-5%TiO_2	B-2
3	Al 7075-9%Al_2O_3-5%B_4C-5%TiO_2	B-3

4 Mechanical Characterization

Experimentations were conducted on the material to find out the mechanical properties of the materials like hardness, impact test, and tensile test for various nodes. Mechanical properties were measured for the reinforced material and test procedures discussed in the following sections.

4.1 Hardness Test

Hardness of the specimen was tested, and the results have been computed using Brinell hardness test. All the test specimen size is maintained as per the ASTM E-18 standard size. The specimen has undergone hardness test with the load of 100 kgf for five different position, and the average is taken as the hardness value of the material. The ball intender dimension is 1/16 throughout the test.

4.2 Impact Test

Using Charpoy impact testing machine, impact test was done. The test specimens were made using casting process, and the material was machined as per ASTM E-23 standard size. Square cross sections of size (10 mm × 10 mm × 55 mm) with single V-notches are calculated for research. The dimensions of V-notches as per the literature review are 45° and 2 mm depth which will be more effective. The effect of roughness factor was indomitable when fracture takes place.

4.3 Tensile Test

For tensile test, 100 mm length and 12 mm diameter specimen has been taken as per AETME-08 standard. With universal testing machine (TUE-C1000), the mechanical properties has been validated and tabulated below.

5 Result and Discussion

5.1 Hardness Test

The testing shows the hardness values of the cross metal matrix composites and that has been tabulated. The hardness test was carried out on Brinell hardness testing

Table 5 Hardness value of cross composites

S. No	Loads (kgf)	Code	Hardness of Al 6061
1	100	A-1	92
2	100	A-2	95.7
3	100	A-3	95.3
S. No	Loads (kgf)	Code	Hardness of Al 7075
1	100	B-1	91
2	100	B-2	102.3
3	100	B-3	105.3

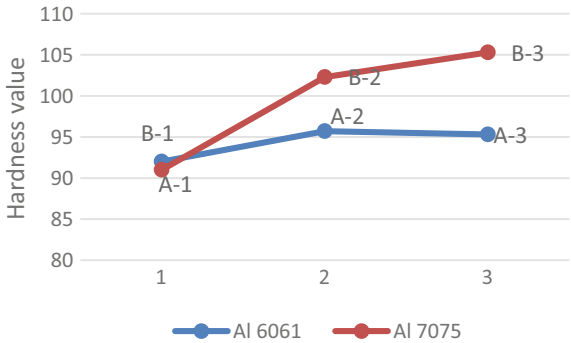

Fig. 1 Hardness value of Al 6061 and Al 7075 cross matrix composites

machine as per ASTM standard. The casted cross composites are machined for required dimension. 100 kgf load is applied to the specimen at three different places. The average values of the hardness are taken as hardness value of the cross metal matrix composites (Table 5).

From the table, it is shown that the hardness value of the Al 7075 cross matrix composites has higher hardness value compared to Al 6061 cross metal matrix composites. For all three different compositions of the cross composites, Al 7075 has high hardness value (Fig. 1).

5.2 *Impact Test*

Table shows the impact factor value of the Al 6061 and Al 7075 cross metal matrix composites. The impact test was carried out on Charpoy impact test machine as per ASTM standard. The casted composites are machined for required dimension (Table 6).

From the table, it is shown that the Al 6061 cross composite have higher impact factor value compared to Al 7075 cross composites. For all three different compositions of the cross composite Al 6061, cross matrix composites have higher impact value (Fig. 2).

Table 6 Impact value of cross composites

S. No	Code	Impact value of Al 6061
1	A-1	4
3	A-3	2
S. No	Code	Impact value of Al 7075
1	B-1	2
2	B-2	4
3	B-3	2

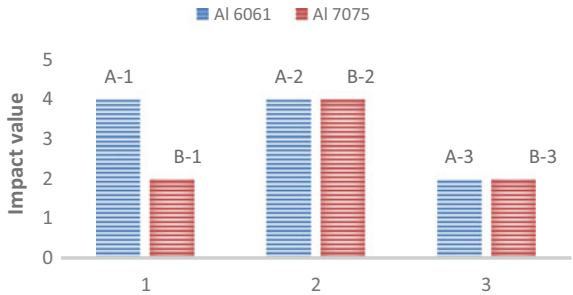

Fig. 2 Impact factor value of Al 6061 and Al 7075 cross matrix composites

5.3 Tensile Test

Table shows the tensile value of the Al 6061 and Al 7075 composites. The tensile test was carried out on universal testing machine as per ASTM standard. The casted composite was machined for required dimension. From the test, mechanical properties of the materials are measured (Table 7).

From the table, it is shown that the tensile stress value of the Al 6061 cross metal matrix composite has higher value compared to Al 7075 cross metal matrix composite. For all three different compositions of the composite Al 6061 have higher tensile strength (Fig. 3).

Table 7 Impact value of cross composites

S. No	Code	Peak load	Ultimate stress	Yield stress	% of Elongation
1	A-1	2.905	58	50	14.50
2	A-2	13.04	259	200	17.0
3	A-3	10.805	215	165	13.6
4	B-1	8.81	175	140	16
5	B-2	3.57	71	56	13
6	B-3	3.575	71	55	12

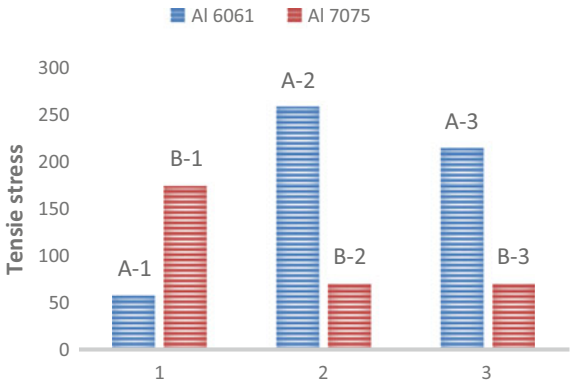

Fig. 3 Tensile stress value of the Al 6061 and Al 7075 cross metal matrix composites

6 Conclusions

In this work, the stir casting method is used to produce the cross composites with ceramic particles in different weigh percentage. Mechanical properties of alloys after reinforcing with ceramic particles have been increased. The other method of increasing mechanical properties is preheating of molds that help to reduce the porosity. Three different compositions of cross composites are produced and machined as per ASTM standard. The cross composites are heat-treated into T-6 condition successfully. The Al 7075 cross matrix composites have higher hardness value compared to Al 6061 cross metal matrix composites. Al 6061 cross matrix composites have higher impact factor value and tensile stress, yield stress, and % of elongation compared to Al 7075 cross metal matrix composite.

References

1. Wojciechowski, S., Talar, R., Zawadzki, P., Legutko, S., Maruda, R., & Prakash, C. (2020). Study on Technological Effects of a Precise Grooving of AlSi13MgCuNi Alloy with a Novel WCCo/PCD (DDCC) Inserts. *Materials*, *13*(11), 2467.
2. Uddin, M., Basak, A., Pramanik, A., Singh, S., Krolczyk, G. M., & Prakash, C. (2018). Evaluating hole quality in drilling of Al 6061 alloys. *Materials*, *11*(12), 2443.
3. Basak, A. K., Pramanik, A., & Prakash, C. (2019). Deformation and strengthening of SiC reinforced Al-MMCs during in-situ micro-pillar compression. *Materials Science and Engineering: A*, *763*, 138141.
4. Singh, S., Prakash, C., Antil, P., Singh, R., Królczyk, G., & Pruncu, C. I. (2019). Dimensionless Analysis for Investigating the Quality Characteristics of Aluminium Matrix Composites Prepared through Fused Deposition Modelling Assisted Investment Casting. *Materials*, *12*(12), 1907.
5. Prakash, C., Singh, S., Sharma, S., Garg, H., Singh, J., Kumar, H., & Singh, G. (2020). Fabrication of aluminium carbon nano tube silicon carbide particles based hybrid nano-composite by spark plasma sintering. *Materials Today: Proceedings*, *21*, 1637–1642.

6. Raheja, G. S., Singh, S., & Prakash, C. (2020). Processing and characterization of Al5086-Gr-SiC hybrid surface composite using friction stir technique. *Materials Today: Proceedings*. https://doi.org/10.1016/j.matpr.2020.04.729.
7. Boq-Kong, H., Su-Jien, L. & Min-Ten, J. (1996). The interfacial compounds and SEM fractography of squeeze-cast SiCp/6061 Al Composites. *Materials Science and Engineering, A, 206*, 110–119.
8. Hashim, J., Looney, L., & Hashmi, M. S. J. (1999). Metal matrix composites: production by the stir casting method. *Journal of Materials Processing Technology, 92*(93), 1–7.
9. Xua, H, Wangb, F., Zhub, J., & Xie, Y. (2011). Microstructure and mechanical properties of HoAl-Al_2O_3/Ti Al composite. *Materials and Manufacturing Processes, 26*(4), 559–561.
10. Uvaraja, V.C., & Natarajan, N. (2002) Comparison on Al 6061 and Al 7075 alloy with SiC and B4C reinforcement cross metal matrix composites. *IJART, 2*(2), 1–12. ISSN NO: 6602-3127.
11. Baradeswaran, A., et al. (2014). Experimental investigation on mechanical behaviour, modelling and optimization of wear parameters of B4C and graphite reinforced aluminium cross composites. *Materials and Design, 63,* 620–632.
12. Prakash, C., Singh, S., Singh, M., Antil, P., Aliyu, A. A. A., Abdul-Rani, A. M., & Sidhu, S. S. (2018). Multi-objective Optimization of MWCNT Mixed Electric Discharge Machining of Al–30SiC p MMC Using Particle Swarm Optimization. In *Futuristic Composites* (pp. 145–164). Singapore: Springer.
13. Vijaya Ramnath, B., et al. (2014). Evaluation of mechanical properties of aluminium alloy–alumina–boron carbide metal matrix composites. *Materials and Design, 58,* 332–338.
14. Masjuki, Mohammad Tajally, & Zainul Huda, H. H. (2010). A comparative analysis of tensile and impact- toughness behavior of cold-worked and annealed 7075 aluminum alloy. *International Journal of Impact Engineering, 37*(4), 425–432.
15. Doel, T. J. A., & Bowen, P. (1996). Tensile properties of particulate-reinforced metal matrix composites. *Composites Part A: Applied Science and Engineering, 27*(8), 655–665.
16. Baradeswaran, A., & Elaya Perumal, A. (2014). Wear and mechanical characteristics of Al 7075/graphite composites. *Composites Part B Engineering, 56,* 472–476.

Tensile and Flexural Behaviour of Areca Husk Fibre Reinforced Epoxy Composite

Sakshi S. Kamath, D. N. Punith, S. Preetham, S. N. Gautham, Janardhan, K. Lalith Yashwanth, and Basavaraju Bennehalli

Abstract Nowadays, because of the issues related to the environment, it is becoming mandatory for the usage of eco-friendly products for betterment of the people. Hence, here is an attempt made where the harmful synthetic fibre composites used for marine, automobile, constructive applications can be replaced by eco-friendly, biodegradable natural areca fibre composites. Physical properties of areca husk fibre were studied, and it revealed that maximum fibres have length range from 40 to 50 mm with the diameter ranging from 0.200 to 0.299 mm. These untreated and 1% NaOH treated fibres were used for composite fabrication at different fibre loadings like 45, 50, 55, 60, and 65%. It was found that 50% is the optimum fibre percentage. Tensile strength and flexural strength for untreated fibre composite at 50% fibre loading were found to be 7.40 N/mm^2 and 4.01 N/mm^2, respectively, and 54.91 N/mm^2 and 6.81 N/mm^2, respectively, for alkali-treated fibre composites.

Keywords Areca husk fibre · Mercerization · Linear density diameter method · Tensile testing · Flexural testing

1 Introduction

Increasing environmental awareness and decrease in fossil fuels are influencing researchers to use biodegradable natural material in composite manufacture as the substitute for synthetic fibres. The non-biodegradability, environmental impact and high cost of the synthetic fibres used as the reinforcing material in the composite manufacture is questioning the mankind about its usage and hence finding an alternative for using natural fibres as the substitute for composite fabrication [1]. The advantages

S. S. Kamath · B. Bennehalli (✉)
Department of Chemistry, Alva's Institute of Engineering & Technology, Mijar 574225, Karnataka, India
e-mail: basavaraju@aiet.org.in

D. N. Punith · S. Preetham · S. N. Gautham · Janardhan · K. L. Yashwanth
Undergraduate Students, Alva's Institute of Engineering & Technology, Mijar 574225, Karnataka, India

© Springer Nature Singapore Pte Ltd. 2021

C. Prakash et al. (eds.), *Advances in Metrology and Measurement of Engineering Surfaces* , Lecture Notes in Mechanical Engineering,
https://doi.org/10.1007/978-981-15-5151-2_4

like biodegradability, low density, high stiffness, low cost and high aspect ratio of the natural fibres such as kenaf, areca, abaca, jute, cotton, hemp draw the attention in replacing artificial fibres such as kevlar, glass, carbon with these natural fibres [2]. In recent days, research is done on wide variety of naturally obtained fibre reinforced polymer composites which has a high usage and demand in the marine industry, transport, construction industries and automotive applications [3, 4].

The areca fibres are one such example which can be used in composite fabrication to replace the synthetic fibre composites. The study carried out based on the maturity level of the fibres [5], Investigation done with respect to various chemical treatments which resulted in betterment of mechanical properties of the areca fibre composites [6], surface modification of fibres, which improved mechanical, acoustic and thermal properties at 10% fibre loading [7], the roughness of the surface of treated fibres and presence of trichomes improving the mechanical properties at 30% fibre loading [8] proves areca fibre is a promising material to be used as reinforcing material in composite fabrication as a substitute for artificial fibres.

The demerit of using any natural fibre in composite fabrication is its inadaptability towards polymeric matrix. The fibres being hydrophilic in nature form a poor bonding with hydrophobic resin as a result of which the stress transfer from reinforcing fibre to resin becomes difficult [9]. This results in the composites, exhibiting poor mechanical properties. This is solved by modifying fibre surface with certain chemical agents, thereby replacing hydrophilic −OH group of the fibres with certain other side groups like peroxide, silane, permanganate, ester linkage and others [10] which can form a better compatibility with polymeric resin. This leads to greater stability of the composites manufactured and provides better mechanical property to the composite materials produced. The primary treatment which has to be done prior to any treatment is mercerization. Hence, in the current study, the consequences of fibre percentage and alkaline effect on the mechanical properties of composite manufactured are carried out to stabilize optimum fibre loading required for further composite fabrication.

2 Materials and Methods

2.1 Fibre Extraction

Areca husk was collected from a local village at Moodbidri, Karnataka. The husk was immersed in water for 3 days. This loosens the fibres and helps in its easy removal. The fibres were collected and air-dried. These fibres were then oven-dried for 15 h at 70 °C to ensure complete removal of moisture content. The fibres were cut into pieces with its length ranging from 10 mm to 15 mm.

2.2 Surface Treatment

The oven-dried cut fibres were exposed to 1% NaOH solution for one hour. Mercerized fibres were washed repeatedly with de-ionized water to eliminate excess alkali from the surface. The fibres were treated with concentrated HCl for neutralizing the solution. Final washing was done with water to expel final traces of acid. These fibres were then kept in oven for 15 h at 70 °C for complete removal of moisture content [11].

2.3 Composite Fabrication

The raw fibres and the alkali-treated fibres were used for composite fabrication. The composite was manufactured using treated and untreated fibres at different fibre loadings like 45%, 50%, 55%, 60%, and 65%, respectively. The composite was manufactured using compression moulding unit (Santec). The resin used for composite manufacture is epoxy resin because of its low shrinkage, high strength and good durability [12]. The composites were fabricated under pressure of 40 atm for 24 h and cured at laboratory temperature for 15 days after which they were cut according to the ASTM standards and were subjected to mechanical testing.

2.4 Mechanical Characterization

The composites with different fibre loading using treated and untreated fibres were subjected to mechanical characterizations like tensile strength and flexural strength using Universal Testing Machine (Mecmesin Multi-test 2.5-xt). Five samples of each were considered to analyse tensile behaviour and flexural behaviour of composites. The composites were cut into strips according to ASTM D638-03 for tensile testing and ASTM-D790 for flexural testing [13]. The samples were placed in an oven for 6 h before testing so as to remove moisture content [14]. The average of five readings was considered for result analysis. Both the characterizations were carried out at laboratory temperature 35 ± 2 °C.

3 Results and Discussions

3.1 Physical Characterization

Areca fibres extracted from areca husk were taken, and the length of individual fibres was measured for hundred different samples. The diameter of fibre was measured

throughout the length of each fibre using Optical Microscope (LEICA DM750M). The fibres were sorted out according to their length distribution. The range of the fibre length having the highest number of fibres was found to be 40–50 mm as shown in Fig. 1 which was selected for further calculation. The mass of the selected fibres was calculated. The density of fibre was calculated using the linear density diameter method [15]. The mass of the fibre (M) and the diameter (d) and the length of the fibre (l) were used to estimate the density of fibre using Formula (1).

$$\rho = \frac{M}{\pi l d^2/4} \tag{1}$$

The physical properties of the areca husk fibres like the fibre length range, diameter range and the density of the fibre calculated are summarized in the given Table 1.

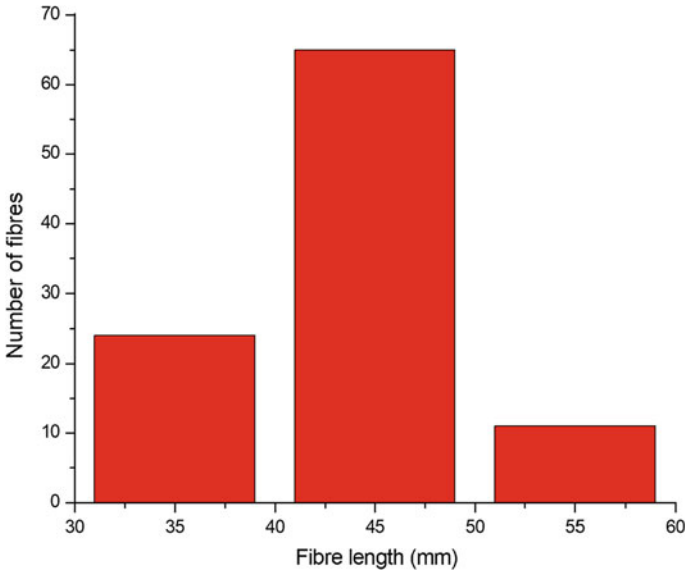

Fig. 1 Fibre length distribution

Table 1 Physical properties of areca husk fibre

Sample	Length (mm)	Diameter (mm)	Density (g/cm^3)
Areca husk fibre	40–50	0.200–0.299	1.6277

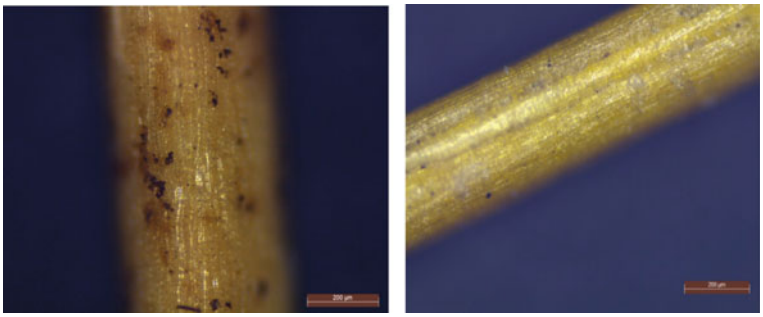

a) Untreated areaca husk fibre b) Treated areca husk fibre

Fig. 2 **a** Untreated areca husk fibre. **b** Treated areca husk fibre

3.2 Surface Morphology

The surface morphology of raw fibre and mercerized fibre taken in Optical Microscope (LEICA DM750M) is shown in Fig. 2a, b, respectively. Figure 2b reveals that the impurities like lignin, fat and pectin are removed from the surface of the fibres in case of mercerized fibres [16]. As a result of this, the fibre diameter reduces in case of mercerized fibres compared to raw fibres. The roughness of surface of fibre is further enhanced after alkali treatment, reduces hydrophilic nature of fibre and hence helps in better fibre resin adhesion.

3.3 Tensile Strength

The tensile strength with respect to load versus displacement curve of alkali-treated fibre epoxy composite is revealed in Fig. 3. The graph reveals that the tensile strength is maximum when the fibre loading is 50%. As the fibre loading further increases, drastic decrease in composite tensile strength is observed due to agglomeration of fibres in certain places, resulting in improper interaction between fibre and resin. Thus, stress transfer from reinforcing fibre material to resin becomes difficult which leads to the breakdown of composite manufactured [17]. The comparative study of tensile strength is shown in Fig. 4 which reveals that, tensile strength of the untreated fibre composites at 45%, 50%, 55%, 60% and 65% fibre loading is 7.40 N/mm^2, 10.06 N/mm^2, 2.80 N/mm^2, 4.28 N/mm^2 and 4.59 N/mm^2, respectively. Whereas for alkali-treated fibre composites, it was observed to be 35.12 N/mm^2, 54.91 N/mm^2, 42.17 N/mm^2, 15.62 N/mm^2 and 18.55 N/mm^2, respectively. This drastic changes in tensile strength of raw fibre and mercerized fibre composites reveal that in alkali-treated fibres, the −OH group of the cellulose is replaced by −ONa, as a result of which fibres behave hydrophobic in nature. The moisture absorption thereby decreases, and interaction between fibre and matrix increases. This leads to increase

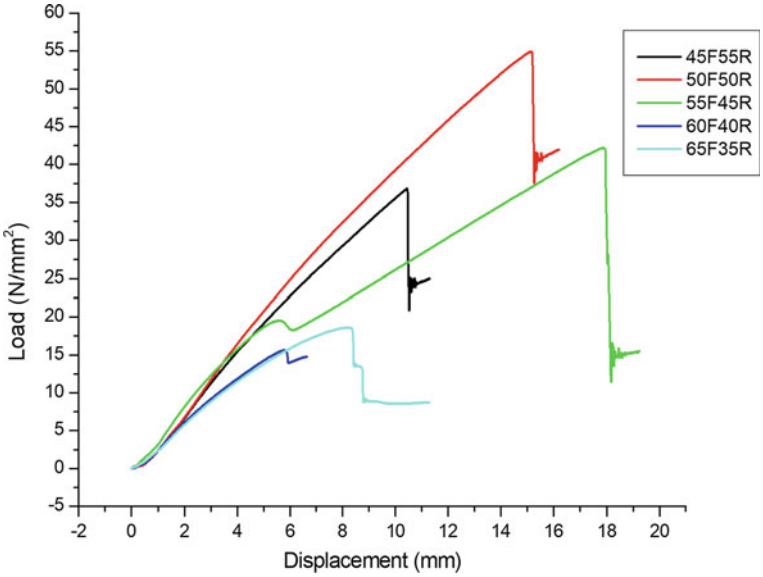

Fig. 3 Load versus displacement curve of 1% NaOH treated areca composite

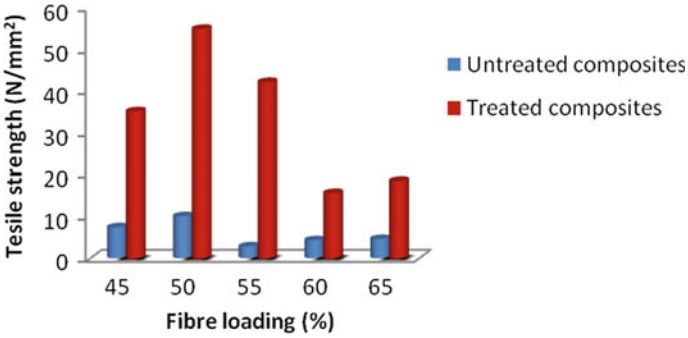

Fig. 4 Comparative study of tensile strength

in tensile strength of treated areca fibre epoxy composite. Tensile testing and the flexural testing of the samples are as given in Fig. 5a, b, respectively.

3.4 Flexural Strength

Flexural behaviour of treated areca composites is shown in Fig. 6. Flexural strength of mercerized fibre epoxy composite is 4.68 N/mm^2, 6.81 N/mm^2, 5.67 N/mm^2, 6.36 N/mm^2 and 4.87 N/mm^2 for composites at different fibre loadings like 45%,

a) Tensile testing b) Flexural testing

Fig. 5 **a** Tensile testing. **b** Flexural testing

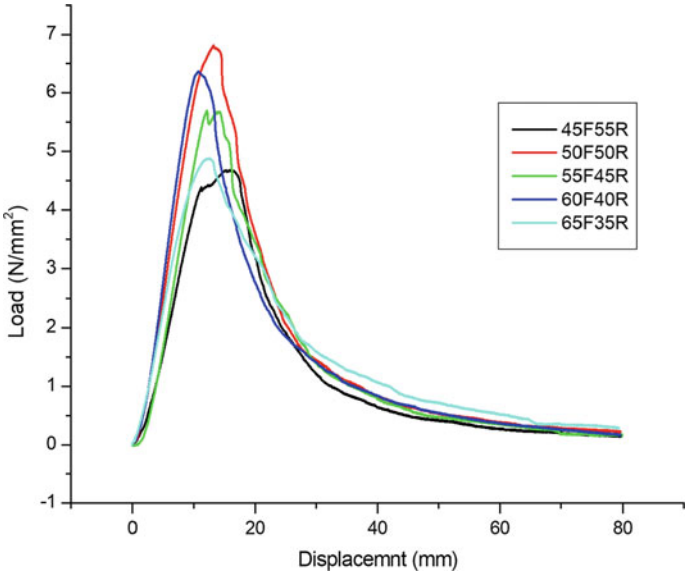

Fig. 6 Load versus displacement curve of 1% NaOH treated areca composite

50%, 55%, 60% and 65%, respectively. Flexural strength of untreated fibre composites is 3.93 N/mm^2, 4.01 N/mm^2, 3.40 N/mm^2, 3.03 N/mm^2 and 3.60 N/mm^{2}at different fibre loadings. The comparison between the flexural behaviour is shown in Fig. 7. Flexural strength for treated fibre composites is much greater in comparison with untreated fibre composites. In both the cases, flexural strength is maximum at

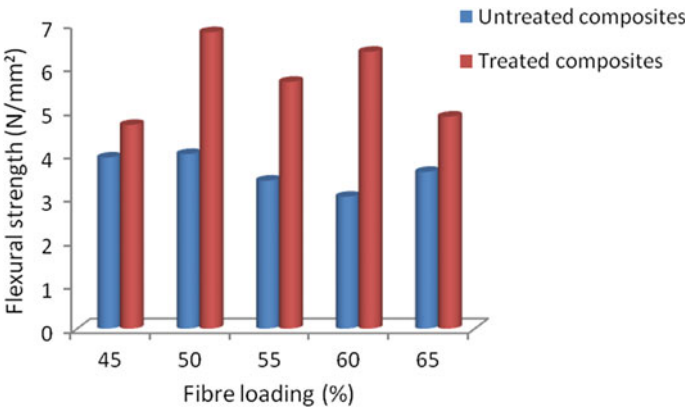

Fig. 7 Comparative study of flexural strength

50% fibre concentration. The reason for this is, at greater fibre concentration, clustering of fibre takes place which results in non-uniform transfer of stress from fibre to resin.

4 Conclusion

The tensile and flexural behaviour of raw and 1% NaOH treated fibres were studied at different fibre loadings from 45% to 65%. The study witnessed that in both the cases, strength is maximum at 50% fibre loading. Hence, 50% fibre loading is selected as optimum loading for future work. The comparative studies revealed that tensile strength and flexural strength of 1% NaOH treated fibre composites are elevated compared to untreated fibre composites. Hence, it proves that mercerization enhances the properties of composites and the need for the identification of different chemical treatments possible which would improve the strength of composites becomes necessary.

References

1. Fiore, V., Bella, G. D., & Valenza, A. (2015). The effect of alkaline treatment on mechanical properties of kenaf fibres and their epoxy composites. *Composites: Part B, 68*, 14–21.
2. Sakshi, S. K., Dhanalakshmi, S., & Basavaraju, B. (2017). A review on natural areca fibre reinforced polymer composites. *Ciencia dos Technologia Materiais, 29,* 106–128.
3. Balakrishnan, P., John. M. J., Pothen, L., Sreekala, M. S., & Thomas S. (2016). Natural fibre and polymer matrix composites and their applications in aerospace engineering. *Advanced Composite Materials for Aerospace Engineering,* 365–383.

4. Mohan, T. P., & Kanny, K. (2019). Compressive characteristics of Unmodified and nanoclay treated banana fiber reinforced epoxy composite cylinders. *Composites Part B Engineering, 169,* 118–125.
5. Yusriah, L., Sapuan, S. M., Zainudin, E. S., & Mariatti, M. (2012). Exploring the potential of betel nut husk fibre as reinforcement in polymer composites- effect of fibre maturity. *Procedia Chemistry, 4,* 87–94.
6. Ashok R. B., Srinivasa C. V. & Basavaraju B. (2018). A review on the mechanical properties of areca fibre reinforced composites. *Science and Technology of Materials, 30*, 120–130.
7. Elammaran, J,. Sinin, H., Md. Rezaur, R., & Md. Khusairy, B. B. (2014). Investigation of fiber surface treatment on mechanical, acoustical and thermal properties of betelnut fibre polyester composites. *Procedia Engineering, 97*, 545–554.
8. Hazarika, S. B., Choudhary, S. U., Panja, S. S. & Ray, B. C. (2015). Natural fibre reinforced polyester based biocomposite: agro waste utilization. *Journal of Scientific and idustrial research, 74*, 589–594.
9. Lai, W. L., Mariatti, M., & Jani, S. M. (2008). The properties of Woven kenaf and betel palm reinforced unsaturated polyester composites. *Polymer-Plastic Technology and Engineering, 47,* 1193–1199.
10. Xue, L., Lope, G. T., & Satyanarayan, P. (2007). Chemical treatments of natural fibre for use in natural fibre reinforced composites: A review. *Journal of Polymer Environment, 15,* 25–33.
11. Augustine, P., Joseph K., & Thomas, S. (1997) Effect of surface treatments on the electrical properties of low-density polyethylene composites reinforced with short sisal fibres. *Composites Science and Technology, 57*, 67–79.
12. Muralidhar, N., Vadivuchezhian, K., Arumugam, V., & Srinivasula R. (2019). A study on areca husk fibre extraction, composite panel preparation and mechanical characteristics of the composites. *Journal of the Institution of Engineers*.
13. Hazarika, S. B., Choudhury, S. U., Panja S. S., Dolui S. K., & Ray B. C. (2015). Natural fiber reinforced polyester biocomposite: Agro waste utilization. *Journal of Scientific and Industrial Research*, 589–594.
14. Jyun-Kai, H., & Wen-Bin, Y. (2019). The mechanical, hygral and interfacial strength of continuous bamboo fibre reinforced epoxy composites. *Composites Part B Engineering, 166,* 272–283.
15. Truong M., Zhong W., Boyko, S., & Alcock, M. (2009). A comparative study on natural fibre density measurement. *The journal of the Textile Institute, 100*(6), 525–529.
16. Dhanalakshmi, S., Ramadevi, P., & Basavaraju, B. (2015). Effect of chemical treatments on tensile strength of areca fibre reinforced natural rubber composites. *Journal of Applied Chemistry, 8,* 43–52.
17. Hassan, M., Wagner, M. H., Zaman, H. U., & Mubarak, K. (2010) Physico-Mechanical performance of hybrid betel nut short fiber/seaweed polypropylene composite. *Journal of Natural Fibres, 7*, 165–177.

Control Techniques and Failure Mode of Active Magnetic Bearing in Machine Tool System

Shishir Bisht, Nitin Kumar Gupta, and G. D. Thakre

Abstract Bearing is an integral part of the machine tools system, but due to contact stress, wear is induced, which decreases the life of the machine tools and bearing system. Stress developed due to contact between mating surfaces, i.e., contact stress and friction forces, is the main factor which is affecting the efficiency of a system. To achieve efficiency or to make contact-less levitation, active magnetic bearing are most suitable. This paper gives a basic idea on control techniques and failure modes and their effect on the active magnetic bearing system, by which frictional forces and the vibration should be minimised, which are the primary cause of wear and tear and decentralisation of the shaft. AMB systems are more suitable to increase the life and performance of the machine tools.

Keywords Active magnetic bearing · Control techniques · Failures in AMB

1 Introduction

Bearings play a major role in machine tools system; they are used to minimise the friction between two components whenever there is a relative motion between them. An electromagnetic bearing uses a magnetic force which will levitate the shaft; hence, due to absence of mechanical wear, it reduces friction and also increases its reliability and life [1, 2]. Magnetic bearings are generally of two types, namely active magnetic bearings (AMB) and passive magnetic bearings (PMB). There is no feedback control in passive magnetic bearings, i.e., passive magnetic bearings [3, 4] do not require active control. However, in active magnetic bearings (see Fig. 1), there is feedback

S. Bisht (✉) · N. K. Gupta
Department of Mechanical Engineering, DIT University, Dehradun, India
e-mail: shishirbisht@gmail.com

N. K. Gupta
e-mail: ghotnitin@gmail.com

G. D. Thakre
CSIR (IIP), Dehradun, India

© Springer Nature Singapore Pte Ltd. 2021

C. Prakash et al. (eds.), *Advances in Metrology and Measurement of Engineering Surfaces* , Lecture Notes in Mechanical Engineering,
https://doi.org/10.1007/978-981-15-5151-2_5

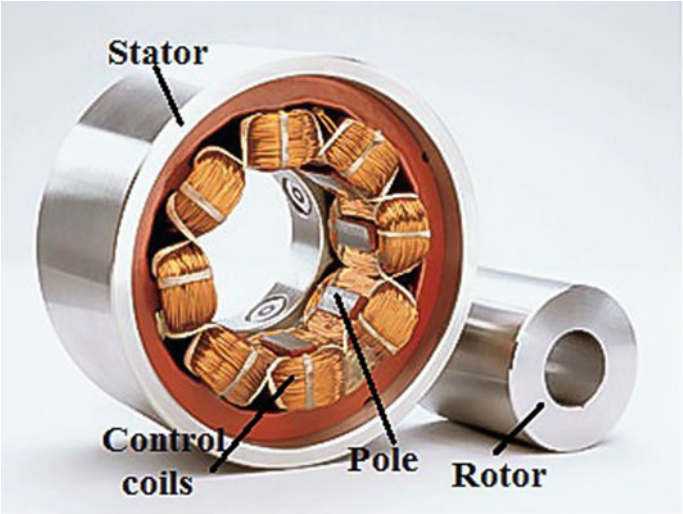

Fig. 1 Typical active magnetic bearing [1]

control or closed-loop control which ensure that there is no physical contact between the rotor and the stator.

Electromagnetic forces are used for rotor levitation, which will be developed when some amount of current flow through the copper wires. An active magnetic bearing consist of three major components which are a position sensor which indicates or measures the rotor's position from its initial position and gives actively feedback to the controller; a stator consists of electromagnets which generate the electromagnetic force and the rotor or shaft [5, 6]. Active magnetic bearing (AMB) have several advantages if compared with the traditional or mechanical bearings [2, 7], including contact-less operation hence less mechanical wear and friction, the absence of lubrication, lower maintenance costs, higher life, etc. (Fig. 2).

Although these bearings have some disadvantages include limitation in size, high initial cost as well as high running cost. But, due to many advantages, active magnetic bearings have wide area of applications, such as in machine tool systems, magnetically levitated vehicle, high-speed turbines, flexible rotor dynamic systems, compressors [2].

1.1 Active Magnetic Bearing—Control Techniques

To control the high amplitude vibrations in AMB system, it is necessary to select an appropriate control technique which will affect the life as well as performance of the AMB system. Following are some control techniques used in the AMB system [1, 8]:

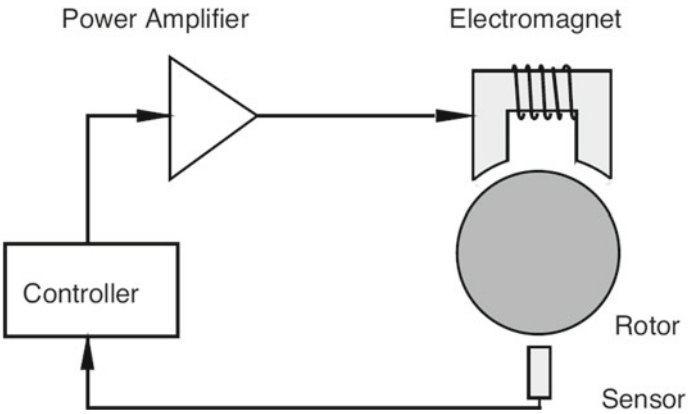

Fig. 2 Basic working principle of an active magnetic bearing [5]

PID. The proportional-integral-derivative (PID) is a traditional closed-loop feedback control technique, and because of its ease of use, this technique has been widely used in AMB systems. But because of unmeasured parameters variations and unavoidable external disturbances, this control technique is not very accurate; therefore, many kinds of control techniques have been developed such as fuzzy control and sliding mode control. These control techniques not only improve the stability of AMBs systems but also improve their performance in many ways.

Fuzzy Control. It is based on fuzzy logic, and fuzzy logic is the logic which can be expressed as "partially true" instead as 'true' or 'false'. It describes the problem's solution in a form that can be easily understood by human operators, so it is easy to utilise in the design of the controller. Because of its nonlinear properties, fuzzy control has advantages in magnetic suspension system applications, and also, it is widely used in applications related to machine control system.

Sliding Mode Control. It is a nonlinear control technique to change the dynamic behaviour of the said system into a linear system by use of a discontinuous control signal. SMC technique is usually used in the field of magnetic bearings due to its associated robustness. Chattering will affect the stability and precision of SMC technique which can be easily controlled by the filtering method.

Model Predictive Control. Model predictive control technique has the advantage that with wide bandwidth, it can easily control the current which passes through the coils in order to improve the performances of the active magnetic bearing system. MPC can easily apply over other techniques because of its fast dynamic response and unavailability of modulation.

Fault Tolerant Control. In any AMB system, the rotor displacement from its initial position has to be measured precisely for its better working performance and stability. But if there is any error in the position sensor, the stability as well as the performance of the AMB system gets affected. So to avoid this, self-sensing technology is used, in which rotor displacements is directly calculated from the

Table 1 Comparison of different control techniques [1, 8]

Control techniques	Advantages	Disadvantages
PID	Development process is simple	Not suitable for unknown and variable model
Fuzzy control	For unknown or variable model	It does not provide the précised control to the system
Sliding mode control	Completely self-adaptive against external disturbances	Chattering will affect the precision and stability of the AMB system
Model predictive control	Fast dynamic response, unavailability of modulation	Difficult to apply for the nonlinear and time-varying system
Fault tolerant control	Reduce the risk of failure in the AMB systems whenever there is any unexpected component failure occurs	Difficult for fault detection and identification of nonlinear system

current that passes through the coils and its voltage, so it provides a new and effective method for achieving controlled stability of the AMB system, and this causes the system to be more reliable. Table 1 presents various type of control technique with their advantages and disadvantages.

2 Literature Review

This current review paper deals with the control aspects and failure modes of the AMB system.

2.1 Active Magnetic Bearing

Ludvig and Kuczmann [9] did an analysis on an active magnetic bearing (AMB) system to find out the optimal shape and dimensions of the legs of the stator and air gap for the maximum electromagnetic force. The analysis was done with the help of finite element method and the magnetic vector potential formulation. The study focused on the eight-pole bearing that contains eight electromagnets. His calculation was done with a maximum and the constant current value of 12 A (DC) and 80 turns on each leg, the number of turns will also be constant, and then, it determines the maximum holding force. He has done his simulation on COMSOL Multiphysics software, which has a user-friendly interface, and after many calculations simulated, AMB can provide maximum 800 N as holding force over 1 mm thick air gap.

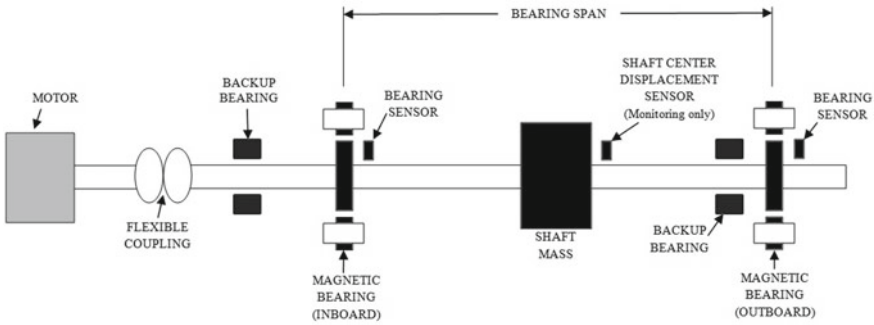

Fig. 3 Experimental rotor: Williams et al. [11]

PID means proportional-integral-derivative, and this control method is based on voltage control for the determination of K_P, K_D and K_I which governs the PID controller that has been proposed by Muzakkir and Lijesh [10]. The main motive is to levitate the shaft statically by the implementation of a voltage controller. The PID controller has been designed using LABVIEW software. The result of his experiment was that by voltage control method, the system was easily controllable using only K_P value and it did not depend on the K_D and K_I for its static levitation. In PID method, the output will be calculated by the measured error and the three controller gains which are K_P, K_I, K_D means proportional gain, integral gain and derivative gain, respectively.

An approach has been presented which aims to design an active magnetic bearing system and test a digital control system for its stability, and the AMB is having an eight-pole configuration [11]. A test rig has been made in which the flexible shaft test rotor has to be supported by two of these bearings. Theoretical relationships are created to make relationship between the characteristics of a controller transfer function and the stiffness and damping properties of an active magnetic bearing system. A demonstration has been shown regarding the digitally controlled magnetic bearing's flexibility by the use of algorithm, which includes integral feedback and second derivative. The design approach shows the effect of these new algorithms on the active magnetic bearing performance.

For the reshaping of the part in the damping curve which consists of high-frequency, second derivative feedback was utilised and to make sure the effects of the algorithm on the rotor response that it would be effectively anticipated integral feedback was implemented (Fig. 3).

2.2 Identification of Faults and Failure in AMB System

Failure modes were found out by a test rig and seen that mostly the failure occurred was due to high vibration [12]. The conventional compression trains would be

replaced by an AMB system in a hermetically sealed compressor. An AMB test rig has developed with two radial AMBs which are connected by an external controller and manipulated by computer software.

A test rig has been made (see Fig. 4) which is used to find out AMB failure modes. The primary cause of radial vibration in AMBs is to be the axial separation between the position sensor and bearing actuator. The failure modes that have been observed during normal machine operation are summarised in Table 2.

Failure of any component in AMB affects its performance, and hence, some major failure modes and their effects on the performance of AMBs have been identified [7] to make necessary changes in design to prevent these failures. So, failure modes and their effect have been found out for an AMB which will termed as FMEA means failure mode and effect analysis [12]. Risk Priority Number (RPN) will be discovered

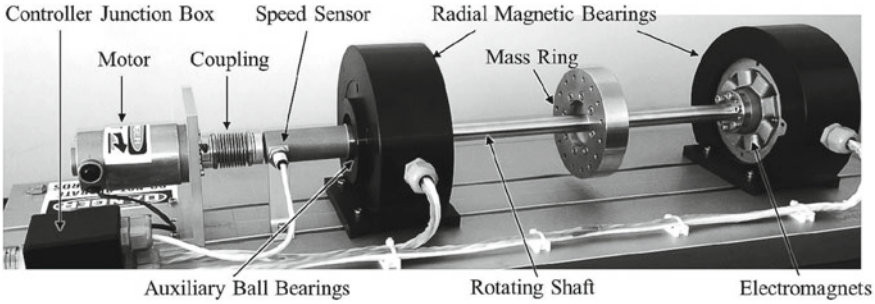

Fig. 4 Test rig schematic: Prof. Melinda Hodkiewicz et al. [12]

Table 2 Observed failure modes of AMB [12]

Item and function	Functional failure	Failure mode—cause of failure
Radial AMB: support shaft and minimises shaft vibration	High vibration amplitudes	Super-synchronous vibration—controller tuning unsuitable for damping structural resonances
	Radial vibration	Axial vibration—coupling not sufficiently robust to damp axial vibration
Controller: control and monitor shaft rotation and levitation	Rotation deviates from command	CW motor acceleration following a deceleration to 0 RPM from CCW rotation—motor control logic failure
	Rotation prevented	Rotation disallowed by controller—max. allowed de-levitations onto auxiliary bearings reached

by the assistance of severity, occurrence and detection of failures modes. In FMEA, first the system failures in the various components have been found out in each of the components of AMB system [13]. After that, the ranking is provided on a rating scale of 1–5 based on severity, occurrence and detection of each failure mode to calculate the Risk Priority Number (RPN). Hence, by the aid of Risk Priority Number, critical failure modes of AMB system have been found out. After identifying the critical failure mode and applying the control methods, the value of RPN is again calculated. The final FMEA worksheet is given in Table 3.

Table 3 Failure mode and effect analysis worksheet [7]

Components	Root-cause modes	Effects	RPN
Amplifier	Condition of external environment	Results in reduction in speed	5
	Over loading due to excess current supply	Results in reduction in speed	12
	Short circuit	Results in reduction in speed	10
Position sensors	Failure in electric circuit	Results in reduction in speed	20
	Physical contact between sensor and rotor	Rotor will levitate away from its original position	18
	Shaft will be damaged	Rotor will levitate away from its original position	8
	Presence of debris	Rotor will levitate away from its original position	3
Coil	Wire insulation decay	Results in reduction in speed	4
Software error	Failure occurs in operating condition	Rotor will levitate away from its original position	16
Rotor in dynamic loading	Loading condition has been changed	Rotor will levitate away from its original position	12
Motion in abnormal condition	Vibration from external source	Rotor will levitate away from its original position	24
	Mounted in portable applications	Rotor will levitate away from its original position	128
Active magnetic bearing touchdown bearings	Permanent damage	Results in reduction in speed	6
	Temporary errors in the system	Rotor will levitate away from its original position	4

3 Conclusion

Active magnetic bearing provides contact-less operation, hence, mechanical wear and frictional losses reduce, and there is no use of lubrication, so the maintenance cost reduces, and life and reliability of the bearing will increase.

In this paper, different control techniques studied, from which PID has been widely used in industrial control system and AMB systems in comparison with others. Also, failure modes have been studied to minimise the faults and failures in AMB and to increase its life, performance and reliability. It has been observed that the high vibrations are the main cause of failure of AMBs which results in decentralised of the shaft and minimises the life as well as the overall efficiency of the system.

Work is ongoing in many project areas, mainly to reduce or to control the vibration in the AMB system. The current areas of exploration include to control the multiple axes magnetic bearing and decentralisation of shaft and to reduce the high amplitude vibrations.

References

1. Zhang, W., & Zhu, H. (2017). Radial magnetic bearings: An overview. *Result in Physics*, 3756–3766.
2. Schweitzer, G., & Maslen E. H. (2009). *Magnetic bearings, theory, design, and application to rotating machinery*.https://doi.org/10.1007/978-3-642-00497-1
3. Samanta P., & Hirani, H. (2008, February). Magnetic bearing configurations: Theoretical and experimental studies. *IEEE Transactions on Magnetics, 44*(2). https://doi.org/10.1109/tmag.2007.912854.
4. Yuan, Y., Sun, Y., & Xiang, Q. Design and analysis of a magnetic bearings with three degrees of freedom. *Chinese Journal of Mechanical Engineering*. https://doi.org/10.1186/s10033-019-0320-3.
5. Madhura, S., & Govindaraju, T. V. (2017). Design and testing of an active magnetic bearing. *International Journal of Advance Research in Science and Engineering, 6*(10), 257–263.
6. Naikwad, S. (2016, April). Study of active magnetic bearing. *International Journal of Engineering and Technical Research (IJETR), 4*(4). ISSN: 2321-0869 (O) 2454-4698 (P).
7. Lijesh, K. P., & Hirani, H. (2016). Failure mode and effect analysis of active magnetic bearing. *Tribology in Industry, 38*(1), 90–101.
8. Pewekar, M. (2018, April) *Analysis of active magnetic bearings*. Thesis. https://doi.org/10.13140/rg.2.2.28631.37286.
9. Ludvig, T., & Kuczmann, M. (2008). Design of active magnetic bearing. *Journal of optoelectronics and advanced materials, 10*(7), 1834–1836.
10. Muzakkir, S. M., & Lijesh, K. P. (2015, August). Studies on control aspects of active magnetic bearings. *International Journal of Current Engineering and Technology, 5*(4).
11. Williams, R. D., Joseph Keith, F., & Allaire, P. E. (1990, February). Digital control of active magnetic bearings. *IEEE Transactions on Industrial Electronics, 37*(1), 19–27.
12. Schmidt, E. *Design of active magnetic bearing*. SzéchenyiIstván University, Department of Telecommunication, Laboratory of Electromagnetic Fields.
13. Hirani, H., & Samanta, P. (2007). Hybrid (hydrodynamic + permanent magnetic) journal bearings. *Proceedings of the Institute of Mechanical Engineers, Part J, Journal of Engineering Tribology, 221*(J8), 881–891.

14. Jozˇef RITONJA, Bosˇtjan POLAJZˇER, et al. (2010). Active magnetic bearings control. In Proceedings of the 29th Chinese Control Conference, July 29–31, 2010, Beijing, China, pp. 5604–5609.
15. Polajzer, B. (2000). *Design of horizontal shaft active magnetic bearing*, Slovenia, 2000.

A Technological Review on Temperature Measurement Techniques in Various Machining Processes

Vineet Dubey, Anuj Kumar Sharma, and Rabesh Kumar Singh

Abstract The cutting temperature and the amount of heat produced at the tool–chip interface during different machining operations have been recognized as main factors that influence the cost of machining as well as the cutting tool performance in terms of surface finish and the production time involved while machining. Cutting tool efficiency is largely affected by temperature generated while machining which limits the quality of the finished product. This paper presents a review of various methods for the measurement of tool and workpiece temperature distribution in different machining processes. Different temperature-sensing techniques are discussed along with their limitations. A comparison between several sensing methods has been done in terms of cost-benefit, accuracy, ease in measurement and response time in order to find out the best-suited method.

Keywords Cutting temperature · Sensors · Thermocouple · Infrared · Experimental method · Machining

1 Introduction

The surface quality of the part developed in material removal process is mainly dependent upon the efficiency of cutting tool. Hence, proper monitoring of the cutting tool is required. During the tool–workpiece interaction, large amount of heat is generated because of friction. Mainly, three types of deformation zones are encountered, namely primary, secondary and tertiary deformation zones as shown in Fig. 1. Primary deformation zone is affected largely as very high temperature is reported due to localized heating resulting in material softening. Further heat liberation is encountered in secondary zone in deformation of chips and to counteract the sliding friction at tool–chip interface. Due to the rubbing action between flank face of the tool and the machined surface, heat is liberated at the tertiary deformation zone in

V. Dubey (✉) · A. K. Sharma · R. K. Singh
Department of Mechatronics, Centre for Advanced Studies, Dr. A.P.J. Abdul Kalam Technical University, Lucknow 226031, India
e-mail: dubey.vin1324@gmail.com

© Springer Nature Singapore Pte Ltd. 2021

C. Prakash et al. (eds.), *Advances in Metrology and Measurement of Engineering Surfaces* , Lecture Notes in Mechanical Engineering,
https://doi.org/10.1007/978-981-15-5151-2_6

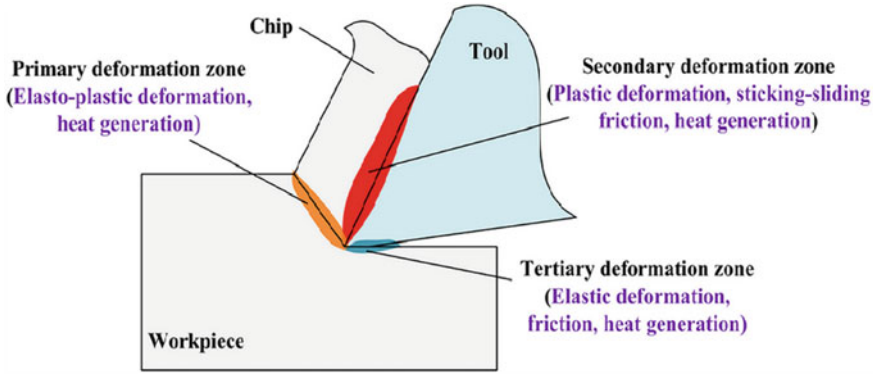

Fig. 1 Sources of heat liberation in the orthogonal machining process [1]

order to overcome friction. Various researchers have worked in this area to estimate the temperature at the tool–chip interface.

Shan et al. [2] performed orthogonal turning on titanium alloy Ti6Al4V for validating their experiment. In order to predict the temperature distribution, they developed an analytical model depending on moving heat source. K-type thermocouple was used for temperature measurement, and it was reported that the temperature difference recorded from the predicted model and the experiment performed are within 0.49–9%. Baumgart et al. [3] utilized two-color pyrometer to estimate the temperature in cylindrical grinding. It was observed that at low coolant supply variation in thermal load was from 265 K/s at 1.5 mm to 11,300 K/s at 0.5 mm. Ranc et al. [4] also used pyrometer along with CCD camera in machining of low-carbon steel and observed the highest temperature of 730 °C and minimum temperature of 550 °C. Using this setup, they also recorded the formation of chip during machining. Li et al. [5] inserted thin-film sensor on the rake face of tungsten carbide insert where the microgrooves were prepared and performed turning operation. Evaluation of temperature was seen in continuous as well as intermittent test. Sharma et al. [6] worked with in-house developed K-type thermocouple in the tool holder in machining AISI 304 steel using alumina and alumina–MWCNT hybrid nanofluid mist. They simulated using conjugate heat transfer method and found a variation of 5.79% with experimental work. Alvarez et al. [7] used two-color pyrometer technique while turning Inconel 718 at a different speed and feed rate. It was revealed that the temperature recorded reduced as the applied feed was increased. Davoodi and Hosseinzadeh [8] utilized infrared sensor in which voltage signal is inducted as the temperature raises. The amount of voltage is used in estimating temperature. High response rate was achieved with infrared sensor. Ghafarizadeh et al. [9] performed milling operation on CFRP and used K-type thermocouples for estimation of cutting temperature at low feed and medium-speed cutting. The temperature recorded raised linearly as per cutting speed. Chaudhary and Bartarya [10] performed orthogonal turning on EN 24 steel using HSS tool and utilized tool–work thermocouple method in order to sense the temperature. They observed rise in the temperature at cutting zone as the

cutting speed as well as feed rate was increased. Yashiro et al. [11] employed various techniques for calculating temperature while machining of carbon fiber-reinforced plastics. Embedded as well as tool–workpiece thermocouple, and infrared camera was used. The temperature reached up to 180 °C at a speed of 25 m/min. The aim of the experiment was to control the glass transition temperature of the matrix resin. Prakash et al. [12] applied electrical discharge coating and achieved surface modification of Ti6Al4 V alloy using partially sintered Ti-Nb electrode. Uddin et al. [13] performed experiment on drilling in order to evaluate the hole quality in case of aluminum alloy. Gupta et al. [14] performed machining on Inconel-800 superalloy in near dry machining condition and observed reduction in cutting force as well as improvement in the surface quality. Pradhan et al. [15] used FEA modeling to investigate the performance of microgroove textured cutting tool and observed lower cutting temperature as well as cutting force. Dubey and Singh [16] studied powder-mixed EDM on aluminum alloy and found that recast layer is decreased at lower setting of parameters. Tiwari et al. [17] performed drilling operation and studied the effect of drilling speed on micro-residual stress distribution in the proximity of hole using nanoindentation.

The present paper discusses the research work of past ten years in various machining processes such as turning drilling and milling. An attempt has been made to measure the cutting tool–workpiece temperature while machining. The researches focused on temperature measurement technique during machining as given in Table 1. The table describes the machining process, the tool–workpiece material used, along with the various sensing techniques involved in machining. Furthermore, the paper discussed the different temperature-measuring methods.

2 Study of Various Temperature-Sensing Techniques

Temperature-measuring techniques are basically categorized into conduction and radiation method. In case of conduction, interaction of energy among the particles from higher energy to lower energy happens. The temperature difference between the two regions in contact is calculated. Different methods under conduction techniques are shown in Fig. 2. The radiation technique depends upon the emissivity and temperature of the body. The accuracy of emissivity decides the precise measurement given by the radiation measurement instrument. The sub-categories of conduction and radiation methods are discussed.

2.1 Thermocouples

Thermocouples work on the principle of Seebeck effect. This effect produces difference in the voltage within the hot and cold junction whenever there is temperature difference [30]. In order to measure temperature rise at cutting zones, the obtained

Table 1 List of past work done in estimating temperature in various machining operations

Authors	Machining processes	Temperature-sensing technique/equipment	Tool/workpiece	Remarks/findings
Shan et al. [2]	Turning	K-type armored thermocouple	Carbide tool insert	With rise in feed rate, the high-temperature area is changing away from nose of tool
Zhang et al. [18]	Drilling	Thermocouple and platinum resistors	S45C steel	Temperature rise was maximum at bit regolith region
Kesriklioglu [19]	Milling	K-type thin-film thermocouple	Tungsten carbide	It was noticed that in case of climb and conventional milling the peak temperature is very close
Li et al. [5]	Turning	K-type thin-film thermocouple	Tungsten carbide insert	Proper linearity and uniformity are seen in estimating when the sensors are insulated with the alloy substrate
Baumgart et al. [3]	Cylindrical grinding	Two-color pyrometer	Cold work tool steel	Variation in thermal load can be seen from 265 to 11,300 K/s
Nunez et al. [20]	CNC milling	Infrared camera/thermogram	High-speed steel end milling tool	For finding of the interest zones, the image collected was useful
Urgoiti et al. [21]	Grinding	Pyrometer	GG-30 cast iron	There has been a decrease of measurement error by 60% when temperature estimation of the surface was done while grinding operation using this technique

(continued)

Table 1 (continued)

Authors	Machining processes	Temperature-sensing technique/equipment	Tool/workpiece	Remarks/findings
Rizal et al. [22]	Milling	Thermocouple	ACK 300 tungsten carbide tool	Thermocouple used was found to be reliable for interpreting machining signals. The signals obtained are co-related to flank wear stare
Werschmoeller and Li [23]	CNC milling	Thin-film micro-thermocouple	Polycrystalline boron nitride (PCBN)	Thin-film micro-thermocouple exhibited good linearity as well as quick response time
Alvarez et al. [7]	Turning	Two-color pyrometer	Triangular uncoated carbide insert	It was reported that despite harsh environmental conditions, this pyrometer technique has shown good performance in measuring temperature where emissivity can play an important role
Sorrentino et al. [24]	CNC drilling	K-type thermocouple	Tungsten carbide	The highest temperature estimated on the tool rises with the cutting speed and decreases with increasing feed rate
Tapetado et al. [25]	Turning	Two-color pyrometer	Carbide insert	The experiment results revealed a temperature error of 14%
Gosai et al. [26]	Turning	K-type thermocouple	Coated carbide insert	The obtained mathematical model was validated, and the error reported was less than 10%

(continued)

Table 1 (continued)

Authors	Machining processes	Temperature-sensing technique/equipment	Tool/workpiece	Remarks/findings
Baohai et al. [27]	End milling	Single-wire thermocouple	Milling cutter with carbide insert	An inverse trend of temperature change was found against cutting speed
Sugita et al. [28]	Turning	Micro-thermocouple sensor	Carbide insert	This sensor can be used with non-conducting materials and applied to medical devices

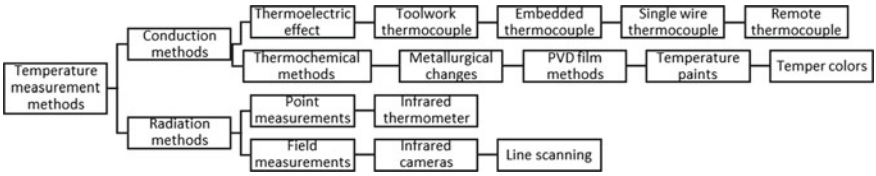

Fig. 2 Temperature-sensing methods [29]

voltage difference is calibrated. This mode of temperature measurement is beneficial to relate various machining parameters like depth of cut, feed rate and the speed involved to the variation of temperature. Different thermocouple techniques are discussed below.

2.1.1 Embedded Thermocouple

This technology involves introducing thermocouples into suitable sized hole in the workpiece material referring to as an 'embedded thermocouple.' These thermocouples are generally mounted in proximity to the surface where the temperature needs to be calculated. Figure 3 depicts the use of embedded thermocouples in case of milling operation.

2.1.2 Tool/Workpiece Thermocouple

The experimental setup of this technique is quiet simple as shown in Fig. 4. In this case, the machining temperature is associated with the emf produced across the hot interface between tool and workpiece. Application of this methodology is largely seen in case of tool inserts. This technique poses limitation in finding temperature

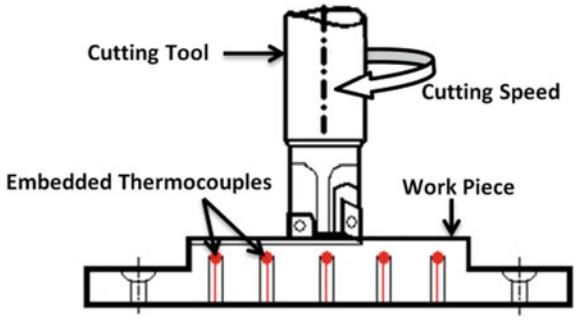

Fig. 3 Milling temperature measurement using embedded thermocouples [31]

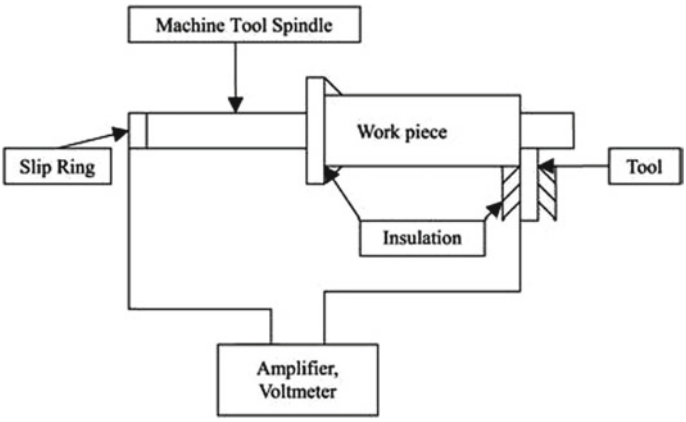

Fig. 4 Tool/workpiece thermocouple experimental setup [31]

distribution at various points of the tool in single setup. Like embedded thermocouple, this technique is too limited to dry cutting while it has a good dynamic response.

2.1.3 Single-Wire Thermocouple

In this thermocouple as the name suggests, an insulated wire is inserted through the workpiece by dividing the part into two across the line of cutting as depicted in Fig. 5.

The thin wire is cut during milling, exposing it and forming a thermocouple between the wire and the cutting tool [32] as shown in Fig. 6. In this method, very short signal duration is seen only during electrical contact with the wire. Thus, high sampling rate is necessary in order to record the signal during the short measurement interval [29]. With this technique, remote measurement is feasible and setup is simple. Several repetitions as well as variance analysis are desirable due to short contact times and electrical conduction problems.

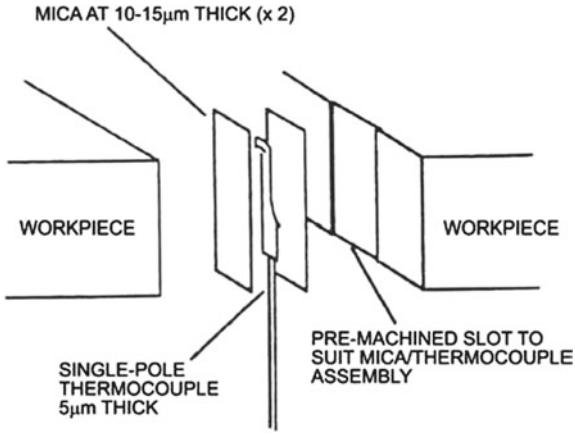

Fig. 5 Installation of single-wire thermocouple

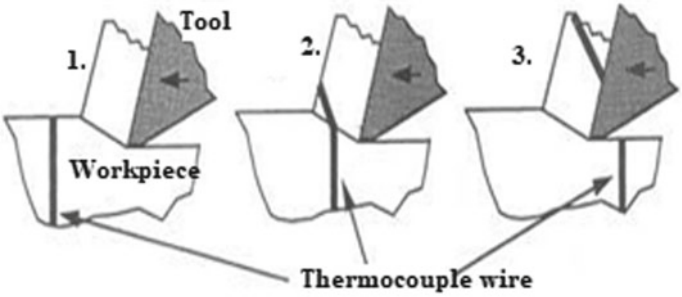

Fig. 6 Single-wire thermocouple measuring process

2.1.4 Transverse Thermocouple

These thermocouples are used in finding the tool temperature distributions on the rake face of the tool at the chip–tool interface [33]. The setup of transverse thermocouple arrangement is depicted in Fig. 7. The thermoelectric junction comprises the tool material and the probe material. As the position of the sharp probe changes, the readings of the temperature distribution relative to a specific edge are recorded [33].

Therefore according to the need, wherever the temperature is of interest the sharp probe can move on the tool surface which enables measurements of 3D temperature distribution. Though the experimental setup is complex, yet this method helps in predicting the position of tool wear.

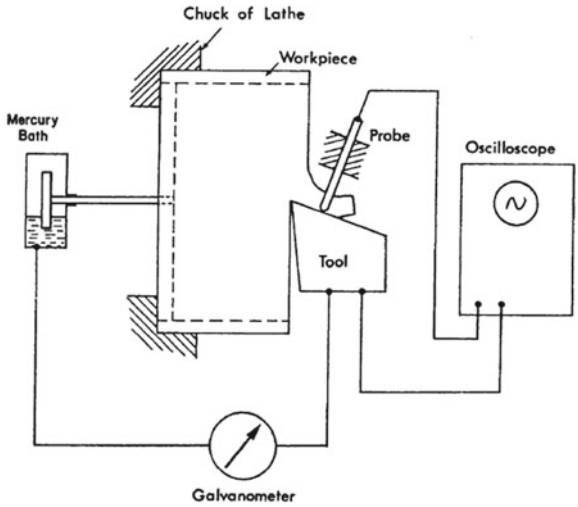

Fig. 7 Transverse thermocouple setup [16]

2.2 *Thermochemical Powders*

This method involves shaping the cutting tool in two divisions having symmetrical interface. While assembling, a coating of powder is applied to the region. Thermochemical powders having varying melting points are used, at a time, and the temperature distribution is determined by repeating the experiments. Isotherms are generated using this method which indicate temperature distribution as seen in Fig. 8. With this technique, it is simple to detect boundaries and also no calibration is required, because of the constant melting points of the powders used. The different thermochemical powders used in this technique along with their melting and boiling point are mentioned in Table 2.

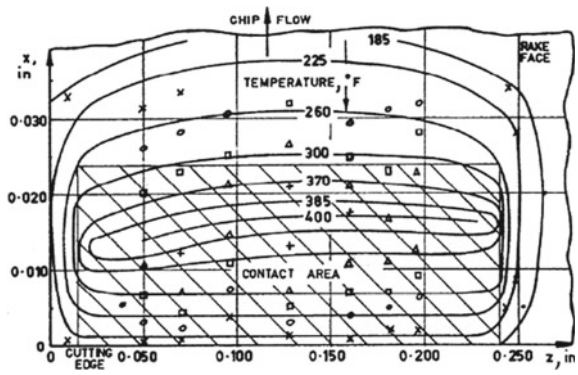

Fig. 8 Temperature isotherms on rake face [34]

Table 2 Thermochemical powders and their respective melting points [31]

Chemical substance	Melting point (°C)	Boiling point (°C)
NaCl	800	1413
KCl	776	1500
CdCl	568	960
$PbCl_2$	501	964
AgCl	455	1550
Zn	419	907
KNO_3	339	–
Pb	327.4	1750
$SnCl_2$	246.8	623
Sn	231.9	2270

2.3 Thermal-Sensitive Paint Method

In order to estimate the temperature distribution, another method called thermal-sensitive paint method is employed, in which the specimen is coated with the thermo-sensitive paints which change their color at known temperatures. For tracing the isothermal lines, this technique is found to be suitable [30]. It is reported that this method finds its best suitability for qualitative comparison of temperatures. The limitations of this method are the response time and accuracy for small temperature variations. This technique is of low cost and is easy to use. The limitation of this method is that it requires controlled heat transfer environment and is not suitable for use with cooling/lubrication.

2.4 Metallurgical Method

This method utilizes metallurgical deformation and hardness change which the cutting tool possesses post-machining operation which can be correlated with temperature. With the help of metallographic investigation, the structural changes can be examined. The microstructure obtained from the tool/workpiece is matched to reference microstructures, which aids in calculating temperature. These structural changes make it suitable to map the temperature distribution. On the other hand, micro-hardness measurements can be performed on the tool after the cutting to determine temperature counters. This method is time consuming and requires accurate hardness measurement [33]. Application is restricted to suitable conditions like high range of temperature and materials like high-speed steel. This method proves to be insensitive when there is no microstructural change.

2.5 Infrared Camera

It is a technique to estimate the surface temperature of the body based on the thermal energy produced by the body. This technique is accessible for point measurement as in case of infrared pyrometers and infrared thermograph. The radiation method offers rapid response and material safety, and allows measurements on objects over thermoelectric technique. However, proper measurement location has to be opted as it may hinder the accuracy by chip obstruction. Calculation of the tool–chip interface temperature also becomes difficult due to chip obstruction, hence avoided. Exact emissivity of the surface is desirable as it affects the measured temperature [8].

3 Results and Discussion

As per the review from the above works mentioned on various techniques of temperature-sensing, an exact approach for measuring temperature depends as per the problem, like the ease with the sensor can be installed to the location desired, accuracy required, setup cost, data acquisition and analysis, innovations in sensor technology measurement. In case of embedded thermocouple, frequent repetition as well as several variance analyses has to be performed. In case of transverse thermocouple using sharp probe, temperature can be determined at different locations. Using infrared technique, safety of the workpiece as well as tool can be ensured as no harm is imposed on the material unlike other sensing techniques. Some of the techniques find itself suitable for a particular condition in temperature detection, while some methodology poses limitation on temperature calculation. In the present paper, it can be seen that the temperature detection techniques are applied on turning, milling as well as grinding operations with tool material especially tungsten carbide.

4 Conclusion

- In metal cutting, most of the literature is related to turning, milling and grinding operation. There is a scope of estimating temperature in various other conventional as well as non-conventional machining operations.
- Calculation of temperature in the close proximity of the chip–tool interface is still a challenge.
- The use of embedded thermocouple is found to be better in terms of cost, ease of calibration and response time.
- Infrared techniques have certain advantages over other sensing techniques, but its limitation is the lack of emissivity value of novel materials as well as the hard and soft coatings done on the cutting tool.

- This review can help the new researchers working in the field of thermal sensors in machining as well as the industries in getting a brief idea of work carried out in recent years in different machining operations.

Acknowledgements The authors wish to express their gratitude to the Dr. A.P.J. Abdul Kalam Technical University, Lucknow, Uttar Pradesh, for the financial assistance provided to this study under Visvesvaraya Research Promotion Scheme (VRPS), letter no. Ref.: Dr. APJAKTU/Dean-PGSR/2019/4236-46/5109 dated June 8, 2019.

References

1. Abukhshim, N. A., & Mativenga, P. T. (2006). Heat generation and temperature prediction in metal cutting: A review and implications for high speed machining. *International Journal of Machine Tools and Manufacture, 46*(7–8), 782–800.
2. Shan, C., et al. (2019). An improved analytical model of cutting temperature in orthogonal cutting of Ti6Al4V. *Chinese Journal of Aeronautics, 32*(3), 759–769.
3. Baumgart, C., Heizer, V., & Wegener, K. (2018). In-process workpiece based temperature measurement in cylindrical grinding. *Procedia CIRP, 77*, Hpc, 42–45.
4. Ranc, N., et al. (2018). Temperature measurement by visible pyrometry: Orthogonal cutting application. To cite this version: HAL Id: hal-00283490 Temperature Measurement by Visible Pyrometry: Orthogonal Cutting Application.
5. Li, J., et al. (2018). Built-in thin film thermocouples in surface textures of cemented carbide tools for cutting temperature measurement. *Sensors and Actuators A: Physical, 279,* 663–670.
6. Sharma, A. K., et al. (2018). Prediction of temperature distribution over cutting tool with alumina-MWCNT hybrid nanofluid using computational fluid dynamics (CFD) analysis. *International Journal of Advanced Manufacturing Technology, 97*(1–4), 427–439.
7. Díaz-Álvarez, J. (2017). Temperature measurement and numerical prediction in machining inconel 718. *Sensors (Switzerland), 17*(7).
8. Davoodi, B., & Hosseinzadeh, H. (2012). A new method for heat measurement during high speed machining. *Measurement: Journal of the International Measurement Confederation, 45*(8), 2135–2140.
9. Ghafarizadeh, S., et al. (2016). Experimental investigation of the cutting temperature and surface quality during milling of unidirectional carbon fiber reinforced plastic. *Journal of Composite Materials, 50*(8), 1059–1071.
10. Choudhury, S. K., & Bartarya, G. (2003). Role of temperature and surface finish in predicting tool wear using neural network and design of experiments. *International Journal of Machine Tools and Manufacture, 43*(7), 747–753.
11. Yashiro, T., et al. (2013). Temperature measurement of cutting tool and machined surface layer in milling of CFRP. *International Journal of Machine Tools and Manufacture, 70,* 63–69.
12. Prakash, C., et al. (2019). Surface modification of Ti–6Al–4V alloy by electrical discharge coating process using partially sintered Ti-Nb electrode. *Materials (Basel), 12*(7).
13. Uddin, M., et al. (2018). Evaluating hole quality in drilling of Al 6061 alloys. *Materials (Basel), 11*(12).
14. Gupta, M.K., et al. (2018). Machinability investigations of Inconel-800 super alloy under sustainable cooling conditions. *Materials (Basel), 11*(11).
15. Pradhan, S., et al. (2019). Micro-machining performance assessment of Ti-based biomedical alloy: A finite element case study. *Biomanufacturing*, 157–183.
16. Dubey, V., & Singh, B. (2018). Study of material removal rate in powder mixed EDM of AA7075/B 4 C composite. *Materials Today: Proceedings, 5*(2), 7466–7475.

17. Tiwari, A.K., et al. (2019). Investigation on micro-residual stress distribution near hole using nanoindentation: Effect of drilling speed. *Measurement and Control*, 002029401985810.
18. Zhang, T., et al. (2019). Experimental technique for the measurement of temperature generated in deep lunar regolith drilling. *International Journal of Heat and Mass Transfer, 129,* 671–680.
19. Kesriklioglu, S., & Pfefferkorn, F. E. (2018). Real time temperature measurement with embedded thin-film thermocouples in milling. *Procedia CIRP, 77*(i), 618–621.
20. Ramirez-Nunez, J. A., et al. (2018). Smart-sensor for tool-breakage detection in milling process under dry and wet conditions based on infrared thermography. *International Journal of Advanced Manufacturing Technology, 97*(5–8), 1753–1765.
21. Urgoiti, L., et al. (2018). On the influence of infra-red sensor in the accurate estimation of grinding temperatures. *Sensors (Switzerland), 18*(12), 1–10.
22. Rizal, M., et al. (2018). An embedded multi-sensor system on the rotating dynamometer for real-time condition monitoring in milling. *International Journal of Advanced Manufacturing Technology, 95*(1–4), 811–823.
23. Werschmoeller, D., & Li, X. (2017). MSEC2010-. 1–7.
24. Sorrentino, L., et al. (2017). In process monitoring of cutting temperature during the drilling of FRP laminate. *Composite Structures, 168,* 549–561.
25. Tapetado, A., et al. (2016). Two-color pyrometer for process temperature. *IEEE Journal of Lightwave Technology, 34*(4), 1380–1386.
26. Gosai, M., & Bhavsar, S. N. (2016). Experimental study on temperature measurement in turning operation of hardened steel (EN36). *Procedia Technology, 23,* 311–318.
27. Baohai, W. (2016). Cutting tool temperature prediction method using analytical model for end milling. *Chinese Journal of Aeronautics, 29*(6), 1788–1794.
28. Sugita, N., et al. (2015). Cutting temperature measurement by a micro-sensor array integrated on the rake face of a cutting tool. *CIRP Annals—Manufacturing Technology, 64*(1), 77–80.
29. Longbottom, J. M., & Lanham, J. D. (2005). Cutting temperature measurement while machining—A review. *Aircraft Engineering and Aerospace Technology, 77*(2), 122–130.
30. Uchida, K., et al. (2008). Observation of the spin Seebeck effect. *Nature, 455*(7214), 778–781.
31. Conradie, P. J. T., Oosthuizen, G. A., & Treurnicht, N. F. (2011). Overview of workpiece temperature measurement techniques for machining of Ti6Al4V#. *South African Journal of Industrial Engineering, 23*(2), 116–130.
32. Da Silva, M. B., & Wallbank, J. (1999). Cutting temperature: Prediction and measurement methods—A review. *Journal of Materials Processing Technology, 88*(1), 195–202.
33. Komanduri, R., & Hou, Z. B. (2001). A review of the experimental techniques for the measurement of heat and temperatures generated in some manufacturing processes and tribology. *Tribology International, 34*(10), 653–682.
34. Arndt, G., & Brown, R. H. (1967). On the temperature distribution in orthogonal machining. *International Journal of Machine Tool Design and Research, 7*(1), 39–53.

Development of a Model for the Number of Bends During Stirrup Making Process

S. N. Waghmare, Sagar D. Shelare, C. K. Tembhurkar, and S. B. Jawalekar

Abstract Stirrup making is a process to angling reinforcement bars at expected edges into civil engineering work. Hand-operated bar bending requires vigorous physical exercise, which is generally done in a bad ergonomic atmosphere at construction site. This could begin to prolonged musculoskeletal complications such as profound back disorder among bar benders. Current research explains a numerical model for number of bends, torque and required time to process of a stirrup making method using human fortified flywheel motor based on testing data collected, applying a method of design for experimentation. Out of the above three models, the numerical model and its analysis for a number of bend for the stirrup producing process is described here. Findings obtained by the numerical model for a number of bends positively describes the degree of interaction of multiple independent parameters for stirrup producing operation.

Keywords Stirrup · Bar bending · Human power · Sensitivity analysis

1 Introduction

The civil construction business is the other most significant businesses in India giving work to higher than 35 million people, that is nearly 16 percentage of India's serving people [1]. However, an industry creates work possibilities on a massive scale, and over 80 percent of the workers are untrained [2]. Globally, construction places are intrinsically terrible, and every year, the industry proceeds to register few most significant levels of misfortune and destructiveness among all industrial divisions [3–5]. Also, by large safety management orders and enactment in place, industrial accidents continue a pervasive, yet preventable dilemma [4, 6, 7]. In civil engineering works, bending of the bar is a method to provide angle to reinforcement bars applied

S. N. Waghmare (✉) · S. D. Shelare · C. K. Tembhurkar · S. B. Jawalekar
Priyadarshini College of Engineering, Nagpur, M.S 440019, India
e-mail: subhashwaghmare1981@gmail.com

© Springer Nature Singapore Pte Ltd. 2021

C. Prakash et al. (eds.), *Advances in Metrology and Measurement of Engineering Surfaces* , Lecture Notes in Mechanical Engineering,
https://doi.org/10.1007/978-981-15-5151-2_7

as stirrups and support [8]. Although stirrups have been practiced since decades, various problems, such as getting the most effective geometrical stirrup pattern, are still subjects of constant investigation [3, 9, 10]. Stirrup bending is manual in most entire emerging countries, because of its cost-effectiveness [11].

At smaller civil construction site work, labors bend stirrup by the traditional approach [11]. No alternative significant method for crating the stirrup with the fewer human attempts same time; the detailed investigation of present manual stirrup-producing process shows that the process experiences different drawbacks.

In this paper, the stirrup is made from stirrup-creating setup driven by human-powered flywheel motor (HPFM) [12]. The stirrup-producing unit comprises two spur gears, and it is having 3/4 and 1/4 teeth; the gear drive is used to transmit the motion from energy unit to process unit shaft [13]. The rectangular helical spring is provided for tension and getting back the circular disk to its original position, it also provides the fixed pin which is utilized for bending the rod by 90 degrees by pressing the foot lever.

The conceptual design of stirrup producing consists of mainly pedal, sprocket, chain drive, flywheel and process unit (stirrup bending mechanism) as per Fig. 1. Fabricated setup of stirrup-producing machine is as per Fig. 2. Setup mainly consists of energy unit, transmission unit and process unit. The operator energizes the flywheel by pedaling conveniently. After storing the sufficient amount of energy, pedaling is stopped, and the energy is transferred with clutch. Five bending operations make the stirrups. The stirrup rod is first cut in predetermined length, and marking by chock then the five bending operations are performed as follows. Primarily, a smaller length of the rod is bent through inserting it into a guiding slot. By putting the rod at a centre

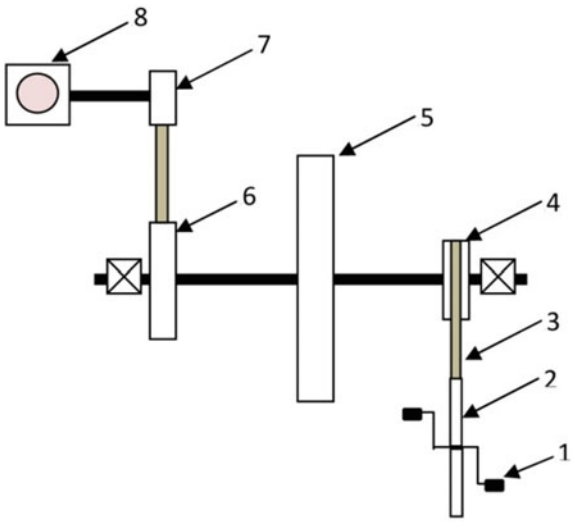

Fig. 1 Conceptual design of stirrup-producing machine. Where 1-pedal, 2-big sprocket, 3-chain drive, 4-smaller sprocket, 5-flywheel, 6-sprocket, 7-sprocket, 8-process unit (stirrup bending mechanism)

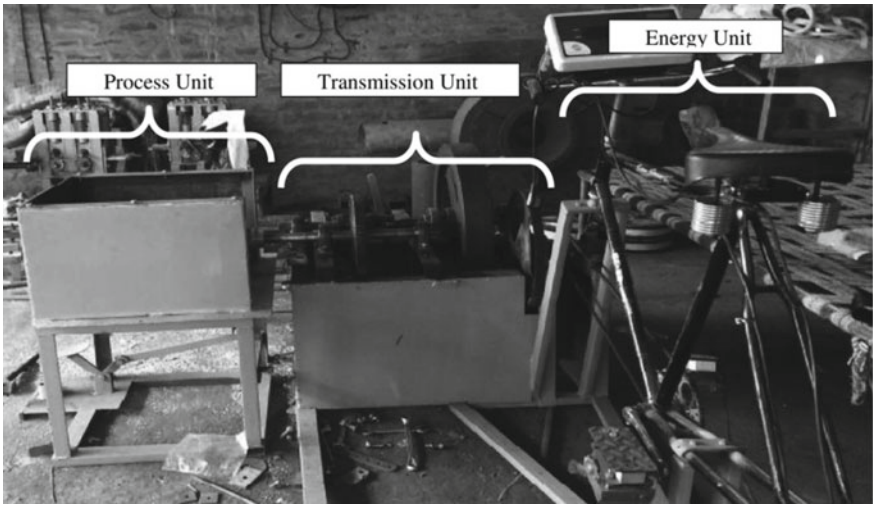

Fig. 2 Fabricated setup of stirrup producing the machine

position of the disc, operator needs to push and move the lever by foot. For the second bend, follow the same process based on the size of stirrup. Similarly third, fourth and fifth bend is made to obtain the perfect rectangular shape as per requirement.

2 Materials and Method

2.1 Experimental Model Formulation

For the model formulation, the method proposed as per Hilbert Schenck is used. This helps for deciding the minimum processing torque required, and human energy to be supplied to the system for getting bending operation for rod in minimum time [14]. By knowing this, one can form a relation for stirrup-creating method. This would be conceivable if we have a quantitative relationship among different dependent, independent parameters of the system. This relationship is the analytical model of stirrup-creating process. Notably, model of stirrup making cannot be made logically. The only alternative method is to form an innovative data-based model. In this methodology, all independent variables differ over a permissible range, a response data is gathered, and the relationship is established analytically.

In this experimentation process [15], torque (T_r), time to process (t_p) and no. of bends (n_b) are dependent or response variables whereas various independent variables are flywheel energy (E_f), angular speed (ω_f), time required to speed (t_f), stirrup

diameter (d_s), stirrup size (s), bend angle (θ), stirrup hardness (H_s), pin and center distance (r), ratio of gear (G), spring stiffness (k), rotating disk diameter (d_r), rotating disk thickness (t_r), acceleration because of gravity (g), stirrup length (L_s), elasticity modulus for stirrup (E_s).

2.2 Experimental Procedure

For experimentation, the stirrup rod of 6 mm plain, 6 mm TMT holding the equivalent diameter is prepared in the machine at three separate lengths, i.e., 968.4, 1068.4 and 1220.4 mm, at four separate speeds, ranging between 300 and 600 rpm, and at three separate gear ratios 1/2, 1/3 and 1/4. Hence, two diverse materials are utilized for experimentation to control an exact use of machine. Speed need to be achieved is shown in the GUI with instrumentation system. During the experimentation process, time, torque, bend number, flywheel time to speeding, etc., are noted by a uniquely designed electronic kit, i.e., instrumentation system presented in Fig. 3 [16] (Tables 1, 2 and 3).

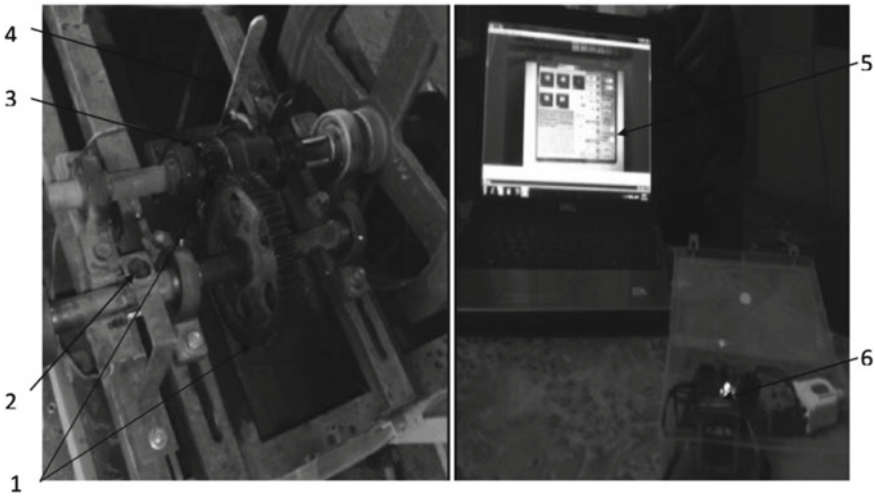

Fig. 3 Experimental arrangement and electronic kit for speed measurement with software and sensors. Where 1-speed rising gear pair, 2-sensor, 3-jaw clutch, 4-jaw clutch engaging disengaging lever, 5-instrumentation GUI showing speed, 6-electronic kit

Table 1 Plan of experimentation and observations when G.R = 0.5

S. No.	Size type	P.D	Rod type	G.R	(N)	(t_f)	(T_p)	(n_b)
1	Type-I	45.0	6-plain	0.5	300	35	56	7
2	Type-I	67.5	6-plain	0.5	300	35	63	11
3	Type-I	45.0	6-twist	0.5	300	35	91	15
4	Type-I	67.5	6-twist	0.5	300	42	91	19
5	Type-I	45.0	6-plain	0.5	400	28	32	10

Where $G.R$ gear ratio, $P.D$ pin distance, t_f flywheel time to speeding, N speed in rpm, T_p processing time, n_b no. of bend, Type-I-179 × 229 mm

Table 2 Plan of experimentation and observations when G.R = 0.33

S. No.	Size type	P.D	Rod type	G.R	(N)	(t_f)	(T_p)	(n_b)
1	Type-I	45.0	6-plain	0.33	300	28	42	6.5
2	Type-I	67.5	6-plain	0.33	300	21	42	10.5
3	Type-I	45.0	6-twist	0.33	300	42	91	16
4	Type-I	67.5	6-twist	0.33	300	56	77	17.5
5	Type-I	45.0	6-plain	0.33	400	28	42	9

Where $G.R$ gear ratio, $P.D$ pin distance, t_f flywheel time to speeding, N speed in rpm, T_p processing time, n_b no. of bend, Type-I-179 × 229 mm

Table 3 Plan of experimentation and observations when G.R = 0.25

S. No.	Size type	P.D	Rod type	G.R	(N)	(t_f)	(T_p)	(n_b)
1	Type-I	45.0	6-Plain	0.25	300	35	49	8
2	Type-I	67.5	6-Plain	0.25	300	28	63	10.5
3	Type-I	45.0	6-Twist	0.25	300	49	77	15
4	Type-I	67.5	6-Twist	0.25	300	30	80	19
5	Type-I	45.0	6-Plain	0.25	400	28	56	8

Where GR gear ratio, PD pin distance, t_f flywheel time to speeding, N speed in rpm, T_p processing time, n_b no. of bend, Type-I-179 × 229 mm

2.3 Formulation of Model by Dimensional Analysis

As per the dimensional analysis, bend number is written in function form as [17]:

$$n_b = f_2(E_f, \omega_f, t_f, d_s, s, \theta, H_s, r, G, k, d_r, t_r, g, L_s, E_s)$$

Total independent variables, $n = 15$ and no. of fundamental units, $m = 3$.
No. of Π terms $= n - m = 15 - 3 = 12$.
A mathematical model of bend number (n_b) is obtained as-

$$(n_b) = f_2\left\{\left(\frac{E_f}{L_s^3 * E_s}\right)(\omega_f * t_f)\left(\frac{K}{L_s * E_s}\right)\left(\frac{H_s}{E_s}\right)\left(\frac{d_s * r * d_r * t_r}{L_s^4}\right)\left(\frac{S}{L_s^2}\right)(\theta * G)\right\} \quad (1)$$

2.4 Design of Experiments

In this experimentation, 144 experiments were designed based on sequential classical experimental design technique, generally proposed for engineering applications, Hilbert Schenck. The basic classical plan consists of keeping all but any independent parameters constant and changing this one variable over its range. The basic reason of experiments is to find correlation in 12 independent process variables with 3 dependent responses for stirrup-creating process optimization. Simultaneously varying the all 12 independent parameters was confusing as well as complicated. Therefore, every 12 independent process variables were decreased by dimensional analysis. Buckingham π theorem was accommodated to produce dimensionless π terms for reduction of process variables [18].

3 Analysis of Model

3.1 Analysis of Model for No. of Bends

For analysis of model for dependent pi term of number of bends n_b (Fig. 4)

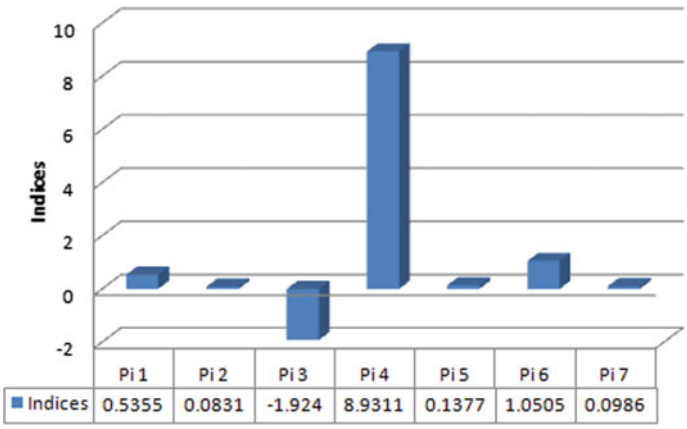

Fig. 4 Indices of dependent pie term for no. of bends

$$(n_{\mathrm{b}}) = 02.59656979 \times 10^{-9} \left\{ \begin{array}{c} \left(\frac{E_{\mathrm{f}}}{L_{\mathrm{s}}^3 * E_{\mathrm{s}}}\right)^{0.5355} (\omega_{\mathrm{f}} * t_{\mathrm{f}})^{0.0831} \left(\frac{K}{L_{\mathrm{s}} * E_{\mathrm{s}}}\right)^{-1.9243} \left(\frac{H_{\mathrm{s}}}{E_{\mathrm{s}}}\right)^{8.9311} \\ \left(\frac{d_{\mathrm{s}} * r * d_{\mathrm{r}} * t_{\mathrm{r}}}{L_{\mathrm{s}}^4}\right)^{0.1377} \left(\frac{S}{L_{\mathrm{s}}^2}\right)^{1-.0505} (\theta * G)^{0.0986} \end{array} \right\}$$

The reduced relationship for this pie term is given by $\pi_{02} = n_{\mathrm{b}}$.

It would be seen that equation is model for a pi term containing several bends (n_{b}) as a response variable.

The following primary outcome can be justified from the earlier model.

(i) The absolute index of π_4 is highest, viz. 8.9311. The factor π_4 is related to properties of material; i.e., elasticity and hardness are the common growing terms. Value of this index is positive, showing the correlation within ratio for elasticity and material hardness has a sturdy impact on π_{02}, and π_{02} is immediately changing concerning π_4.

(ii) The absolute index of π_2 is lowest, viz. 0.0831. Thus, π_2, the term related to angular speed and time required speeding up of flywheel angular speed and time needed to speeding of flywheel, is the least influencing term in model. The low value of absolute index indicates the factor, angular speed and time required to speeding of flywheel demand growth.

(iii) Importance of other independent pi terms existing in model is π_1, π_5, π_6 and π_7 having an absolute index of 0.5355, 0.1377, 1.0505 and 0.0986. The indices of π_3 are negative, viz. -1.924, respectively. The positive indices are indicating the need for improvement. The negative indices are showing that π_{02} varies inversely concerning π_3.

(iv) The constant in this model is $2.59656979 \times 10^{-9}$. This value is a lesser amount than one. So, it has no magnification outcome in the importance calculated from multiplication of various terms of model.

3.2 Sensitivity Analysis

An impact of the different independent π terms has investigated through examining an indices of those different π terms in a model [19]. When series of a change of $\pm 10\%$ is added in a value for independent pi term π_1, a change of about 10.72% occurs in quantity of π_{02} (computed from the model). The change brought in a value of π_{02} because of change into quantity of the other independent pi term π_2 is only 1.667%. Similarly, variation about 39.23, 195.2, 2.761, 21.01 and 1.978% takes place because of change in values of π_3, π_4, π_5, π_6 and π_7, respectively. It is observed that the biggest change is due to pi term π_4, whereas the least change takes place due to the pi term π_2. Thus, π_4 is the most sensitive pi term, and π_2 is the least sensitive pi term. The order of the different pie terms in the ascending order of sensitivity is π_2, π_7, π_5, π_1, π_6, π_3 and π_4 (Figs. 5 and 6).

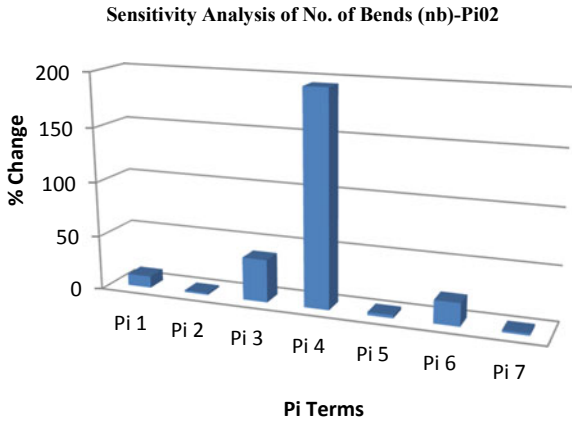

Fig. 5 Graphs illustrating sensitivity analysis, indices for Pi02

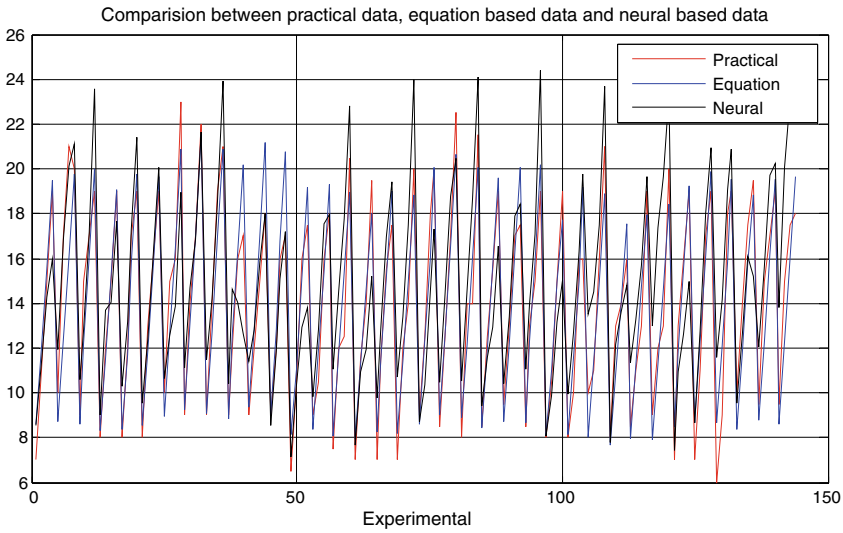

Fig. 6 Comparison of actual and computed data by ANN (for no. of bends n_b)

4 Conclusions

1. Sensitivity analysis shows stiffness of spring, rod material hardness, modulus elasticity of material is predominant over the considered independent parameters.
2. The machining attributes of stirrup-producing procedure are proved by the theory of experimentation, which was hidden in earlier cited investigation.
3. Presently most utmost, stirrups are created by the hand by the workers, and the stirrup-producing machines are operated utilizing electrical power, but the current machine uses HPFM creating a stirrup.

4. The data of stirrup-creating process is collected by performing actual experimentation. Due to this, the finding of study positively represents superiority of interplay of several independent variables. The standard error of estimate of predicted/computed dependent parameter values is found to be very low. This gives authenticity to improved analytical models and ANN.
5. The calculated choice of stirrup-forming method parameters with dimensional analysis gives practical direction to the production technicians so that they can minimize the time for optimal performance.
6. Developed setup produces intermittent energy, due to which speed obtained during operation is retarding, and a newer mechanism may be developed for constant speed.

References

1. Indian Construction Industry Overview. http://www.indianconstructionindustry.com/overview.html, [online].
2. Skill Development In Construction Sector. http://www.skillconindia.in/skillcon2013presentations/DAT213032013/SCSBIAG/DrMangeshKorgaonker.pdf, [online].
3. Tam, C. M., Zeng, S. X., & Deng, Z. M. (2004). Identifying elements of poor construction safety management in China. *42*, 569–586. https://doi.org/10.1016/j.ssci.2003.09.001.
4. Choudhry, R. M., Fang, D., & Lingard, H. (2009). Measuring safety climate of a construction company. 890–899.
5. Chi, C., Yang, C., & Chen, Z. (2009). In-depth accident analysis of electrical fatalities in the construction industry. *International Journal of Industrial Ergonomics, 39,* 635–644. https://doi.org/10.1016/j.ergon.2007.12.003.
6. Accident The (1981). Accident proneness: a conceptual.
7. Cheng, E. W. L., Ryan, N., & Kelly, S. (2012). Exploring the perceived influence of safety management practices on project performance in the construction industry. *50*, 363–365.
8. Group, R. B. (2006). Ergonomic assessment of bar cutting process in construction Venkatesh Balasubramanian and G. Swami Prasad.
9. De, Corte W., & Boel, V. (2013). Effectiveness of spirally shaped stirrups in reinforced concrete beams. *Engineering Structures, 52,* 667–675. https://doi.org/10.1016/j.engstruct.2013.03.032.
10. Berke, P. Z., & Massart, T. J. (2018). Modelling of stirrup confinement effects in RC layered beam finite elements using a 3D yield criterion and transversal equilibrium constraints. *International Journal of Concrete Structures and Materials*. https://doi.org/10.1186/s40069-018-0278-z.
11. Balasubramanian, V., & Prasad, G. S. (2007). Manual bar bending—An occupational hazard for construction workers in developing nations. 791–797.
12. Khope, P., Modak, J., & Singh, M. (2014). Development of human powered energy unit for fodder cutting. 4487, 158–160.
13. Modak, J. P., & Bapat, A. R. (1994). Formulation of a generalized experimental model for a manually driven flywheel motor and its optimization. *Applied Ergonomics, 25,* 119–122.
14. Schenck, H., Jr. *Theory of engineering experimentation*. New York, NY: McGraw Hill.
15. Waghmare, S. N., Sakhale, C. N., Tembhurkar, C. K., & Shelare, S. D. (2020). Assessment of average resistive torque for human-powered stirrup making process. In: B. Iyer, P. Deshpande, S. Sharma & U. Shiurkar (Eds.), *Computing in Engineering and Technology. Advances in Intelligent Systems and Computing* (Vol. 1025). Singapore: Springer. https://doi.org/10.1007/978-981-32-9515-5_79

16. Undirwade, S. K., Singh, M. P., & Sakhale, C. N. (2015). Experimental investigation of processing time, number of slivers and resistive torque required for human powered bamboo sliver cutting operation. *Journal of Bamboo and Rattan, 14,* 33–51.
17. Nwakuba, N. R., Ejesu, P. K., & Okafor, V. C. (2017). A mathematical model for predicting the drying rate of cocoa bean (*Theobroma cacao* L.) in a hot air dryer. *19*, 195–202.
18. Sakhale, C. N., Waghmare, S. N., K. S., Sonde, V. M., Singh, M. P. (2014). Formulation and comparison of experimental based mathematical model with artificial neural network simulation and RSM (response surface methodology) model for optimal performance of sliver cutting operation of bamboo. *Procedia Materials Science, 6*, 877–891.
19. Undirwade, S. K., Singh, M. P., & Sakhale, C. N. (2015). Experimental investigation of processing time, number of slivers and resistive torque required for human powered bamboo sliver cutting operation. *14*, 33–51.

Numerical Analysis of Heat Transfer in Ferrofluid Under Constant External Magnetic Field

Jaswinder Singh Mehta, Rajesh Kumar, Harmesh Kumar, and Harry Garg

Abstract This paper reports the numerical analysis of single-phase kerosene-based ferrofluid that passes through a circular-shaped closed loop. Permanent magnet has been employed to generate the magnetic field, and fluid flows as per thermo-magnetic convection principle. A two-dimensional, incompressible, and laminar flow has been considered while performing the time-dependent heat transfer study for the ferrofluid. The governing equations such as continuity, momentum, and energy equations are solved for steady-state incompressible flow using a partial differential equation based multiphysics finite element software, COMSOL Multiphysics 5.0. Simulation results indicate that magnitude of Kelvin body force rises with time as fluid flows with increased velocity resulting in successful dissipation of heat flux.

Keywords Heat transfer · Thermo-magnetic convection · Kelvin body force · Kerosene-based ferrofluid · Velocity contour

1 Introduction

Heat transfer augmentation is of paramount concern in electronics cooling and various other industrial cooling systems. Nanofluids, as of date, are used quite frequently for various applications requiring high rate of heat dissipation, and plethora of research work [1–9] in this field signify the interest of research community to explore various nanofluids for such applications. Recently, ferrofluids have caught the researchers' eye as the fluid can be manipulated in the presence of magnetic field. Ferrofluid is a distinct class of nanofluid whose thermo-physical properties could be customized as per system requirements, and variation in its flow rate can also be

J. S. Mehta (✉) · R. Kumar · H. Kumar
UIET, Panjab University, Chandigarh 160014, India
e-mail: jsmehta@pu.ac.in

H. Garg
CSIR-CSIO, Chandigarh, India

© Springer Nature Singapore Pte Ltd. 2021

C. Prakash et al. (eds.), *Advances in Metrology and Measurement of Engineering Surfaces* , Lecture Notes in Mechanical Engineering,
https://doi.org/10.1007/978-981-15-5151-2_8

made by changing the strength/frequency of magnetic field. The fluid is composed of magnetic particles of size usually less than 10 nm, and uniform suspension in a non-magnetic carrier fluid can be reasonably approximated [10].

The influence of asymmetrical magnetic field on heat transfer and pressure differential of water-based ferrofluid was experimentally examined. The fluid flows through uniformly heated parallel-plate channels, and the flow rate was varied between Reynolds number 20–1200. An augmentation in convective heat transfer coefficient was noticed with velocity and frequency of magnetic field while increase in volume fraction of fluid led to rise in pressure drop [11]. The effect of two kinds of magnetic arrangement on convective heat transfer coefficient of water-based ferrofluid was experimentally examined. The fluid passes through a stainless steel tube, and magnets were arranged in two different configurations along the flow direction. The authors observed higher augmentation of heat transfer coefficient for double in-line magnet arrangement as compared to single in-line arrangement at fixed flow rates. A significant enhancement in heat transfer capability of fluid was also found in the presence of magnetic field [12]. Cooling capability of thermo-magnetically pumped ferrofluid in vertical flow loop was studied. There was substantial decrease up to about 75% in size of heat sink with the use of ferrofluid. Also, high heat transfer enhancement factor was noted at higher static magnetic field strengths [13]. Flow and heat transfer characteristics of water-based ferrofluid were numerically investigated using CVFEM method. Rayleigh number, magnetic number, and particle volume fraction have direct bearing on average heat coefficient; however, with increase in Hartmann number, heat transfer coefficient was observed to decrease [14]. An experimental heat transfer analysis of a copper oscillating heat pipe filled with kerosene-based ferrofluid was performed. At a liquid filled ratio of 50%, the effect of magnetic field on temperature distribution and alteration in thermal resistance of the pipe was calculated. The authors compared the heat transfer of Fe_2O_3 nanofluid-charged oscillating heat pipe with kerosene-charged OHP and concluded that in the presence of magnetic field, substantial improvement in the former case was noticed due to reduction in its overall thermal resistance [15]. The effect of Reynolds number, location of line dipoles, and magnetic flux intensity on heat transfer characteristics of water-based ferrofluid passed through a two-dimensional duct was studied numerically using simple finite volume method. Increase in Reynolds number and magnetic field strength lead to improvement in convection heat transfer rate [16]. Convective heat transfer characteristics of water-based ferrofluid under different temperatures and magnetic field strengths varying from 100 to 200 G were analyzed experimentally. The fluid was passed through a hollow circular pipe, and convective heat transfer coefficient was observed to decrease under the effect of constant and uniform magnetic field. The intensity of magnetic field also had negative correlation with heat transfer coefficient. The authors argued that low Brownian motion along with increased viscosity might be the possible cause for reduction in heat transfer coefficient [17]. The impact of alternating magnetic field on convective heat transfer was examined, and it was deduced that heat transfer performance was enhanced with strength and frequency of the field. Non-accumulation of nanoparticles in vicinity to tube wall when the field was alternated was the primary cause behind augmentation

of heat transfer coefficient [18]. The performance of a miniature automatic energy transport device was measured experimentally. A temperature-sensitive magnetic fluid was allowed to flow through the loop. Flow behavior of magnetic fluid was envisaged using particle image velocimetry technique. With increase in applied heat flux, fluid flow velocity was found to increase and performance of the device was shown to be dependent on structure of the loop [19]. Heat transfer characteristics for a ferrofluid flowing through a square-shaped duct were experimentally evaluated. Higher volume fraction resulted in increase in Nusselt number while reverse trend was noted for mass flow rates when magnetic field was applied perpendicular to the heat flux [20].

The present work reports the numerical simulation of convective heat transfer of single-phase kerosene-based ferrofluid in a circular-shaped closed loop under the influence of an external magnetic field. Governing equations were solved using COMSOL Multiphysics 5.0, an FEA-based solver. Simulation results concluded that Kelvin body force was generated inside the ferrofluid when spatial thermal gradient exist along with non-uniform magnetic field. Velocity tends to grow with the passage of time resulting in movement of ferrofluid without the need of any external pump.

2 Computational Method

2.1 Geometrical Model

Figure 1 shows the schematic of the geometry employed for numerical analysis. A circular closed loop of outer diameter 180 mm and thickness 2 mm is taken. The ferrofluid flows through the annular space having outer and inner diameter as 178 mm and 175.5, respectively. A permanent magnet of size 25 × 7 mm and intensity 1T

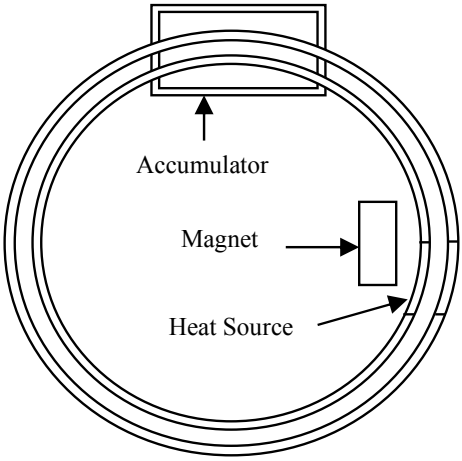

Fig. 1 Two-dimensional geometrical model

Table 1 Thermo-physical properties of ferrofluid

Sr. No.	Parameters	Value
1	Viscosity,μ	2 cP
2	Density,ρ	910 kg/m^3
3	Thermal conductivity,k	0.174 W/(m K)
4	Curie temperature of the fluid	65 °C
5	Surrounding temperature	20 °C
6	Magnetic susceptibility	0.386
7	Relative permeability	1.386

is being employed for generating external magnetic field. A constant heat flux of 2 W/cm^3 was applied. The problem undertaken was considered to be two dimensional, steady, and incompressible while flow was assumed to be non-turbulent in nature. No slip boundary conditions were assumed at the inner wall surface. The fluid was synthesized, and their thermo-physical properties were determined experimentally by the supplier and are used as such for the present study, the details of which are listed in Table 1.

2.2 Governing Equations

Since the magnetic nanoparticle size is less than 10 nm, the fluid is treated as homogenous fluid, and accordingly single-phase approach is adopted for modeling ferrofluid. The continuity, momentum, and energy equations [21] that govern the ferrofluid flow through the closed loop are as follows:

Mass continuity equation:

$$\frac{\partial \rho}{\partial t} + \nabla \cdot (\rho \vec{u}) = 0 \tag{1}$$

Momentum equation:

$$\rho \partial \vec{u}/\partial t + \rho \vec{u} \cdot \nabla \vec{u} = -\nabla p + \nabla \cdot \left(\mu \left(\nabla \vec{u} + \left(\nabla \vec{u}\right)^T\right) + \vec{F}\right. \tag{2}$$

Energy equation:

$$\rho c_p \left(\frac{\partial T}{\partial t} + \vec{u} \cdot \nabla T \right) = k \nabla^2 T \tag{3}$$

Magnetic induction:

$$\vec{B} = \mu_\circ \left(\vec{H} + \vec{M} \right) \tag{4}$$

Table 2 Grid independence study for the selected domain

Grid size	Fluid velocity (mm/s)
Normal	7.2765
Fine	7.6948
Finer	7.7257
Extra fine	7.7318
Extremely Fine	7.7311

Kelvin body force:

$$\vec{F} = \left(\vec{M} \cdot \nabla\right)\vec{B} \tag{2.5}$$

2.3 Grid Independence Test

Mesh size for the two-dimensional model was determined by conducting grid independence test. Velocity of the ferrofluid was estimated for all the grid settings used, and results are displayed in Table 2.

However, any mesh settings can be used, but physics-controlled fine mesh is being adopted for the selected domain as the best settings since no significant variations in the velocity values were observed upon increasing the mesh density further in order to access the velocity measurements accurately as shown in Fig. 2.

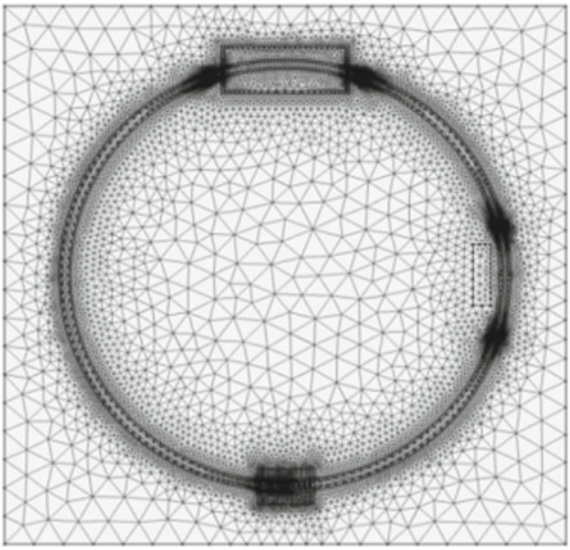

Fig. 2 Grid distribution used in the study

3 Results and Discussions

Figure 3 illustrates the temperature distribution inside the closed loop at different instant of time. As can be seen, the temperature of fluid keeps on rising up to its Curie temperature as the time progresses. A high temperature gradient exists near the heat source where permanent magnet is positioned.

The spatial thermal differential and non-uniform magnetic field were primarily the basis for generation of Kelvin body force. The Kelvin body force, thus, becomes the driving force, and fluid begins to flow due to this.

The velocity field inside the loop at different length of time is depicted in Fig. 4. There has been a spontaneous increase in velocity with time. The region of maximum velocity is found where the magnet is positioned and at the instant just when the fluid is about to enter into the heated length. The existence of higher temperature gradient and non-uniform magnetic field at that location is the principal reason for generation of Kelvin body force.

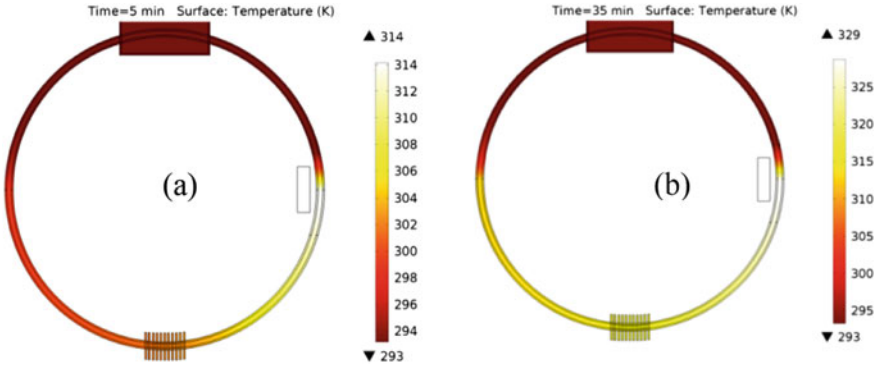

Fig. 3 Temperature distribution inside loop at different length of time **a** 5 min **b** 35 min

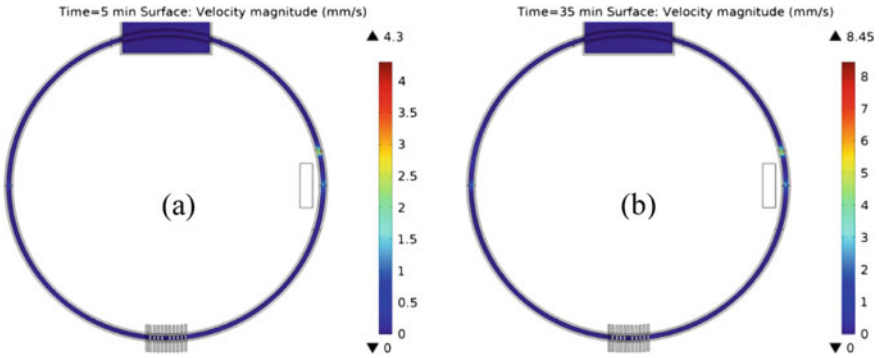

Fig. 4 Velocity contours (mm/s) inside the loop at different point of time **a** 5 min **b** 35 min

Velocity vectors showing the direction of flow of ferrofluid in the loop have been represented in Fig. 5. The fluid flows in clockwise direction under the effect of magnetic field generated by permanent magnet. Velocity profile of the ferrofluid as depicted in Fig. 6, clearly indicating the growing magnitude of velocity with time.

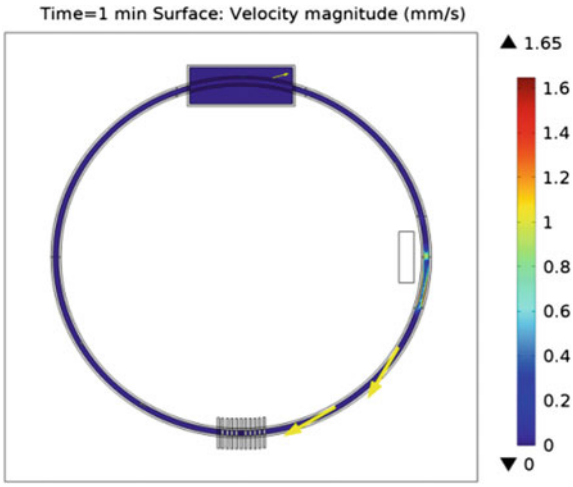

Fig. 5 Velocity vectors indicating fluid flow direction

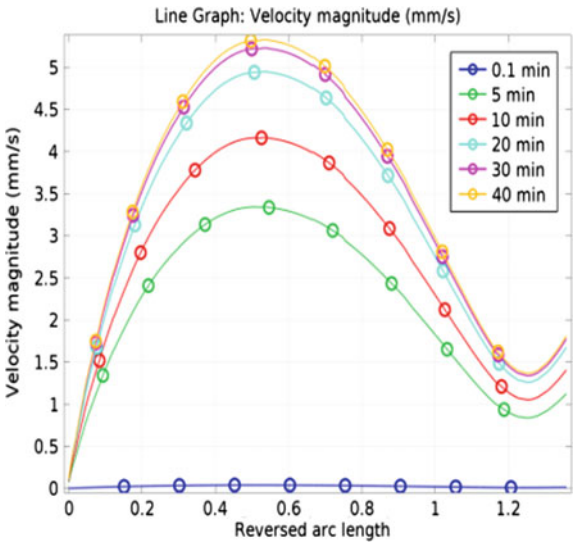

Fig. 6 Fluid velocity profile

4 Conclusions

Following conclusions could be drawn from the simulation study:

1. Temperature contours representing the variations of temperature in the loop reaffirm the movement of ferrofluid under the effect of external magnetic field. Colder fluid displaces the hot fluid as it passes through the heated length due to Kelvin body force, and as the fluid travels, it dissipates its heat to the surrounding air.
2. Velocity contours and velocity profile signify the increase in magnitude of fluid velocity with time. With the passage of time, fluid was heated in close vicinity to its Curie temperature resulting in existence of higher thermal differential, and thus, strength of Kelvin body force increases and it in turn leads to faster fluid movement that result in quick extraction of heat. This effect is very much similar to natural convection where hot, lesser dense fluid is displaced by colder, denser fluid.
3. Maximum fluid velocity of 8.45 mm/s was found at $t = 35$ min near the location where permanent magnet is positioned. The flow was also found to be continuous and laminar in nature with parabolic velocity profile.

Simulation results illustrate the heat transfer potential of ferrofluid and the distinct advantage of ferrofluid-based miniature cooling system is that system is totally passive in nature. The fluid can be tailored as per design requirement and maneuvered under the influence of magnetic field.

5 Future Recommendations

Further laboratory testing aided by numerical simulations would help to better understand the behavior of ferrofluid when subjected to magnetic field. The effect of different angles of magnet orientation and nanoparticle volume fraction on the heat transfer effectiveness of ferrofluid-based cooling system should be recommended for future studies.

References

1. Lomascolo, M., Colangelo, G., Milanese, M., & de Risi, A. (2015). Review of heat transfer in nanofluids: Conductive, convective and radiative experimental results. *Renewable and Sustainable Energy Reviews, 43*, 1182–1198.
2. Raja, M., Vijayan, R., Dinesh, K. P., & Venkatesan, M. (2016). Review on nanofluids characterization, heat transfer characteristics and applications. *Renewable and Sustainable Energy Reviews, 64,* 163–173.
3. Sheikholeslami, M., & Ganji, D. D. (2017). Nanofluid flow and heat transfer in the presence of constant magnetic field. Micro and nano technologies. In *Applications of nanofluid for heat transfer enhancement* (pp. 279–384). William Andrew Publishing.

4. Li, Q., Xuan, Y., & Wang, J. (2003). Investigation on convective heat transfer and flow features of nanofluids. *Journal of Heat Transfer, 125,* 151–155.
5. Duangthongsuk, W., & Wongwises, S. (2009). Heat transfer enhancement and pressure drop characteristics of TiO_2-water nanofluid in a double-tube counter flow heat exchanger. *International Journal of Heat and Mass Transfer, 52,* 2059–2067.
6. Colangelo, G., Favale, E., Milanese, M., de Risi, A. Laforgia D. (2017). Cooling of electronic devices: Nanofluids contribution. *Applied Thermal Enginering, 127*, 421–435.
7. Agromayor, R., Cabaleiro, D., Pardinas, A. A., Vallejo, J. P., Fernandez-Seara, J., & Lugo, L. (2016). Heat transfer performance of functionalized graphene nanoplatelet aqueous nanofluids. *Materials, 9,* 455.
8. Zhang, H., Shao, S., Xu, H., & Tian, C. (2013). Heat transfer and flow features of Al_2O_3-water nanofluids flowing through a circular microchannel-experimental results and correlations. *Applied Thermal Engineering, 61,* 86–92.
9. Heris, S. Z., Etemad, S. G., & Esfahan, M. N. (2006). Experimental investigation of oxide nanofluids in laminar flow convective heat transfer. *International Communications in Heat and Mass Transfer, 33,* 529–535.
10. Rosensweig, R. E. (1997). *Ferrohydrodynamics* (2nd ed.). New York, NY: Dover Pub. Inc.
11. Goharkhah, M., Ashjaee, M., & Shahabadi, M. (2016). Experimental investigation on convective heat transfer and hydrodynamic characteristics of magnetite nanofluid under the influence of an alternating magnetic field. *International Journal of Thermal Sciences, 99,* 113–124.
12. Asfer, M., Mehta, B., Kumar, A., Khandekar, S., & Panigrahi, P. K. (2016). Effect of magnetic field on laminar convective heat transfer characteristics of ferrofluid flowing through a circular stainless steel tube. *International Journal of Heat and Fluid Flow, 59,* 74–86.
13. Aursand, E., Gjennestad, M. A., Lervåg, K. Y., & Lund, H. (2016). Potential of enhancing a natural convection loop with a thermomagnetically pumped ferrofluid. *Journal of Magnetism and Magnetic Materials, 417*, 148–159.
14. Sheikholeslami, M., & Rashidi, M. M. (2015). Effect of space dependent magnetic field on free convection of $Fe3O_4$–water nanofluids. *Journal of the Taiwan Institute of Chemical Engineers*, 1–10.
15. Goshayeshi, H. R., Goodarzi, M., & Dahari, M. (2015). Effect of magnetic field on the heat transfer rate of kerosene/Fe_2O_3 nanofluid in a copper oscillating heat pipe. *Experimental Thermal and Fluid Science, 68,* 663–668.
16. Ghorbani, B., Ebrahimi, S., & Vijayaraghavan, K. (2018). CFD modeling and sensitivity analysis of heat transfer enhancement of a ferrofluid flow in the presence of a magnetic field. *International Journal of Heat and Mass Transfer, 127,* 544–552.
17. Sha, L., Ju, Y., Zhang, H., & Wang, J. (2017). Experimental investigation on the convective heat transfer of Fe_3O_4/water nanofluids under constant magnetic field. *Applied Thermal Engineering, 113,* 566–574.
18. Mohammad, G., Armia, S., Mehdi, A., & Mahmoud, S. (2015). Convective heat transfer characteristics of magnetite nanofluid under the influence of constant and alternating magnetic field. *Power Technology, 274,* 258–267.
19. Lian, W., Xuan, Y., & Li, Q. (2009). Characterization of miniature automatic energy transport devices based on the thermomagnetic effect. *Energy Conversion and Management, 50*(1), 35–42.
20. Cherief, W., Avenas, Y., Ferrouillat, S., Kedous-Lebouc, A., Jossic, L., & Petit, M. (2017). Parameters affecting forced convection enhancement in ferrofluid cooling systems. *Applied Thermal Engineering, 123,* 156–166.
21. Neuringer, J. L., & Rosensweig, R. E. (1964). Ferrohydrodynamics. *Physics of Fluids, 7*, 1927 (1964).

Formulation of a Mathematical Model for Quantity of Deshelled Nut in Charoli Nut Deshelling Machine

Sagar D. Shelare, Ravinder Kumar, and Pravin B. Khope

Abstract Charoli (Buchanania lanzan) is a vital multipurpose tree and essential plant for a rural and tribal economy. Charoli tree gives food, fuel, fodder, wood, and medicine to the local rural and tribal society. In traditional ways, this Charoli kernel removal is made manually by using hammer and hands due to which there is lower efficiency with damaged and broken kernels. Hence, there is a demand to create an indigenous and sustainable design of Charoli nut desheller for improvement in Charoli nut processing efficiency and reducing the wastage occurring due to kernel damage. In this investigation, a theoretical mathematical model based on a dimensional analysis method was disclosed to identify the quantity of deshelled nut of a Charoli nut deshelling process. Dimensional analysis applying the Buckingham Pi (π) theorem was adopted to get an effective relationship among the quantity of deshelled nut and independent variables. Independent variables comprise diameter of grinding disk, thickness of grinding disk, number of grinding disk, clearance between two rotating disks, energy of flywheel, angular speed, time to speed up the flywheel, % moisture content, hardness of nut, moment of inertia of flywheel, gear ratio, bulk density of nut, and feed rate. Established relation is useful to the prediction of behavior between dependent and independent variables corresponding to the different process conditions.

Keywords Quantity of deshelled nut · Dimensional analysis · Buckingham pi (π) theorem · Mathematical model · Prediction equation

S. D. Shelare · R. Kumar (✉)
School of Mechanical Engineering, Lovely Professional University, Phagwara, Punjab 144411, India
e-mail: ravindernitcad@gmail.com

P. B. Khope
Department of Mechanical Engineering, Priyadarshini College of Engineering, Nagpur, M.S 440019, India

© Springer Nature Singapore Pte Ltd. 2021

C. Prakash et al. (eds.), *Advances in Metrology and Measurement of Engineering Surfaces* , Lecture Notes in Mechanical Engineering,
https://doi.org/10.1007/978-981-15-5151-2_9

1 Introduction

Charoli or chironji or belonged to the species Anacardiaceous and was first reported by Francis Hamilton in 1798. It is utilized as fuel, food particularly for buffalos, and oil for soaps and beautifying products [1]. The kernels are incredibly nutritious which are being used in confectionery products. Charoli oil is utilized as a replacement for almond and olive oil toward glandulous injury of the neck, and Charoli nuts are diuretic. Kernels are also used as a medicine in epidermis diseases [2]. Charoli tree yields amber benzoin alike but secondary to that of Styrax benzoin. It is an exceptional tree of agroforestry and social forestry for wasteland improvement; it finds high importance due to its diverse applications and ability to resist the unfavorable climatic situation [3]. Currently, it is developing below forest condition as underexploited products and provides a portentous compensation for the tribal population. Charoli is worthy and located in dry woodland everywhere in the country [4, 5]. The pulp of the matured Charoli is tasty and is most of the time eaten fresh or dried. Mesocarp of the ripened Charoli is nutritious and adored by minors [6]. Charoli oil is healthy and is fit for individual consumption [7]. Apart from these advantages of Charoli nut, there is still no proper mechanism to deshell it. For this purpose, there is a scope to develop an indigenous and sustainable design of Charoli nut desheller for improvement in Charoli nut processing [8].

Dimensional analysis is a dominant and clear way applied to reduce the real, multifaceted difficulties into the purest form [9]. It is a renowned technique utilized in material science and popular engineering regions so as to approve the model formulation and to cut endeavors in the exact evaluation stages [10]. Physical factors, like mass, length, and time, give the link among science and the physical world [11]. As all know, particular notice of physical dimensions can provide a significant understanding of similarities between physical values. Mathematical modeling is a craft of creating mathematical relations which depict a procedure. A model empowers analysts to sort out the hypothetical guesses and accurate perceptions about the framework and to derive the profound meanings of the association [12]. In such manner, the Buckingham Pi theorem states that "any equation modeling a physical issue can be revised and improved utilizing a set of dimensionless factors so that the number of factors initially used to depict the issue can be decreased by the number of independent fundamental physical quantities utilized in the first equation" [13–18]. Buckingham's π theorem is a precise method in setting a forecast equation of several systems [19]. Confined work has been carried out on the deshelling process of Charoli, and no one has formed the mathematical model for output parameters of the Charoli nut deshelling. Hence, the existing research is undertaken to establish a mathematical model for predicting the quantity of deshelled nut of a Charoli nut deshelling process using the dimensional analysis.

2 Materials and Method

2.1 Experimental Setup

Experimental setup mainly comprises pedaling unit, energy unit, and process unit [20].

1. Pedaling Unit: Pedaling unit primarily consists of a bicycle, chain sprocket, pedal, chain, freewheel, bearings for bicycle side, and speed amplification gear pair.
2. Energy Unit: Energy unit mainly comprises a flywheel, torque amplification gear pair, bearings, and clutch
3. Process Unit: Process unit includes mostly a pair of an abrasive stone disk, cross plate, pair of the shaft, pair of bevel gear, three-layer screens with reducing grade size, and cam system.

where 1—seating arrangement, 2—large sprocket, 3—pedal, 4—chain, 5—small chain sprocket, 6—shaft B1, 7—bearing for bicycle, 8—gear I, 9—pinion, 10—shaft B2, 11—bearing, 12—flywheel unit, 13—clutch, 14—lever, 15—gear II, 16—gear III, 17—shaft B3, 18—shaft B4, 18—shaft B4, 19—clutch for process, 20—process unit.

In this current work, the peddling process of bicycle mechanism transmits the human energy to the kinetic energy of the flywheel [21]. The stored energy of the flywheel will be utilized as per need for the actual deshelling process. So, operations could be performed intermittently. Modak [22] reports on the functional feasibility and financial viability of bicycle operated mechanism.

A computer-aided model of proposed Charoli nut desheller setup is as given in Fig. 1. A driver sited on seat peddles pedal and converts the oscillatory motion into the rotational motion of flywheel, thereby increasing speed. The inertia required to the flywheel provided by the legs of the rider is only. The rider needs to store the energy in the flywheel as per his/her capacity. Thus, with the help of this human mechanism, human muscular strength gets converted into the rotational kinetic energy of the flywheel. It was essential to develop the energy unit of a similar kind for Charoli desheller scientifically.

2.2 Development of a Model to Predict the Quantity of Deshelled Nut

The homogeneity principle of the dimensional variable is utilized to determine a correlation among different physical quantities. To infer a physical relation, the dependent variables of a proposed substantial number are found. Then, final dimensional equation is written in the form of mass (M), length (L), and time (T) [23]. Comparing the powers of M, L, and T of the dimensional equation, three equations are formed to

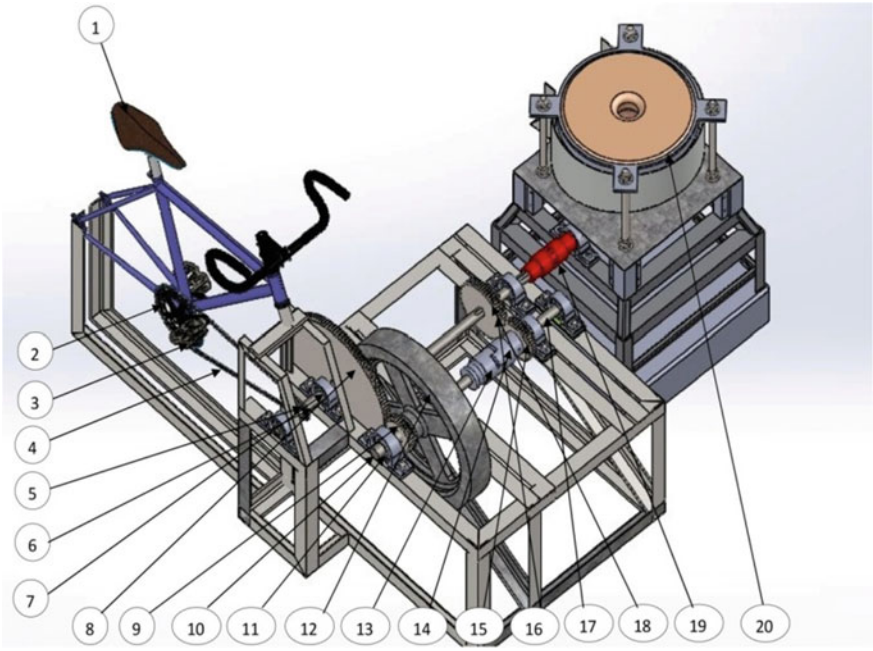

Fig. 1 Computer-aided model of Charoli nut desheller

estimate unknown powers. By substituting obtained values, the pure form of relation is achieved [24]. Table 1 expresses various fundamental units used in the model.

The physical parameters affecting the separation are:

a. Nut factor: % moisture content, the hardness of nut, and bulk density.
b. Machine factors: Diameter of grinding disk, the thickness of the grinding disk, number of grinding disk, clearance between two rotating disks, energy of flywheel, angular speed of flywheel, time to speed up the flywheel, moment of inertia of flywheel, gear ratio, and feed rate.

Dimensional analysis of the Buckingham pi π method was used to obtain the mathematical model.

For the calculation of the dimensionless pi terms, all dependent and independent variables need to express in terms of basic physical quantities first. Table 2 repre-

Table 1 Fundamental units used in the model

S.No.	Dimensions	Symbol	Unit
1	Length	*L*	m (meter)
2	Mass	*M*	Kg (Kilogram)
3	Time	*T*	sec (Second)

Table 2 Selected parameters and their corresponding dimensions

Type of variable	Description of variables	Symbol	Unit	Dimensions
Dependent	Quantity of deshelled Nut	Q	Kg	$[M^1L^0T^0]$
	Instantaneous Torque on grinding disk	Ti	N-m	$[M^0L^2T^{-2}]$
	Process time for deshelling	T	S	$[M^0L^0T^1]$
Independent	Diameter of grinding disk	d	m	$[M^0L^1T^0]$
	The thickness of the grinding disk	t	m	$[M^0L^1T^0]$
	Number of grinding disk	N	–	$[M^0L^0T^0]$
	Clearance between two rotating disks	Cl	*m*	$[M^0L^1T^0]$
	Energy of Flywheel	Fe	N-m	$[M^0L^2T^{-2}]$
	The angular speed of flywheel	ω	Rad/sec	$[M^0L^0T^{-1}]$
	Time to speed up the flywheel	tf	S	$[M^0L^0T^1]$
	Moment of Inertia of a flywheel	I	Kg-m^2	$[M^1L^2T^0]$
	Gear Ratio	G	–	$[M^0L^0T^0]$
	% Moisture content	Mc	d.b.	$[M^0L^0T^0]$
	Hardness of Nut	Hn	N/m^2	$[M^0L^{-1}T^{-2}]$
	Bulk density	ϱ	Kg/m^3	$[M^1L^0T^{-3}]$
	Feed rate	F	kg/hr	$[M^1L^0T^{-1}]$

sents the various parameters involved in this research work in terms of fundamental physical quantities [25].

For development of model, the following assumptions were made [26],

1. Dimensions of nut dimension are constant at the identical moisture content,
2. Shell thickness is equal at the identical moisture content,
3. Age of the nut is the identical,
4. Weight and volume of every nut are constant at identical moisture content.

The quantity of deshelled nut can be expressed as follows:

$$Q = f(t, N, \text{Cl}, \text{Fe}, tf, I, G, \text{Mc}, \text{Hn}, F, d, \omega, \varrho) \tag{1}$$

The variables of interest that determine the quantity of deshelled (Q) are 14 and the number of units is 3; so, the number of π terms is 11. It follows that π1; π2; π3; π4; π5; π6; π7; π8; π9; and π10 for independent variables and π01 for dependent variable will be formed. From the above matrix, N, G, and Mc are dimensionless and therefore excluded from the dimensionless terms determination and are added when other dimensionless terms are determined [26].

$$Q = f(t, \text{Cl}, \text{Fe}, \text{tf}, I, \text{Hn}, F, d, \omega, \varrho) \tag{2}$$

The dimensional equation is as follows:

$$f(Q, t, \text{Cl}, \text{Fe}, \text{tf}, I, \text{Hn}, F, d, \omega, \varrho) = 0 \tag{3}$$

Before initiating the investigation of the problem, it is required to choose the repeating variables. While selecting repeating variables, ensure certain variables must include all of the fundamental dimensions, i.e., (M, L, T). A combination of the repeating variables must not form a dimensionless group and must be measurable [27]. As per the criteria, diameter of grinding disk (d), angular speed of flywheel (ω), and bulk density (ϱ) are selected as repeating variables.

The dimensionless groups based on the Buckingham's π theorem are made by using all of the left variables,

$$(\pi_1) \text{ for thickness of grinding disk, } \pi_1 = \frac{t}{d} \tag{4}$$

$$(\pi_2) \text{ for number of grinding disk, } \pi_2 = N \tag{5}$$

$$(\pi_3) \text{ for clearance between two rotating disks, } \pi_3 = \frac{C_l}{d} \tag{6}$$

$$(\pi_4) \text{ for energy of flywheel, } \pi_4 = \frac{F_e}{d^2\omega^2} \tag{7}$$

$$(\pi_5) \text{ for time to speed up the flywheel, } \pi_5 = t_f \frac{1}{\omega} \tag{8}$$

$$(\pi_6) \text{ for moment of inertia of flywheel, } \pi_6 = I \frac{\omega}{\varrho d^5} \tag{9}$$

$$(\pi_7) \text{ for gear ratio, } \pi_7 = G \tag{10}$$

$$(\pi_8) \text{ for \% moisture content, } \pi_8 = M_c \tag{11}$$

$$(\pi_9) \text{ for hardness of nut, } \pi_9 = H_n \frac{\mathrm{d}}{\omega^2} \tag{12}$$

$$(\pi_{10}) \text{ for feed rate, } \pi_{10} = F \frac{1}{d^3 \varrho \omega} \tag{13}$$

Formulation of Pi terms for dependent parameters

$$(\pi_{01}) \text{ for quantity of deshelled Nut, } \pi_{01} = \frac{Q}{d^3 \varrho} \tag{14}$$

Putting respecting π term in Eq. (3),

$$f(\pi_{01}\pi_1\pi_3\pi_4\pi_5\pi_6\pi_9\pi_{10}) = 0$$

$$f\left\{\left(\frac{Q}{d^3\varrho}\right)\left(\frac{t}{d}\right)\left(\frac{C_l}{d}\right)\left(\frac{F_e}{d^2\omega^2}\right)\left(\frac{t_f}{\omega}\right)\left(I\frac{\omega}{\varrho d^5}\right)\left(H_n\frac{d}{\omega^2}\right)\left(\frac{F}{d^3\varrho\omega}\right)\right\} = 0 \quad (15)$$

$$(Q) = (d^3\varrho)K\left\{\left(\frac{t}{d}\right)\left(\frac{C_l}{d}\right)\left(\frac{F_e}{d^2\omega^2}\right)\left(\frac{t_f}{\omega}\right)\left(I\frac{\omega}{\varrho d^5}\right)\left(H_n\frac{d}{\omega^2}\right)\left(\frac{F}{d^3\varrho\omega}\right)\right\} \quad (16)$$

3 Results and Discussion

The prediction equation of quantity of deshelled nut in a Charoli nut deshelling machine is developed as below

$$(Q) = (d^3\varrho)K\left\{\left(\frac{t}{d}\right)\left(\frac{C_l}{d}\right)\left(\frac{F_e}{d^2\omega^2}\right)\left(\frac{t_f}{\omega}\right)\left(I\frac{\omega}{\varrho d^5}\right)\left(H_n\frac{d}{\omega^2}\right)\left(\frac{F}{d^3\varrho\omega}\right)\right\}$$

The diameter of the grinding disk and the bulk density plays a crucial role in the quantity of deshelled nut. Quantity of deshelled nut is directly affected by the diameter of the grinding disk and the bulk density [28]. To maximize the quantity of deshelled nut, most of the attention needs to pay on the diameter of the grinding disk and the bulk density. Quantity of deshelled nut is directly proportional to the cube of the diameter of the grinding disk and the bulk density.

The dimensionless ratio for individual dependent and independent variable is formed and is given in Table 3

The performance of data in non-dimensional groups enables the utilization of innovative relationship to wide range physical conditions. The dimensionless ratio/π values provide the concept related to the consolidated impact of process variables in

Table 3 Dimensionless ratio for individual parameters/π term

Type of variable	Dimensionless ratio/π term	Nature of basic physical parameters
Independent	$\pi_1 = \frac{t}{d}$	The thickness of the grinding disk
	$\pi_2 = N$	Number of grinding disk
	$\pi_3 = \frac{C_l}{d}$	Clearance between two rotating disks
	$\pi_4 = \frac{F_e}{d^2\omega^2}$	Energy of Flywheel
	$\pi_5 = t_f\frac{1}{\omega}$	Time to speed up the flywheel
	$\pi_6 = I\frac{\omega}{\varrho d^5}$	Moment of Inertia of flywheel
	$\pi_7 = G$	Gear Ratio
	$\pi_8 = M_c$	% Moisture content
	$\pi_9 = H_n\frac{d}{\omega^2}$	Hardness of Nut
	$\pi_{10} = F\frac{1}{d^3\varrho\omega}$	Feed rate
Dependent	$\pi_{01} = \frac{Q}{d^3\varrho}$	Quantity of deshelled Nut

that π value. A mild alteration in individual process variables in the group helps the researcher to optimize the output as per requirement.

4 Conclusions

A theoretical mathematical model for the quantity of deshelled nut was developed based on the Buckingham pi theorem concerning to dimensional analysis phenomena, considering the various Charoli nut and machine parameters. The mathematical model has been predicted for maximization of the quantity of deshelled nut, i.e., $(Q) = (d^3\varrho)K\left\{\left(\frac{t}{d}\right)\left(\frac{C_l}{d}\right)\left(\frac{F_e}{d^2\omega^2}\right)\left(\frac{t_f}{\omega}\right)\left(I\frac{\omega}{\varrho d^5}\right)\left(H_n\frac{d}{\omega^2}\right)\left(\frac{F}{d^3\varrho\omega}\right)\right\}$. Model for quantity of deshelled nut is described in terms of thickness of grinding disk, a number of grinding disk, clearance between two rotating disks, the energy of flywheel, time to speed up the flywheel, a moment of inertia of the flywheel, gear ratio, % moisture content, and hardness of nut feed rate. Dimensional analysis using the Buckingham Pi theorem could be a veritable tool in the modeling of agricultural and food engineering studies. The developed models provide a highly simplified representation to optimize the quantity of deshelled nut. The model can thus be used to predict the quantity of deshelled nut for a Charoli nut deshelling machine.

References

1. Hiwale, S. (2015). Sustainable horticulture in semiarid dry lands. Sustain Hortic Semiarid Dry Lands, pp. 1–393. https://doi.org/10.1007/978-81-322-2244-6.
2. Das, D., & Agrawal, V. S. (1991). *Fruits Drug Plants of India* (p. 250). New Delhi: Kalyani Publisher.
3. Kumar, J., Prabhakar, P. K., Srivastav, P. P., & Bhowmick, P. K. (2016). Moisture Dependent Physical Properties of Chironji (Buchanania lanzan) Nut. *Journal Agriculture Engineering, 53*(2), 45–54.
4. Singh, R. V. (1982). *Fodder Trees of India* (p. 663). New Delhi: Oxford and IBH Publication.
5. Singh, S., Singh, A. K., Bagle, B. G. (2006). Chironji (Buchnania Lanzan Spreng.). A boon for tribals. Intensive Agriculture, March–April, pp. 35–36.
6. Munde, V. M., Shinde, G. S., Sajindranth, A. K., Prabu, T., & Machewad, P. M. (2003). Correlation and path analysis studies in Charoli (Buchanania lanzan Spreng). *South Indian Hortic, 50,* 517–521.
7. Bandyopadhyay, A., & Banerjee, S. (2014). Buchanania lanzan spreng: A veritable storehouse of phytomedicine. *Asian Journal Pharm Clinical Research, 8,* 18–22.
8. Kumar, J., Vengaiah, P. C., Srivastav, P. P., & Bhowmick, P. K. (2012). Chironji nut (Buchanania lanzan) processing, present practices and scope. *Indian Journal Traditional Knowledge, 11,* 202–204. https://doi.org/10.5935/1806-6690.20150001.
9. Jamadar, I. M., Vakharia, D. P. (2016). A numerical model for the identification of the structural damages in rolling contact bearings using matrix method of dimensional analysis, 138, 1–12. https://doi.org/10.1115/1.4031989.
10. Nwakuba, N. R., Ejesu, P. K., Okafor, V. C. (2017). A mathematical model for predicting the drying rate of cocoa bean (Theobroma cacao L.) in a hot air dryer, *19*, 195–202.

11. Too, D. (2003). Factors affecting performance in human powered vehicles : a biomechanical model. Kinesiology, Sport Studies and Physical Education Faculty Publications, *99*.
12. Kawuyo, U.A. (2018). Mathematical modeling of draught characteristics of animal-drawn implements on upland soils of Samaru, Nigeria, vol. 9, pp. 6–18.
13. Miragliotta, G. (2011). The power of dimensional analysis in production systems design. *International Journal Production Economics, 131,* 175–182. https://doi.org/10.1016/j.ijpe.2010.08.009.
14. Reddy, G. M., & Reddy, V. D. (2014). Theoretical investigations on dimensional analysis of Ball Bearing parameters by using Buckingham Pi-Theorem. *Procedia Engineering, 97,* 1305–1311. https://doi.org/10.1016/j.proeng.2014.12.410.
15. Rostampour, A., Mohammad, H. (2013). Improve regression-based models for prediction of internal-bond strength of particleboard using Buckingham' s pi-theorem, *24*. https://doi.org/10.1007/s11676-013-0412-3.
16. Singh, R., & Singh, S. (2017). Sciencedirect modelling of dimensional accuracy in precision investment casting using Buckingham' s Pi approach. *Mater Today Proceeding, 4,* 1598–1605. https://doi.org/10.1016/j.matpr.2017.01.183.
17. Sakhale, C. N., Waghmare, S. N., Sonde, V. M., & Singh, M. P. (2014). Formulation and comparison of experimental based mathematical model with artificial neural network simulation and RSM (Response Surface Methodology) model for optimal performance of sliver cutting operation of Bamboo. *Procedia Mater Science, 6,* 877–891. https://doi.org/10.1016/j.mspro.2014.07.105.
18. Russo, L., Sorrentino, M., Polverino, P., & Pianese, C. (2017). Application of Buckingham p theorem for scaling-up oriented fast modelling of Proton exchange membrane fuel cell impedance. *Journal of Power Sources, 353,* 277–286. https://doi.org/10.1016/j.jpowsour.2017.03.116.
19. Hanche-olsen, H. (2004). *Buckingham's pi-Theorem* (p. 50). New Delhi: Kalyani Publisher.
20. Modak, J. P., & Bapat, A. R. (1994). Formulation of a generalized experimental model for a manually driven flywheel motor and its optimization. *Applied Ergon, 25,* 119–122. https://doi.org/10.1016/0003-6870(94)90075-2.
21. Khope, P. B., Modak, J. P. (2013). Design of experimental set-up for establishing empirical relationship for chaff cutter energized by human powered flywheel motor, *9*, 779–791.
22. Khope, P. B., Modak, J. P. (2014). Development of mathematical model for forage cutting process energized by human powered flywheel motor, pp. 4–10.
23. Simonyan, K. J., Yiljep, Y. D., Mudiare, O.J. (2006) .Modeling the lSorghum Thresher. Agriculture Engineering International: The CIGR Ejournal, VIII, 1–17.
24. Oluwafemi, I. D., Kehinde, O.O. (2017). Mathematical modelling of the performance of an impact snake gourd (Trichosanthes cucumerina. L) seed sheller, *19*, 142–149.
25. Voicu, G., Ndroiu, T., & Stan, G. (2007). Using the dimensional analysis for a mathematical model to predict the seeds losses at the cleaning system of the cereals harvesting combines. *U.P.B. Science Bull Series D, 69,* 29–39.
26. Simonyan, K. J., Mudiare, O. J., & Yiljep, Y. D. (2010). Development of a mathematical model for predicting the cleaning efficiency of stationary grain threshers using dimensional analysis. *Applied Engineering in Agriculture, 26,* 189–196.
27. Pobedrya, B. E., Georgievskii, D. V. (2006). On the proof of the Π—theorem in dimension theory, 13, 431–437. https://doi.org/10.1134/S1061920806040066.
28. Pradhan, R. C., Naik, S. N., Bhatnagar, N., & Vijay, V. K. (2010). Design, development and testing of hand-operated decorticator for Jatropha fruit. *Applied Energy, 87,* 762–768. https://doi.org/10.1016/j.apenergy.2009.09.019.

On Investigation of Dimensional Deviation for Hybrid Composite Matrix of PLA

Sudhir Kumar, Rupinder Singh, T. P. Singh, and Ajay Batish

Abstract This paper deals with the investigations for controlling dimensional deviations of 3D printed thermoplastic composite matrix-based prototypes with fused deposition modelling (FDM). The dimensional deviation results suggested that infill density 60%, infill angle 45° and infill speed of 70 mm/s are the optimized printing condition, but only infill density is the significant parameter in the present investigation. Surface hardness analysis supported the observed trend for dimensional deviation. It has been observed that the 3D printed prototype held very low electrical conductivity ($<10^{-6}$ S/cm) and was suitable for structural engineering applications.

Keywords Dimensional deviation · Hybrid magnetostrictive polymeric composite · Electrical conductivity · Optimization · Four-probe method

1 Introduction

FDM-based 3D printing for four-dimensional (4D) applications is one of the thrust areas of research [1]. Researchers are exploring this feature for drug loading, drug delivery, scaffold manufacturing, etc. [2, 3]. The range of input parameters of processing conditions for 3D printing is one of the foremost advantages of FDM technique [4, 5]. PLA which is biodegradable thermoplastic is being widely used by researchers for its medical field application such as in the production of scaffold, artificial joints and drug delivery agent [6, 7]. PLA has been reinforced with different reinforcements (such as rayon fibres, posidonia oceanica (PO) seagrass, chitin powder, graphite, natural sisal fibres) and has been analysed for their effect on the mechanical, chemical and surface properties of as-composite matrix [8–11]. It has been observed that with the reinforcement of external fillers, the mechanical performance of PLA composite has been improved for tensile and flexural properties [8–11]. Dimensional characteristics of reinforcement have also an important contribution towards the

S. Kumar · R. Singh (✉) · T. P. Singh · A. Batish
Mechanical Engineering Department, TIET, Patiala, India
e-mail: rupindersingh78@yahoo.com

Mechanical Engineering Department, GNDEC, Ludhiana, India

© Springer Nature Singapore Pte Ltd. 2021

C. Prakash et al. (eds.), *Advances in Metrology and Measurement of Engineering Surfaces* , Lecture Notes in Mechanical Engineering,
https://doi.org/10.1007/978-981-15-5151-2_10

thermal properties of polymeric composites. It has been observed that graphene and boron nitride have improved the thermal conductivity of PLA composite by 35 times [12, 13]. The inner structural design of composite may also be optimized for the higher thermal and electrical conductivity application as it has been observed that highly dense structure has provided maximum thermal and electrical conductance [14]. PLA itself acts as insulator whose thermal conductivity varies in the range of 0.2–0.3 W/mK and electrical conductivity in the range of 3.8×10^{-7} S/cm [15]. From the literature survey, it has been observed that various polymeric composites have been prepared for 3D printing application, but hitherto very little has been reported on investigation for dimensional deviation and electrical conductance of PLA-based hybrid composite for the FDM processing parameters.

This work is an extension of previously reported work [16] in which magnetic filler-based hybrid composite was prepared and optimized TSE processing conditions. In present work, an effort has been made on the investigation of dimensional deviation and electrical conductivity for 3D printed prototype with FDM set-up.

2 Materials and Methods

As this work is an extension of previously reported work [16], the compositions of PLA matrix as (i) virgin PLA 50 wt%, (ii) PVC 25 wt%, (iii) Fe_3O_4 20 wt% and (iv) wood powder 5 wt% and TSE conditions (load of 5 kg, screw temperature of 170 °C and screw torque of 0.13 Nm) for feedstock development were same as optimized for the reported work. In present work disc of Ø110 mm and thickness 1.74 mm was 3D printed using prepared feedstock filament from the selected composite on commercial FDM machine (Make: Divide by Zero, Pune, India). Three prototypes of each setting as per Table 1 have been printed so that the standard deviation of processing conditions may also be noted. From reported literature, it has been observed that infill density, infill angle and infill percentage has a vital role to play in mechanical,

Table 1 Taguchi L9 OA for statistical optimization of properties

S. No.	Fill density (%)	Fill angle (°)	Infill speed (mm/s)
1	60	45	50
2	60	60	70
3	60	90	90
4	80	45	70
5	80	60	90
6	80	90	50
7	100	45	90
8	100	60	50
9	100	90	70

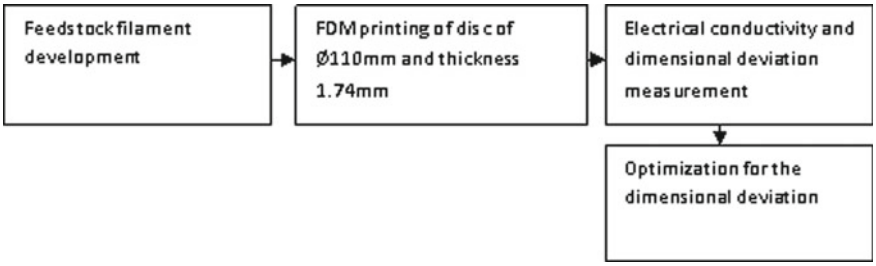

Fig. 1 Methodology for the present investigation

thermal and surface properties of 3D printed prototypes; therefore, these parameters were selected as input processing parameters for FDM machine. Electrical conductivity of 3D printed disc was measured using four-probe instrument, and dimensional deviation has been measured using a digital vernier caliper. Table 1 shows the Taguchi L9 orthogonal array (OA) which has been used for the optimization of dimensional deviations. Figure 1 shows the methodology used for the present investigation.

3 Results and Discussion

3.1 Electrical Conductivity Results

Four-probe testing method of capacity 10^{-6} to 10^{6} S/cm was used for electrical conductivity measurement of 3D printed samples, and it has been observed that the samples held very low electrical conductivity ($<10^{-6}$) due to which it was impossible to quantify the electrical conductivity. Hence, it may be observed that 20 wt% of magnetite powder in PLA matrix has not shown improvement in electrical conductivity of the composite matrix. This may be due to the fact that the presences of PVC and wood dust which are basically insulators have dominated in electrical behaviour of the composite. This also suggested that electrical properties were independent of FDM processing conditions as no improvement was observed in electrical conductance.

3.2 Dimensional Deviation Results

Table 2 shows the dimensional deviations in 3D printed part on the FDM set-up. From Table 2, it is clear that for sample as per S. No. 1, 2 and 3, the deviation recorded in diameter and thickness was lower in comparison with other samples. Further, it has been observed that as infill density of samples was increased, the deviation got enhanced. This may be due to the fact that as the sample density increases

Table 2 Observed dimensional deviations for FDM printed discs

S. No.	Printed diameter (mm)	Original diameter (mm)	Printed thickness (mm)	Original thickness (mm)	ΔD (mm)	ΔT (mm)
1	110.86	110	1.67	1.74	0.86 ± 0.21	-0.07 ± 0.02
2	110.62	110	1.71	1.74	0.62 ± 0.19	-0.03 ± 0.01
3	110.9	110	1.73	1.74	0.9 ± 031	-0.01 ± 0.01
4	111.62	110	1.83	1.74	1.62 ± 0.21	0.09 ± 0.09
5	112.64	110	1.82	1.74	2.64 ± 0.19	0.08 ± 0.04
6	112.57	110	1.85	1.74	2.57 ± 0.30	0.11 ± 0.03
7	112.92	110	1.92	1.74	2.92 ± 0.19	0.18 ± 0.05
8	112.85	110	2.07	1.74	2.85 ± 0.24	0.33 ± 0.04
9	112.56	110	2.16	1.74	2.56 ± 0.28	0.42 ± 0.09

the voids/porosity reduced resulting into better structure formation, but due to low internal vacant space, the material after solidification has shown more deviation for thickness as well as for diameter. But for lower infill density, the vacant space as voids/porosity was more available due to which the expansion of material while solidifying filled the vacant space first due to which low-dimensional deviations has been observed. Further, the values of ΔD (printed diameter—original diameter as per drawing) and ΔT (printed thickness—original thickness) were subjected to MiniTab 17 statistical software package tool for analysis of variance (ANOVA) optimization of dimensional deviations for minimum which is the better case (as less deviation is required for the production of prototypes to eradicate the extra post-processing of product) (Table 3). Figure 2 shows the main effect plot for signal-to-noise (SN) ratio of ΔD which suggested that least infill density (60%), low infill angle of 45° and medium infill speed of 70 mm/s were the optimized condition for least dimensional deviation for 3D printed disc on FDM set-up. Table 3 shows the ANOVA for SN ratios of ΔD, from which it was observed that infill density was the only significant parameter for the dimensional deviation feature for printed discs and has contributed maximum (91.83%), while other two selected parameters of FDM processing were

Table 3 ANOVA for SN ratios of ΔD

Source	DF	Seq SS	Adj SS	Adj MS	F	P	% CB
Infill density	2	206.476	206.476	103.238	140.82	0.007	91.83
Infill angle	2	1.815	1.815	0.907	1.24	0.447	0.81
Infill speed	2	15.067	15.067	7.534	10.28	0.089	6.71
Residual error	2	1.466	1.466	0.733	–	–	0.65%
Total	8	224.824	–	–	–	–	–

DF degree of freedom; *Seq SS* sum of squares; *Adj SS* adjusted sum of squares; *Adj MS* adjusted mean of squares; *F* fisher value; *P* probability; *% CB* percentage contribution

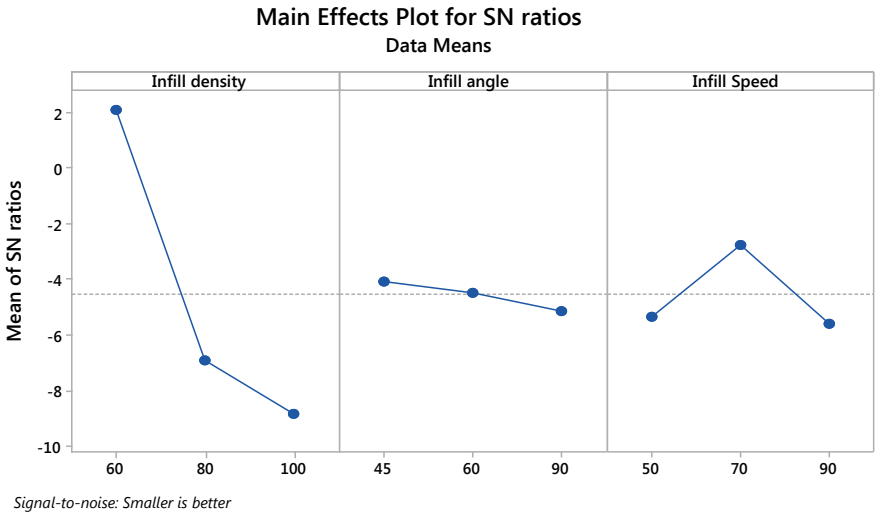

Fig. 2 Main effect plot for SN ratio of ΔD

insignificant. It should be noted that the optimized/suggested conditions were outside the design of experimentation (DOE), but from ANOVA analysis (Table 3), it was clear that the infill angle and infill speed were least significant for processing conditions and moreover in S. No. 1 as per Table 1, the suggested infill density and infill angle were present therefore in place of suggested/optimized condition one may take S. No. 1 as per Table 1 as the standard conditions for the printing of discs on FDM set-up.

Table 4 shows the rank table for SN ratios of ΔD which clearly suggested that the infill density was ranked 1st as per its contribution towards the output, whereas infill speed was ranked 2nd and infill angle was ranked at 3rd position. From ANOVA table, it was observed that the used statistical model was significant as the total residual error was 0.65% of total error; thus, the used model and observed values for FDM setting were correct up to 95% confidence interval. From percentage contribution, it has been observed that infill density has contributed the most (91.83%), whereas the other two factors were not significant for the current investigation. It is known that surface properties such as hardness and electrical properties (electrical conductivity)

Table 4 Rank table for SN ratios of ΔD

Level	Infill density	Infill angle	Infill speed
1	2.126	−4.063	−5.329
2	−6.940	−4.459	−2.734
3	−8.856	−5.149	−5.608
Delta	10.982	1.087	2.874
Rank	1	2	3

are greatly dependent over the inner structure (porosity holes, bonding between polymer and reinforcements, proper adhesion between different molecules) of printed prototypes, and therefore in the present case, infill density has played a significant and maximum role towards the observed surface hardness and electrical properties. Moreover, the dimensional deviations are also the result of structural formation; therefore for the observed properties, only infill density has a maximum role to play.

3.3 Optimization for the Dimensional Deviation

The SN ratios obtained from the ANOVA optimization were used for calculation of optimized/predicted value of dimensional deviation and electrical conductivity to compare it with actually observed values of the property. Equations 1 and 2 were used for optimization/prediction of output for ΔD.

$$\vartheta \text{ opt} = T + (\text{TA} - T) + (\text{TC} - T) \tag{1}$$

$$Y^2(\text{opt}) = (1/10)\vartheta(\text{opt})/10 \text{ for smaller is better case} \tag{2}$$

$$\vartheta(\text{opt}) = T + (\text{TA} - T) + (\text{TB} - T) + (\text{TC} - T)$$

T SN mean of $\Delta D = -4.56$
TA max SN for infill density from Table 4 = 2.126
TB max SN for infill angle from Table 4 = −4.063
TC max SN for infill speed from Table 4 = −2.734

$$\begin{aligned}\vartheta(\text{opt}) &= T + (\text{TA} - T) + (\text{TB} - T) + (\text{TC} - T)\\ &= -4.56 + (2.126 - (4.56)) + (-4.063 - (4.56)) + (-2.734 - (4.56))\\ &= 4.443\end{aligned}$$

$$Y^2(\text{opt}) = (1/10)(4.443)/10$$

$$Y(\text{opt}) = 0.60$$

It has been observed that the predicted value for ΔD was almost similar to the observed value which clearly signified that the 3D printing condition as per S. No. 1 (see Table 2) may also be used as optimized processing condition for least dimensional deviation in place of suggested processing condition as per main effect plot (see Fig. 2). This was solely due to the reason that infill density was the maximum contributing input factor and only significant parameter for output properties. Similar

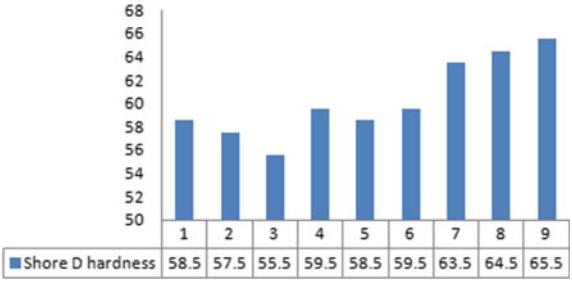

Fig. 3 Surface hardness plot for 3D printed discs

studies have been performed for all other properties, and it has been observed that all other properties also exhibited similar trends as for the ΔD.

3.4 Shore D *Hardness*

The 3D printed discs were subjected to surface hardness testing, and it was observed that the disc with least dimensional deviation held the lowest hardness which clearly signifies the presence of voids/porosity in inter-molecular spacing. This may be due to the fact that when the samples were printed with least infill density, the material deposited in inter- as well as intra-layer was not optimum which resulted into voids/porosity, whereas when the samples were printed with higher density and high infill rate, the deposition of material in layer fashion was subsequently higher resulting into better structure formation with least voids/porosity. Thus, low voids/porosity ultimately improved the surface hardness of 3D printed prototype as the result suggested. The results are in line with observations made by other investigators [17, 18] Fig. 3 shows the observed shore *D* hardness for 3D printed specimens.

4 Conclusions

The present study dealt with the exploration of electrical conductivity and optimization for dimensional deviation for the 3D printing processing conditions of FDM set-up. Following were the observations from the present investigation

1. Electrical properties have been independent of FDM processing conditions as no improvement was observed in electrical conductance. The prepared composite has shown very low electrical conductivity ($<10^{-6}$ S/cm) which was favourable for non-structural engineering applications.
2. From dimensional deviation results, it has been observed that infill density 60%, infill angle 45° and infill speed of 70 mm/s are the optimized/suggested printing condition, but S. No. 1 as per DOE may also be taken as the optimized condition as

only infill density was the significant parameter of the present investigation. The surface hardness results have also supported the observed trend for dimensional deviation.

Acknowledgements The authors are highly thankful to TIET, Patiala, and MRL laboratory of GNDEC, Ludhiana, for their continuous support.

References

1. Singh, S., Singh, G., Prakash, C., & Ramakrishna, S. (2020). Current status and future directions of fused filament fabrication. *Journal of Manufacturing Processes*, *55*, 288–306.
2. Singh, R., Kumar, R., & Ahuja, I. P. (2018). Mechanical, thermal and melt flow of aluminum-reinforced PA6/ABS blend feedstock filament for fused deposition modeling. *Rapid Prototyping Journal, 24*(9), 1455–1468.
3. Kumar, R., Singh, R., & Ahuja, I. P. (2019). Friction stir welding of ABS-15Al sheets by introducing compatible semi-consumable shoulder-less pin of PA6-50Al. *Measurement, 131,* 461–472.
4. Kumar, S., Singh, R., Singh, T. P., & Batish, A. (2019). On investigation of rheological, mechanical and morphological characteristics of waste polymer-based feedstock filament for 3D printing applications. Journal of Thermoplastic Composite Materials. 0892705719856063. https://doi.org/10.1177%2F0892705719856063.
5. Pandey, A., Singh, G., Singh, S., Jha, K., & Prakash, C. (2020). 3D printed biodegradable functional temperature-stimuli shape memory polymer for customized scaffoldings. *Journal of the Mechanical Behavior of Biomedical Materials*, 103781.
6. Kumar, S., Singh, R., Singh, T. P., & Batish, A. (2019). Investigations of polylactic acid reinforced composite feedstock filaments for multimaterial three-dimensional printing applications. In *Proceedings of the Institution of Mechanical Engineers, Part C: Journal of Mechanical Engineering Science*, p. 0954406219861665.
7. Poomathi, N., Singh, S., Prakash, C., Patil, R. V., Perumal, P. T., Barathi, V. A., Balasubramanian, K. K., Ramakrishna, S. & Maheshwari, N. U. (2019). Bioprinting in ophthalmology: current advances and future pathways. *Rapid Prototyping Journal*.
8. Singh, S., Prakash, C., Singh, M., Mann, G. S., Gupta, M. K., Singh, R., & Ramakrishna, S. (2019). Poly-lactic-Acid: Potential Material for Bio-printing Applications. In *Biomanufacturing* (pp. 69–87). Cham: Springer.
9. Mann, G. S., Singh, L. P., Kumar, P., Singh, S., & Prakash, C. (2019). On briefing the surface modifications of polylactic acid: A scope for betterment of biomedical structures. *Journal of Thermoplastic Composite Materials*, 0892705719856052.
10. Singh, H., Singh, S., & Prakash, C. (2019). Current trends in biomaterials and biomanufacturing. In *Biomanufacturing* (pp. 1–34). Cham: Springer.
11. Scaffaro, R., Lopresti, F., & Botta, L. (2018). PLA based biocomposites reinforced with Posidonia oceanica leaves. *Composites Part B Engineering, 139,* 1–11.
12. Nasrin, R., Biswas, S., Rashid, T. U., Afrin, S., Jahan, R. A., Haque, P., et al. (2017). Preparation of Chitin-PLA laminated composite for implantable application. *Bioactive Materials, 2*(4), 199–207.
13. Lewis, J. S., Barani, Z., Magana, A. S., Kargar, F., & Balandin, A. A. (2019). Thermal and electrical conductivity control in hybrid composites with graphene and boron nitride fillers. *Materials Research Express, 6*(8), 085325.
14. Liu, C., Dong, Y., Lin, Y., Yan, H., Zhang, W., Bao, Y., et al. (2019). Enhanced mechanical and tribological properties of graphene/bismaleimide composites by using reduced graphene oxide with non-covalent functionalization. *Composites Part B Engineering, 165,* 491–499.

15. Yu, B., Wang, M., Sun, H., Zhu, F., & Han, J. (2007). Bhat G Preparation and properties of poly (lactic acid)/magnetic Fe_3O_4 composites and nonwovens. *RSC Advances, 7*(66), 41929–41935.
16. Kumar, S., Singh, R., Singh, T. P., & Batish, A. (2019). Investigations for magnetic properties of PLA-PVC-Fe_3O_4-wood dust blend for self-assembly applications. *Journal of Thermoplastic Composite Materials*. 0892705719857778.
17. Kumar, S., Singh, R., Singh, T. P, & Batish, A. (2019). Multimaterial printing and characterization for mechanical and surface properties of functionally graded prototype. In *Proceedings of the Institution of Mechanical Engineers, Part C: Journal of Mechanical Engineering Science*, 0954406219867984.
18. Singh, R., Kumar, R., & Kumar, S. (2017). Polymer waste as fused deposition modeling feed stock filament for industrial applications. *Reference Module in Material Science and Engineering*, 1–12.

Performance Evaluation of Graphene-Gear Oil Nanolubricants in Rayleigh Step Bearing

Gaurab Kumar Ghosh, Ankit Kotia, Niranjan Kumar, and Subrata Kumar Ghosh

Abstract In this paper, the contribution of dispersed graphene nanoparticles in graphene-gear oil nanolubricant has been analyzed. Synthesis of nanolubricant has been performed using the two-step method. The nanoparticles have been dispersed in the range of 0.03–1.8% by volume in industrial gear oil (SAE EP90). Viscosity and density of nanolubricant are measured by using Stabinger viscometer (SVM 3000, M/S Anton-Paar). Rheological properties have been experimentally tested in the temperature range of 20–80 °C, and the results have been compared with theoretically available models in open literature. The performance characteristics of nanolubricants in hydrodynamic lubrication regime have been evaluated by considering the standard Reynolds equation. For this purpose, the geometry of an infinite Rayleigh step slider bearing (one dimension) is considered with defined boundary conditions. Finite difference method (FDM) is used to obtain the solution of boundary value problem. Results confirm that the dispersion of graphene nanoparticles in gear oil enhances the performance of lubrication.

Keywords Graphene-gear oil nanolubricant · Rayleigh step bearing · Reynolds equation · FDM

Abbreviations

X	Non-dimensional pad width
l	Pad width
P	Non-dimensional pressure of the nanolubricant film
$h(x)$	Thickness of nanolubricant film
H	Non-dimensional film thickness

G. K. Ghosh · N. Kumar · S. K. Ghosh (✉)
Indian Institute of Technology (Indian School of Mines), Dhanbad, India
e-mail: subratarec@yahoo.co.in

A. Kotia
Lovely Professional University, Phagwara, Punjab, India

© Springer Nature Singapore Pte Ltd. 2021

C. Prakash et al. (eds.), *Advances in Metrology and Measurement of Engineering Surfaces* , Lecture Notes in Mechanical Engineering,
https://doi.org/10.1007/978-981-15-5151-2_11

η_0 Viscosity at $p = 0$ (Pa s)
ρ_0 Density at $p = 0$ (kg/m^3)
ρ^* Non-dimensional density
η^* Non-dimensional viscosity

1 Introduction

Conservation of energy is a major concern for a sustained ecosystem. The main reason for energy loss in any mechanical system is due to wear of its components which can be reduced by efficient lubrication. Efficient lubrication is basically an ideal selection of base lubricant and proper additives. With the advancement of technology, researchers have come up with newer lubricants comprising of nanoparticles as additives dispersed in base lubricants termed as 'Nanolubricants'. Nanolubricants are found to have enhanced thermophysical, rheological and tribological properties over conventional lubricants. Adding nanoparticles in traditional lubricants for enhancing tribological and thermal properties in recent years is extensively studied [1]. Kotia et al. [2] observed that Al_2O_3 nanoparticles in industrial gear oil (SAE EP-90) enhanced viscosity to 1.7 times of base lubricant with a concentration of 2% by volume of nanoparticles. Aberoumand et al. [3] expressed viscosity as an important consideration for industrial application and presented a correlation for the same. Berman et al. [4] introduced graphene as a new emerging potential additive to the lubricating oils. Graphene nanoparticles with their sheet-like structure enhance surface area, thereby reducing metal to metal contact resulting in transmitting heat more efficiently [5]. Yang et al. [6] confirmed that graphene-based lubricants remarkably reduce the wear and coefficient of friction by 91 and 53%, respectively, compared to base lubricant. Adding graphene nanoparticles in base oils has indicated remarkable increment in heat transfer properties within optimum concentration range beyond which agglomeration takes place leading to high friction and wear [7, 8]. Furthermore, many noteworthy works have been conducted regarding the enhancement of tribological properties of lubricants by adding graphene nanoparticles [9, 10].

In this paper, the nanolubricant has been prepared by dispersing graphene nanoparticles in gear oil (SAE EP90). Rheological and thermophysical properties at varying temperature and particle volume fraction are experimentally evaluated. Performance parameters considering Rayleigh step bearing geometry are numerically obtained using finite difference method.

2 Governing Equations

2.1 Reynolds Equation

A 1D Reynolds equation for incompressible flow is given as:

$$\frac{\partial}{\partial x}\left(\frac{\rho h^3}{\eta}\frac{\partial \rho}{\partial x}\right) = 6U\frac{\partial}{\partial x}(\rho h) \tag{1}$$

Where h denotes the film thickness, p denotes the pressure of the nanolubricant film, ρ and η denotes the density and viscosity of the nanolubricant, respectively, and U is the sliding velocity of the moving surface.

In Eq. (1), the parameters have been presented in the non-dimensional form as:

$$\frac{\partial}{\partial X}\left(\frac{\rho^* H^3}{\eta^*}\frac{\partial P}{\partial X}\right) = \frac{\partial(\rho^* H)}{\partial X} \tag{2}$$

where $X = \frac{x}{l}$, $P = \frac{ph_2^2}{6Ul\eta_0}$, $H = \frac{h}{h_2}$, $\rho^* = \frac{\rho}{\rho_0}$, $\eta^* = \frac{\eta}{\eta_0}$.

2.2 Load Carrying Capacity

Load carrying capacity per unit width (W) of the plate is given as:

$$\frac{W}{B} = \int_0^{L_1} P_1 dx + \int_{L_1}^{L_2} P_2 dx \tag{3}$$

$$\frac{W}{B} = \frac{3\eta U L L_2 (L - L_2)(a-1)}{\left(L_2 a^3 + L - L_2\right)h_2^2} \tag{4}$$

$$\text{Where } a = \frac{h_1}{h_2}$$

3 Modelling

A schematic representation of the geometry of Rayleigh step bearing is shown in Fig. 1. The sliding direction is along the x-coordinate considering the location of origin at the entry. The flow of nanolubricant is assumed to take place from left to

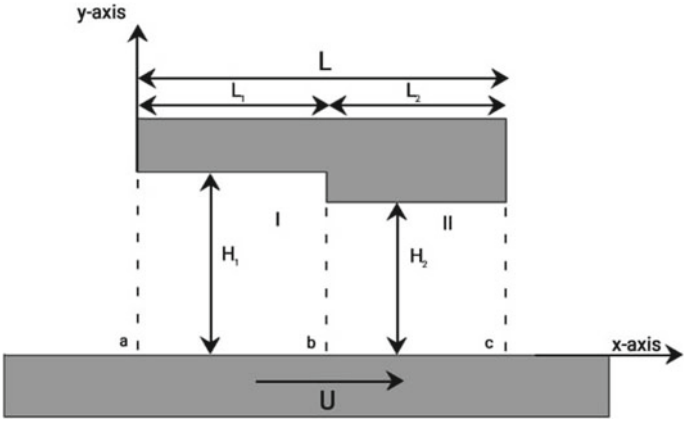

Fig. 1 Pictorial representation of Rayleigh step bearing

right. The surface of the pad has a step zone with initial film thickness h_1 and final film thickness along a land zone as h_2.

The boundary conditions used herein are: At entry, $P = 0$ for $X = 0$, $P = P_c$ *at* $X = L_1/L$, and at exit, $P = 0$ for $X = 1$.

4 Experimental Procedures

Graphene nanoparticles, sheet thickness 2–5 nm, 2–4 layers with surface area 380 m^2/g, density 2.2 g/ml have been dispersed in industrial gear oil (SAE EP90). Samples were prepared comprising of plain gear oil and graphene-gear oil nanolubricants with varying particle concentration of 0.3, 0.6, 0.9, 1.2, 1.5 and 1.8% by volume fractions. The nanoparticles appropriate weight (W) is calculated using the following Equation [5] in terms of volume fraction (ϕ):

$$\phi = \frac{W_p/\rho_p}{W_p/\rho_p + W_l/\rho_l} \tag{5}$$

where $'\rho'$, $'p'$ and $'l'$ represent particle density, nanoparticle and base lubricant, respectively. Digital weighing balance (least count 0.001 mg) was used to obtain the accurate measure of mass for the nanoparticles. Nanoparticles in base lubricants were uniformly mixed by magnetic stirring for 30 min at 600 rpm followed by half an hour ultra-sonication (20 kHz) to de-agglomerate the nanoparticles. The following table shows the details of instruments used for measuring density, viscosity and shear variations (Table 1).

All the readings from these instruments were recorded in Dhanbad at an estimated height of 232 m above mean sea level.

Table 1 Details of instruments

Instrument	Make	Model
Viscometer	Anton Parr	SVM300
Rheometer	Malvern Instrument, UK	Bohlin Gemini

5 Results and Discussions

5.1 Density and Viscosity Variation

Figure 2 represents the density plots of graphene/EP-90 nanolubricant with temperature at varying nanoparticle volume fraction. The density decreases with temperature in all cases following a constant gradient at all particle concentrations. Error bars are incorporated to include uncertainty in the analysis. The temperature range (20–80 °C) has been set to get the nature of the data points. With increasing temperature, the graph approaches a constant value asymptotically. The data points are measured with an estimated maximum uncertainty within 3%.

Figure 3 represents the viscosity–temperature variation of graphene/EP-90 nanolubricant with varying concentration of nanoparticles. The dependence of viscosity of nanolubricant with temperature affirms asymptotic nature as a result of weakening inter-molecular adhesion force with increasing temperature. Measurements are reported with an estimated maximum uncertainty within 2% (Table 2).

Figure 4 represents the relative viscosity plots of graphene/EP-90 nanolubricant between theoretical models and experimental data. It can be seen that with increasing particle concentration, the relative viscosity also increases. The viscosity enhancement of nanolubricant respect to base lubricant is about 22–32% with varying particle concentration of 0.3–1.8%. MATLAB (2014) is used to develop a correlation between relative viscosity and volume fraction as expressed below:

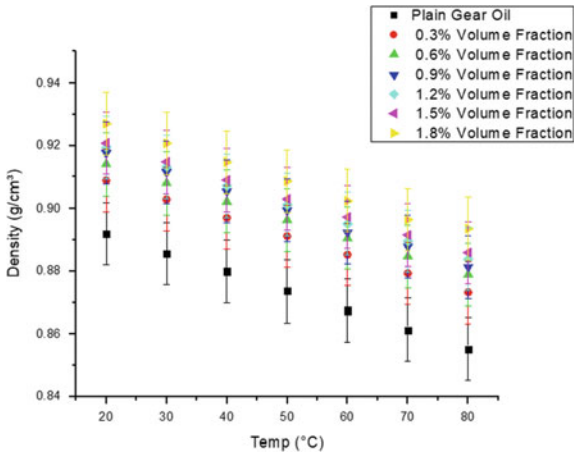

Fig. 2 Density–temperature variation

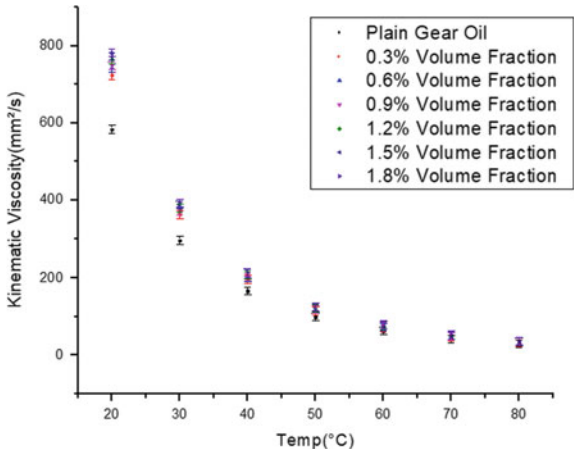

Fig. 3 Kinematic viscosity–temperature variation

Table 2 Theoretical viscosity models proposed by various researchers

Authors	Predictive model
Einstein [11]	$\mu_{\text{eff}} = \mu_f(1 + 2.5\phi)$
Brinkman [12]	$\mu_{\text{eff}} = \mu_f(1 - \phi)^{-2.5}$
Lundgren [13]	$\mu_{\text{eff}} = \mu_f\left(1 + 2.5\phi + \frac{25}{4}\phi^2\right)$
Pak and Cho [14]	$\mu_{\text{eff}} = \mu_f\left(1 + 39.11\phi + 533.9\phi^2\right)$
Wang et al. [15]	$\mu_{\text{eff}} = \mu_f\left(1 + 7.3\phi + 123\phi^2\right)$

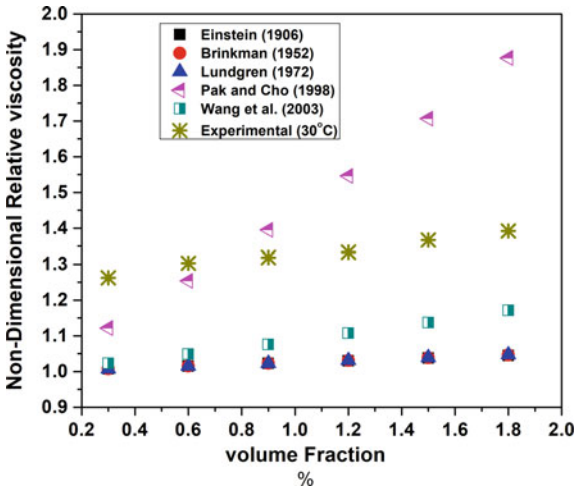

Fig. 4 Variation of relative viscosity with volume fraction

$$\mu_{\text{eff}} = 1.205\mu_f\left(1 + 5.138\phi + (26.71\phi)^2\right) \tag{6}$$

5.2 Rheological Variations

Figure 5 depicts the shear stress with shear rate variation of graphene/EP-90 nanolubricant at varying concentration of graphene at 30 °C. It is evident that at relatively low volume fraction, the variation is almost linear indicating Newtonian behaviour, while at higher volume fraction, this variation approaches towards nonlinearity showing non-Newtonian nature. Figure 6 represents the viscosity–shear rate trends of

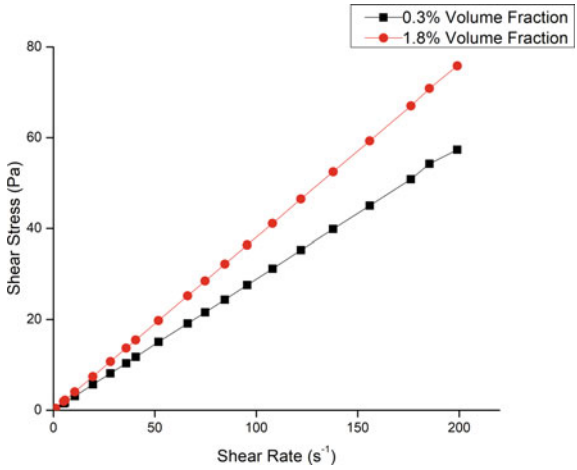

Fig. 5 Shear stress–shear rate variation

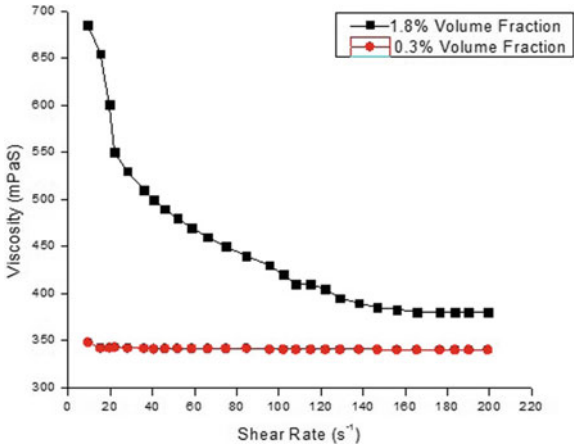

Fig. 6 Viscosity–Shear rate variation

Table 3 Basic inputs

Geometry	Notations	Inputs
Slider width	L	10 mm
Film thickness gap	$h_1 - h_2$	100 nm
Sliding velocity	U	0.05 m/s
Length of step zone	L_1	7 mm
Length of land zone	L_2	3 mm
Optimum film thickness ratio	a	1.86

graphene/EP-90 nanolubricant at varying concentrations. It confirms that nanolubricant exhibits significant shear thinning characteristics at higher volume fraction and viscosity declines asymptotically at a higher shear rate.

5.3 Performance Curves

To evaluate the performance characteristics in the step bearing with nanolubricant, the following geometrical inputs have been used for the study (Table 3).

Figure 7 shows the pressure distribution with non-dimensional length over the width of the slider. It is evident that the pressure profile shows an increasing trend with volume fractions in all cases. The peak pressure is achieved at the common point of step and zone land. Figure 8 depicts the profile of maximum load-carrying capacity with volume fraction at 30 °C and found to increase with volume fraction under optimum film thickness ratio condition, i.e. 1.86.

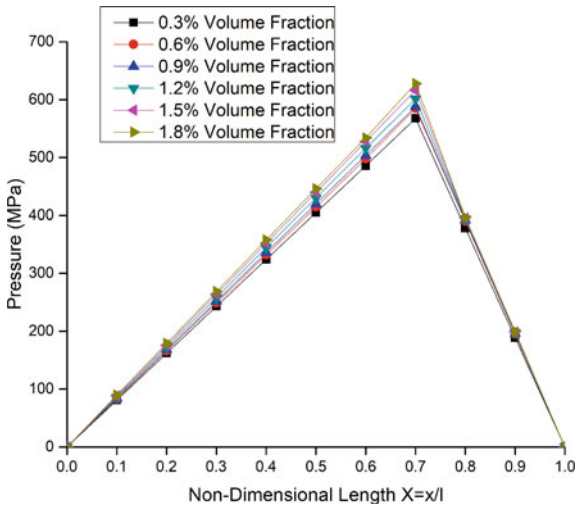

Fig. 7 Pressure profile with non- dimensional length

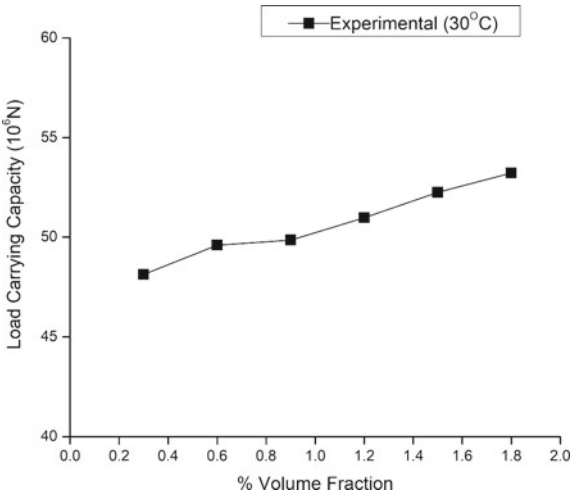

Fig. 8 Variation of load-carrying capacity with particle volume fraction

6 Conclusions

In this present work, the effects of dispersing graphene nanoparticles in gear oil (SAE EP-90) have been experimentally investigated. Improvement in rheological properties have been obtained and compared with previous research works. Shear-thinning behaviour has been observed with increasing nanoparticle volume fraction. The performance characteristics of nanolubricants in hydrodynamic lubrication regime assuming the geometry of 1D Rayleigh step bearing have been obtained by considering the standard Reynolds equation. Basic inputs from the earlier study have been used for calculating the performance parameters. It has been observed that the dispersion of graphene enhances the performance of lubrication.

References

1. Rajendhran, N., Palanisamy, S., Shyma, A. P., Venkatachalam, R. (2018). Enhancing the thermophysical and tribological performance of gear oil using Ni-promoted ultrathin MoS_2 nanocomposites. *Tribology International*. https://doi.org/1.20180.106/j.triboint.2018.03.030.
2. Kotia, A., & Ghosh, S. K. (2015). Experimental analysis for rheological properties of aluminium oxide (Al_2O_3)/gear oil (SAE EP-90) nanolubricant used in HEMM. *Indian Lubricants Tribology, 67,* 600–605.
3. Aberoumand, S., Jafarimoghaddam, A., Moravej, M., Aberoumand, H., & Javaherdeh, K. (2016). Experimental study on the rheological behavior of silver-heat transfer oil nanofluid and suggesting two empirical based correlations for thermal conductivity and viscosity of oil based nanofluids. *Applied Thermal Engineering, 101,* 362–372.
4. Berman, D., Erdemir, A., & Sumant, A. V. (2014). Graphene: a new emerging lubricant. *Materials Today, 17*(1), 31–42.
5. Zhao, C., Chen, Y. K., & Ren, G. (2013). A study of tribological properties of water-based ceria nanofluids. *Tribology Transactions, 56*(2), 275–283.

6. Yang, J., et al. (2017). Synthesis of the liquid-like graphene with excellent tribological properties. *Tribology International, 105,* 118–124.
7. Rasheed, A. K., Khalid, M., Javeed, A., Rashmi, W., Gupta, T. C. S. M., & Chan, A. (2016). Heat transfer and tribological performance of graphene nanolubricant in an internal combustion engine. *Tribology International, 103,* 504–515.
8. Lin, Y., et al. (2015). Wear and friction characteristics of surface-modified aluminium alloys. *International Journal of Surface Science and Engineering, 9*(2–3), 109–123.
9. Rasheed, A. K., & Khalida, M. (2016). Study of graphene nanolubricant using thermogravimetric analysis. *Journal of Materials Research, 31*(13), 1939–1946.
10. Lin, J., Wang, L., & Chen, G. (2011). Modification of graphene platelets and their tribological properties as a lubricant additive. *Tribology Letters, 41*(1), 209–215.
11. Einstein, A. (1905). A new method for determination of the molecular dimensions. *Annalen der Physik, 19*(2), 89–306.
12. Brinkman, H. C. (1952). The viscosity of concentrated suspensions and solution. *Journal of Chemical Physics, 20*(4), 571–581.
13. Lundgren, T. S. (1972). Slow flow through stationary random beds and suspensions of spheres. *Journal of Fluid Mechanics, 51*(2), 273–299.
14. Wang, B. X., Zhou, L. P., & Peng, X. F. (2003). A fractal model for predicting the effective thermal conductivity of liquid with suspension of nano particles. *International Journal of Heat and Mass Transfer, 46*(11), 2665–2672.
15. Pak, B. C., & Cho, Y. I. (1998). Hydrodynamic and heat transfer study of dispersed fluids with submicron metallic oxide particles. *Experimental Heat Transfer: A Journal of Thermal Energy Generation, Transport, Storage, and Conversion, 11*(2), 151–170.

The Effect of Two-Step Austempering on Abrasion Wear Characteristics of the Ductile Cast Iron

C. S. Wadageri, R. V. Kurahatti, Dayanand M. Goudar, Vijaykumar Hiremath, and V. Auradi

Abstract This paper focuses on the effect of two-step austempering on abrasion wear characteristics of the ductile cast iron. The single-step (conventional) and two-step austempering were employed for the samples. There were four treatments. For all samples, austenitization at 900 °C was done. The first treatment comprised of conventional austempering at 400 °C. The second one consisted of conventional austempering at 320 °C. The third one consisted of austempering at 400 °C followed by austempering at 320 °C. The fourth one comprised of austempering at 320 °C followed by austempering at 400 °C. The results showed that samples with two-step austempered at 320 °C followed by 400 °C exhibited enhanced abrasion resistance. The reason for this behavior is discussed considering the microstructure parameters.

Keywords Ductile iron · Two-step austempering · Abrasion resistance

1 Introduction

Recent studies [1–3] have shown that ductile iron can be utilized in applications requiring sudden impact loading and wear resistance. Examples of uses are automotive parts like transmission gears and crankshafts, agricultural implements and

C. S. Wadageri
Department of Mechanical Engineering, Maratha Mandal Engineering College, Belagavi 591 113, Karnataka, India

R. V. Kurahatti (✉)
Department of Mechanical Engineering, Basaveshwar Engineering College, Bagalkot, Karnataka 587 102, India
e-mail: rajukurahatti@gmail.com

D. M. Goudar
Department of Mechanical Engineering, Tontadarya Collge of Engineering, Gadag, Karnataka 582 101, India

V. Hiremath · V. Auradi
Department of Mechanical Engineering, Siddaganga Institute of Technology, Tumakuru, Karnataka 572 103, India

© Springer Nature Singapore Pte Ltd. 2021

C. Prakash et al. (eds.), *Advances in Metrology and Measurement of Engineering Surfaces* , Lecture Notes in Mechanical Engineering,
https://doi.org/10.1007/978-981-15-5151-2_12

defense equipments. Austempered ductile iron (ADI) parts used are frequently subjected to abrasive wear. Most studies [3–6] focused on adhesive and abrasive wear performance of ADI. Zimba et al. [2] inferred that ADI could be used as alternate material for earth moving equipment. Zhou and Zhou [4] and Shepperson et al. [5] investigated the rolling wear characteristics of ductile iron. Studies on fatigue performance of ductile iron are found in the literature [3].

The wear of ADI gears was investigated by Magalhaes and co-workers [6]. The effect of superiority of casting on the abrasion performance was studied by several researchers. The effect of graphite nodule shape and size on the sliding wear of ductile iron was studied by Hatate et al. [7]. The authors noted that the change in nodule shape, i.e., from spheroid to flake, was the main cause for lower wear loss in ADI. Very few studies threw a light on the role of austempering temperature and time on the wear resistance of ductile iron. Zhou and Zhou [4] studied the wear (on oiled surface) performance of ductile iron and showed that wear resistance initially reduced and eventually increased substantially with increased austempering temperature. Other studies [8, 9] confirmed the beneficial effects of microstructure parameters on the abrasive wear behavior.

This paper compares the effect of conventional and two-step austempering temperature and time on the abrasion resistance of ductile iron. The microstructure details and their effect on the wear behavior are considered.

2 Details of Experiment

2.1 Materials

The ingredients of the ductile iron in weight percentage were C (3.48%), Si (2.4%) Mn (0.31%) Cu (0.03%) P (0.01%) S (0.01%) and Mg (0.05%).

2.2 Heat Treatment Procedures

The following heat treatments were carried out on ADI samples. Figure 1 shows the procedures schematically.

- Austenitization at 900 °C was done for all samples.
- Sample 1: Conventional austemepering (CA-1) at 400 °C for 150 min
- Sample 2: Conventional austempering (CA-2) at 320 °C for 150 min
- Sample 3: Two-step austempering (TSA-1), i.e., austempering at 400 °C for 30 min followed by austempering at 320 °C for 120 min
- Sample 4: Two-step austempering (TSA-2), i.e., austempering at 320 °C for 30 min followed by austempering at 400 °C for 120 min

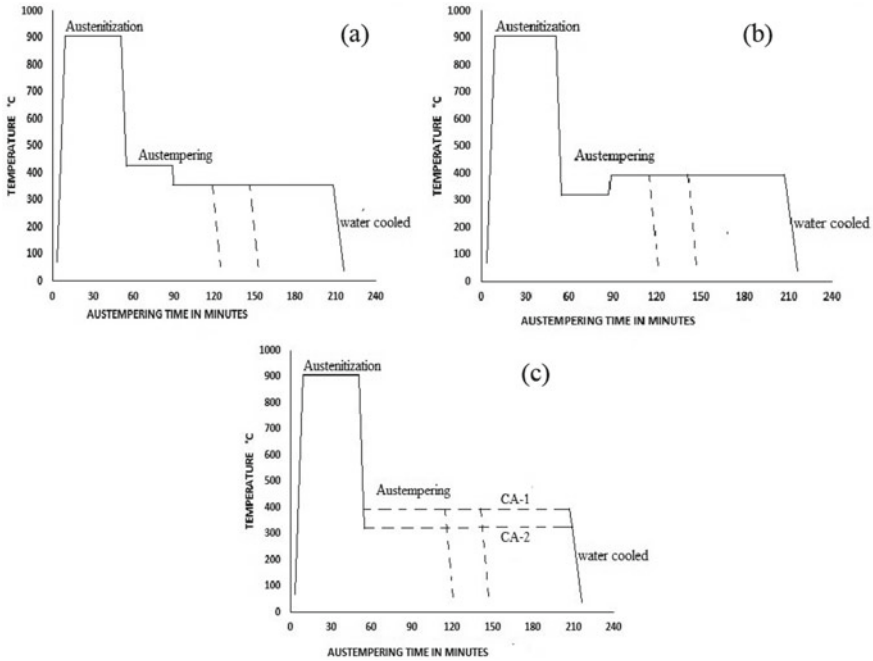

Fig. 1 Schematic diagrams of two-step austempering **a**, **b** and conventional austempering processes **c**

2.3 Quantitative Analysis

The contents (volume percentage) of microconstituents like austenite and carbon in austenite were determined using the X-ray diffractometer, as per ASTM E975-84 [10, 11].

2.4 Abrasion Wear Test

Figure 2 shows the abrasion test setup. The abrasion test was conducted according to ASTM standard G132-96. A load of 65 N was used. The disk rotated at 22 rpm; it traveled a distance of 13 m at 0.04 m/s. 0.1 mg accuracy weighing equipment was used. The sample weights before and after the wearing tests were noted and weight loss was determined. Three readings were noted and the average value was used for reporting. Rockwell hardness test (C scale) was utilized to determine the hardness of the worn-out surfaces. Vickers hardness test was used for testing the hardness of untreated and heat-treated samples.

Fig. 2 Abrasion test setup

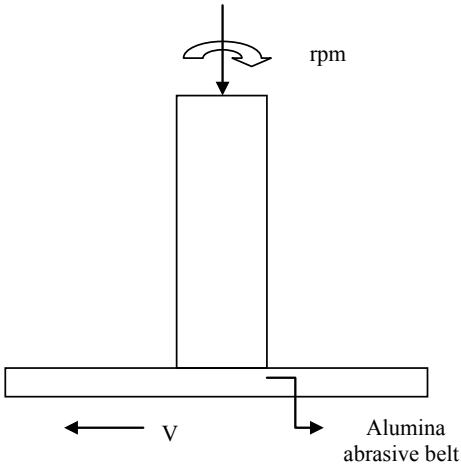

3 Results and discussion

3.1 Microstructural details

Table 1 shows the microstructural details such as contents of austenite (Xγ), carbon in austenite (Cγ) and austenitic carbon (XγCγ) as obtained from heat treatment procedures mentioned. It is clear that more austenitic carbon content (XγCγ) was obtained from TSA-2 (400 °C, 150 min) process. The mechanism of microstructure development is found in the literature [12]. Table 2 shows the weight loss details of the tested samples.

Table 1 Microstructural details of the samples

Samples	Austenite Xγ (vol. %)	Carbon in austenite Cγ (vol. %)	Total carbon in matrix, XγCγ (vol. %)
TSA-1 (320 °C, 60 min)	0.3	1.89	0.56
TSA-1 (320 °C, 90 min)	0.28	1.8	0.5
TSA-1(320 °C,150 min)	0.16	1.7	0.27
TSA-2 (400 °C, 60 min)	0.19	1.85	0.35
TSA-2 (400 °C, 90 min)	0.35	1.95	0.68
TSA-2 (400 °C, 150 min)	0.38	2.01	0.76
CA-1 (400 °C, 150 min)	0.15	1.7	0.25
CA-2 (320 °C, 150 min)	0.36	1.96	0.71

Table 2 Weight loss details of the samples

Sample	Weight loss (milligrams, mg)
Untreated ductile iron	85.2
TSA-1 (320 °C, 60 min)	79.3
TSA-1 (320 °C, 90 min)	79.2
TSA-1 (320 °C, 150 min)	74
TSA-2 (400 °C, 60 min)	78.1
TSA-2 (400 °C, 90 min)	77.8
TSA-2 (400 °C, 150 min)	70
CA-1 (400 °C, 150 min)	76.2
CA-2 (320 °C, 150 min)	74.9

Table 3 Hardness and tensile properties of ADIs (austempering time: 150 min)

Austempering temperature	Hardness (VHN)		Yield strength (MPa)		Tensile strength (MPa)		Elongation (%)	
Untreated ductile iron	280		550		880		1.8	
	CA	TSA	CA	TSA	CA	TSA	CA	TSA
320 °C	480	435	822	855	1092	1126	2.1	2.2
400 °C	310	410	618	811	976	1076	5.2	2.6

Table 3 shows the effect of conventional and two-step austempering on the hardness and tensile properties of samples. It is observed that as the austempering temperature increased, hardness and strengths were decreased. This was due to the fact that austenite and ferrite become coarser at higher temperature (400 °C). The coarse grains formed result in the remarkable decrease in strengths. This is only true for conventional and two-step austempering (400 °C). The strength values are higher in CA and TSA processes (320 °C). This is due to grain size effect. The finer grains at 320 °C result in higher tensile properties (Hall–Petch equation). Relatively higher strengths and lower ductility were observed in TSA processed materials.

3.2 Abrasion properties

Numerous workers [3–6] concluded that it was the austempering temperature and time that is main reason for modification of microstructure The modified microstructure ultimately determines the wear behavior of the samples. This has become true in our study. By TSA-2 (400 °C, 150 min) process, the microstructure constituents as observed in Table 1, i.e., higher austenite Xγ (vol.%) and higher total carbon in matrix, XγCγ (vol.%) were obtained. The hardness of ADIs has drastically improved

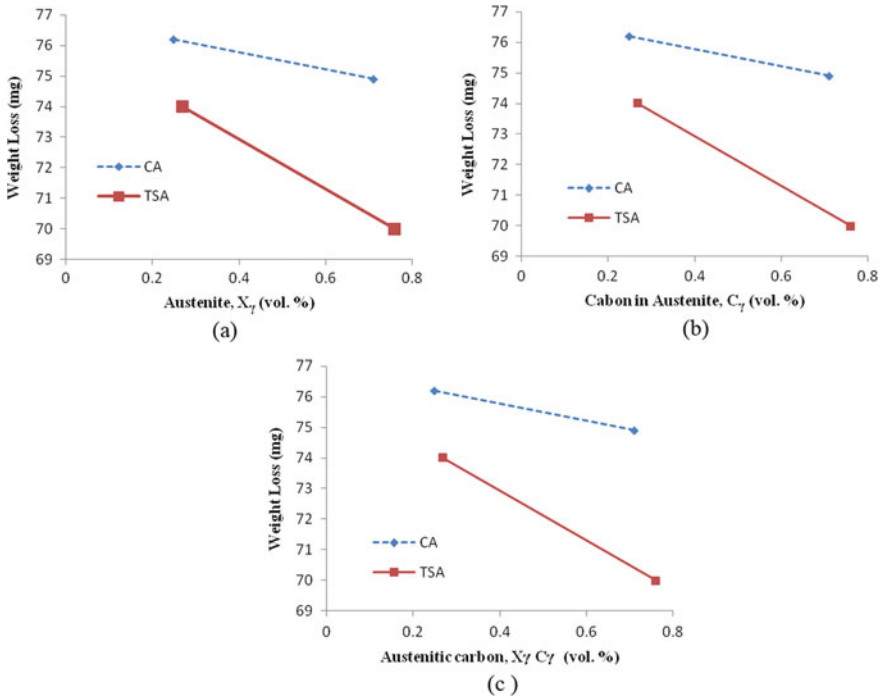

Fig. 3 Weight loss versus vol. % of austenite (Xγ) **a** weight loss versus vol. % of carbon content in austenite (Cγ) **b** weight loss versus vol. % of austenitic carbon (XγCγ) **c** (austempering time: 150 min)

due to this microstructure evolution. The improved abrasion wear resistance may be attributed to the enhanced hardness and tensile properties of the materials (Table 3).

From Fig. 3a, it is clear that the wear loss increased as the austenite volume fraction increased. It is further noticed that for same volume fraction of austenite, TSA-2 (400 °C, 150 min) samples exhibited lesser weight loss. The austenite with FCC structure is soft and capable of undergoing higher work hardening. The BCC ferrite is not so. So considering this argument, the more austenite should have been the cause for more wear loss. TSA-2 processes have created more austenite than the TSA-1 processes. On the contrary, the wear loss appeared lesser as compared to TSA-1 processes. This behavior was attributed to work hardening of the austenite during the abrading process. The work hardening phenomenon could be confirmed by the hardness readings obtained after the abrasion test (Table 4).

Figure 3b, c clearly shows that the carbon content in austenite and austenitic carbon has identical effect on weight loss of materials. Normally diffusion of carbon atoms in austenite is more at higher temperature. This results in carbon enriched austenite. The carbon atoms form the interstitial solid solution within FCC austenite lattice. The strength of austenite phase thereby increases. The strengthened matrix naturally gives rise to improved abrasion resistance.

Table 4 Hardness of samples prior to and after abrasion test

Samples	Hardness prior to wear (HRC)	Worn surface hardness (HRC)
TSA-1 (320 °C, 60 min)	19	30.4
TSA-1 (320 °C, 90 min)	23	36.4
TSA-1 (320 °C, 150 min)	38	45
TSA-2 (400 °C, 60 min)	35	36.5
TSA-2 (400 °C, 90 min)	38.5	41.2
TSA-2 (400 °C, 150 min)	47	48.5
CA-1 (400 °C, 150 min)	39.5	45
CA-2 (320 °C, 150 min)	22.5	30.4

It becomes clear from Table 4 that hardness of the worn surfaces has increased. There is more increment in hardness in TSA-2 samples particularly in TSA-2 (400 °C, 150 min). Gundlach, Janowak [13] and other researchers [4, 5] indicated the hardness increase and they concluded that after the wearing, work hardening and the strain-induced martensite were the cause for this behavior [14].

Optical examination of worn surfaces of ADIs exhibits that surface morphology (Fig. 4) consisted of typical shallow scars and grooves. The worn surfaces showed a look of semi-polished metallographic surface consisting of coarse interwoven abrasive grooves. It seems that the grooves and scars may have been formed by hard abrasive particles that exist in belt while undergoing abrasion test. Deep grooves, shear lips existed near the abraded areas. This occurrence was more evident in TSA-2 samples. This shear lips broke finally and formed the abrasion debris.

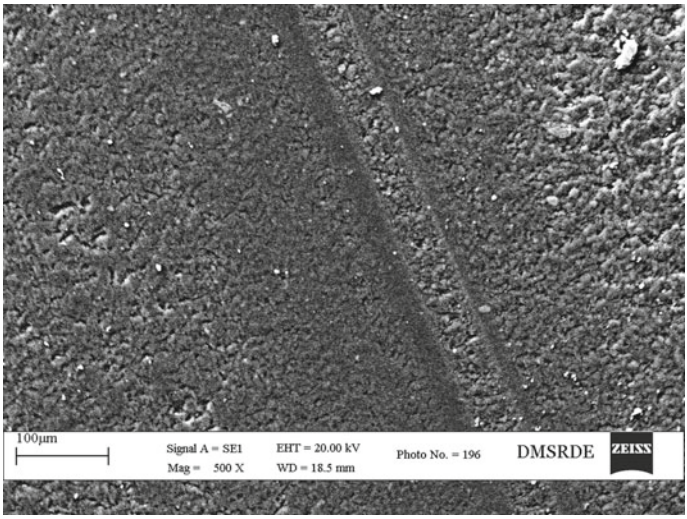

Fig. 4 Worn surface morphology of two-step austempered ductile iron sample (400 °C, 150 min)

4 Conclusion

Based on the present study, the following conclusions were made.

1. Due to two-step process, the microstructure of ductile iron sample consisted of fine ferrite and more austenitic carbon. This microstructure was the reason for enhanced hardness and strength values in the samples.
2. The materials processed by TSA-2 (400 °C, 150 min) exhibited lowest wear loss of 70 mg compared to as-cast sample 85.2 mg. This was due to higher austempering temperature and time.
3. Higher worn surface hardness was observed for material having greater wear resistance.

References

1. Zimba, J., Samandi, M., Yu, D., Chandra, T., Navara, E., & Simbi, D. J. (2004). *Materials and Design, 25*(5), 431–438.
2. Zimba, J., Simbi, D. J., & Navar, E. (2003). *Cement Concrete Composite, 25*(6), 643–649.
3. Dommarco, R. C., & Salvande, J. D. (2003). *Wear, 254*(3–4), 230–236.
4. Zhou, W.-S., & Zhou, Q.-D. (1993). *Wear, 162–164,* 696–702.
5. Shepperson, S., & Allen, C. (1988). *Wear, 121,* 271–287.
6. L. Magalh˜aes, J. Seabra, Wear 215 (1–2) (1998) 237–246.
7. Hatate, M., Shiota, T., Takahashi, N., & Shimizu, K. (2001). *Wear, 251*(1–2), 885–889.
8. Larsen-Basse, J. (1990). *Scripta Metallurgica et Materialia, 24*(5), 821–826.
9. K.-H. Zum Gahr, in: K.C. Ludema, et al. (Eds.), Wear of Materials, ASME, New York, 1979, pp. 266–274.
10. Cullity, B. D. (2001). *Elements of X-ray diffraction* (3rd ed.). Upper Saddle River: Prentice Hall.
11. Rouns, T. N., & Rundman, K. B. (1987). Constitution of austempered ductile iron and kinetics of austempering (retroactive coverage). *AFS Trans, 95,* 851–874.
12. Yang, J., & Putatunda, S. K. (2004). *Materials and Design, 25*(3), 219–230.
13. Gundlach, R. B., & Janowak, J. F. (1983). *AFS Trans., 94,* 377–388.
14. Garin, J. L., & Mannheim, R. L. (2003). *Journal of Materials Processing Technology, 143–144,* 347–351.

Effect of Particle Content and Temperature on Steady-State Creep in Thick Composite Cylinder

Gagandeep Singh Kohli, Tejeet Singh, and Harwinder Singh

Abstract In the present work, the effect of particle content and operating temperature on secondary stage creep in the thick composite cylinder is analyzed. The cylinder is made of Al-SiC_p and is exposed to internal pressure only. Threshold's creep law is used for creep analysis of the thick composite cylinder under plane stress. The analysis is carried out and results are obtained by varying material parameters. Marginal variations in radial, tangential and effective stresses are noticed. However, strain rates show considerable change by increasing the particle content and decreasing operating temperature.

Keywords Thick composite cylinder · Plane stress · Threshold's creep law

1 Introduction

In various industries, cylindrical vessels are used for transportation of high-pressurized fluid or gases from one place to another where they are subjected to high temperature and pressure. Keeping in view, the working condition of the cylinders, a large amount of research has been done to study creep behavior in the thick cylinders [1, 2]. Further, in application involving high temperature and mechanical loadings, creep plays an important role whose effect is to decrease the service lifetime of the cylinders [3, 4]. A large amount of research was done to study the creep behavior in the cylinders made of monolithic material. The cylinder was subjected to internal pressure and it was found that the change in dimension was very small and the deformation was referred with respect to the original dimensions of the cylinder

G. S. Kohli (✉)
Ph.D Research Scholar, IKGPTU, Jalandhar, Punjab, India
e-mail: engg_kohli@yahoo.co.in

T. Singh
Mechanical Department, SBSSTC, Ferozepur, Punjab, India

H. Singh
Mechanical Department, GNE, Ludhiana, Punjab, India

© Springer Nature Singapore Pte Ltd. 2021

C. Prakash et al. (eds.), *Advances in Metrology and Measurement of Engineering Surfaces* , Lecture Notes in Mechanical Engineering,
https://doi.org/10.1007/978-981-15-5151-2_13

[5–7]. Bhatnagar and Gupta [8] had analyzed creep in thick-walled orthotropic cylinders and found that creep anisotropy had a significant effect on cylinder behavior. Bhatnagar el al. [9] found that as per design consideration, the orthotropic cylinder could be better and a safe choice when comparison with isotropic cylinders.

Further, in number of applications such as automobile, military and aerospace industry, reducing the weight of a component is a big challenge. To overcoming this challenge, composites play important role especially metal matrix composites (MMCs). MMCs with aluminum (Al) as matrix reinforced with ceramic material in the form of fibers/whiskers/particles and functionally graded materials (FGMs) were found to be very useful as they can resist deforming under harsh conditions. According to some experimental studies, with the use of ceramic particle like silicon carbide in aluminum/aluminum alloys creep rate could be reduced to several orders in comparison to pure aluminum/aluminum alloys [10, 11]. Keeping this in view, You et al. [12] had analyzed creep in an internally pressurized FGM cylinder and found that by altering the material parameter along radial direction, the stresses in circumferential and axial directions were considerably affected. Chen and Lin [13] had done elastic analysis in the thick cylinder made of FGMs and they found that the property of gradation significantly affects the stress variation along radial direction. Singla et al. [14] had derived a mathematical model for secondary creep in a thick cylinder made of orthotropic material and the obtained results were compared with the isotropic cylinder and significant variation was observed. Jamian et al. [15] analyzed creep in FG thick cylinder and found that the property of the FGM significantly affects stress in radial direction. Nejad et al. [16] had studied that how material parameters used in Norton's law affects stresses in various directions and shown that stresses and strain rates were considerably reduced in radial direction. From literature review, it was found that in most of these studies, creep behavior of the cylinder is predicted by using Norton's law. However, in composites made of aluminum, the study of creep behavior using Norton's law was not approved because of high values of apparent stress exponent and apparent activation energy [17]. Keeping in mind, the present study is done to study the creep behavior of a Al-SiC_p cylinder under plane stress using threshold stress-based law in place of Norton's power law. The steady-state condition of stress is assumed and the applied pressure is held constant during the entire loading history. Further, primary creep deformations are neglected being small.

2 Basic Creep Equations and Parameters

According to threshold's law, the effective creep rate ($\dot{\varepsilon}_e$) in Al composites undergoing steady creep is given by Eq. (1) [2, 18],

$$\dot{\varepsilon}_e = [M(\sigma_e - \sigma_o)]^n \tag{1}$$

Table 1 Values of creep parameters used for Al-SiCP composite [2]

P (μm)	T (°C)	V (vol%)	M (s-1/5/MPa)	σ_o (MPa)	Coefficient of correlation
1.7	350	10	0.00435	19.83	0.945
		20	0.00263	32.02	0.995
		30	0.00227	42.56	0.945
1.7	350	20	0.00263	32.02	0.995
	400		0.00414	29.79	0.974
	450		0.00592	29.18	0.916

where

$$M = \frac{1}{E}\left(A' \exp \frac{-Q}{RT}\right)^{\frac{1}{n}}$$

where E, A', Q, R, T, n, σ_e and σ_o represent Young's modulus, structure dependent parameter, true activation energy, gas constant, working temperature stress exponent, von Mises effective stress and threshold stress. The creep parameters M and σ_o as shown in Eq. (1) depend upon material type, operating temperature (T), particle size (P) and particle volume (V). Singh and Gupta [2] had used creep data reported by Pandey et al. [18] and plotted individual set of that data as $\dot{\varepsilon}^{1/5}$ versus σ on a linear scale and obtained the values of M and σ_o, as shown in Table 1.

3 Analysis and Solution

Assume a thick composite cylinder composed of Al-SiC$_p$ having internal radius "a" as 25.4 mm and external radius "b" as 50.8 mm. The cylinder is under application of internal pressure "p" of 85.25 MPa as shown in Fig. 1.

The radial strain rate ($\dot{\varepsilon}_r$) and tangential strain rate ($\dot{\varepsilon}_\theta$) in a cylinder are given by:

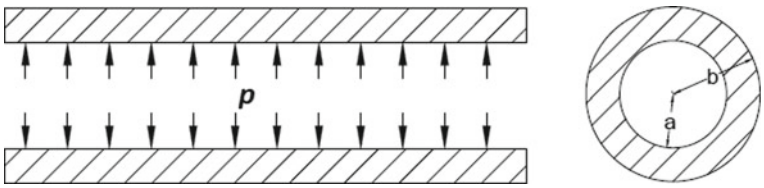

Fig. 1 Schematic diagram of open end, thick-walled composite cylinder subjected to internal pressure

$$\dot{\varepsilon}_r = \frac{\mathrm{d}\dot{u}_r}{\mathrm{d}r} \tag{2}$$

$$\dot{\varepsilon}_\theta = \frac{\dot{u}_r}{r} \tag{3}$$

where $\dot{u}_r = \frac{\mathrm{d}u}{\mathrm{d}t}$ indicates the displacement rate in radial direction and u represents radial displacement.

$$r\frac{\mathrm{d}\dot{\varepsilon}_\theta}{\mathrm{d}r} = \dot{\varepsilon}_r - \dot{\varepsilon}_\theta \tag{4}$$

Applied boundary conditions are,

$$\sigma_r = -p, \text{at}\, r = a$$
$$\sigma_r = 0, \text{at}\, r = b$$

The equilibrium equation is obtained by balancing the forces acting on a small cylindrical element in radial direction [3]

$$r\frac{\mathrm{d}\sigma_r}{\mathrm{d}r} = \sigma_\theta - \sigma_r \tag{5}$$

Since it is assumed that the volume of the cylinder do not change, therefore,

$$\dot{\varepsilon}_r + \dot{\varepsilon}_\theta + \dot{\varepsilon}_z = 0 \tag{6}$$

Considering a plane stress case ($\sigma_z = 0$), the generalized constitutive Eqs. for creep in composites along the principal directions of r, θ and z are given as [17]

$$\dot{\varepsilon}_r = \frac{\mathrm{d}\dot{u}_r}{\mathrm{d}r} = \frac{\dot{\varepsilon}_e}{2\sigma_e}[2\sigma_r - \sigma_\theta] \tag{7}$$

$$\dot{\varepsilon}_\theta = \frac{\dot{u}_r}{r} = \frac{\dot{\varepsilon}_e}{2\sigma_e}[2\sigma_\theta - \sigma_r] \tag{8}$$

$$\dot{\varepsilon}_z = -\frac{\dot{\varepsilon}_e}{2\sigma_e}[\sigma_r + \sigma_\theta] \tag{9}$$

where σ_r, σ_θ, σ_z represent the stress in the radial, tangential and axial direction.

According to von Mises yield criterion, effective stress is given by [19]

$$\sigma_e = \frac{1}{\sqrt{2}}\left[\sigma_\theta^2 + \sigma_r^2 + (\sigma_r - \sigma_\theta)^2\right]^{\frac{1}{2}} \tag{10}$$

Divide Eq. (7) by (8) and taking $\frac{\sigma_r}{\sigma_\theta} = x$ we have,

$$\frac{\mathrm{d}u_r}{\mathrm{d}r} \cdot \frac{r}{u_r} = \frac{2x-1}{2-x} = \phi(r) \tag{11}$$

Integrating Eq. (5) between limits a to b, and applying the boundary conditions, we get

$$\int_a^b \sigma_\theta \mathrm{d}r = ap \tag{12}$$

Solving Eqs. (7), (8), (9), (10) and (12), we have

$$\sigma_\theta = \left[\frac{ap}{\int_a^b T(r)\mathrm{d}r} - \frac{\int_a^b K(r)\mathrm{d}r}{\int_a^b T(r)\mathrm{d}r} \right] \cdot T(r) + K(r) \tag{13}$$

where

$$T(r) = \left\{ \frac{2\left(1+x^2-x\right)^{\frac{1-n}{2}}}{(2-x)r} \cdot \exp\left[\int_a^r \frac{\phi(r)}{r}\mathrm{d}r \right] \right\}^{\frac{1}{n}} \tag{14}$$

$$K(r) = \frac{\sigma_o}{\sqrt{1+x^2-x}} \tag{15}$$

Or Eq. (13) may be written as

$$\sigma_\theta = \left[\frac{\sigma_{\theta_{\mathrm{av}}}(b-a)}{\int_a^b T(r)\mathrm{d}r} - \frac{\int_a^b K(r)dr}{\int_a^b T(r)dr} \right] \cdot T(r) + K(r) \tag{16}$$

where $\sigma_{\theta_{\mathrm{av}}} = \frac{ap}{b-a}$

And $\sigma_{\theta_{\mathrm{av}}}$ is average tangential stress

Integrating Eq. (5) between limits a to r,

$$\sigma_r = \frac{1}{r}\int_a^r \sigma_\theta \mathrm{d}r - \frac{ap}{r} \tag{17}$$

To calculate the first approximation of $x = (x)_1$, taking $\sigma_\theta = \sigma_{\theta_{\mathrm{av}}}$ in Eq. (17), we get first approximation of $\sigma_r = \sigma_{r1}$, as

$$\sigma_{r1} = \frac{ap}{r}\left(\frac{r-b}{b-a}\right) \tag{18}$$

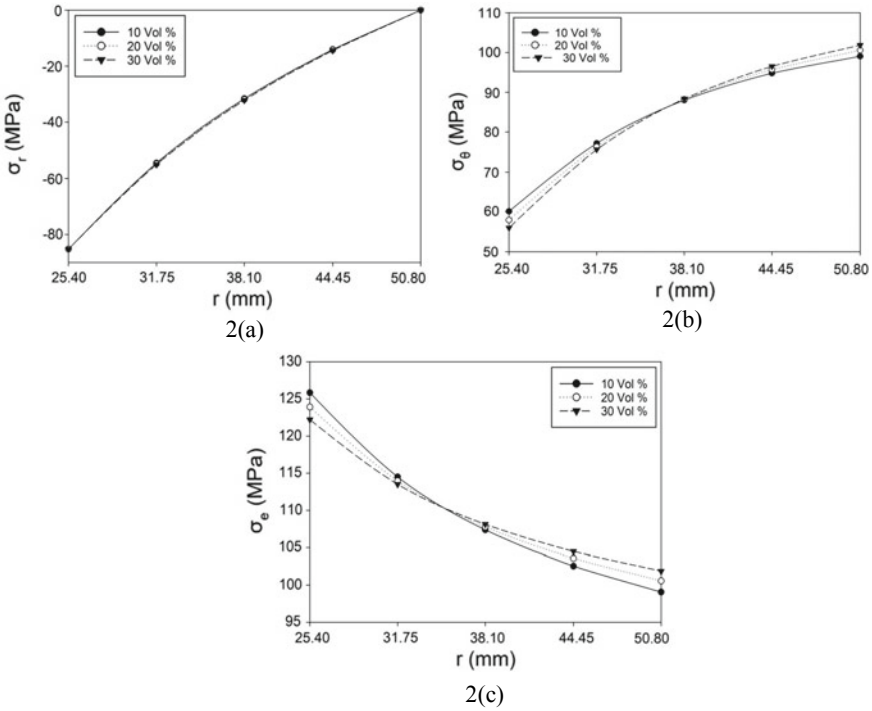

Fig. 2 **a–c** Effect of varying particle content of on creep stresses

And

$$(x)_1 = \frac{\sigma_{r1}}{\sigma_{\theta_{\text{av}}}} = 1 - \frac{b}{r} \tag{19}$$

Put $(x)_1$ in Eq. (11) we get $\phi(\mathrm{r})_1$, from this by numerical integration, we find, $\exp \int_a^r \frac{\phi(r)}{r} \mathrm{d}r$.

Using this in Eq. (14) together with $(x)_1$ for (x), the value of $T(r)_1$ is obtained. And similarly, value of $K(r) = K(r)_1$ is also obtained with $(x)_1$ for $(\boldsymbol{x})$.

Using the above values in Eq. (16), we obtain σ_{θ_1}. Again using σ_{θ_1} in Eq. (17), we get σ_{r_2} and so on.

4 Results and Discussion

4.1 Effect of Particle Content

Figure 2a–c shows the effect of changing the particle content (SiC_P) from 10%, to 30% by volume on the creep stresses in a thick composite cylinder. Figure 2a shows that a no significant change has been observed on the radial stress which is found to be of compressive nature by changing the content of reinforcement. Figure 2b shows the variation of stress in the tangential direction and it is found that tangential stress increases from inner to outer radius of a cylinder. It is also observed that with the change in particle content (SiC_P) from 10 to 30%, the tangential stress decreases at the inner radius and increases toward the outer radius. The tangential stress with 30% SiC_p content at the inner radius is 56.01 MPa and at the outer radius stress is 101.87 MPa, whereas with 10% SiC_p content, the tangential stress at inner radius 60.14 MPa, and at outer radius, stress found is 99.05 MPa. Figure 2c shows the graph for effective stress by varying SiC_p content. The effective stress decreases throughout the radius and the effective stress with 30% SiC_p content is on the lower side in comparison to 10% SiC_p content at the inner radius and increases toward outer radius. The effective stress with 30% particle content at the inner radius is 122.22 MPa and at the outer radius is 101.87 MPa, whereas with 10% particle volume, the effective stress at the outer radius is 125.84 MPa and at the inner radius is 99.05 MPa.

Figure 3 shows variation in stress difference ($\sigma_e - \sigma_o$) for different particle content and it shows a significant decrease over the entire radius by increasing particle content. The variation in the stress at internal radius is more as compared to external radius.

With the increase in SiC_p content, the effective strain rate decreases significantly as shown in Fig. 4a. This decrease in the effective strain is because of decreasing creep parameter M and increasing threshold stress σ_o with the increase in particle content as given in Table 1.

Figure 4b–d shows the effect of variation in radial, tangential and axial strain rates ($\dot{\varepsilon}_r$, $\dot{\varepsilon}_\theta$, and $\dot{\varepsilon}_z$) by varying particle content. The effect of the radial and tangential strain rate is similar to that of the effective strain rate; however, radial strain rate shows compressive nature and tangential strain rate shows tensile nature.

Similarly, the axial strain rate is less for 30% particle content than the strain rate for 10% particle content. With the increase in SiC_p content in composite cylinder, the spacing between the particles decreases which results in increasing the threshold stress [20] and decreasing creep parameter M (Table 1), and together these parameters significantly reduces strain rates. Similar results had been reported by Neih [10] that by increasing content of SiC_w in aluminum alloy (6061 Al), creep rate could be reduced significantly. Pandey et al. [18] had also found a significant decrease in strain rate under uniaxial test.

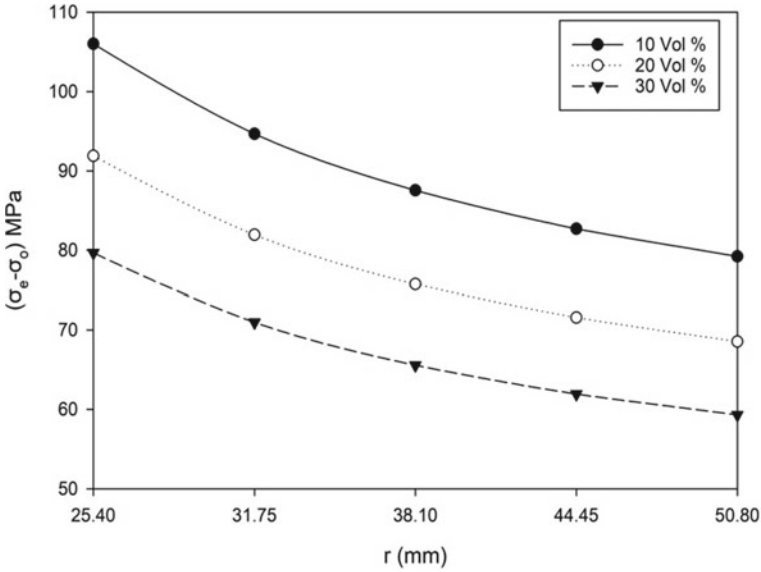

Fig. 3 Effect of varying particle content of on stress difference

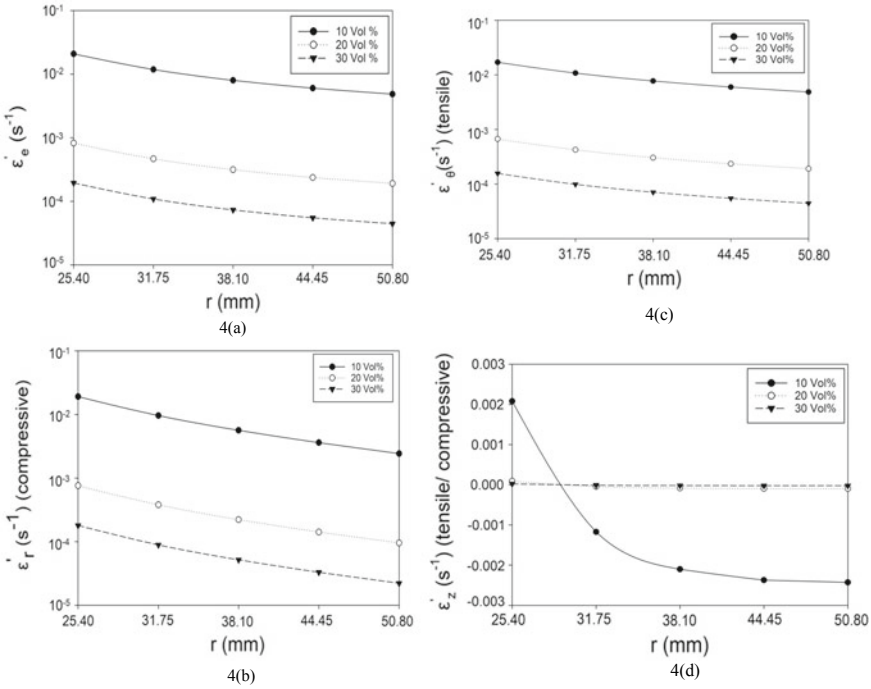

Fig. 4 **a–d** Effect of varying particle content of on creep strain rates

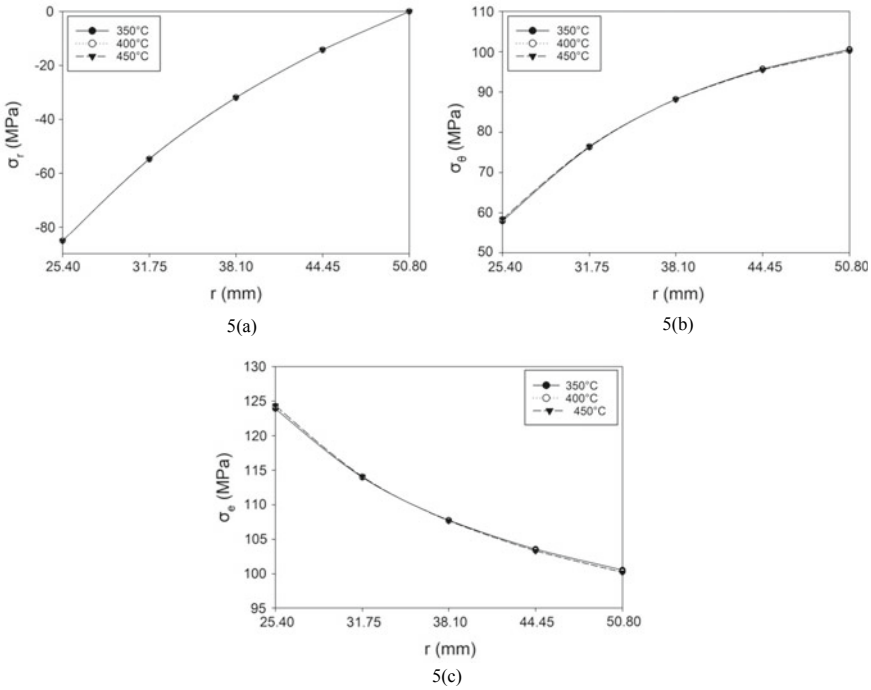

Fig. 5 **a–c** Effect of temperature variation of on creep stresses

4.2 Effect of Changing Operating Temperature

Figure 5a–c shows the effect of temperature variation on creep stresses in a cylinder. Figure 5a shows that radial stresses are negligibly affected by the variation in the operating temperature. Whereas the stress in tangential direction decreases marginally by decreasing the operating temperature from 450 to 350 °*C* as shown in Fig. 5b. The tangential stress for operating temperature 450 °C at the inner radius is 58.45 MPa and at the outer radius is 100.21 MPa, whereas for 350 °C, it is 57.94 MPa at the inner radius and 100.56 Mpa at the outer radius.

Figure 5c shows the graph for the effective stress, which shows that the effective stress for operating temperature 350 °C is on lower side at the inner radius and goes on increasing toward the outer radius. The stress difference ($\sigma_e - \sigma_o$) decreases throughout the entire radius with the decrease in operating temperature as shown in Fig. 6.

Figure 7a–d shows the effect of temperature variation on strain rate in a cylinder. It is found that with the decrease in temperature from 450 to 350 °C, the threshold stress σ_o increases and creep parameter M decreases due to which the strain rate decreases to a significant level. Similar results had been found by Pandey et al. [18] for Al-SiC_p for uniaxial test.

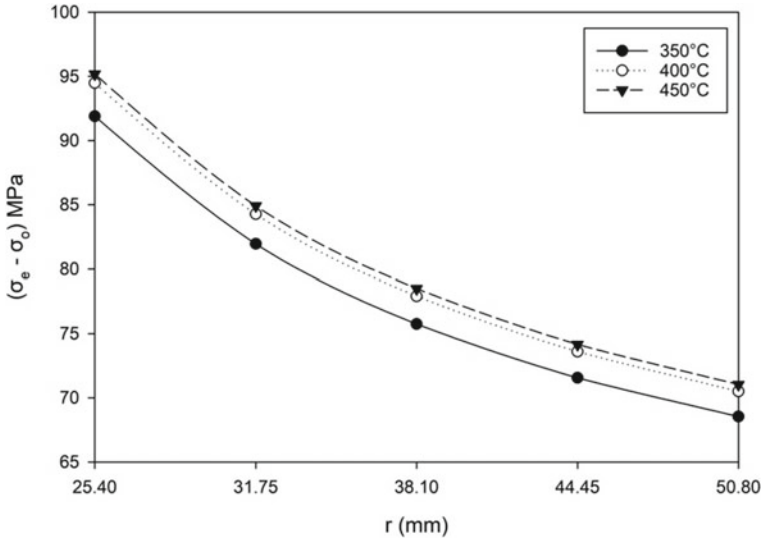

Fig. 6 Effect of temperature variation of stress difference

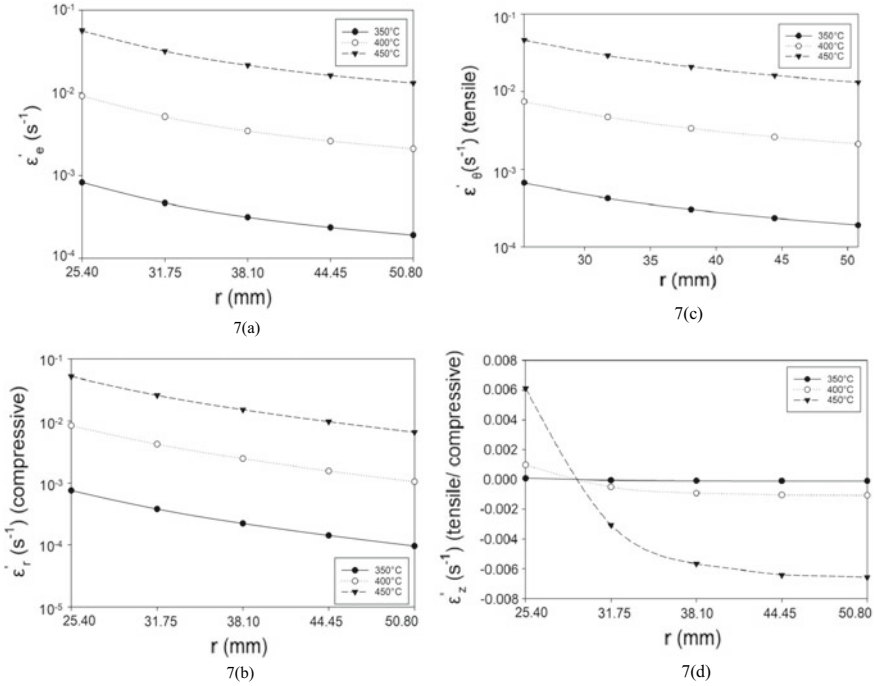

Fig. 7 **a–d** Effect of temperature variation on strain rates

5 Conclusion

1. The radial stress shows negligible variation by varying particle content and working temperature.
2. The tangential and effective stresses decrease near the inner radius and increase toward outer radius by increasing particle content and with the decrease the working temperature. The stress in the tangential direction increases throughout the radius. However, von Mises effective stress decreases throughout.
3. The radial and tangential strain rates decrease on moving from the internal to external radius. A significant decrease in strain rate was observed by increasing particle content and with the decrease the working temperature.
4. The axial strain rate at inner radius was tensile in nature and becomes compressive at outer radius and increases toward outer radius. However, it was observed that for thick composite cylinder, this change could be reduced to a considerable level by using more particle content operating at lower temperature.

References

1. You, Z., & Buttlar, W. G. (2005). Application of discrete element modeling techniques to predict complex modulus of asphalt-aggregate hollow cylinders subjected to internal pressure. *Transportation Research Record, 1929,* 218–226.
2. Singh, T., & Gupta, V. K. (2009). Effect of material parameters on steady state creep in a thick composite cylinder subjected to internal pressure. *The Journal of Engineering Research, 6*(2), 20–32.
3. Gupta, S. K., & Pathak, S. (2001). Thermo creep transition in a thick walled circular cylinder under internal pressure. *Indian Journal of Pure and Applied Mathematics, 32*(2), 237–253.
4. Hagihara, S., & Miyazaki, N. (2008). Finite element analysis for creep failure of coolant pipe in light water reactor due to local heating under severe accident condition. *Nuclear Engineering and Design, 238*(1), 33–40.
5. Weir, C. D. (1957). The creep of thick-walled tube under internal pressure. *Journal of Applied Mechanics, 24,* 464–466.
6. King, R. H., & Mackie, W. W. (1967). Creep of thick-walled cylinders. *ASME Journal of Basic Engineering, 89*(4), 877–884.
7. Pai, D. H. (1967). Steady state creep analysis of thick walled orthotropic cylinders. *International Journal of Mechanical Sciences, 9*(6), 335–348.
8. Bhatnagar, N. S., & Gupta, S. K. (1969). Analysis of thick-walled orthotropic cylinder in the theory of creep. *Journal of the Physical Society of Japan, 27*(6), 1655–1662.
9. Bhatnagar, N. S., Kulkarni, P. S., & Gupta, S. K. (1984). Creep analysis of an internally pressurized orthotropic rotating cylinder. *Nuclear Engineering and Design, 83,* 379–388.
10. Basak, A. K., Pramanik, A., & Prakash, C. (2019). Deformation and strengthening of SiC reinforced Al-MMCs during in-situ micro-pillar compression. *Materials Science and Engineering: A*, *763*, 138141.
11. Prakash, C., Singh, S., Sharma, S., Garg, H., Singh, J., Kumar, H., & Singh, G. (2020). Fabrication of aluminium carbon nano tube silicon carbide particles based hybrid nano-composite by spark plasma sintering. *Materials Today: Proceedings*, *21*, 1637–1642.
12. You, L. H., Ou, H., & Zheng, Z. Y. (2007). Creep deformations and stresses in thick-walled cylindrical vessels of functionally graded materials subjected to internal pressure. *Composite Structures, 78,* 285–291.

13. Chen, Y. Z., & Lin, X. Y. (2008). Elastic analysis for thick cylinders and spherical pressure vessels made of functionally graded materials. *Computational Material Science, 44,* 581–587.
14. Singla, A., Garg, M., Deepak, D., & Gupta, V. K. (2012). Creep modeling in an orthotropic FGM cylinder. *ARME, 1*(2), 55–61.
15. Jamian, S., Sato, H., Tsukamoto, H., & Watanabe, Y. (2013). Creep analysis of functionally graded material thick walled cylinder. *Applied Mechanics and Materials, 315,* 867–871.
16. Nejad, M. Z., Hoseini, Z., Niknejad, A., & Ghannad, M. (2015). Steady state creep deformations and stresses in FGM rotating thick cylindrical pressure vessels. *Journal of Mechanics, 31*(1), 1–6.
17. Gupta VK, Singh SB, Chandrawat HN and Ray S. Modeling of creep behavior of a rotating disc in presence of both composition and thermal gradients. *ASME The Journal of Engineering Materials and Technology*, *127*(1), 97–105 (2005).
18. Pandey, A. B., Mishra, R. S., & Mahajan, Y. R. (1992). Steady state creep behavior of silicon carbide particulate reinforced aluminum composites. *Acta Metallurgica et Materialia, 40*(8), 2045–2052.
19. Dieter, G. E. (1988). *Mechanical metallurgy*. London: McGraw-Hill.
20. Li, Y., & Langdon, T. G. (1999). An examination of a substructure-invariant model for the creep of metal matrix composites. *Materials Science and Engineering: A, 265*(1), 276–284.

Comparative Study on Wind Tunnel Calibrating Instruments

Akhila Rupesh, J. V. Muruga lal Jeyan, V. M. Ram Mohan, K. Praveen Kumar, T. Abhishek, T. Ashish, K. V. V. M. Reddy, and Greeshma Maddireddy

Abstract In the present study, we use wind tunnel model as a medium to calculate and analyze the flow velocity of the air passes through any aerodynamic medium and besides automobile too. An experimental study was carried out on a wind tunnel to evaluate and optimize the performance and results of the model obtained. Experiments were carried out with four different instruments, i.e., Yaw Sphere, Claw Yaw Meter, Pressure Sphere (multi-hole probe), Turbulence Sphere to obtain velocity data. According to the experiments and studies carried out, Pressure Sphere provides us with exact velocity and pressure value when compared to the other three instruments. Using this new kind of instrument, faults can be minimized when compared to the previous instruments.

Keywords Wind tunnel · Measuring methods · Flow velocity · Pressure measurement

1 Introduction

Wind tunnel is an instrument utilized in aerodynamically testing for studying the results of air passing over the model to be tested. A wind tunnel consists of a tubular passage way with the test section where the model is to be tested. Air is moved over the model by the fan system which is having an electric motor to control speed. The instrument is associated with suitable sensors to measure forces and pressure. Different velocity data can be obtained and calculated by examining the wind tunnel using various types of instruments. Before discussing the experimental use of these instruments, we should have knowledge about where these instruments are put to

A. Rupesh (✉) · J. V. Muruga lal Jeyan · G. Maddireddy
Department of Aerospace Engineering, Lovely Professional University, Phagwara, Punjab 144411, India
e-mail: akhilarupesh56@gmail.com

V. M. Ram Mohan · K. Praveen Kumar · T. Abhishek · T. Ashish · K. V. V. M. Reddy
Department of Mechanical Engineering, Lovely Professional University, Phagwara, Punjab 144411, India

© Springer Nature Singapore Pte Ltd. 2021

C. Prakash et al. (eds.), *Advances in Metrology and Measurement of Engineering Surfaces* , Lecture Notes in Mechanical Engineering,
https://doi.org/10.1007/978-981-15-5151-2_14

use and the purpose they serve with regards to the equipment they are placed with. These instruments are interlinked and accompanied by various wind tunnels.

The wind tunnel is a device which provides air flow continuously under the guidance of the model of interest which is to be tested using an operational view of point. The wind tunnel is usually classified as low-speed tunnels, high-speed tunnels and special purpose tunnels. Experimental information toward solving aerodynamic problems could be obtained in a various number of ways such as flight experiments, rocket sleds, drop tests, ballistic ranges and wind tunnels are some of the ways by which aerodynamic data can be obtained. Wind tunnel is further classified 1. Based on speed and Mach number range into five types. Mach number = speed of object/speed of sound in air. $M = V/C$ where subsonic is having high Mach number up to $M < 0.8$, transonic is having Mach number between $0.8 < M < 1.2$, supersonic is having high Mach number with $M > 1.2$, hypersonic is having Mach number with greater $M > 5$ and sonic is with Mach number $M = 1$ and 2. Based on the test section wind tunnel is classified as (a) Open wind tunnel, (b) Closed wind tunnel and (c) Semi-enclosed wind tunnel. Even in today's world, the utilization of wind tunnels to compute both complex and normal aerodynamics issues is required. Wind tunnels showcase unique flow visualization to compute and solve complex problems and to find a solution. Perfect lift, drag and efficiency can be easily complex problems [1].

2 Circular Cross-Section with Three-Hole Probe (CTHP) Measurement and Calibrating for the Long Angular Area

It is the new approach for calibrating the three-hole probe measurement. The new calibrating consideration popular CTHP is the angular distance between the holes remains sixty degrees. The advantage of using a multi-hole probe is to measure unstable flows and also turbulence. The pressure probes represent a classical obtrusive methodology for measurement of rate fields.

2.1 Pressure Probe Consists of Two Methods

Non-Nulling Mode: A probe is situated at a continuous angle of the test section. The calibrating system of a probe is found on the location of the order of the probe within and termed as flow field. The five-hole and three-hole probes give a restricted entire performance. The pressure in holes is determined only through pressure constant.

Nulling Mode: The probe is arranged in the flow direction, and therefore, the angle of attack with respect to the essential hole is to be '0'.

The reducing factors of CTHP are velocity range is measurable. The frequency reaction of the probe is the von Karman vortex sheet analysis is used in a frequency response limiting issue. The intention of this inquiry is for measurement

of an extremely complicated and incompressible flow that is approximately the same within the radial plane (mid-span) however present in giant nonuniformities within the circumferential direction [2].

3 Hot-Wire Measurement Technique for Stream Rate Vector Measurement in 2D Gasoline Streams Created on Substitute Indifferent Arrangement

The hot-wire amount could be an ordinarily used technique for gas flow rate vector measurements. To search out the purpose of the rate vector in the 2D flow, a focused hot-wire probe with valves is often used, and such a probe contains four wires linked in sets settled in perpendicular planes. A calculation formula used to date is predicated on the material copy that does not take the probe arrangement addicted to consideration. Throughout testing, the probe is being located within the central point of the test section, in order that its axis is vertical to the chamber axis.

According to king and Jorgen Sens equation, rate of velocity elements can be arranged. During this technique, most qualified faults of four hundred for every element were obtained. All these faults unit areas were because of the utilized physical model. The nonaligned arrangement was formerly utilized for calibrating an alone hot-wire probe below numerous circumstances for calibrating two two-wire probes. The network was enforced with the help of MATLAB atmosphere and therefore the nonaligned arrangement tool case. The production sheet of the arrangement includes two linear activations performing neurons. Everybody of these neurons is associated with only rate vector element. The Levenberg–Marquardt variable metric formula was used.

In resemblance to the one-step technique, the nonaligned arrangement performs with nearly ten times minimum mistake. The purpose of the rate vector parts at one measurement points employing a nonaligned arrangement lasted close to 20 ms whereas spending the one-step technique in the order of 2 ms. Accordingly, the nonaligned arrangement works close to 10 times slower. The most disadvantage of the nonaligned arrangement service lies within the proven fact that it is costly [3].

4 Going on the Utilization of the Linear Exclamation Methodology Within Measuring Process of Seven-Hole Pressure Probe

The seven-hole probe could be pressure measuring device capable of giving measurable data regarding three parts of the velocity, similarly regarding total and dynamic pressure. A linear exclamation methodology performed larger than the information calibrating matrices provided. The presentation of this methodology, in conditions

of measurement faults, is being compared with the standard individual. During calibration, the probe is aligned in such a manner to record the flow parameters. Within the casing of stream among small angles of occurrence that it does not take place disconnection at any purpose of probe extremity, a tangent reference is used. Non-dimensional constant area unit has been considered so far during the calibration process.

Wind tunnel testing is distributed to check developer apparatus for the given calibrating technique. A flow field investigation has been conducted on a stationary wing with free stream velocity of 40 m/s.

The use of linear exclamation technique on seven-hole probe calibrating verified to associate degree possibility which improves the measure preciseness. It is predictable with the intention of outcome will be increased if the next variety calibrating point is employed. The use of next preciseness mechanism within the angular position of the probe throughout the calibrating method will increase the standard of outcomes [4].

5 Method of Recovery of Gas Flow Pressure Based on the Results of Measurements in Short-Duration Wind Tunnels

5.1 Gas Flow Pressure

The constant flow (CV) may be a principle that is employed to search out importance flow below varied circumstances to pick proper importance for flow purpose. The CV was planned to use with fluid flows, and it conveys the flow in gallons per minute of 60 degrees of water with pressure drop with a value of 1 psi.

Quasi-Solution: An organized answer of an exact ill-posed downside that (under sufficiently organized conditions) satisfies, in distinction to a correct answer, the condition of being well-posed.

5.2 Piezoelectric Sensor

The device that uses the piezo effect and measures the amendment of pressure, temperature, strain, acceleration by changing them into electrical charge

The device should be a linear dynamical system so that the calculations will be easy. During solving and examining the signals if the faults exceed than expected, then linear Volterra integral equations of the first kind of the convolution type are utilized to obtain exact solutions. The problems detected raise the antenna resolving power and detect a weak signal against a background of anisotropic noise and non-parametric identification of linear stationary systems which reduces to solve linear

Volterra integral equations of the first kind of convolution type. The problem is solved by using Lavrent'ev method of regularization as a combination with the model experiments to determine the regularization parameters. The Lavrent'ev method with the combination of least square has more advantage to solve the problems. The problems noted are normal pressure and derivative is zero at the initial time. The quasi-solution is to be kept at an initial position on a set of N intervals from $[0, T]$. We are assuming that equations are average at every interval. So at least at one interval, the equation holds accurate, and faults become average. The number of intervals and the distribution of their lengths are calculated from the approximate solution and by minimizing the root mean square method is called quasi-solution.

The normal response is calculated through experiment, we do not require mathematical expressions possible for simple cases, and the pressure is used as a linear dynamic object for loads elastic. Deformation, the temperature of the sensor and dimensions of the sensor as (diameter $(d) = 5 \times 10^{-3}$ m) and thickness $(h) = 0.5 \times 10^{3}$) which is responsible for the weak output signal. Normal Pressure at the sensor is $u(t)$. So, the input equation is given. As $g(t)$ and output is $f(t)$, then the linear Volterra integral equation of the first kind is mathematical relations to be filled. Quasi-solutions are solved using piecewise constant and piecewise linear functions.

Piecewise Constant Function: Even in this, we use linear Volterra integral equations of the first kind. All the mathematical calculations are done in definite integrals by trapezoid methods.

6 Recovery of the Load Acting on the Pressure Sensor

For normal pressure, a device is used with the sensor, electromagnet holding a metal ball with radius r with initial height h along with piezoelectric element and recording device. Once the electromagnet is turned off, the ball began to fall. The aerodynamic drag with respect to gravity mg is used for motion of the ball in the air [5].

7 Flow Measurement and Instrumentation

The creation and calibration of a small multi-hole pressure probe for measuring the 3D stream field have the ability to give static and total pressure distributions along with all the components of speed. These probes are used in turbomachinery for study, requiring a quick response to local factor interrupts and in elevation flow angle. Therefore, the size of the probe should be as low as potential. The minor size of the probe can prevent the flow and reduce equivalent limited barriers of the flow field, particularly when blade channels reach a solid boundary. The friction and calibration of sub-smallness in the five-hole probe are used in difficult internal flow area in turbomachine study. The five holes as in a corner of a pitot tube probe assessment tool commonly used to measure 3D flow fields with correct arrangement,

such probes had been proved to obtain scalar and vectors attributes as total pressure and static pressure, along with high-tech systems for 3D vector in sustainable flow field, as hot-wire anemometry, laser Doppler velometric and particle velometric, and some losses were geometrically complicated configurations. Their geometry, multi-hole as in a corner of a pitot tube, requires significant skill to build small sizes.

7.1 Manufacture of the Probe

The structure of a five-hole miniature probe was a tough job. Special care should be taken when assembling this size. The employment of many short article tubes reduces their response to the construction of such probes, when it stops over time, takes liquefied to transmission faults through the tubing, especially when assessment less velocity 3D currents. In addition, the danger of tubing was there when the probe is formed with a desired structure, and they can replace five tiles with the crosslet position until the silver is sold. In the appropriate sense, the continuance of the probe during the grinding processing is used to prevent the probe's tip. It is attached on a minor multi-angle vise clamp at the tip of the probe is tangent to the tang cone when a small surface grinder accommodates the longitudinal axis of the center.

7.2 Pressure Data Acquisition System

For close inspection at the plenum manifold, five types of pressure mechanical energy are available, for each of the probes related. This is controversial in advance, which gives a faster reaction by reducing the volume of the thread, and therefore, the three probes are within the simplest connection tube that connects each probe to the detectors of pressure.

7.3 Calibrating Rig and Calibrating Method of the Five-Hole Probe

7.3.1 The Yaw–Probes Traverse Mechanism

It is the non-nulling type, where the process of incorporating the flow into the stream is known for experimentation and then revolves around yaw and pitch. This promotes probe within the limits of the yaw (φ) and the probes (θ) at each combination point. This leads to pressure information matrix, from which the amount of pressure and parallel calibrating constant can be calculated. It is implemented through a computer-driven powered system that can transmit the probe to combination with

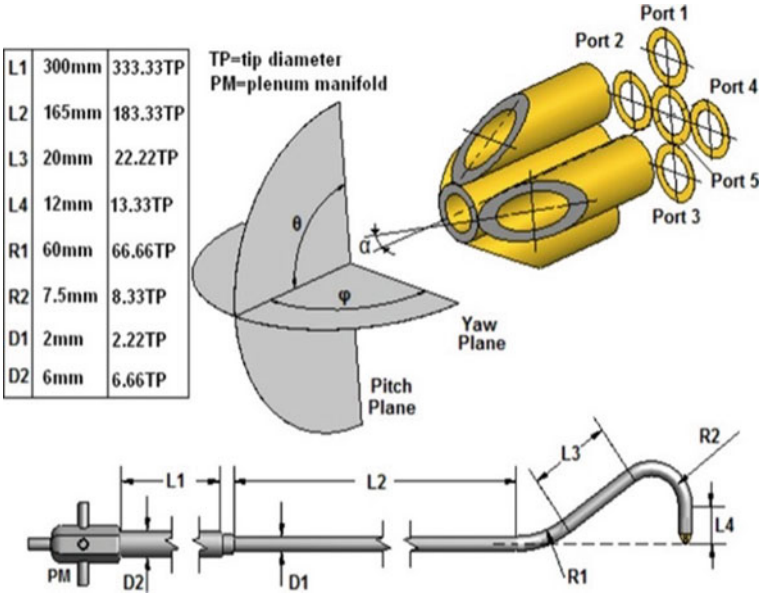

Fig. 1 External dimensions and appearances of the five-hole probe

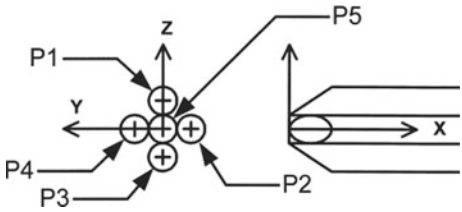

Fig. 2 Representation of a standard five-hole pressure probe

the correctness (Figs. 1 and 2). The five hole probe is an example of this mechanism which is shown in Fig. 2 and the external appearance of the five hole probe is shown in Fig. 1.

8 Determining the Calibrations by a Four-Hole Pressure Probe

To find out the mean velocity compounds among turbulent single phase flows, we utilize multi-hole pressure probes, and when the mean flow direction comes to swirling flow, there will be unknown. The calibrating method provided to the local fluid means static pressure as the variation of the total and dynamic pressure. Pressure probes

are being calibrated within steady flows of low turbulence force, besides even to a particular range of yaw and pitch angles, ratios of the various pressure readings provided by probe head valves can be built up to determine the angle of velocity vector which is unknown and also relative with respect to the axis of the probe. Previously, we followed the Cobra probe geometry that was proposed by shepherd. Shepherd along with his colleagues had looked and researched and tested both of the hemispherical head pressure probes and also conventional five-hole conical. The results showcased that Cobra probe provided less Reynolds number sensitivity among the velocity range between 16 and 110 m/s when compared to five-hole hemispherical and conical probes. Later, experiment is being carried out utilizing the Cobra pressure probe in a swirled free jet which had been earlier explained, where both the mean and turbulent flow structure were related to an upper-frequency limit of 1.5 kHz. However, no relative measurements were taken with respect to Reynolds stresses by either hot-wire or laser Doppler anemometry was being set up for this flow. This research showcases results for a modified turbulent pipe flow, which accepts a comparison with provided data to be made. The results were provided for this calibrating flow for two probe sizes. Interrelations among turbulent velocity components inside pipe flow and static pressure are provided. The final outcomes provided in this paper and in previous work denote that the high-frequency Cobra probe sustains or needs a new method for measuring the complex turbulent flows [6].

9 Conclusion

In the analysis, it is noted that the sensitivities of the calibrating instruments are most once it is either cone or wedge formed. The larger wedge or cone gives more accurate results but it is impossible to provide larger cone or wedge due to formation of detached wave.

References

1. Arifuzzaman, M., & Mashud, M. (2012). Design construction and performance test of a low cost subsonic wind tunnel. *IOSR Journal of Engineering, 2*(10), 83–92.
2. Díaz, K. A., Oro, J. F., & Marigorta, E. B. (2009). Cylindrical three-hole pressure probe calibration for large angular range. *Flow Measurement and Instrumentation, 20*(2), 57–68.
3. Socha, K., & Socha, M. (2015). Hot-wire anemometric method for flow velocity vector measurement in 2D gas flows based on artificial neural network. *Flow Measurement and Instrumentation, 46*, 163–169.
4. Silva, M. G., Pereira, C. A. C., & Cruz, J. M. S. (2003). On the use of a linear interpolation method in the measurement procedure of a seven-hole pressure probe. *Experimental thermal and fluid science, 28*(1), 1–8.
5. Derevyanko, V. A., Kukushkin, S. V., & Latypov, A. F. (2014). Method of recovery of gas flow pressure based on the results of measurements in short-duration wind tunnels. *Journal of Applied Mechanics and Technical Physics, 55*(6), 970–978.

6. Hooper, J. D., & Musgrove, A. R. (1997). Reynolds stress, mean velocity, and dynamic static pressure measurement by a four-hole pressure probe. *Experimental Thermal and Fluid Science, 15*(4), 375–383.

Wear and Friction Study of the Coated Piston Rings Material

Vinayak Goel, Mudit Shukla, and Vipin Kumar Sharma

Abstract Present work discusses the role of metal coatings on the piston rings material for the enhancement of its wear and friction properties. Coatings of zinc (Zn) and zinc and chromium (Cr) have been developed on the piston rings material using the electroplating technique. Wear and friction properties were evaluated using a linear reciprocating tribometer (LRT) in unlubricated condition. It is observed that zinc and zinc + chromium both the coatings have improved the wear resistance of the piston rings material; however, the improvement by Zinc alone was not that much significant. There was an improvement of 11% by zinc coating and 59% by zinc and chromium coating in the wear resistance. The coefficient of friction between the piston rings material and cylinder linear reduced up to 17% with the zinc and chromium coating. A finite element model has also been modeled for the prediction of maximum stress and strain area on the pin and plate surface for all the considered experimental runs.

Keywords Coating · Cylinder linear · Friction · Piston rings · Wear

1 Introduction

Usage of advanced materials, design patterns, and surface coatings are the famous methods which are being used nowadays for enhancing the performance of the reciprocating combustion engines. Friction between the sliding pairs in the reciprocating engine is the main power loss factor. Up to 50% of energy loss occurs due to friction. In order to reduce the friction, several different technique and methods have been utilized by researchers. Wopelka et al. [1] coated a series of piston rings with different surface coatings of alumina-matrix nano-composite materials. Wear tests were performed, and comparisons were made with standard CKS-36 (a commercial coating

V. Goel (✉) · M. Shukla · V. K. Sharma
Department of Mechanical and Automation Engineering, Maharaja Agrasen Institute of Technology (GGSIPU), Rohini, Delhi 110086, India
e-mail: vinayakgoel11@gmail.com

© Springer Nature Singapore Pte Ltd. 2021

C. Prakash et al. (eds.), *Advances in Metrology and Measurement of Engineering Surfaces* , Lecture Notes in Mechanical Engineering,
https://doi.org/10.1007/978-981-15-5151-2_15

comprising chromium plating reinforced with alumina particles) coated cast iron piston rings. Two types of wear mechanism were observed by the authors, micro-scale cohesive failure and smooth wear. The latter mechanism resulted in lower wear rates. The predominance of a given wear mechanism was found to depend on the coating composition and type of grinding operation used to finish the nano-composite coated piston rings. The testing was performed at 40KN with load and 40 Hz frequency. The average sliding speed was 1.2 m/s. The tests were performed at 200 °C temperature for 6 h of time duration. The high rate of wear was noticed in case of A1203-SiC coatings as compared to available coatings like CSK-36. Wear was maximum when 5% of SiC coatings were used and minimum when the 2.5% SiC coatings were used. Wear was maximum when 5% SiC coatings were used and minimum when the 2.5% SiC coatings were used. Oladijo et al. [2] used the thermal HVOF spray process to deposit the coatings of CrC–NiCr on piston rings material. The effects of residual stresses developed during the process were analyzed for the determination of abrasive wear resistance of the coating. The nano-HVOF coating with power size less than 10 μm presented a high wear specific energy, representing that higher energy is necessary to generate wear. This coating presented lower fuel consumption in engine tests. The CrN/TiN coating was also selected due to the low wear in the piston ring produced both in simulated and engine tests. Deepa et al. [3] produced the nickel-doped SnO_2 particles with the help of combustion and later used as additive for Zn-composite coating for steel material. Electroplating technique was used to deposit the coating. It is reported by authors that the inclusion of Ni-doped SnO_2 in Zn coating increased the corrosion resistance as compared to Zn-deposits. The surface of Zn–Ni-doped SnO_2 coating resulted with low deterioration as compared to Zn-deposited.

Kapsiz et al. [4] valuated the tribological properties of piston ring and cylinder liner tribopair. Taguchi methodology was used to optimize the minimum weight loss and friction. Friction force, wear and surface temperature were measured using the reciprocating test. Dead weights were used to apply load (60 and 80 N) on the pin under different loads sliding velocity (60, 90,120 and 150) and oil type (15W40 and 10W40). The low load and high sliding speed combinations were reported to the optimal parameters. Zabala et al. [5] studied the effects of oil, lubrication technique, surface roughness and coatings on the tribological properties of cylinder linear with piston ring material. Reciprocating linear motion tribometer was used for the experimentation with input parameter selected as used in the actual piston ring and cylinder assembly. The experimental results were used in a specific simulation model which verifies the results within an error of 5%. It is observed that, for the coated samples, MoS_2, DLC and CrN coating were deposited using the physical vapor deposition method. DLC coatings capitulate the minimum friction and wear rate. Usage of 5W30 oil for lubrication leads to the formation of protective tribolayer spontaneously on uncoated rings. This layer with anti-wear properties was responsible for considerable friction undermining. Based on the literature review, it is observed that coating on the piston rings of the engine assembly has proved to improve the tribological properties. So, in the present work, two different coatings of zinc (Zn) and zinc + chromium (Cr) have been developed on the piston rings materials, and reciprocating sliding tests were conducted for the evaluation of the effect of coatings.

Based on the literature review, it is observed that the deposition of coatings on the components of any system helps in enhancing the service life of the component. In this paper, attempts have been made to improve the tribological properties of the piston rings material. For this, zinc (Zn) and zinc and chromium (Cr) coating were applied on the piston rings materials, and tribological behavior was evaluated using a reciprocating pin disk tribometer. For the comparison of tribological properties, experiments were performed at room temperature conditions. The results from this study can be extended to perform in actual engine conditions.

2 Materials and Method

2.1 Coating Deposition

The material used to replicate the piston rings and cylinder liner material is cast iron [6]. The pin and plate samples were prepared from the raw cast iron and finished by using various grades of the emery paper and finally by alumina powder. Table 1 presents the chemical composite of the cast iron material used in this study. A surface roughness tester (Taylor Hobson Talysurf) was used to measure the roughness of the pin and plate samples. The roughness values were measured at various locations, and average roughness value achieved for the pin and plate surfaces lies between 0.2 and 0.4 μm. The pin samples were then treated to deposit the zinc (Zn) and Zn-tri chromium passivation coating. For the coating process, the electroplating method was used. The Zn is known to be the best ally of steel surfaces to protect the steel from corrosions.

The Zn coating on the pin samples was obtained by immersing the samples into a zinc salt bath, and during this, electric current was passed which deposited the Zn from the salt bath to the pin surfaces. This immersion produces zinc coatings that prevent oxidation of the pin samples. Hexavalent chromium is remarkably versatile and exhibits many desirable and essential characteristics. However, there are some environmental concerns with hexavalent chromium coatings. Trivalent chromium eliminates those concerns related with the hexavalent chrome plating.

Table 1 Chemical composition of cast iron used to prepare specimens

Element	C	Cr	Mn	Si	Fe
wt%	3.52	1.05	0.58	2.96	92

Table 2 Input parameter for the reciprocating wear test

Input parameters used	
Parameter	Value
Load	30 N
Temperature	Room temperature
Stroke length	2 mm
Frequency	10 Hz
Test duration	12 min

2.2 Reciprocating Sliding Wear Testing

Rotary pin on disc and reciprocating pin on disc are the two famous method for evaluating the wear and friction [6–8]. Since the piston rings undergo reciprocating sliding in the actual engine assembly, a reciprocating pin on disc tribometer was used to evaluate the wear and friction behavior of the coated piston rings material [9]. This setup consists of a pin and plate assembly. The plate remains stationary, and pin reciprocates under the effect of some load on the plate sample. The frequency and applied load can be changed as per the requirements.

The wear from the used pin samples was evaluated by weighing the weight of the samples before using the pin and after the test runs. A digital weighing balance having 0.0001 g accuracy was used for this purpose. Before starting the experimentation, each sample was cleaned with acetone properly and dried well in air. Table 2 presents the experimental conditions and specification of the reciprocating tribometer. The selection of input parameters was done to compare the tribological behavior of the applied coating. However, the actual input conditions for the engine and cylinder assembly would be different.

2.3 Finite Element Analysis

In this work, an ANSYS modeling was also performed to provide the theoretical background to the reciprocating testing. In this, the areas of maximum stress on the plate and pin surfaces were evaluated for the reciprocating sliding tests. A finite element model was developed using ANSYS 19. Models of pin and plate with exact dimensions and material as used in the experimental tests were used and analyzed for maximum stress and stains. The ANSYS modeling was done to verify the wear nature of wear from the pin and plate specimens.

Analysis Steps

The following steps were taken to perform the analysis on the assembly [10–12]:

1. The static structural option is selected from the analysis systems toolbox.

2. The engineering data option is selected, and the desired material of the model is chosen. In our case, it was gray cast iron.
3. Next design modeler is opened by clicking geometry option. The model is now designed. In our case, the model was imported from Solidworks.
4. After the design is completed, the model option is selected, and Ansys Mechanical window opens.
5. The desired size of the mesh is selected, and meshing is done.
6. The bottom face is fixed, and a load of 30 N is applied on the top face using insert option on the static structural tab.
7. Displacement is given to the pin in steps of 2 mm so that it performs reciprocating motion just like in linear tribometer.
8. The model is solved using the given boundary conditions. The solution is thus obtained, and maximum and minimum value of strain and stress are obtained (Fig. 1).

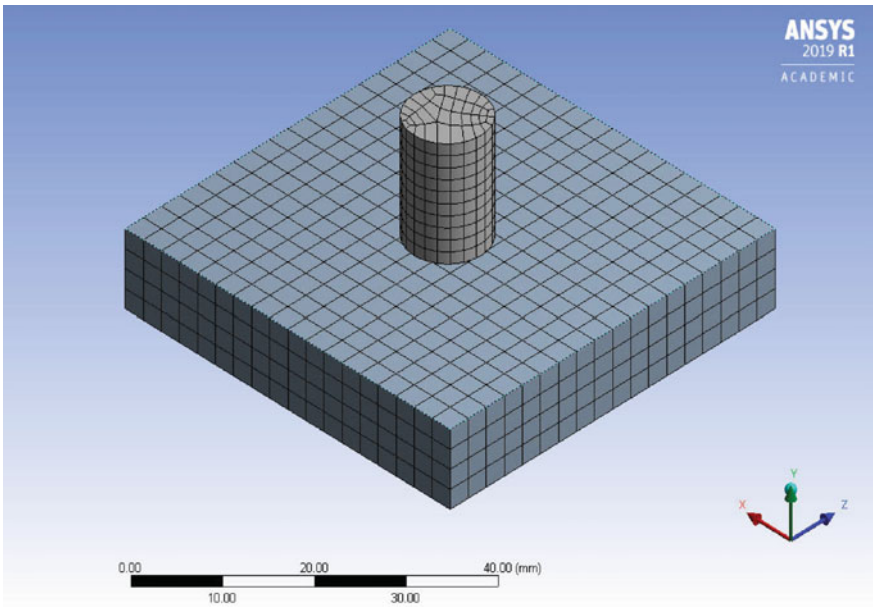

Fig. 1 Meshing of pin and plate model in ANSYS

3 Results and Discussion

3.1 Wear and Friction Analysis

For the identification of the wear mechanism, the wear and friction tests were performed in dry and lubricated conditions. Table 3 shows the amount of mass loss from the pin surface for the three considered cases.

It is seen from Table 2 and Fig. 2c that the pin specimen coated with Zn + Cr resulted in the least amount of mass loss. The Zn and Cr coated helped in protecting the pin surface from the heavy wearing as compared to the uncoated pin. The Zn alone also helped in providing wear resistance to the material; however, the improvement in wear resistance is very low. There is an improvement of about 11% in wear resistance with the Zn coating, which increased to 59% with the addition of Cr in the coating media. Figure 3 presents the micrographs (50× magnification) for the worn pin surfaces.

Deep grooves along with heavy wear area have been reported on the uncoated pin samples (Fig. 3a). These grooves and wear wedges resulted in the maximum amount of wear. Comparatively, thin wear wedges along with smaller wear grooves were observed in Zn coated sample (Fig. 3b). The Zn coating on the pin sample helped in protecting the pin surfaces for some time. The Zn + Cr coated sample resulted in very few thin wear lines. The worn surface was seen to be smoother as compared to the other samples. This indicated low wearing on the Zn + Cr coated pin samples (Fig. 3c).

Table 3 Mass loss from the pin specimens

	Initial weight (g)	Final weight (g)	Cumulative wear loss of pin (g)
Uncoated Pin	9.2951	9.0853	0.2098
Zn coated pins	9.3952	9.2217	0.1753
Zn + Cr coated pin	9.3109	9.2271	0.0838

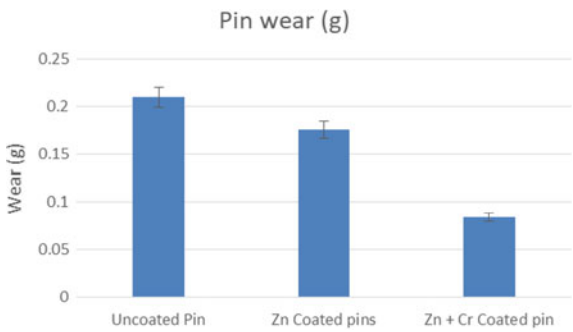

Fig. 2 Variation of wear for the pin samples

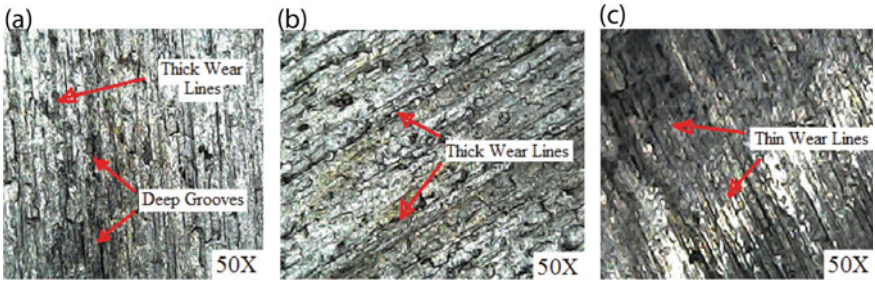

Fig. 3 Micrographs for the worn plate samples of **a** uncoated sample, **b** Cr coated sample and **c** Cr + Zn coated sample

For analyzing the wear nature, wear from the plate samples was also recorded. Table 4 presents the mass loss from the plate samples. The heavy wearing for the uncoated pin samples produced more amount of debris which in result generated heavy and deeper wear marks on the plate samples. The maximum amount of mass loss was observed for the uncoated pin and plate tribopair. Figure 4 presents the wear loss for plate and pin tribopair samples.

Figure 5 presents the variation of the coefficient of friction between the pin and plate samples. The coefficient of friction was continuously measured for the complete tribological study and plotted against time. The average coefficient of friction value for uncoated, Zn coated and Zn + Cr coated samples was 0.62, 0.61 and 0.51 respectively. It is seen that Zn coated was not that much effective in reducing the COF values; however, when the Zn + Cr coated was applied on the pin and tested

Table 4 Mass loss from the plate specimens

	Initial weight (g)	Final weight (g)	Cumulative wear loss of plate (g)
Uncoated pin	101.8818	101.7609	0.1209
Zn coated pins	101.99	101.8882	0.1018
Zn + Cr coated pin	101.0537	101.0037	0.0500

Fig. 4 Wear for the plate samples

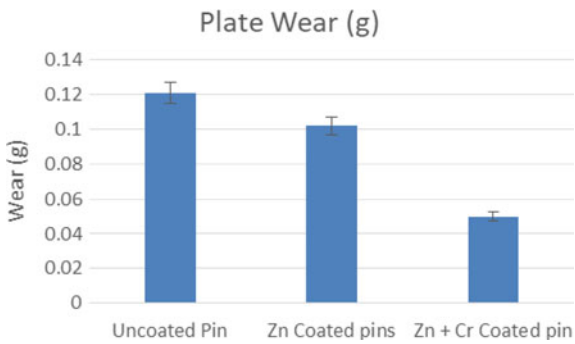

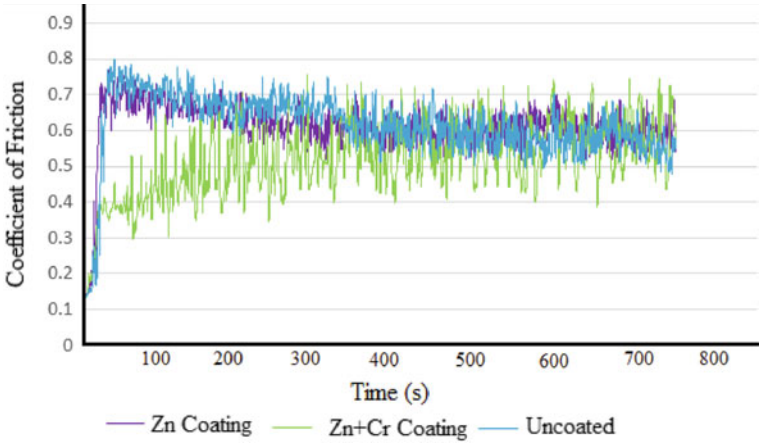

Fig. 5 Variation of the coefficient of friction with time

against the plate surface, the COF reduces to about 17% as compared to the uncoated pin. The presence of chromium helped in reducing the COF and wear between the tribopairs. It is also worth mentioning that the COF value for the Zn + Cr coating was also lower during the initial sliding than the Zn coating. The debris produced during the initial sliding further increases the COF for the Zn + Cr coating and stabilizes after 400 s of sliding.

3.2 Finite Element Analysis

The equivalent stress generated on the pin and plate specimens is presented in Fig. 6a, b. During the experiments, the maximum amount of stress was generating on the pin surface. The outer edge of the pin was most influenced by the stress which leads to maximum wear from that portion of the pin. The wear in the form of strain developed in the pin and plate is represented in Fig. 7a, b. This simulation is an accurate representation of the working of a linear tribometer. It is seen that the value of strain on the pin is greater than that on the plate. It suggests that more deformation per unit length takes place on the pin than the plate. Similarly, the stress developed on the pin is also greater than the stress developed on the plate which suggests that to reduce wear the focus should be on the pin. The maximum value of stress and strain was developed in the direction in which the reciprocation motion takes place on the circumference of the cylindrical pin (Table 5).

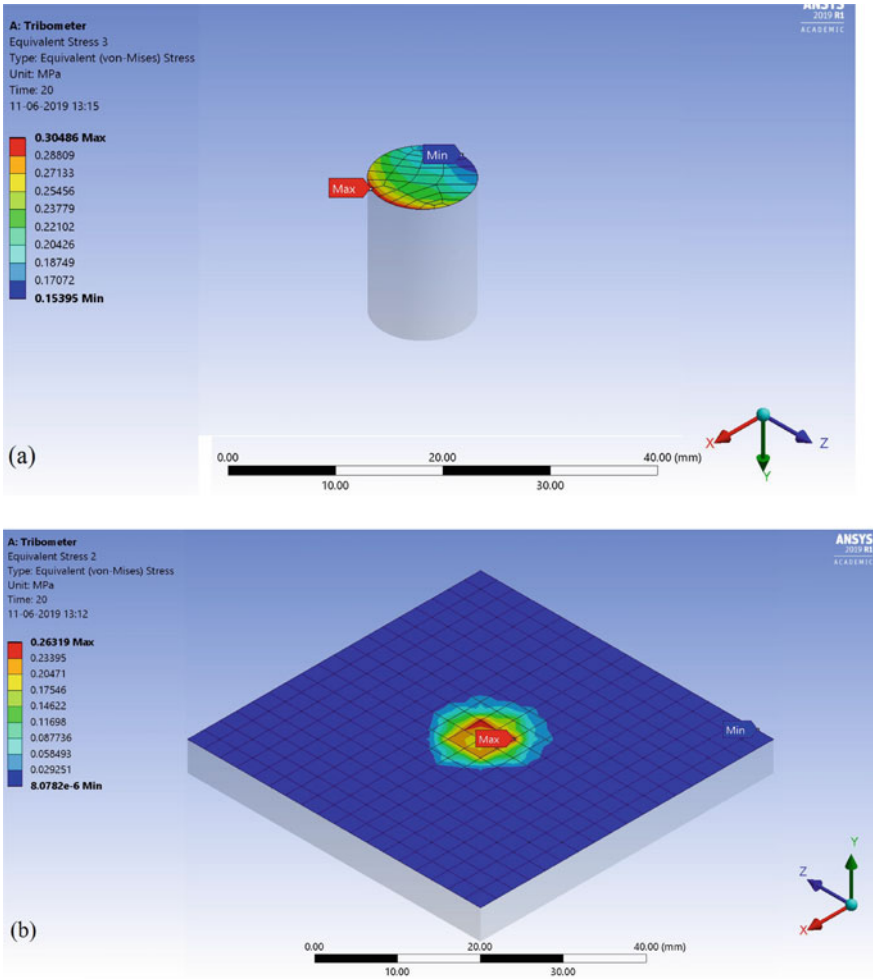

Fig. 6 Maximum stress generation **a** for uncoated pin sample, **b** for plate sample

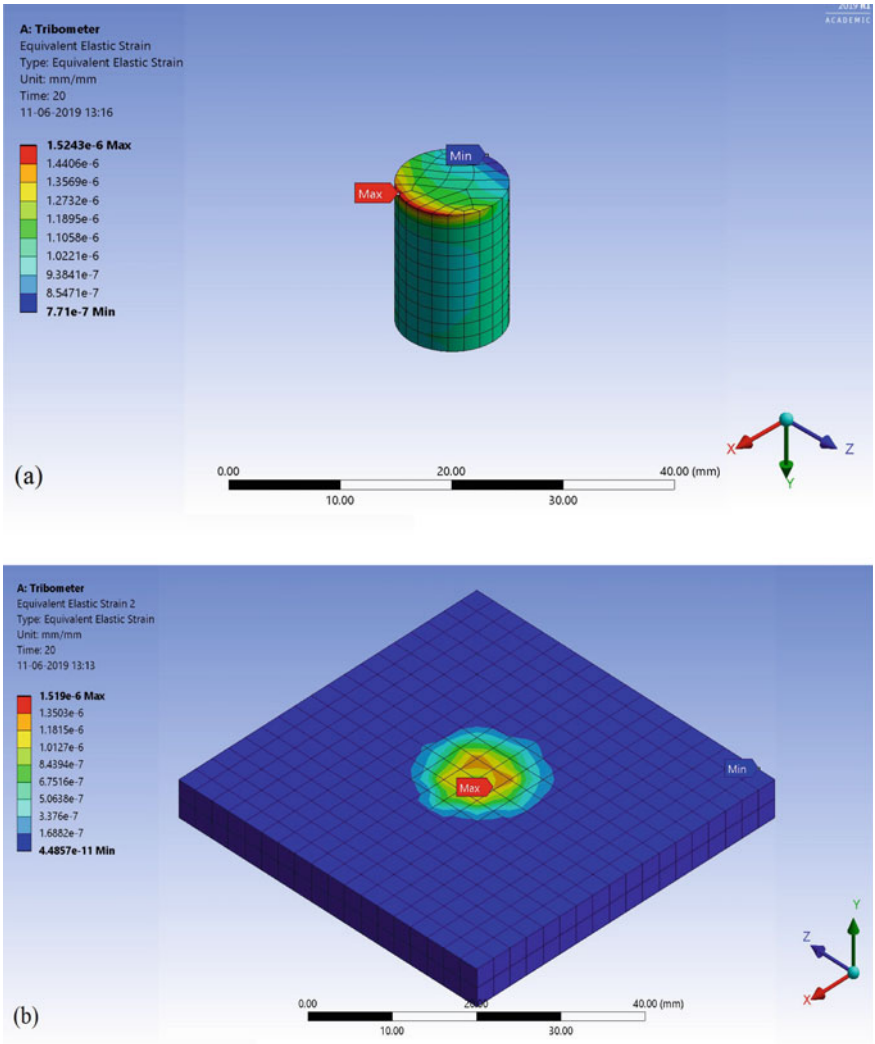

Fig. 7 Maximum strain generation for **a** for pin sample, **b** for plate sample

Table 5 ANSYS result summary

Object	Maximum strain (mm/mm)	Minimum strain (mm/mm)	Maximum stress (MPa)	Minimum stress (MPa)
Plate	1.4656e−6	7.1833e−11	0.21272	1.3674e−5
Pin	1.5628e−6	8.0674e−7	0.31254	0.1611

4 Conclusions

In the present work, Zn and (Zn + Cr) coating were applied on the piston rings material. Wear and friction tests were performed. It is concluded that zinc + chromium coating helped in improving the tribological properties of the piston rings material. There was an improvement of 59% in the wear resistance and a 17% reduction in the coefficient of friction value. The zinc alone was not able to reduce the friction coefficient at the considered experimental conditions. A finite element modeling was also proposed to represent the working of the linear tribometer. The modeling also suggested low amounts of stress on the plate specimens during the tribological testing.

References

1. Wopelka, T., Cihak-Bayr, U., Lenauer, C., Ditrói, F., Takács, S., Sequard-Base, J., et al. (2018). Wear of different material pairings for the cylinder liner—piston ring contact. *Industrial Lubrication and Tribology, 70*(4), 687–699.
2. Oladijo, O., Venter, A., & Cornish, L. (2014). Correlation between residual stress and abrasive wear of WC–17Co coatings. *International Journal of Refractory Metals & Hard Materials, 44,* 68–76.
3. Deepa, K., & Venkatesha, T. (2018). Combustion synthesis of Ni doped SnO_2 nanoparticles for applications in Zn-composite coating on mild steel. *Journal of Science: Advanced Materials and Devices, 3*(4), 412–418.
4. Kapsiz, M., Durat, M., & Ficici, F. (2011). Friction and wear studies between cylinder liner and piston ring pair using Taguchi design method. *Advances in Engineering Software, 42*(8), 595–603.
5. Zabala, B., Igartua, A., Fernández, X., Priestner, C., Ofner, H., Knaus, O., et al. (2017). Friction and wear of a piston ring/cylinder liner at the top dead centre: Experimental study and modelling. *Tribology International, 106,* 23–33.
6. Sharma, V. K., Singh, R. C., & Chaudhary, R. (2018). Wear and friction behaviour of aluminium metal composite reinforced with graphite particlesInt. *International Journal of Surface Science and Engineering, 12,* 419.
7. Sharma, V. K., Singh, R. C., & Chaudhary, R. (2017). Effect of flyash particles with aluminium melt on the wear of aluminium metal matrix composites. *Engineering science and Technology, an International Journal, 20*(4), 1318–1323.
8. Singh, R. C., Chaudhary, R., & Sharma, V. K. (2019). Fabrication and sliding wear behavior of some lead-free bearing materials. *Materials Research Express, 6*(6), 066533.
9. Sharma, V. K., Singh, R. C., Chaudhary, R., Saxena, M., & Anand, M. (2019). Effects of flyash addition on the dry sliding tribological behavior of aluminum composites. *Materials Research Express, 6*(8), 0865f4.
10. Skill lync, Advanced structural analysis for FSAE and BAJA using Ansys course provided.
11. Alawadhi, E. M., Finite Element Simulations Using ANSYS.
12. Tickoo, S., Ansys Workbench 14.0: A Tutorial Approach.

Thermal Conductivity Analysis of Graphene Oxide Nanofluid Using Three-Level Factorial Design

Munish Gupta, Jodh Singh, Harmesh Kumar, and Rajesh Kumar

Abstract Nanofluids improve the performance of thermal systems. Graphene oxide nanoparticles were characterized to confirm the structure, using X-ray diffraction and field-emission scanning electron microscopy. Water-based grapheme oxide nanofluids were synthesized. Three-level (3^2) factorial design was used to examine the effects changes in temperature and nanoparticle loading on the thermal conductivity of prepared nanofluids. Significance of model used was tested using analysis of variance at a 95.0% confidence interval. The results revealed that thermal conductivity varies directly with temperature as well as weight concentration. 30.4% thermal conductivity enhancement is observed at optimum conditions, i.e. high level of temperature (60 °C) and medium level of weight concentration (0.1 wt%).

Keywords Graphene oxide · Nanofluids · Heat transfer · Thermal conductivity · Factorial design

1 Introduction

The trend of miniaturization and increased heat loads in most of the industries call for the efficient heat transfer systems. Heat transfer depends mainly on thermal conductivity of the fluids. The thermal conductivity of generally used fluids, i.e., water, vegetable oil, engine oil, etc., can be improved by adding solid nanoparticles. Such two phase homogeneous mixtures of nanoparticles having size below 100 nm in conventional base fluids are known as nanofluids. Heat transfer occurs through conduction as well as convection. This leads to enhance heat transfer rate [1].

M. Gupta
Mechanical Engineering Department, GJUST, Hisar, Haryana, India

J. Singh (✉)
SSB University Institute of Chemical Engineering and Technology, Panjab University, Chandigarh, India
e-mail: jodhme@gmail.com

H. Kumar · R. Kumar
Mechanical Engineering Department, UIET, Panjab University, Chandigarh 160014, India

© Springer Nature Singapore Pte Ltd. 2021

C. Prakash et al. (eds.), *Advances in Metrology and Measurement of Engineering Surfaces* , Lecture Notes in Mechanical Engineering,
https://doi.org/10.1007/978-981-15-5151-2_16

Table 1 Summary of literature on GO/water nanofluid

Nanofluid parameter	Range of parameters studied		Enhancement in thermal conductivity	References
	Concentration	Temperature (°C)		
GO/water	0.01–0.5 wt%	25–60	55.2% at 0.5% and 60 °C	[4]
GO/water	0.05–0.25 wt%	10–40	47.5% at 0.25% and 40 °C	[5]
r-GO/water	0.02–0.08 wt%	20–40	35.7% at 0.1% and 40 °C	[6]
GO/water	0.01–0.07 vol%	20–50	30% at 0.07% and 50 °C	[7]
GO/water	0.05–0.2 vol%	30–50	27% at 0.2 vol% and 50 °C	[8]

Graphene is consisting of single layer of carbon in two-dimensional lattice. It shows fascinating thermal properties because of larger surface area. Generally, oxide (GO) nanoparticles get dispersed in polar base fluids [2]. GO nanoparticles show higher thermal conductivity and long-term stability when dispersed in water. This is because of the hydrophilic nature and the presence of functional groups [3]. Therefore, GO and distilled water were selected for this work. Several studies are available on the heat transfer application of GO/water. Table 1 shows the summary of some experimental studies related to water-based GO nanofluids.

Studies witnessed the significant influence of temperature and nanoparticle loading on the thermal conductivity. There is an optimum value of particle concentration at specific temperature which maximizes thermal conductivity with minimum increase in viscosity [9]. Literature review shows that studies based on GO nanofluids using factorial design are not often found.

This paper discusses the effects of changes in temperature and nanoparticle loading on the thermal conductivity of GO/water nanofluids by using 3^2 factorial design.

2 Materials and Methods

Distilled water and GO nanoparticles were selected for preparing nanofluid samples. GO nanopowder was purchased from Nanoshel Company, Willmington, the USA. Specifications of GO as provided by supplier are given in Table 2. Specification and properties were further verified by characterizing nanoparticles.

Table 2 Composition of graphene oxide nanoparticles

Parameter	Purity	Layers	Thickness	Lateral dimensions	Surface area	Carbon	Oxygen	Others
Value	99%	1–3	1–4 nm	5–10 μm (X and Y)	200 m^2/g	77%	22%	1%

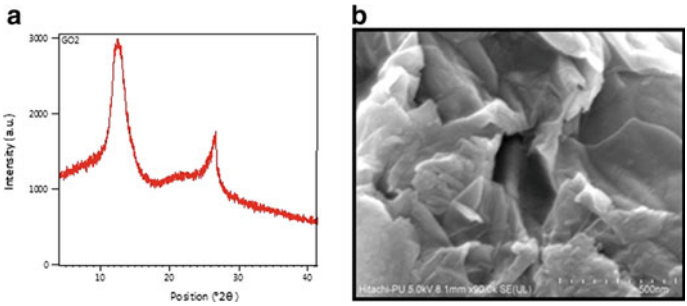

Fig. 1 **a** X-Ray diffraction result of GO, **b** FESEM result of GO

2.1 Characterization of Nanoparticles

XRD analysis of purchased powder was performed. One high-intensity (2900 a.u.) peak appeared at about 2θ value of 13 corresponding to (002) diffraction plane of graphite. XRD patterns are shown in Fig. 1a. Results confirmed the properties of GO. FESEM image in Fig. 1b showed the layers of graphene oxide surface. Size of sheets was in range of 5–10 μm. Nanosheets were tending to form multilayer clusters.

2.2 Synthesis of Nanofluids

Two-step method is generally used for oxide nanoparticles [10]. Three samples at 0.03, 0.1 and 0.3% weight concentration were prepared through this method by dispersing specified amount of GO nanoparticles in distilled water. Values of concentration levels were selected randomly on the basis of literature to examine the effects of low, medium and high concentration. Hydrophilic nature of GO shows good compatibility with water. So, no surfactant was used. Magnetic stirring of the samples was performed for two hours using the magnetic stirrer followed by ultrasonication for four hours in bath sonicator equipment. Stability was checked by sedimentation test. The prepared nanofluids were stable for ten days without any surfactant and after twelve days settled down completely.

Table 3 Design of experiment

Factors	Levels			Base runs	Replicate	Total runs	Blocks
	Low	Medium	High				
Temperature, *A* (°C)	30	45	60	9	2	18	2
Concentration, *B* (wt%)	0.03	0.1	0.3				

2.3 Factorial Design

Factorial design creates all possible experimental combinations for different factors at all the levels. Two factor three-level factorial (3^2) design was used in this work. Temperature and weight concentrations were selected as variable factors and thermal conductivity as response factor. To get the possible curve in response variable, three levels of each factor were considered. All the runs were randomly assigned in two blocks to distribute the error in the whole range of experiments. Table 3 shows the summary of the design. Total 18 runs at two replicates of nine experimental sets were performed as shown in Table 4.

2.4 Thermal Conductivity Measurement

KD2 Pro thermal analyzer (Decagon Devices, the USA) which is working on transient hot wire technique was used for the measurement. A water bath was used to get three different temperatures, i.e., 60, 45 and 60 °C, which were selected randomly. Samples were kept inside the bath after setting the required temperature. After getting the set temperature, samples were kept remained inside for further 10 min to achieve equilibrium. Then, each measurement was taken twice and recorded in Table 4. Measurements for distilled water were also performed at 30, 45 and 60 °C and found as 0.589, 0.618 and 0.625 W/mK, respectively.

3 Results and Discussion

Main and interaction effects of variable factors, i.e., temperature (*A*) and weight concentration (*B*) on response factor, i.e., thermal conductivity were studied through analysis of variance (ANOVA) by using MINITAB 19.

The results revealed that maximum value of thermal conductivity (0.95 W/mK) was found at high level of *A* and *B*, whereas minimum value (0.61 W/mK) was found at low level of A and B as shown in Table 3. Thus, 3.6–52% thermal conductivity enhancement was recorded when compared to distilled water at the same

Table 4 Factorial design layout

Standard order	Run order	Blocks	Temperature, *A* (°C)	Concentration, *B* (wt%)	Thermal conductivity (W/mK)
3	1	1	30	0.30	0.891
5	2	1	45	0.10	0.781
6	3	1	45	0.30	0.910
8	4	1	60	0.10	0.820
1	5	1	30	0.03	0.610
4	6	1	45	0.03	0.701
7	7	1	60	0.03	0.741
9	8	1	60	0.30	0.950
2	9	1	30	0.10	0.690
13	10	2	45	0.03	0.692
12	11	2	30	0.30	0.870
16	12	2	60	0.03	0.746
15	13	2	45	0.30	0.918
18	14	2	60	0.30	0.946
14	15	2	45	0.10	0.782
17	16	2	60	0.10	0.810
11	17	2	30	0.10	0.700
10	18	2	30	0.03	0.622

conditions. In Pareto chart A, B and $A * B$ extended the reference line which shows that main effects and interactive effects of the factors are significant for response factor. Figure 2b shows that response factor varies directly with temperature and concentration of particles. The interaction effects of A and B are shown in Fig. 2c. If some points are away from the fitted line, this indicates that effects are real and important as well [11]. Figure 2d shows that some points are away from fitted line. This indicates the reality and importance of effects. Points in residuals plots followed a straight line. Such results indicate the normality of the data and error distribution.

3.1 Analysis of Variance

In this analysis, significance and fitness of the present model were checked. Large F-value, small P-value and value of R square (R^2) near 100% indicates a good fit model and ensures validity of model [12]. Results are shown in Table 5.

P-value is zero for both factors A and B. This indicates that A and B are significant for response factor, i.e., thermal conductivity. However, F-value for factor A and B was 281.04 and 1345.27, respectively. Small P-values and high F-values indicate that

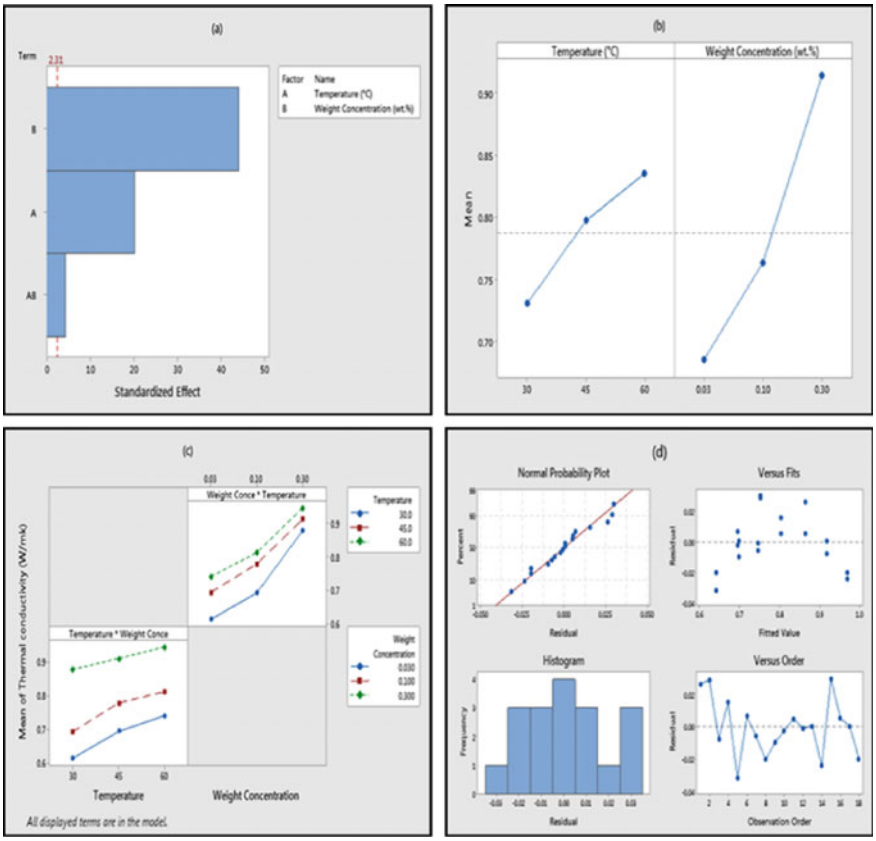

Fig. 2 **a** Pareto chart, **b** main effects, **c** interactive effects, **d** residual plots

present model is a valid model. Values of different R square are shown in Table 5. High value of R square (99.76%) proves this model being a good fit model. This indicates that the model is capable of responding to 99.7% variability in response factor. High value of adjusted R square (99.49%) indicates that the model is most significant. The least difference between R^2 and adjusted R^2 indicates the absence of any insignificant factor [13]. All the values of R^2 are close to each other. This proves that selected factors are very significant.

3.2 *Response Optimization and Proposed Equation*

The goal is to maximize thermal conductivity with low value of 0.61 W/mK and target value of 0.95 W/mK. The fit optimum value for thermal conductivity predicted by design software, based on the present model, is 0.815 W/mK with 95% confidence

Table 5 ANOVA table

Source	Degree of freedom	Adjusted sum of squares	Adjusted mean sum of squares	*F*-Value	*P*-Value	Significance
Model	9	0.198781	0.022087	366.25	0.000	Significant
Blocks	1	0.000004	0.000004	0.06	0.814	Not significant
Linear	4	0.196151	0.049038	813.15	0.000	Significant
A	2	0.033897	0.016948	281.04	0.000	Significant
B	2	0.162254	0.081127	1345.27	0.000	Significant
Two way interaction	4	0.002626	0.000657	10.89	0.003	Significant
$A * B$	4	0.002626	0.000657	10.89	0.003	Significant
Error	8	0.000482	0.000060			
Total	17	0.199263				
R^2	99.76%					
Adj. R^2	99.49%					
Pred. R^2	98.77%					

interval which is near to actual experimental values, i.e., 0.81 and 0.82. Optimum thermal conductivity (0.815 W/mK) with 30.4% enhancement was observed at high level of *A* (60 °C) and medium level of *B* (0.1 wt%).

Through this ANOVA-based factorial design, the following equation regarding the variable factors, i.e., *A* and *B*, is proposed for the prediction of thermal conductivity (k).

$$k = 0.5118 + 0.003500 * A + 0.8264 * B \tag{1}$$

The model values show good correspondence between actual and predicted data. Figure 2d shows the plots for residuals (difference between actual and fitted values) which show the normal error distribution and no specific pattern of the residuals. This also confirms the compatibility of actual and predicted values of thermal conductivity.

3.3 Contour and Surface Plots

The contour plots show the relationship between a fitted response, i.e., thermal conductivity and variable factors, i.e., *A* and *B*. Surface plots give three-dimensional view of the surfaces, generated by connecting the points that have same response. These plots give the information regarding the trend and pattern of effects of different factors on the thermal conductivity. Figure 3a, b indicates that both parameters show significant influence on response factor. With rise in variable factors, thermal

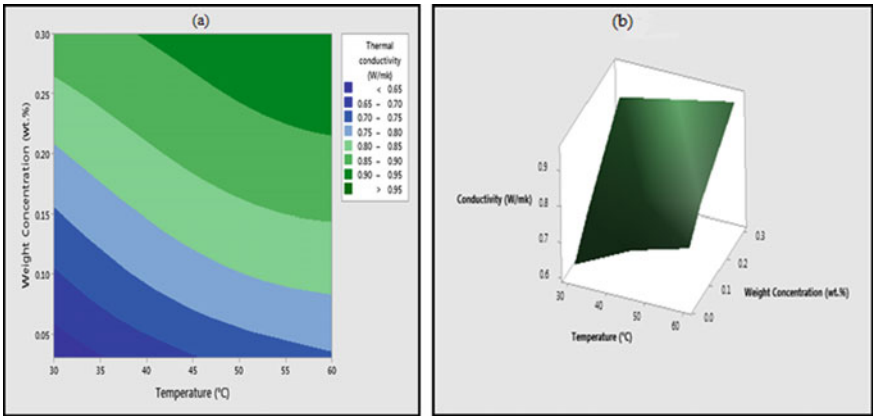

Fig. 3 **a** Contour plots, **b** surface plot for interactive effects of factors

conductivity shows rising trend. Thermal conductivity shows linear relationship with temperature. Significance of this trend increases toward higher side of weight concentration. Trends of these plots were in compliance with values of Table 3. The highest and the lowest thermal conductivity were obtained, respectively, at high and low level of *A* and *B*. This indicates the linear relationship of thermal conductivity with temperature (*A*) as well as weight concentration of particles (*B*). This linear trend may be due to increase in the number of particles as well as collisions among them at high concentration and high temperature.

4 Conclusion

The prepared nanofluids were stable for ten days without any surfactant. The maximum thermal conductivity (0.95 W/mK) was found at high level of temperature (60 °C) and weight concentration of nanoparticles (0.3 wt%), whereas the minimum value (0.61 W/mK) was found at low level of both factors, i.e., 30 °C and 0.03 wt%. Thus, total enhancement in thermal conductivity using nanofluid varies from 3.6 to 52%. The study confirms that the addition of nano-sized GO particles in water enhances its thermal conductivity.

Main effects as well as interactive effect of temperature and weight concentration were significant in affecting the thermal conductivity. It is confirmed that temperature and weight concentration show linear relation with thermal conductivity.

Optimum thermal conductivity (0.815 W/mK) was found at high level of temperature (60 °C) and medium level of weight concentration (0.1 wt%).

Acknowledgements The Authors wish to thank Chairperson, SSB UICET, PU, Chandigarh and Director, CIL, PU, Chandigarh, for their assistance in providing the necessary setup to conduct this work and testing facility.

References

1. Fuskele, V., & Sarviya, R. M. (2017). Recent developments in nanoparticles synthesis, preparation and stability of nanofluids. *Materials Today: Proceedings, 4*(2), 4049–4060.
2. Mukherjee, S. (2013). Preparation and stability of nanofluids—A review. *IOSR Journal of Mechanical and Civil Engineering, 9*(2), 63–69. https://doi.org/10.9790/1684-0926369.
3. Hu, X., Yu, Y., Zhou, J., & Song, L. (2014). Effect of graphite precursor on oxidation degree, hydrophilicity and microstructure of graphene oxide. *Nano, 9*(03), 1–8.
4. Esfahani, M. R., Languri, E. M., & Nunna, M. R. (2016). Effect of particle size and viscosity on thermal conductivity enhancement of graphene oxide nanofluid. *International Communications in Heat and Mass Transfer, 76,* 308–315.
5. Hajjar, Z., Morad Rashidi, A., & Ghozatloo, A. (2014). Enhanced thermal conductivities of graphene oxide nanofluids. *International Communications in Heat and Mass Transfer, 57,* 128–131.
6. Sadri, R., Zangeneh Kamali, K., Hosseini, M., Zubir, N., Kazi, S. N., Ahmadi, G., et al. (2017). Experimental study on thermo-physical and rheological properties of stable and green reduced graphene oxide nanofluids: Hydrothermal assisted technique. *Journal of Dispersion Science and Technology, 38*(9), 1302–1310.
7. Hadadian, M., Goharshadi, E. K., & Youssefi, A. (2014). Electrical conductivity, thermal conductivity, and rheological properties of grapheme oxide based nanofluids. *Journal of Nanoparticle Research, 16*(12), 2788. https://doi.org/10.1007/s11051-014-2788-1.
8. Sen Gupta, S., Manoj Siva, V., Krishnan, S., Sreeprasad, T. S., Singh, P. K., Pradeep, T., et al. (2011). Thermal conductivity enhancement of nanofluids containing graphene nanosheets. *Journal of Applied Physics, 110*(8), 084302. https://doi.org/10.1063/1.3650456.
9. Yanuar, N. P., & Gunawan, M. B. (2011). Flow and Convective heat transfer characteristics of spiral pipe for nanoparticles. *International Journal of Research and Reviews in Applied Sciences, 7*(3), 236–248.
10. Pal, S. L., Jana, U., Manna, P. K., Mohanta, G. P., & Manavalan, R. (2011). Nanoparticle: An overview of preparation and characterization. *Journal of Applied Pharmaceutical Science, 1*(6), 228–234.
11. Plackett, R. L., & Burman, J. P. (1946). The design of optimum multi factorial experiments. *Biometrika, 34,* 255–272.
12. Pramanik, A., Islam, M. N., Basak, A. K., Dong, Y., Littlefair, G., & Prakash, C. (2019). Optimizing dimensional accuracy of titanium alloy features produced by wire electrical discharge machining. *Materials and Manufacturing Processes*, *34*(10), 1083–1090.
13. Prakash, C., Singh, S., Singh, M., Antil, P., Aliyu, A. A. A., Abdul-Rani, A. M., & Sidhu, S. S. (2018). Multi-objective Optimization of MWCNT Mixed Electric Discharge Machining of Al–30SiC p MMC Using Particle Swarm Optimization. In *Futuristic Composites* (pp. 145–164). Singapore: Springer.

Design Optimization of Go-Kart Chassis Frame Using Modal Analysis

A. A. Dere, Manpreet Singh, A. Thakan, Rajeev Kumar, and Harpreet Singh

Abstract The chassis of automobile houses crucial mechanical component such as engine, suspension, steering and transmission system. Therefore, the chassis structure must be strong enough to absorb the static and dynamic loads generated by these mechanical components. In this work, the structural strength of go-kart chassis has been improved against static and dynamic loads through geometrical modifications. The geometrical modifications in the chassis structures were decided individually on each structural element where maximum deformation was analyzed in the modal analysis. This structural element was reanalyzed after making multiple variations in its geometry in attempt to minimize the deformation. When the minimum deformation was achieved in the structural element, then structure was finalized for stage 1. Similarly, other structural elements were also modified in the same continuous iterative process by keeping in consideration the weight constraints. After the termination of each modification torsion test, impact analysis was also carried out to examine torsional rigidity and crashworthiness. In five successive iterations, the optimum results for the chassis structure were obtained with little scope of further improvement. In the final structure, the lowest modal frequency was found to be shifted from 11.691 to 57.318 Hz to that of the initial structure. A significant reduction of 42% in maximum deformation along with a reduction in mode shapes was also witnessed in the final structure. The final structure was also found to be better in the results obtained from torsional analysis and impact testing.

A. A. Dere
Automobile Engineering, Lovely Professional University, Jalandhar, India

M. Singh (✉) · A. Thakan
Department of Mechanical Engineering, Lovely Professional University, Jalandhar, India
e-mail: bainscoolbains@yahoo.com

R. Kumar
Department of Mechanical Engineering, Lovely Professional University, Phagwara, India

Inder Kumar Gujral Punjab Technical University, Kapurthala, India

H. Singh
Department of Planning and Quality, Nettbuss AS, Oslo, Norway

© Springer Nature Singapore Pte Ltd. 2021

C. Prakash et al. (eds.), *Advances in Metrology and Measurement of Engineering Surfaces* , Lecture Notes in Mechanical Engineering,
https://doi.org/10.1007/978-981-15-5151-2_17

Keywords Modal analysis · Chassis structure · Resonance · Dynamic analysis · Vibration analysis

1 Introduction

Go-kart is a single-seated land-racing vehicle with or without bodywork and four nonaligned wheels [1]. This vehicle is prominently used in motorsport and recreation. A chassis is the backbone of a go-kart, as it holds various automobile components and is responsible to withstand dynamic and static loads without undue distortion [2]. Various studies on automobile chassis have shown that the engine movement and road profile are mainly responsible for dynamic excitations [3–5]. When the frequency of excitation from engine or road profile matches with the natural frequency, it may lead to the devastating effect of resonance, which causes loosening of joints, unwanted noise, failure of parts and driver discomfort [6–11]. A number of techniques are presently available to determine the dynamic characteristic of the structure, but among all techniques, modal analysis is one of the most reliable ones [12]. Modal analysis is the procedure to determine the intrinsic dynamic characteristic like the mode shapes, natural frequency and damping factor of a tubular space frame. These characteristics can be employed to formulate a mathematical model for its dynamic behavior. This mathematical modal can be computationally assessed by using FEM analysis for the purpose of improving design [13]. In complicated space frame structure due to a high number of degrees of freedom, a large number of mathematical models are formulated, it is difficult to access this model analytically thus, use of computational simulation-based method becomes adequate [14]. Also, the computational FEA proves to be a handy tool in the design process as it accelerates the design procedure by providing the freedom of making random modifications in the automotive structure and also minimizing physical test [15, 16].

In improving the structural characteristics of chassis, mostly, researchers have changed either material or geometrical structure or both material and geometrical structure. Antonio et al. [14] used a prototype of sports car modified chassis to carry out the modal analysis. They have identified that the static and dynamic properties differ with a change in geometrical structure. Patel and Patel have modified the structure of truck chassis using ANSYS software. The modified structure was found to have lighter in weight and with improved strength [16]. Archit and Dheer have changed the material of chassis structure from steel 52 to epoxy composite. This has not only witnessed the reduction in weight of the chassis but also improved the static and dynamic properties [17]. However, change in material can bring good outcomes in the structure, but it may incur extra cost to the manufacturer. Another effective way to improve the dynamic characteristics of the structure is a geometrical modification. Rao and Bhattu have relocated the members of the truck chassis. Along with relocation, they have also reduced the overall length and the thickness of certain members. So, with the geometrical modification, they have not only reduced the weight but also improved the structural strength of the chassis [6]. Several other

researchers have worked on the various truck chassis and have observed that by changing the geometry of the chassis structure the dynamic characteristic can be improved [18–22]. However, in previous research work, it has been observed that geometrical modification improves dynamic properties significantly, but authors have modified the chassis structure through single modification. In addition to that they have not considered major constraint such as the weight, maximum deformation in structural members and numbers of modes.

In this paper, the design and development of go-kart chassis have been carried out by using ANSYS-based modal analysis. The chassis structure was updated using the computational methodology, and optimum design has been determined after five continuous and progressive iterations within the weight constraints. A dynamic and static characteristic such as deformation in structural elements, crashworthiness and torsional stiffness has been analyzed for all the updated designs.

2 Chassis Design

The chassis of the go-kart vehicle has been constructed with a tubular space frame structure by following the rule book of the competition. However, there is always the provision of structural customization as per the participant's requirement [23]. Generally, these customizations are made to improve the structural and fatigue strength to sustain the dynamic and static loading with low deformation. The other factor such as dimensional limit, manufacturing restriction, weight and financial constraint must also be considered while carrying out the customization [24]. The initial go-kart

Fig. 1 Original go-kart participated in 2018

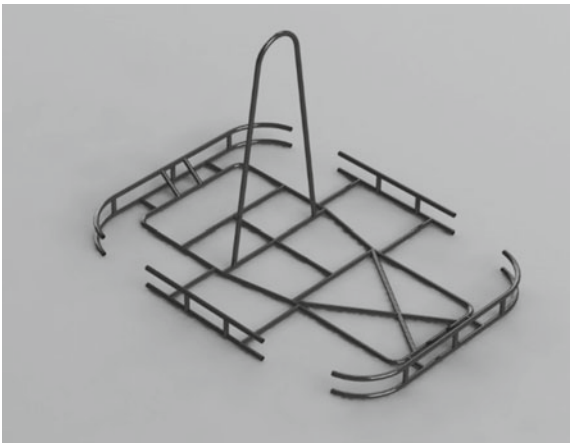

Fig. 2 Model of go-kart chassis drafted in solid edge

and the chassis structure drafted in Solid Edge software are shown in Figs. 1 and 2, respectively.

3 Finite Element Method

Finite element method (FEM) is a numerical method for solving designing problems of complex structures [25]. In this, complex structure is firstly discretized into small elements to form nodes, and then, each element is represented by a separate equation to form the complete solution of the structure [26, 27]. The prevalent steps of FEM which are used in the analysis are as follows [25]:

1. Discretize the body and select the type of element.
2. Select the displacement function.
3. Define the stress–strain and strain–displacement relationship.
4. Derive the stiffness matrix for each element.
5. Derive the global stiffness matrix.
6. Solve for unknown degree of freedom.
7. Determine the stress and strain components and interpret the results.

4 Chassis Analysis

The analysis of go-kart chassis was carried out to check the strength and stability of the structure for static and dynamic loads. Firstly, the existing go-kart chassis structure was drafted in Solid Edge software, and then, modal analysis was carried out on the drafted structure using ANSYS software. Initially, input constraints such

as material properties and meshing size were defined. After the complete introduction of structure to the software, the modes were determined by fixing all the faces of four-wheel mountings. The modes and the natural frequency can be determined by solving the following equation analytically for eigenvalues and eigenvectors [28, 29].

$$[M] \cdot \{\ddot{X}(t)\} + [C] \cdot \{\dot{X}(t)\} + [K] \cdot \{X(t)\} = 0 \tag{1}$$

Here, each eigenvalue is corresponding to one mode shape and respective natural frequency of the structure. But, for higher numbers of the degrees of freedom, it becomes cumbersome to find the solution analytically [14].

In software, the solution can be found by transforming Eq. (1) from time to frequency domain by using the Fourier transform [28].

$$[A(j\omega)]\{x(j\omega)\} = \{0\} \tag{2}$$

where $[A(j\omega)]$ represents system matrix and is given by $[A(j\omega)] = [M](j\omega)^2 + [c](j\omega) + [k]$ and vector of Fourier transformation is represented by $\{x(j\omega)\}$.

The solution of Eq. (2) is a set of unique complex values and eigenvectors; the eigenvalues are in the complex conjugate pair, where the real part presenting the modal damping and the imaginary part as modal frequency. The corresponding eigenvector associated with the eigenvalue represents the mode shape.

So, each mode is defined by a complex conjugate pair of eigenvalues and eigenvector (mode shape). The important conceptual conclusions that could be drawn from the above definition are:

- Modes are unique and inherent to structure.
- Modes are independent of external loads.
- Modes will change only with a change in mass, damping and stiffness property of the structure.

After finding the natural frequency, the modes of the system the software set the structure to vibrate at these natural frequencies to encounter the resonance effect. For each corresponding mode, the maximum deformation in the structural element has been noted, and the geometrical modifications were deciding there in the structure. This process was repeated until the maximum deformations for the structural elements were minimized within the weight constraints defined by the rule book. The methodology adopted for this work is shown in Fig. 3.

To check the structural strength of the chassis against the static load, torsional stiffness test was preferred and performed due to its better relevance with the current structure [14]. In this test, the rear wheel mountings were fixed, and a known twisting moment is applied at front wheel mounting to check the deformation [30]. The low value of the deformation accounts for the better structural strength against static loads.

The torsional stiffness for computational and experimental analysis is shown below [31].

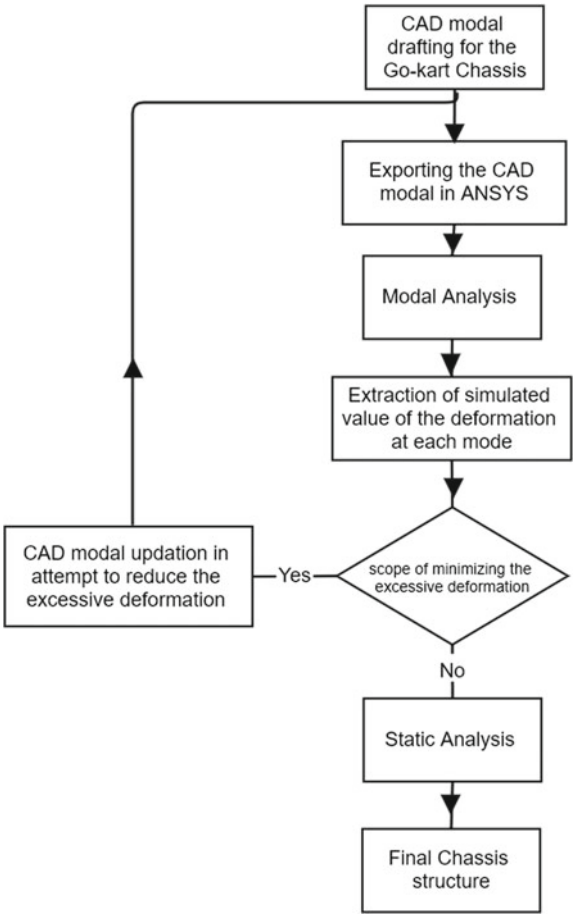

Fig. 3 Methodology adopted for chassis analysis

$$K_T = \frac{\tau}{\varnothing} \tag{3}$$

Twist angle $\varnothing$ is given by the formula,

$$\varnothing = \sin^{-1}\left(\frac{2D}{L}\right) \tag{4}$$

After finding no scope for further reduction in maximum deformation, the final structure for go-kart chassis was recommended. The applied methodology for the chassis analysis is shown in Fig. 3.

5 Geometrical Modification

The frame of the chassis is made up of AISI 1020 tubes with 1-in. diameter and 2 mm wall thickness. The mechanical properties of AISI 1020 are presented in Table 1. The orthographic projections of go-kart chassis along with geometrical specifications are shown in Fig. 4.

Modal analysis on the go-kart chassis was carried out, and on the basis of excessive deformations, multiple geometrical modifications were tried on the structural elements, and on the basis of best outcomes, stage 1 structure was finalized. Similarly, the modal analysis was carried out successively on the modified structures without varying diameter and thickness of the tube. With no room for further improvement in dynamic characteristic after stage 3, the thickness of the tube in certain members was varied. The dotted line in the top view of Fig. 4 represents the members in which thickness was varied from 2 to 3 mm. The variation of thickness was done in the structure by keeping the weight restrictions of the chassis as 28.5 kg. After two more successive iterations, the optimum structure was finalized after ensuring no further scope of improvement within the aforementioned weight constraints. The geometrical modifications made on the basis of modal analysis are represented in Table 2 with the required dimensions.

As seen in Fig. 4,

Table 1 Mechanical properties of chassis material

AISI 1020 properties	
Young's modulus [N/m^2]	2.00×10^{11}
Poisson ratio	0.29
Density [kg/m^3]	7850
Yield strength [N/m^2]	3.5×10^8
Tensile strength [N/m^2]	4.2×10^8
Shear modulus [N/m^2]	8.0×10^8

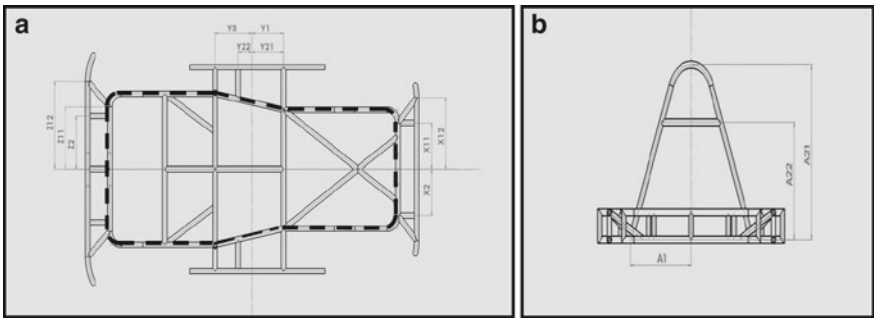

Fig. 4 Orthographic top (**a**) and side view (**b**) of go-kart chassis with geometrical specifications

Table 2 Geometrical modification made in the chassis (values in bold font indicate the points at which geometrical modifications were made)

Stage	Frontal portion			Middle portion						
				Side bumper				Seat section		
	X12	X13	X2	Y1	Y21	Y22	Y3	A1	A21	A22
Initial	203.2	203.2	203.2	235.66	NA	NA	235	279.4	1162.73	NA
1	203.2	203.2	203.2	235.66	**0**	**0**	235	279.4	1162.73	**520.79**
2	**191.63**	**191.63**	**150**	235.66	0	0	235	279.4	**647**	**277.32**
3	**217.17**	**217.17**	**217.17**	235.66	0	0	235	279.4	647	**432.19**
4	**224.37**	**336.55**	**224.37**	235.66	**145.7**	**108.3**	235	**355.6**	647	**433.19**
5	**217.17**	336.55	**217.17**	**146**	**146**	**94**	**204.72**	355.6	647	**434.19**

Stage	Rear portion			Weight of chassis
	Z11	Z12	Z2	
Initial	228.6	228.6	76.2	**26.075**
1	**293.37**	**397.51**	**127**	**28.426**
2	293.37	397.51	127	**26.150**
3	293.37	397.51	127	**26.457**
4	293.37	397.51	**250**	**28.305**
5	293.37	397.51	250	**28.315**

X11 and X12	Distance of intersection of lower support of the front bumper with chassis and the bumper from the center,
X2	Distance of upper support of the front bumper from the center,
Y1 and Y3	Distance of lower support1 of the side bumper with chassis from the center,
Y21 and Y22	Distance of upper support of the side bumper from the center,
Z11 and Z12	Distance of intersection of lower support of the rear bumper with chassis and the bumper from the center,
Z2	Distance of upper support of the rear bumper from the center,
A1	Distance of intersection of seat support with the chassis from the center,
A21	Hight of the seat support,
A22	Distance of intermediate seat support from the center.

6 Result and Discussion

6.1 Modal Analysis

The CAD model of the go-kart chassis structure was imported in ANSYS software for carrying out modal analysis. The material properties referred for AISI 1020 were defined to the imported structure. To define the structure completely for the purpose of modal analysis, meshing was generated with having a minimum edge length of 4.2952×10^{-4} m. The structure was then fixed at the wheel mounting faces, and a frequency of 8000 RPM was applied to the chassis by keeping into consideration all the possible frequencies. The fixed wheel mounting faces are shown in Fig. 5.

Firstly, the modal analysis was carried on original go-kart chassis structure, and in this analysis, 25 modes were obtained along with their corresponding natural frequencies. The values of the deformations at different structural elements were then checked at each of the corresponding natural frequency and are shown in Fig. 7. The maximum deformation was observed as 1.4082 m at 24th mode shape having a corresponding natural frequency as 104.12 Hz. The animated view of total deformation for 24th mode is shown in Fig. 6.

The CAD model was then geometrically modified by following the methodology explained earlier for five times in successive iterations. The total number of mode shapes, maximum deformation with its corresponding mode frequency and frequency of the first mode for all the iterations performed are presented in Table 3. The values of the deformations for the final structure at different modes and the corresponding frequency are shown in Fig. 8. The maximum deformation of 0.8172 m in the final structure was obtained at 8th mode (113.61 Hz).

In the final structure, the total modes have been reduced to 8 from 25 that of in the initial structure. This signifies that the problem of resonant frequencies has reduced in the final structure. The final structure's maximum deformation has also reduced to

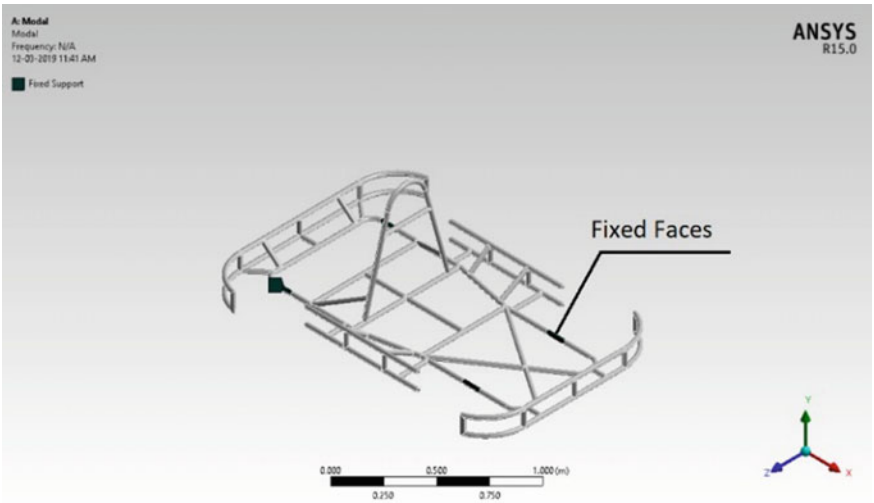

Fig. 5 Isometric view of the chassis which demonstrate the boundary condition applied

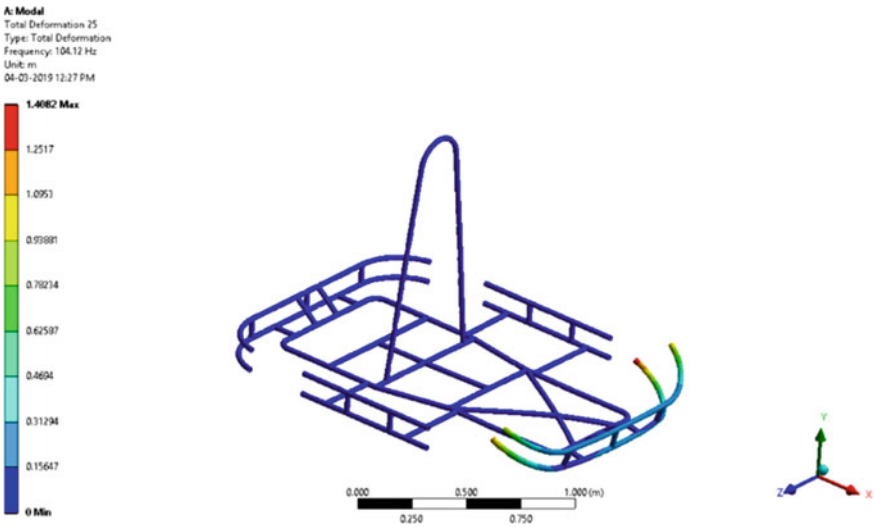

Fig. 6 Isometric view of the original chassis representing the maximum deformation at mode 24

0.8172 m from 1.4082 m (initial structure); therefore, the final structure can be said to have better stability from the past. The first mode frequency in the final structure has also shifted from 11.691 to 57.318 Hz. This ensures that the final structure will not be facing the problem of resonance until the moderate speeds.

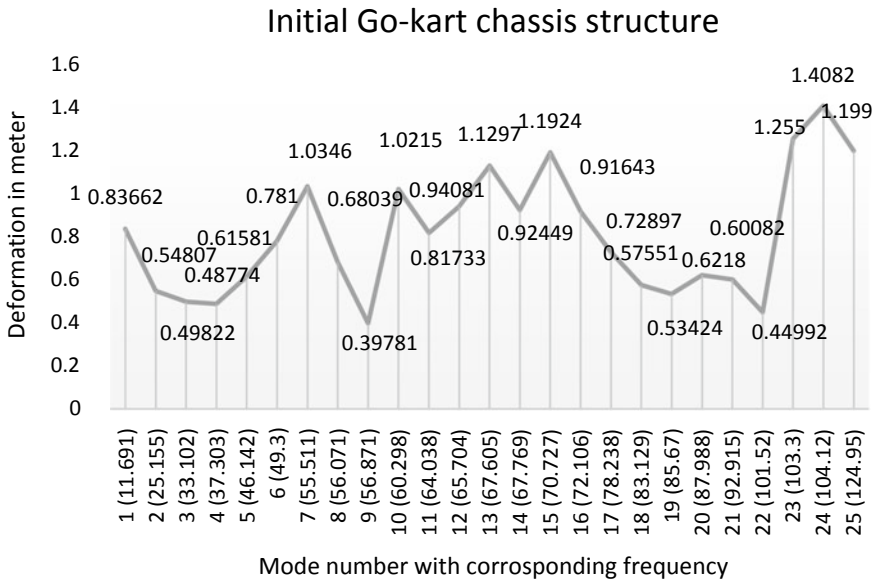

Fig. 7 Graph of maximum deformation and corresponding mode number of initial chassis

Table 3 Result of modal analysis after each modification

Step number	Total number of modes	Maximum deformation (m)	Corresponding frequency (Hz) for maximum deformation (mode number)	The frequency of first mode (Hz)
Initial chassis	25	1.4082	104.12 (24)	11.691
1	21	1.3592	94.306 (14)	25.954
2	17	1.2714	85.536 (9)	45.428
3	16	1.1454	91.038 (8)	46.38
4	8	0.9692	118.24 (7)	54.773
5	8	0.8172	113.61 (8)	57.318

6.2 Torsional Analysis

To calculate torsional rigidity of the go-kart chassis, Thompson methodology was adopted [9]. According to this methodology, the forces of equal magnitude and opposite directions have to be applied on the front wheel mountings by keeping rear wheel mountings fixed. The amount of force to be applied for carrying out torsional analysis can be calculated with reference to the weight of go-kart as defined in the rule book of the competition. In our analysis, the magnitude of force was calculated as 3532 N (magnitude 2G) by considering the maximum weight of go-kart as 180 kg.

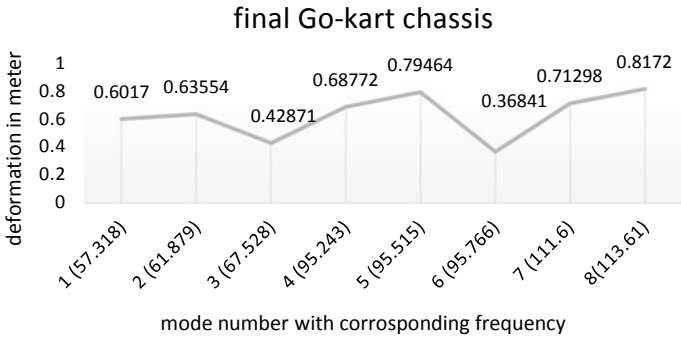

Fig. 8 Graph of maximum deformation and corresponding mode number of stage 6 chassis

The isometric view of the go-kart chassis with applied directional forces and fixed faces is shown in Fig. 9. After the application of the forces, deflection was calculated on the frontal wheel mountings to know the static strength of the structure. This has been done for all the modified structures, and their respective deflections are plotted and shown in Fig. 10.

The values of deformations calculated are showing a downward trend against stage modifications in the structure. This indicates that static structural strength has improved with every geometrical modification.

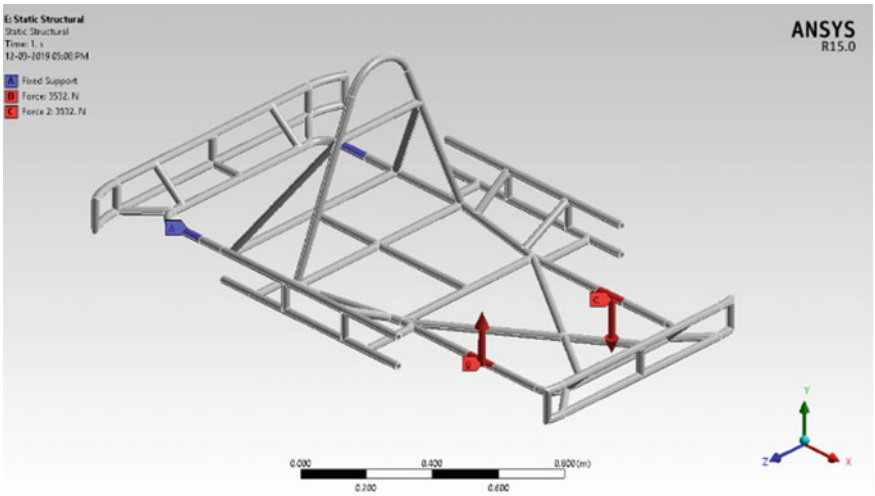

Fig. 9 Isometric view to demonstrate the boundary condition of the torsional test on the initial chassis

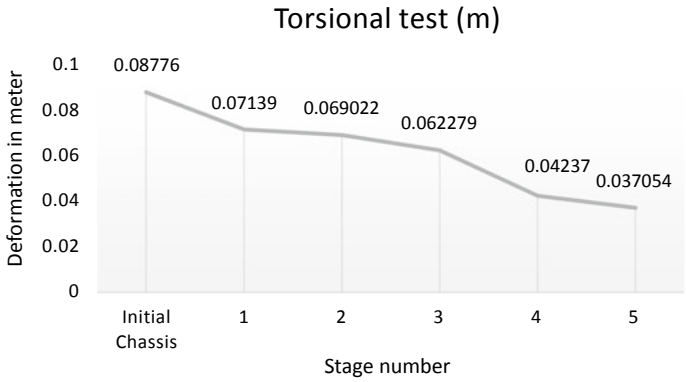

Fig. 10 Graph of deformation due to torsional loading

6.3 Impact Testing

This test is carried out to determine the crashworthiness of an automobile. The members of the go-kart chassis which are prone to crash such as front, rear and side sections are considered for the impact test. In this test, impact loads were applied on each section, and deformation in the same was calculated by fixing the opposite side wheel mountings. The simulation carried out for frontal impact test is shown in Fig. 11. The impact forces considered for frontal and rear impact test were of magnitude 4G (7064 N), and for side impact test, the magnitude was 2G (3532 N) as per the rule book guidelines [20]. The deformations calculated for each section in

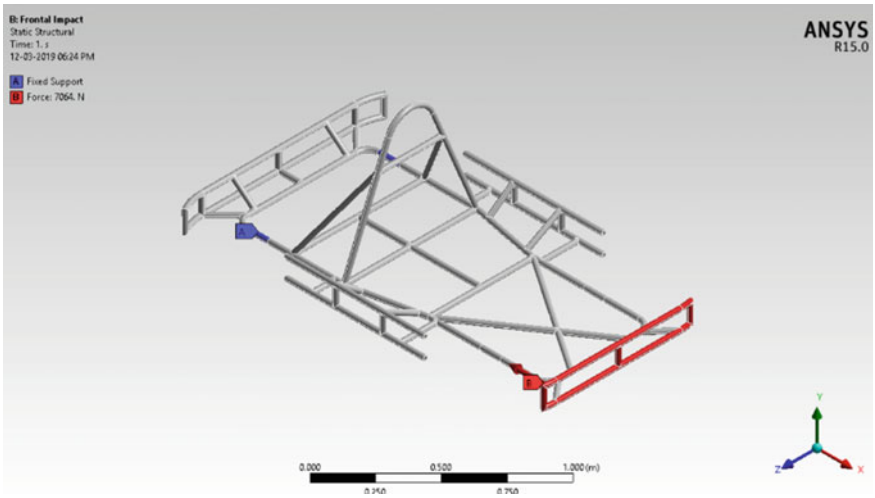

Fig. 11 Boundary condition of frontal impact

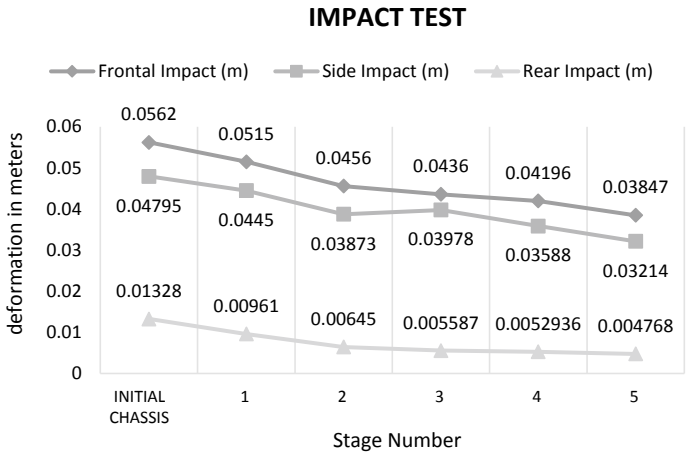

Fig. 12 Graph of deformation due to the impact

the initial chassis structure and after the successive geometrical modified structure are plotted and shown in Fig. 12.

The deformations calculated against impact loads for each section in the structure are decreasing with every modification made in the structure.

7 Conclusion

In this paper, the modal analysis was carried out on go-kart chassis structure, and on the basis of excessive deformation, geometrical modifications were made for five times. The original chassis structure was compared with the final recommended structure, and on the basis of this comparison, the following conclusions can be drawn:

- The maximum deformation in the final structure was found to reduce by 41.96%; this ensures the structural stability against the dynamic loads.
- The problem of the number of resonant frequency in the final structure was reduced significantly as the modes in it were found to be 8 as that of 25 in the initial structure.
- In the final structure, the first natural frequency was found to be shifted from 11.691 to 57.318 Hz. This ensures that the final structure will not be facing the problem of resonance till moderate speeds.
- The torsional rigidity was also found to improve by 57.77%. This means that structural strength of the chassis against static loads has increased in the final structure.

- The results of frontal, rear and side impact have also shown an improvement assuring the increase in crashworthiness of the chassis.

References

1. Abdullah, N. A. Z., Shahrir, S., Mustafizur, R., & Izzuddin, Z. (2017). Dynamics properties of a go-kart chassis structure and its prediction improvement using model updating approach. *International Journal of Automotive and Mechanical Engineering, 14*(1), 3887–3897.
2. Kirpal, S. (2000). *Automotive engineering* (Vol. 1). Standard Publication.
3. Tuononen, A. J., & Lajunen, A. (2016). Modal analysis of different drivetrain configurations in electric vehicles. *Journal of Vibration and Control, 1*(11), 1–11.
4. Pang, H., Li, H. Y., Fang, Z. D., & Shan, N. (2010). Ride comfort optimization and test research on an 8*4 heavy truck. *Noise and Vibration Worldwide, 41*(10), 65–71.
5. Kim, K., & Kim, C. (2005). A study on the body attachment stiffness for the road noise. *Journal of Mechanical Science and Technology, 19*(6), 1304–1312.
6. Feng, Y., & Jun, X. (2018). Modal analysis and improvement of the frame for all-terrain vehicle. *Noise and Vibration Worldwide, 1*(5), 1–5.
7. Shrinidhi, R., & Ajay, B. (2019). *Dynamic analysis and design optimization of automobile chassis frame using FEM. Lecture Notes in Mechanical Engineering* (pp. 671–680). Singapore: Springer Nature Singapore Pte Ltd.
8. Khannukar, K., Kallannavar, V., & Manjunath, B. (2015). Dynamic analysis of automotive chassis using FEA. *International Research Journal of Engineering and Technology, 2*(9), 2167–2170.
9. Jena, D. P., Singh, M., & Kumar, R. (2012). Radial ball bearing inner race defect width measurement using analytical wavelet transform of acoustic and vibration signal. *Measurement Science Review, 12*(4), 141–148.
10. Singh, M., Kumar, R., & Jena, D. P. (2009). Detection of missing ball in bearing using decomposition of acoustic signal. *Asian Journal of Chemistry, 21*(10), 143–147.
11. Singh, M., Shoor, S., & Singh, H. (2018). Shannon entropy a better indice for local defect detection and to study the effect of variable loading conditions for taper roller bearing. *International Journal of Mechanical Engineering and Technology (IJMET), 9*(7), 198–208.
12. Rajappan, R., & Vivekanandhan, M. (2013). Static and modal analysis of chassis by using FEA. *The International Journal of Engineering and Science, 2*(2), 63–73.
13. Jimin, H., & Zhi-Fang, F. (2001). *Modal analysis* (Vol. 1). Oxford: Butterworth-Heinemann Publication.
14. Antonio, F. A. R., André, L. R. P., André, C., Luiz, C. G., Moisés, D. S. P., & Anderson, B. O. (2015). *Static and dynamic analysis of a chassis of a prototype car*. SAE Technical Paper Series, International Congress and Display, Sao Paulo, Brazil, 2015-36-0353.
15. Frederico, M. A. S., Ramon, M. V., Marco, T. C. F., & Flavio, P. D. (2004). *Modal analysis of a tubular structure vehicle chassis*. SAE Technical Paper Series, XIII Congresso e Exposico Internacionals da Tecnologia da Mobilidade Sao Paulo, Brazil, 2004-01-3423.
16. Sane, S. S., Ghanshyam, J., & Anandaraj, H. *Stress analysis of light commercial vehicle using ANSYS* (pp. 1–5). Piaggio Vehicles Pvt Ltd, HTC 08.
17. Archit, T., & Dheer, S. (2016). Static analysis modal analysis and design modification in chassis frame to optimize weight by using composite material. *International Journal of Mechanical Engineering, 5*(1), 2319–2359.
18. Mohammad, R. F., & Rouhollah, H. (2010). Dynamic analysis of a modified truck chassis. *International Journal Advanced Design and Manufacturing Technology, 3*(1), 31–37.
19. Teo, H. F., & Roslan, A. R. (2007). Statics and dynamics structural analysis of a 4.5 ton truck chassis. *Journal Mekanikal, 24,* 56–67.

20. Prasad, S., & Laxman, A. (2018). Design modification of ladder chassis frame based on dynamic analysis. *International Research Journal of Engineering and Technology, 2*(9), 3877–3882.
21. Mousa, H., Farshid, A., Ruhollah, H., & Reza, M. (2011). A study on the vibrational effects of adding an auxiliary chassis to a 6-ton truck. *Journal of American Science, 7*(6), 1219–1229.
22. Rashid, A. Z. Y., Haris, R. R. M. S., & Alias, A. (2014). Improving the dynamic characteristics of body-in-white structure using structural optimization. *Scientific World Journal Hindawi Publishing Corporation, 1,* 1–11.
23. International Go-Kart Championship Rule Book 2018.
24. Oliveira, F. C. G. (2007). Contribuição ao desenvolvimento de uma estrutura veicular tipo SpaceFrame usando o método dos elementos finitos e métodos heurísticos de otimização numérica. Dissertação para obtenção do título de Mestre em engenharia mecânica. Universidade Federal de Uberlândia.
25. Daryl, L. L. (2010). *A first course in the finite element method* (5th ed.). Boston: Cengage Learning.
26. Gandhi, U. N., & Hu, S. J. (1995). Data based approach in modelling automobile crash. *International Journal Impact Engineering, 16*(1), 95–118.
27. Lam, K. P., Behdinan, K., & Cleghorn, W. L. (2003). A material and gauge thickness sensitivity analysis on the NVH and crashworthiness of automotive instrument panel support. *Thin-Walled Structures, 41,* 1005–1018.
28. Rao, S. S. (2010). *Mechanical vibrations* (5th ed.). Upper Saddle River, NJ: Prentice Hall.
29. Lardies, J., & Larbi, N. (2001). Modal analysis of random vibrating systems from multi output data. *Journal of Vibration and Control, 7,* 339–363.
30. Norm FIAT. (2002). Corso Per Progettisti di Scocca, Norma Fiat; Torino.
31. Leandro, P. S., & Felipe, N. (2001). *Application of modal analysis and operating deflection shapes on the study of trucks and buses dynamic behavior*. SAE Technical Paper Series, International Truck and Bus Meeting and Exhibition, Chicago, Illinois, 2001-01-2780.

Effect of Process Parameters on Water Absorption and Impact Strength of Hybrid PLA Composites

Guravtar Singh Mann, Lakhwinder Pal Singh, Pramod Kumar, and Sunpreet Singh

Abstract In the present research work, an effort has been made to study the impact strength and water absorption ability, also the consequences, of the hybrid poly lactic acid composites prepared by using sisal and jute fibers through compression die process. The input process parameters such as compaction pressure (CP), molding temperature (MT), and curing time (CT) have been studied in the response of the observed outcomes through the application of Taguchi-based design of experimentation approach. Further, the surface morphology of the samples after impact and water absorption tests has been studied to understand the mechanism of failure. From the analysis of variance, it has been found that molding temperature (MT) acted as the most influential parameter affecting the observed properties at 95% confidence level.

Keywords Poly lactic acid · Water absorption · Impact strength · Taguchi · Sisal · Jute

1 Introduction

Bio-based polymers have recently been used as sustainable products to replace certain composites arising from petroleum products because of their environmental friendly prospects [1]. These types of materials can replace the non-degradable petroleum-based polymer with degradable biopolymer based on renewable resources, considerably reducing the emissions of hazardous waste and carbon dioxide (CO_2) [2]. Not

G. S. Mann (✉)
School of Mechanical Engineering, Lovely Professional University, Phagwara, India
e-mail: guravtar.14443@lpu.co.in

G. S. Mann · L. P. Singh
Department of Industrial and Production Engineering, Dr. B.R. Ambedkar NIT, Jalandhar, India

P. Kumar
Department of Mechanical Engineering, Dr. B.R. Ambedkar NIT, Jalandhar, India

Sunpreet Singh
Production Engineering Department, GNDEC, Ludhiana, India

© Springer Nature Singapore Pte Ltd. 2021

C. Prakash et al. (eds.), *Advances in Metrology and Measurement of Engineering Surfaces* , Lecture Notes in Mechanical Engineering,
https://doi.org/10.1007/978-981-15-5151-2_18

only environmental issues but biocomposites can also to some extent solve the issue of the packaging industry once they are strengthened with distinct grades of polymers to improve their distinct characteristics and can be utilized in the automotive industry for sustainable construction [3]. Biocomposites when combined with natural/synthetic fibers/fillers have potential to substitute conventional polyolefin/glass fiber composites because they deliver diverse benefits such as recyclability, light weight, and low cost [4]. These composites have fascinating responsiveness in the sector as well as in academia, as they could allow thorough soil degradation through composting processes and make any toxic parts noticeable [5]. Moreover, to investigate, these fibers are combined with other fibers which are also known as hybrid fibers for improving their mechanical properties. These are the composites where both the matrix and the functional fibers are extracted from agricultural resources and are entirely degradable green composites and the other may or may not be biodegradable [6]. These composites have received substantial responsiveness because of their capability to give engineers new liberty to customize composites, thus achieving properties that cannot be achieved in binary systems consisting of a single type of filler/fiber spread in a matrix [7].

It also makes the use of expensive fillers more cost-effective by partly replacing them with inexpensive fibers. Though it is possible to combine diverse fillers into the hybrid system, it would be more advantageous to mix only two kinds of fillers. The performance characteristics of the subsequent composite can be significantly enhanced by a vigilant assortment of the reinforcing fillers [8]. The characteristics of hybrid composites are based on the single constituent, which balances the intrinsic advantages and disadvantages more constructively. The weaknesses of the one filler/fiber could be overlooked by the other filler's advantages [9]. The suitable material structure could achieve a hybrid composite with cost and efficiency balance [10]. Masoodi and Pillai [11] investigated the conduct of moisture and swelling in bio-based jute-epoxy composites and observed the rate of moisture diffusion in composites improved with a rise in the proportion of jute fiber to epoxy. Sanjay and Yogesha [12] studied the impact of hybridization and loading sequences on the various mechanical characteristics of composites of jute/kenaf/glass and epoxy and observed the enhancement of these properties. Chaudhari et al. [13] evaluated the various characteristics of jute, hemp, and flax composites based on epoxy and observed better mechanical characteristics of hybrid composites.

Attempts have been made in the present investigation to develop hybrid composite using jute and sisal fiber, whereas poly lactic acid (PLA) a highly versatile biodegradable polymers obtained from 100% renewable materials is used as resin [14]. The enhancement in mechanical properties like tensile strength and flexural strength has been examined experimentally using Taguchi method. The fiber matrix morphology of the interface region was explored using SEM analysis.

2 Materials and Methods

Poly lactic acid (PLA) was used as matrix material. It was supplied by Nature Works India. It is biodegradable material extracted from corn starch. The tensile strength of the smooth PLA was examined with universal testing machine with 1 mm/min cross velocity and 150 mm gage length. Woven jute and sisal were supplied by Chandra Parkash & Co. located in Jaipur India. Table 1 shows the mechanical properties of jute and Sisal.

2.1 Fabrication of Composites

The surface treatment of the fibers is done before the fabrication of the fibers which is also necessary for improved wettability (adhesion) between the fiber and the matrix as this process eliminates the hemicellulose layer leading to higher crystallinity in fibers. Then, the fabrication of composites was carried using compression molding method. The full setup was fitted with the molding machine for metal die, heating elements, thermocouples, and compression. The metal die was intended to create laminate of 4 mm thick. Four layers of jute fibers have to be used to get 4 mm dense laminate after pilot runs. Treated jute and sisal fibers were cut to the length of 120 mm and were kept in an oven for preheating at 90 °C temperatures for 3 h to remove the moisture. Compression molding die was cleaned and heated to the temperature provided. The Teflon sheet was set once the die temperature exceeded the appropriate temperature. First, the PLA granules were spread evenly into the cavity and afterward, the jute fibers were put in the cavity over the PLA granules and then, the other jute layer was positioned over the sisal fibers. Eventually, remaining PLA granules were scattered over the jute materials contained in the cavity. Finally, pressure is applied. The temperature will be maintained according to the requirement and the load will begin to apply.

Table 1 Properties of sisal and jute

Properties	Sisal	Jute
	Values	Values
Density (g/cm^3)	1.4–1.5	1.3–1.5
Length (mm)	1.5–120	900
Failure strain (%)	1.5–1.8	2.0–2.5
Tensile strength (MPa)	393–800	507–855
Stiffness/Young's modulus (GPa)	10–55	9.4–28
Specific tensile strength (MPa/g cm^3)	300–610	362–610
Specific Young's modulus (GPa/g cm^3)	7.1–39	6.7–20

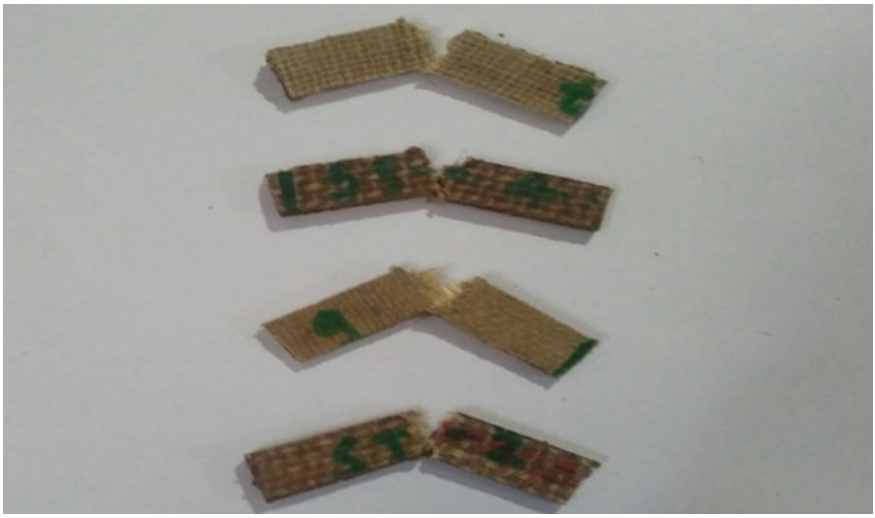

Fig. 1 Fractured Izod specimens

2.2 Impact Test

The Izod test was carried as per ASTM standard D256. The cutting of the samples was as per ASTM specifications 63.5 × 12.7 × 4 mm, and for Charpy test, the specimen samples with 127 lengths × 12.7 width × 4 mm were prepared. Figure 1 shows the fractured Izod specimens.

2.3 Water Absorption

In water absorption test, specimen was prepared 38 mm^2 with a 0.5 mm clearance. The weight of the specimens were measured first in air (WI) and then dipped in distilled water for a while of 24 ± 1 h. After completion of time, the specimens get out from the water and measured the weight ($W2$) within 2 min.

$$\text{Water absorption } (\%) = (W2 - W1)/W1 \times 100$$

$W1$ is the weight of specimen before dipped in distilled water and $W2$ is the weight of specimen after 24 h dipped in water.

3 Optimization Using Taguchi Methodology

Taguchi method provides information on the full set of possibilities for experiments that cover various applications. Moreover, this method reveals the outcome of different parameters on the mean and variance for process parameters. Moreover, experimental designs by Taguchi method helps to implement orthogonal arrays and organizes process parameters which affect the process, and helps in a recommendation of various levels and their variation for achieving the optimized results. Therefore, the number of experiments can be arranged with minimum means and lesser time without affecting the quality of the product [15–17]. For the implementation of the Taguchi method, the objective function is established along with the identification of process parameters with their levels as shown in Table 2. Secondly, the appropriate orthogonal array (OA) is selected for experimentation as shown in Table 3, and Table 4 shows the values obtained. At last confirmation, the experiment is done for the obtained data. The major aim of this technique is to produce high-quality products at minimum cost. Therefore, in the present research is to find the optimal set of parameters for maximum impact test and water absorption test during the fabrication of natural hybrid composites. Taguchi methodology organizes control factors and noise factors which affect the process quality. While noise is the uncontrollable factor, causes variations in the output, contributed due to the experimental environment like the ambient temperature, humidity, etc. Control variables are the most significant variables in determining the characteristics of the product [18]. Therefore, for the

Table 2 Levels of the variables used in the experiment

Levels	Variables		
	A:MT	B:CP	C:CT
1	160	250	30
2	185	300	60
3	210	350	90

Table 3 L_9 orthogonal array

Exp. No.	MT	CP	CT	*S/N*
1	1	1	1	S/N_1
2	1	2	2	S/N_2
3	1	3	3	S/N_3
4	2	1	2	S/N_4
5	2	2	3	S/N_5
6	2	3	1	S/N_6
7	3	1	3	S/N_7
8	3	2	1	S/N_8
9	3	3	2	S/N_9

Table 4 Results of the L_9 orthogonal array experimental design for flexural strength

Trail	Process parameters			Impact strength (N/mm)				Water absorption (%)			
	MT	CP	CT								
	Trail conditions			*R*1	*R*2	*R*3	*S*/*N* (dB)	*R*1	*R*2	*R*3	*S*/*N* (dB)
1	1	1	1	72.23	71.44	73.33	37.185	22.61	23.25	24.25	27.31
2	1	2	2	72.62	73.51	71.22	37.199	26.43	25.21	26.52	28.31
3	1	3	3	71.42	72.33	71.41	37.112	25.81	24.13	24.33	27.86
4	2	1	2	70.24	72.91	70.12	37.032	23.04	22.04	24.04	27.23
5	2	2	3	67.52	68.84	67.33	36.636	23.34	25.52	22.66	27.51
6	2	3	1	68.62	69.32	70.72	36.844	24.25	23.29	24.28	27.57
7	3	1	3	66.22	66.11	67.23	36.458	20.64	20.43	19.64	26.11
8	3	2	1	68.33	67.14	66.12	36.545	19.81	18.13	19.21	25.58
9	3	3	2	67.12	67.32	68.35	36.598	19.04	20.04	20.64	25.96

manufacturing of hybrid composite, the typical control factors include the heating temperature of the die. Taguchi method utilizes *S*/*N* ratio to express scatter around the target value. There are three possible categories for quality characteristics (1) smaller is better (2) nominal is better (3) larger is better. The main objective of the current research is to maximize the composite's impact strength and water adsorption behavior.

Therefore, larger quality features are chosen which is given as It can be observed from Fig. 2 that parameter values at levels A_1, B_2, and C_3 are the best choice in terms of the impact strength and for water absorption values at levels A_1, B_3, and C_2 are the best in terms of optimum levels. These values are plotted in Fig. 3. Table 5 shows the mean values and Table 6 shows ANOVA values.

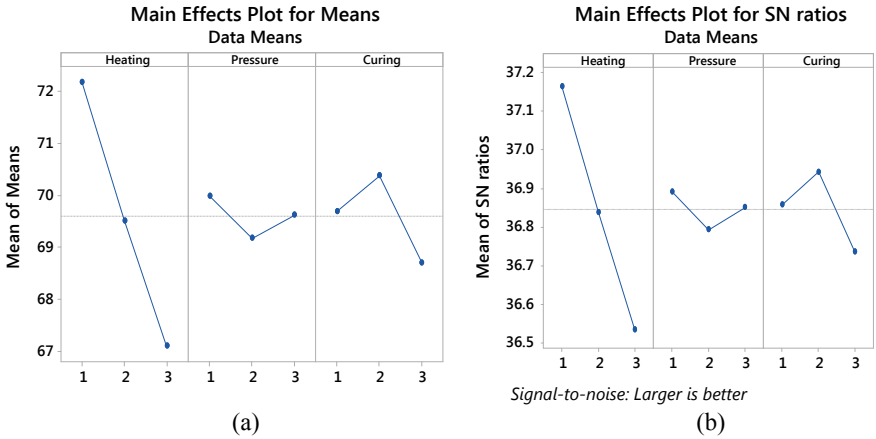

Fig. 2 Mean (**a**) and *S*/*N* plot (**b**) for Izod strength

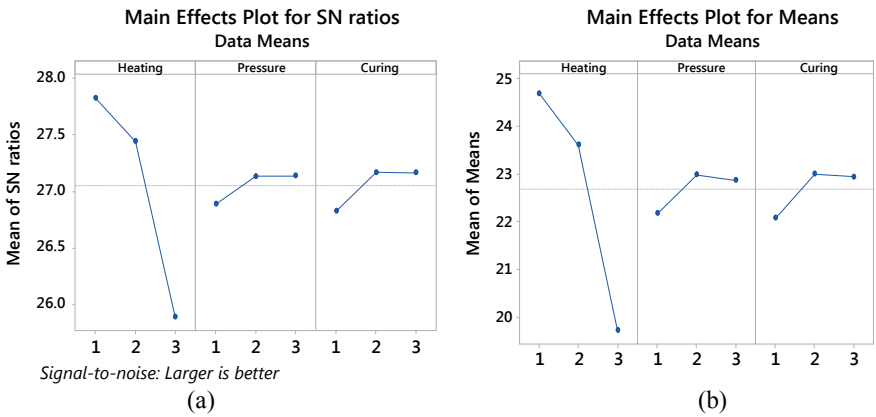

Fig. 3 Mean (**a**) and *S*/*N* plot (**b**) for water absorption

Table 5 Response table for means

Level	Impact strength		CT	Water absorption		CT
	MT	CP		MT	CP	
1	24.69	22.18	22.08	72.17	69.98	69.69
2	23.61	22.98	23	69.51	69.18	70.38
3	19.73	22.87	22.94	67.1	69.62	68.71
Delta	4.96	0.81	0.92	5.06	0.8	1.67
Rank	1	3	2	1	3	2

$$S/N = -10\log\left[1/R\sum_{i=0}^{R} 1/y_i^2\right] \tag{1}$$

$$\boldsymbol{\mu_{Ts} = \overline{A_1} + \overline{B_2} + \overline{C_1} - 2\overline{I_{TS}}} \tag{2}$$

where μ_{Ts} is mean value impact strength, $I_{\mathrm{IS}} = 71.67$ N/mm^2 (Table 6), and $A_1 + B_2 + C_1$ are average values of tensile strength. Therefore, $\mu_{\mathrm{Ts}} = 74.36 \pm 10.84$ N/mm^2. The confidence interval (CI) for the anticipated result can be calculated as:

$$\boldsymbol{CI = \sqrt{F_\alpha(1, f_e)V_e\left[\frac{1}{n_{eff}} + \frac{1}{R}\right]}} \tag{3}$$

where $\boldsymbol{F_\alpha}$ $(1, f_{\mathrm{e}})$ F is-ratio at the confidence level of $(1 - \alpha)$ against DOF 1 and error DOF f_{e}, v_{e} = error variance, η_{eff} is the effective number of repetitions.

$$\mathbf{n_{eff}} = \frac{\mathbf{1}}{\mathbf{1 + \{Total\ DOF\ in\ the\ estimation\ of\ mean\}}} \tag{4}$$

N = Total number of test outcomes (9 * 27) and R is sample size = 3 using the values, $v_{\mathrm{e}} = 18.6$, Table 4, Total DOF in estimation of mean is = 6 and $\eta_{\mathrm{eff}} = 3.87$, $F_{0.05}$ (1, 9) = 5.11 (The tabulated value). Therefore, from the above calculations for the interval at 95% is ±5.31 and the predicted optimum value for impact strength is $67.05 < \mu_{\mathrm{Ts}} < 81.67$ N/mm^2.

Similarly, by using Eqs. 2, 3, and 4, the calculations of the interval at 95% is ±01.84 which resulted in the predicted optimum value water absorption is $23.32 < \mu_{\mathrm{Ts}} < 44$.

4 Results and Discussion

It is observed that although all three parameters, i.e., heating, pressure, and curing play an integral role in the fabrication of hybrid fibers, the adhesion between the

Table 6 Analysis of variance for impact strength and water absorption

Source	DF	SS: I	SS: WA	V: I	V: WA	F-value: I	F-value: WA	P: I	P: WA
MT	2	115.458	122.232	57.729	61.1158	57.16	54.39	0	0
CP	2	2.891	3.423	1.4453	1.7114	1.43	1.52	0.263	0.242
CT	2	12.633	4.79	6.3165	2.3951	6.25	2.13	0.008	0.145
Error	20	20.201	22.474	1.01	1.1237				
Lack-of-fit	2	2.479	7.308	1.2397	3.654	1.26	4.34	0.308	0.029
Pure error	18	17.721	15.166	0.9845	0.8426				
Total	26	151.183	152.919						

where, DF, SS, V, F, P, I, and WA are the degree of freedom, a sum of a square, variance, probability, impact, and water absorption, respectively

fibers is influenced mostly by the heating temperature of the die. When the fibers are fabricated at 160° temperature and 250 kN pressure is applied, minimum impact strength is observed as it can be seen SEM image 4a from the fiber pull out that fracture during the impact test is brittle which makes it more weak in case of impact strength because at this temperature, the PLA does not flow smoothly in all directions and there is no proper adhesion between the fibers and resin. When the temperature is increased to 185 °C and pressure of 300 kN is applied with curing at 60°. The flow of matrix material flows in all directions due to which better bonding takes place which influences the impact behavior of the material and maximum is obtained at these parameters but when the temperature is increased to 210 °C and pressure of 350 kN is applied at 90° curing, the internal fibers get burnt due to which the minimum values of impact strength are obtained, it can be observed from Fig. 4c that voids are seen in samples. These pores and voids can lead to early failure of these composites during loading. Another study which is related to outdoor applications of the natural fibers is water absorption tests. Figure 5 shows SEM images after moisture absorption tests. Initially, the water absorption does not affect the hydrophobic PLA matrix as shown in Fig. 5a–d. Before moisture absorption, the SEM images for hybrid composites display rougher fracture but while SEM images during moisture absorption show smoother fractured surface as shown in Fig. 5e which shows good adhesion between the surface as shown in Fig. 5f but when the temperature and pressure are increased to maximum 210 °C with 350 KN the fibers are burnt due to which poor fiber/matrix interface bonding. This indicates poor fiber/matrix interface

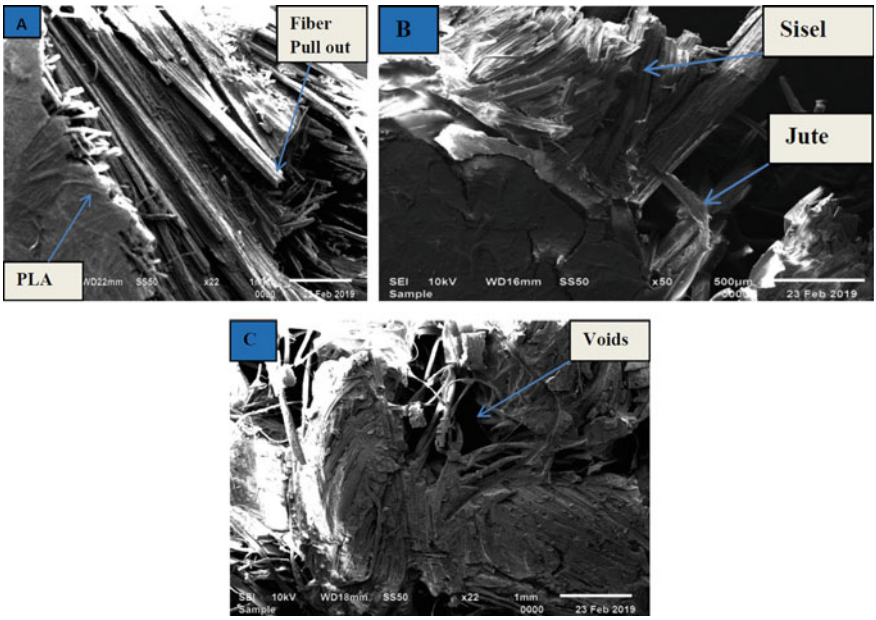

Fig. 4 SEM images of hybrid fibers after impact failure

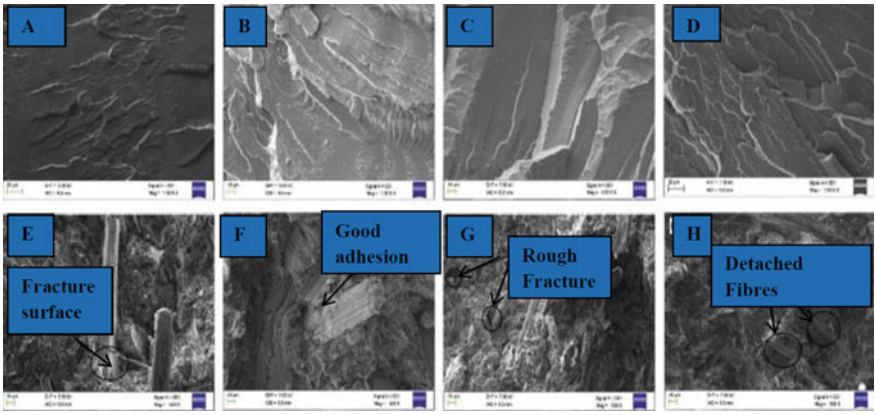

Fig. 5 Hybrid fiber SEM pictures after water absorption experiment

bonding there and therefore poor adhesion is observed as PLA comes out from the die due to high pressure and temperature and fibers are also detached easily during the impact loading as shown in SEM image in 5h. Therefore, optimum parameters where impact strength is maximum are at 185 °C temperature, the pressure of 300 kN, and curing at 60°.

5 Conclusion

Using the Taguchi technique, the impact strength and water absorption behavior of manufactured hybrid sisal and jute composites were explored. Three important parameters, that is the heating temperature, pressure, and curing temperature have been studied. It is possible to draw the following findings from the inquiry: To obtain maximum tensile and flexural strength, optimum heating temperature, pressure, and heating temperature were maintained. The maximum impact strength was observed at the temperature 185 °C, pressure of 300 kN, and curing at 60 °C.

Confirmation tests have been performed to confirm the optimum circumstances predicted. Estimate gain and confirmation gain values have been discovered close to each other. The moisture absorption was maximum when parameters were temperature 185 °C pressure of 300 kN, and curing at 60° when compared to dry samples because of the plasticization effect of diffused water molecules.

References

1. Mishra, V., Singh, G., Yadav, C. B., Karar, V., Prakash, C., & Singh, S. (2019). Precision machining of biopolymers: A brief review of the literature and case study on diamond turning. *Journal of Thermoplastic Composite Materials*, 0892705719856060.

2. Singh, S., Prakash, C., Wang, H., Yu, X. F., & Ramakrishna, S. (2019). Plasma treatment of polyether-ether-ketone: A means of obtaining desirable biomedical characteristics. *European Polymer Journal*, *118*, 561–577.
3. Mann, G. S., Singh, L. P., Kumar, P., & Singh, S. (2018). Green composites: A review of processing technologies and recent applications. *Journal of Thermoplastic Composite Materials*, 0892705718816354.
4. Singh, J. I. P., Singh, S., & Dhawan, V. (2018). Effect of curing temperature on mechanical properties of natural fiber reinforced polymer composites. *Journal of Natural Fibers, 15*, 687–696.
5. Lee, S. H., Wang, S., & Teramoto, Y. (2008). Isothermal crystallization behavior of hybrid biocomposite consisting of regenerated cellulose fiber, clay, and poly(lactic acid). *Journal of Applied Polymer Science, 108,* 870–875.
6. Majeed, K., Jawaid, M., & Hassan, A. (2013). Potential materials for food packaging from nanoclay/natural fibres filled hybrid composites. *Materials & Design, 46*, 391–410.
7. John, M. J., & Thomos, S. (2008). Biofibres and biocomposites. *Carbohydrate Polymers, 71,* 343–364.
8. Alamri, H., & Low, I. M. (2013). Effect of water absorption on the mechanical properties of nanoclay filled recycled cellulose fibre reinforced epoxy hybrid nanocomposites. *Composites Part A: Applied Science and Manufacturing, 44*, 23–31.
9. Gupta, M. K., Choudhary, N., & Agrawal, V. (2018). Static and dynamic mechanical analysis of hybrid composite reinforced with jute and sisal fibres. *Journal of the Chinese Advanced Materials Society, 6*(4), 666–678.
10. Ramesh, M., Palanikumar, K., & Reddy, K. H. (2013). Mechanical property evaluation of sisal–jute–glass fiber reinforced polyester composites. *Composites Part B: Engineering, 48*, 1–9.
11. Masoodi, R., & Pillai, K. M. (2012). A study on moisture absorption and swelling in bio-based jute-epoxy composites. *Journal of Reinforced Plastics and Composites, 31*(5), 285–294.
12. Sanjay, M. R., & Yogesha, B. (2018). Studies on hybridization effect of jute/kenaf/E-glass woven fabric epoxy composites for potential applications: Effect of laminate stacking sequences. *Journal of Industrial Textiles, 47,* 1830–1848.
13. Chaudhary, V., Bajpai, P. K., & Maheshwari, S. (2018). Studies on mechanical and morphological characterization of developed jute/hemp/flax reinforced hybrid composites for structural applications. *Journal of Natural Fibers, 15,* 80–97.
14. Mann, G. S., Singh, L. P., Kumar, P., Singh, S., & Prakash, C. (2019). On briefing the surface modifications of polylactic acid: A scope for betterment of biomedical structures. *Journal of Thermoplastic Composite Materials,* 0892705719856052.
15. Pramanik, A., Islam, M. N., Basak, A. K., Dong, Y., Littlefair, G., & Prakash, C. (2019). Optimizing dimensional accuracy of titanium alloy features produced by wire electrical discharge machining. *Materials and Manufacturing Processes*, *34*(10), 1083–1090.
16. Singh, S., Singh, M., Prakash, C., Gupta, M. K., Mia, M., & Singh, R. (2019). Optimization and reliability analysis to improve surface quality and mechanical characteristics of heat-treated fused filament fabricated parts. *The International Journal of Advanced Manufacturing Technology*, *102*(5–8), 1521–1536.
17. Prakash, C., Singh, S., Singh, M., Gupta, M. K., Mia, M., & Dhanda, A. (2019). Multi-objective parametric appraisal of pulsed current gas tungsten arc welding process by using hybrid optimization algorithms. *The International Journal of Advanced Manufacturing Technology*, *101*(1–4), 1107–1123.
18. Prakash, C., Singh, S., Basak, A., Królczyk, G., Pramanik, A., Lamberti, L., & Pruncu, C. I. (2020). Processing of Ti50Nb50− xHAx composites by rapid microwave sintering technique for biomedical applications. *Journal of Materials Research and Technology*, *9*(1), 242–252.

Comparative Investigation of Different Types of Cutting Fluid in Minimum Quantity Lubrication Machining Using CFD

Payal Chauhan, Anjali Gupta, Amit Kumar Thakur, and Rajesh Kumar

Abstract Minimum quantity lubrication (MQL) is a method where cutting fluid is supplied to the machining zone in the form of droplets (10–500 ml/h). The performance of MQL machining depends on the quality of spray generated by the MQL system. The spray quality is defined by droplet diameter, velocity and the number of droplets. In the present work, computer simulations were performed to study the characteristics of spray generated with internal mixing nozzle using three different types of cutting fluids, namely vegetable oil (VO), synthetic oil (SO) and mineral oil (MO). Effects of air pressure and mass flow rate of these cutting fluids on spray formation were also studied using ANSYS FLUENT. The results showed that with increase in air pressure and mass flow rate of cutting fluids, diameter of droplets decreased, whereas velocity and number of droplets increased. It was observed that not only the spray quality generated using vegetable oil is better than other two cutting fluids, but also the surface heat transfer coefficient (HTC) improved using vegetable oil. Surface heat transfer coefficient (HTC) using vegetable oil (VO) increased by 16.28% over synthetic oil (SO) and 32.16% over mineral oil (MO).

Keywords Minimum quantity lubrication · Computational fluid dynamics · Internal mix nozzle · Cutting fluids

1 Introduction

Machining is the most common practice carried out in manufacturing industries to produce component of desired size and shape by removal of material. The plastic deformation of workpiece and friction at workpiece–tool interface generates large amount of heat in the cutting region. This stimulates the need for use of cutting fluids during machining process. Cutting fluids are required for cooling and lubricating the cutting zone. They not only reduce the temperature of the cutting region by carrying away the heat generated during machining but also reduce friction at workpiece–tool

P. Chauhan (✉) · A. Gupta · A. K. Thakur · R. Kumar
Mechanical Engineering Department, UIET, Panjab University, Chandigarh 160014, India
e-mail: payalchauhan1995@gmail.com

© Springer Nature Singapore Pte Ltd. 2021

C. Prakash et al. (eds.), *Advances in Metrology and Measurement of Engineering Surfaces* , Lecture Notes in Mechanical Engineering,
https://doi.org/10.1007/978-981-15-5151-2_19

interface [1]. This results in improving the surface quality and dimensional accuracy of the workpiece and reduction in cutting forces. Along with these benefits, there are some disadvantages accompanied with the cutting fluids. The disposal of cutting fluids into environment can cause soil and air pollution. Their use has been reported to cause serious health problems to the operators such as respiratory problems, lung cancer, genetic and dermatological diseases [2, 3]. Moreover, it has been reported that use of cutting oils results in an additional 7−17% cost of the total machining cost [4]. Looking at these concerns, efforts are being made to limit their use. Dry cutting (DC) and minimum quantity lubrication (MQL) machining are the suggested alternatives. On one hand, where DC exterminates the ill effects of cutting fluids by completely eliminating the use of cutting fluids, on the other hand, it requires special tooling and coated tools to overcome its limitations such as overheating of tool, poor dimensional accuracy and adhering of chips to rake face of tool. The second method is minimum quantity lubrication (MQL), where cutting fluids are supplied in the form of tiny droplets which are formed as a result of atomization of the cutting fluid with the help of pressurized air [5]. The flow rate of the cutting fluids while machining is very low in MQL (nearly 10−500 ml/h) as compared to wet cutting (WC) where the flow rate is of the order of 60 l/h [6]. Also, the major part of the cutting fluid that is being used in MQL is evaporated. Thus, the cost related to disposal and treatment of cutting fluid after machining, cleaning of workplace and machinery is minimized. Tawakoli et al. [7] obtained better surface finish with MQL machining in comparison with WC and DC during grinding. Coefficient of friction, tangential forces and specific grinding energy were found to be lower with MQL grinding due to better penetration of lubricant. Recently, many experimental investigations have been carried out to show the suitability of using eco-friendly vegetable oil (VO) over petroleum-based mineral oil (MO) in MQL machining. Agrawal et al. [8] performed MQL turning of steel to compare the performance of mineral oil (MO) and aloe vera (VO) at different feeds, depth of cut and speed. It was observed that VO reduced surface roughness (6.7% lower), tool wear (0.14% lower) and environmental pollution as compared to MO. Wang et al. [9] studied the effect of MQL machining and WC on grinding performance using different VOs and MOs. MQL grinding with castor oil (VO) provided better surface finish, low coefficient of friction and low specific grinding energy than MO. Further, MQL grinding resulted in better performance than WC due to better lubrication. Singh et al. [10] performed MQL turning using soyabean oil (VO) and MO. The MQL turning using VO resulted in better surface finish at high speed and reduced pollution (because of its biodegradability) over MO. It can be concluded from the literature survey that MQL results in an improved machining performance over the DC and almost the comparable performance as WC due to better penetration of tiny droplets of cutting fluid into the cutting region. Also, the use of VOs as cutting fluid results in an improved performance over MOs in MQL machining. From the above experimental studies, it can be inferred that VO can be considered as a good substitute over conventional petroleum-based oils. Apart from experimental study, computer-based simulation is a good approach to understand any process well. Simulation saves time as repetitive calculations can be performed in computer to find the optimum value of critical parameters. Computational fluid

dynamics (CFD) is one such approach which is used to study the true characteristics of fluid interactions in internal and external flows [11]. CFD can also be used to simulate the behavior of cutting fluid in MQL machining. The objective of this paper is to develop a CFD-based model for studying the effect of different factors that affect the spray quality in MQL machining. The study also carries out the comparative investigation of the performance of different types of cutting oils by studying their spray characteristics.

2 Parameters Affecting the MQL Machining Performance

MQL machining performance depends on the quality of spray generated by MQL system. Spray quality depends on various parameters such as types of cutting fluid, pressure of inlet air, standoff distance, mass flow rate of cutting fluid, nozzle geometry, nozzle dimensions and nozzle angular position [12, 13]. The spray is characterized by droplets diameter, droplets velocity and the number of droplets. Velocity of droplets should be high enough to diminish the vorticities that may be produced due to aerodynamic interactions between spray and the surrounding atmosphere. Spray which is free of vorticities with uniform droplet size (neither too large nor too small) is considered as more effective in MQL. A small-sized droplet (<4 μm) becomes airborne when inhaled by workers and can cause acute respiratory disorders [14], and large-sized droplet may not penetrate effectively inside the cutting zone. Beside these factors, properties of gaseous medium into which cutting fluid is discharged also affect the spray quality. Density of air also plays important role in atomization of cutting fluid in MQL machining. In addition to this, properties of cutting fluids such as density, viscosity, surface tension, thermal conductivity and specific heat also affect the spray quality. Purpose of this paper is to study the effects of air pressure, mass flow rate and properties of different types of cutting fluid on the spray characteristics. Soyabean oil (VO), paraffin oil (MO) and ester oil (SO) are used for comparative performance. Operating conditions, properties of air and properties of cutting fluids that are being considered for simulations in present work are given in Tables 1, 2 and 3, respectively.

Table 1 Operating conditions

Air pressure (bar)	2, 3 and 4
Mass flow rate of cutting fluid (ml/h)	50, 100, 500

Table 2 Properties of air

Air density (kg/m^3)	1.1845
Air viscosity (kg/m-s)	1.86×10^{-5}
Specific heat (J/kg-k)	1005
Thermal conductivity (W/m-k)	0.02624

Table 3 Properties of cutting fluid

Cutting fluid	Density (kg/m^3)	Dynamic viscosity (kg/m-s)	Specific heat (c_p) (kJ/kg-k)	Surface tension (N/m)
Soybean oil (VO)	917	0.0418	1635	0.0309
Ester oil (SO)	964	0.0513	1905	0.0314
Paraffin oil (MO)	800	0.1181	2130	0.0230

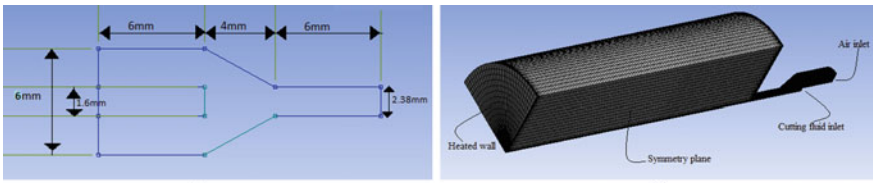

(a) (b)

Fig. 1 **a** Geometry of nozzle with dimensions, **b** one-fourth model of internal mix nozzle [17]

3 Physical Model of Internal Mix Nozzle

3.1 Creating a 3D Model

ANSYS FLUENT software was used to perform the CFD analysis of spray generated using internal mix nozzle. Nozzle geometry as shown in Fig. 1a consists of a concentric pipe where inner pipe carries cutting fluid and outer annular region carries air. Both air and cutting fluid were mixed in mixing chamber, and spray was produced by disintegration of cutting fluid by pressurized air energy and shearing action of the surrounding air. The dimensions of the nozzle considered were same as by Verma et al. [15] so that the model can be validated. Since the geometry is symmetric about x-axis, so one-fourth model of a nozzle (shown in Fig. 1b) is created to minimize the computational time.

3.2 Meshing of 3D Model

Accuracy of results depends on the quality of mesh. A good quality mesh is one with skewness below 0.3 and orthogonality above 0.7. A fine mesh was generated by taking these points into account.

3.3 Boundary Conditions, Governing Equations and Model Validation

Pressure-based solver was used to perform transient calculations by considering the gravity effect. Energy equation with K-ε realizable model was used to take into account the effect of turbulence. Surface injection through cutting fluid inlet surface was created at particular velocity and mass flow rate in discrete phase model (DPM), and simulation of discrete phase was done in Lagrangian frame of reference by Fluent. DPM has been chosen in this study as the amount of cutting fluid used in MQL is very small, and DPM model also requires very small volume fraction (less than 10%) of discrete phase. In DPM, air is taken as continuous (primary) phase and discrete (secondary) phase which comprises oil droplets. Pressure inlet and mass flow rate are given as boundary condition at air inlet surface and cutting fluid inlet surface, respectively. For simulating heat generation 0.5 MW/m^2, heat flux was given at wall. Pressure-based solver is used. ANSYS FLUENT uses mass, momentum and energy equations to solve the flow, and its working is based on three basic laws of fluid dynamics [16]. These laws are the law of mass conservation (continuity equation), the law of momentum conservation and the law of energy conservation. Simulations were first performed to validate the model using research work of Verma et al. [15]. For validation, water with mass flow rate 500 ml/h and air at 4 bar were used. Contours of air velocity obtained are shown in Fig. 2a, and value of Sauter mean diameter obtained is 5.3 μm (Fig. 2b) which are similar to as obtained by [15]. So, the model is validated, and it can be used for further studies.

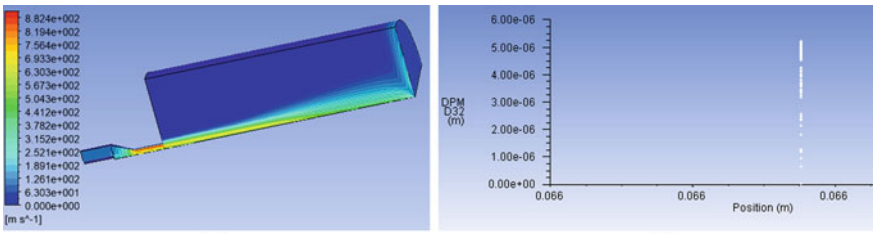

(a) (b)

Fig. 2 **a** Air velocity contour, **b** Sauter mean diameter at 4 bar, 500 ml/h for model validation

4 Results and Discussions

4.1 Characteristics of Spray Formed Using Three Different Cutting Fluids (VO, SO and MO)

Comparison of droplet diameter

Variation of droplet diameter with pressure of air, mass flow rate of cutting fluid and type of cutting fluids is shown in Fig. 3a. It can be seen that for VO, SO and MO droplet diameter decreases with increase in air pressure. This can be attributed to the fact that with increase in air pressure atomization process increases resulting in droplets with smaller diameter. This increased atomization leads to an increase in number of droplets. So diameter decreases and number of droplets increases with increase in air pressure. Further, diameter of droplets formed using VO was medium sized (7.5–16.3 μm) which in turn are more effective in providing better cooling and lubrication during machining operation [17].

Comparison of droplet velocity

Variation of droplet velocity with pressure of air, mass flow rate of cutting fluid and type of cutting fluids is shown in Fig. 3b. Velocity of droplets increased with increase in air pressure because of greater momentum transfer to the droplets. The increase in velocity of cutting fluid droplets helps in droplet penetration into cutting region by overcoming the peripheral velocity of cutting tool. Highest velocity of droplets was obtained for VO in comparison with SO and MO, so better performance is expected from VO.

It can be concluded from the above simulation results that since the droplet diameter is minimum for VO and droplets velocity and number of droplets formed are maximum for VO, the machining performance will be better using VO as compared to SO and MO. These results are consistent with the experimental studies performed by various researchers [7–10].

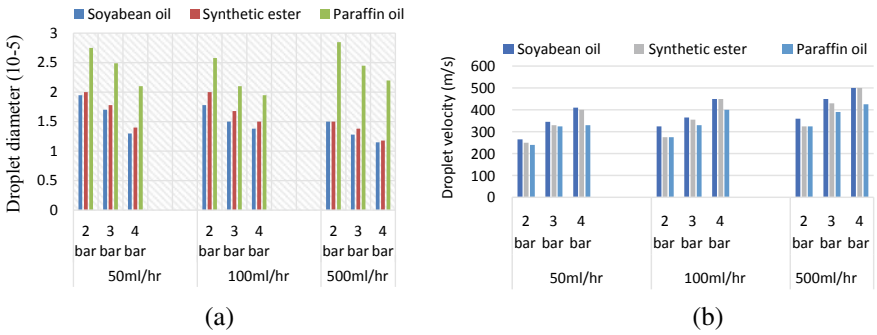

Fig. 3 **a** Variation of droplet diameter, **b** variation of droplet velocity with air pressure, flow rate of cutting fluid and type of cutting fluid

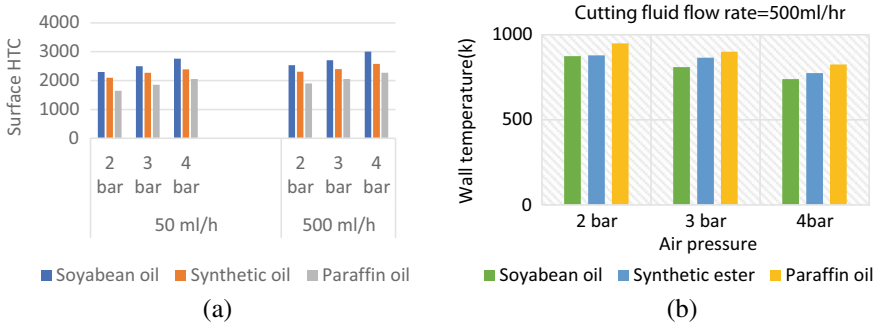

Fig. 4 **a** Surface HTC at 500 ml/h flow rate of VO, SO and MO at different air pressures, **b** wall temperature at 500 ml/h flow rate of VO, SO and MO at different air pressures

4.2 Cooling Performance of Different Cutting Fluids

Comparison of surface HTC and wall temperature

Variation of surface heat transfer coefficient (HTC) and wall temperature at different air pressures and 500 ml/h flow rate for VO, SO and MO is shown in Fig. 4a, b, respectively. Surface HTC increased with increase in air pressure. This is because high air pressure results in high atomization resulting in large number of smaller diameter droplets that reach the cutting region easily and accelerate cooling by carrying away heat. An improvement of about 16.27% over SO and 32.16% over MO is obtained with VO in surface HTC. This results in better cooling with VO. Cooling performance of VO turns out to be best due to its low viscosity. The high viscosity decreases the Brownian movement that limits the heat exchange capacity of oils. Also, the high viscosity results in lower thermal conductivity. As boiling point and viscosity index of VO are higher (than SO and MO), so it can remove large amount of heat effectively. Increase in surface HTC with increase in pressure of air and flow rate of cutting oils decreased the wall temperature. VO have highest surface HTC and thus lowest wall temperature. Also, the high flash point and high molecular weight reduced loss of VO through evaporation and improved heat carrying capability of VO, therefore leading to lower wall temperature.

5 Conclusion

It is concluded from the above simulation studies that with increase in air pressure and mass flow rate of cutting fluid, droplet diameter decreased, whereas droplet velocity and number of droplets increased for same. Spray characteristics of VO favor better machining performance. VO results in medium-sized droplet, high velocity and large number of droplets in comparison with SO and MO and thus proved to be a better

cutting fluid. VO provided highest value for surface HTC and lowest value for wall temperature.

References

1. Pradhan, S., Singh, S., Prakash, C., Królczyk, G., Pramanik, A., & Pruncu, C. I. (2019). Investigation of machining characteristics of hard-to-machine Ti-6Al-4V-ELI alloy for biomedical applications. *Journal of Materials Research and Technology*, *8*(5), 4849–4862.
2. Rapeti, P., Pasam, V. K., Rao Gurram, K. M., & Revuru, R. S. (2016). Performance evaluation of vegetable oil based nano cutting fluids in machining using grey relational analysis—A step towards sustainable manufacturing. *Journal of Cleaner Production, 172,* 2862–2875.
3. Kumar, P., Jafri, S. A. H., Bharti, P. K., & Siddiqui, A. (2014). Study of hazards related to cutting fluids and their remedies. *International Journal of Engineering Research & Technology (IJERT), 3*(7).
4. Adler, D. P., Hii, W. S., Michalek, D. J., & Sutherland, J. W. (2006). Examining the role of cutting fluids in machining and efforts to address associated environmental/health concerns. *Machining Science and Technology, 10*(1), 23–58.
5. Gupta, M. K., Pruncu, C. L., Mia, M., Singh, G., Singh, S., Prakash, C., et al. (2018). Machinability investigations of Inconel-800 super alloy under sustainable cooling conditions. *Materials, 11*(11), 2088.
6. Krolczyk, G. M., Maruda, R. W., Krolczyk, J. B., Wojciechowski, S., Mia, M., Nieslony, P., & Budzik, G. (2019). Ecological trends in machining as a key factor in sustainable production—a review. *Journal of Cleaner Production*, *218*, 601–615.
7. Tawakoli, T., Hadad, M. J., Sadeghi, M. H., Daneshi, A., Stöckert, S., & Rasifard, A. (2009). An experimental investigation of the effects of workpiece and grinding parameters on minimum quantity lubrication-MQL grinding. *International Journal of Machine Tools and Manufacture, 49*(12–13), 924–932.
8. Agrawal, S. M., & Patil, N. G. (2018). Experimental study of non edible vegetable oil as a cutting fluid in machining of M2 steel using MQL. *Procedia Manufacturing, 20,* 207–212.
9. Wang, Y., Li, C., Zhang, Y., Yang, M., Li, B., & Jia, D. (2016). Experimental evaluation of the lubrication properties of the wheel/workpiece interface in minimum quantity lubrication (MQL) grinding using different types of vegetable oils. *Journal of Cleaner Production, 127,* 487–499.
10. Singh, G. (2013). Experimental investigations of vegetable & mineral oil performance during machining of en-31 steel with minimum quantity lubrication. *International Journal of Research in Engineering and Technology, 02*(06), 1030–1037.
11. Habeeb, L., Saleh, F., & Maajel, B. (2019). CFD modeling of laminar flow and heat transfer utilizing Al_2O_3/water nanofluid in a finned-tube with twisted tape. *FME Transactions, 47*(1), 89–100.
12. Pradhan, S., Maity, K., Singh, S., & Prakash, C. (2019). Micro-machining Performance Assessment of Ti-Based Biomedical Alloy: A Finite Element Case Study. In *Biomanufacturing* (pp. 157–183). Cham: Springer.
13. Kim, S. H., Lee, S. W., Han, S., & Kim, S. M. (2019). Numerical investigation of thermal characteristics of spray cooling with minimum quantity lubrication in milling process. *Applied Mathematical Modelling, 65,* 137–147.
14. Thornburg, J., & Leith, D. (2000). Size distribution of mist generated during metal machining. *Applied Occupational and Environmental Hygiene, 15*(8), 618–628.
15. Verma, N., Manojkumar, K., & Ghosh, A. (2017). Characteristics of aerosol produced by an internal-mix nozzle and its influence on force, residual stress and surface finish in SQCL grinding. *Journal of Materials Processing Technology, 240,* 223–232.
16. Tu, J., Yeoh, G.-H., & Liu, C. (2018). Governing equations for CFD: Fundamentals (Vol. V).

17. Balan, A. S. S., Vijayaraghavan, L., & Krishnamurthy, R. (2013). Computational fluid dynamics analysis for predicting the droplet size in MQL during grinding of super-alloy (pp. 1–4).

To Study the Effect of Loading on Defect Signature by Using Statistical Parameters

Rajeev Kumar, Manpreet Singh, Jaiinder Preet Singh, Piyush Gulati, and Harpreet Singh

Abstract Loading can make defect to propagate abnormally in the bearing, and in such circumstances, bearing life estimation can become a difficult task. To deal with this, it is important to understand the effect of variable loading conditions on signature characteristics and later further analysis can be made in this field. In this work, effect of variable loading was studied on vibration signature characteristics originated from defect by carrying out the statistical analysis. Two different sizes of axial groove defects present on the outer race of taper roller bearing were used for the purpose of the study with three different loading conditions in the form of additional mass on the shaft. The trend of different statistical parameters was plotted and investigated for different loading conditions. The analysis reveals that only standard deviation and Shannon entropy (SE) were showing downward trend with an increase in loading. Torsional damping of the shaft increases with an increase in weight (load) on the shaft and that may be the cause of trend shown by standard deviation and SE. To comprehend this relation, statistical analysis was also carried out on theoretically constructed signals with three different damping characteristics and on single burst with having different loading conditions. In both the analysis, same trend was observed for the parameter's standard deviation and SE, which signifies that loading and damping are having commensurate relation. Simple sensitivity index (SSI) was calculated from the responded parameters to find the most sensitive parameter to the loading and the results revealed that SE supersedes standard deviation in dealing with loading conditions.

Keywords Shannon entropy · Standard deviation · Loading · Defect size · Simple sensitivity index

R. Kumar · M. Singh (✉) · J. P. Singh · P. Gulati
Department of Mechanical Engineering, Lovely Professional University, Phagwara, India
e-mail: bainscoolbains@yahoo.com

R. Kumar
Inder Kumar Gujral Punjab Technical University, Kapurthala, India

H. Singh
Department of Planning and Quality, Nettbuss AS, Oslo, Norway

© Springer Nature Singapore Pte Ltd. 2021

C. Prakash et al. (eds.), *Advances in Metrology and Measurement of Engineering Surfaces* , Lecture Notes in Mechanical Engineering,
https://doi.org/10.1007/978-981-15-5151-2_20

1 Introduction

The bearing is one of the major causes of failure in rotating machinery, so special attention is paid by the researchers on bearing in the past two decades [1–3]. Different types of non-destructive techniques are available to detect the bearing defects such as ultrasonic testing, wear analysis, thermal analysis, and vibration signal analysis, which are patronage in designing the maintenance strategies. Vibration signal-based techniques are having high reactivity to incipient fault and non-invasive nature, that is why they are developing at a higher pace over other techniques [4]. Abundance of literature is available based on time–frequency-based signal processing techniques to extract the information of defects and to measure its size. Bains and Kumar [2] have extracted the information of missing ball location from the contaminated signal by using Daubechies-based fourth-order decomposition. He et al. [5] have used mathematical morphological filter based on frequency response analysis to remove the noise from the impulsive features to detect the defect of bearing effectively. Yan et al. [6] proposed an algorithm based on FFT of wavelet coefficient to detect the information of bearing faults. They have also contended the performance of the proposed technique by comparing it with the enveloping-based technique on CWT [6]. Zhu et al. [7] have proposed a hybrid method to detect the bearing faults efficiently. Firstly, faulty components are extracted from the vibration signal by null space pursuit and then S-transform is applied to represent magnitude-frequency and time–frequency contours [7]. Kumar and Singh [3] have proposed Symlet wavelet-based decomposition to measure the axial groove defect size on the outer race of bearing. In this work, the signal was not refined at the entry point of the roller into the defect, but they have reduced the ambiguity by the proposed technique. They have also observed that with an increase in load on the shaft, the accuracy in measurement was better [3]. Singh et al. [8] have successfully measured the axial groove defect size of the inner race of bearing by using Symlet wavelet-based decomposition. The major challenge they have faced in their work is because of non-stationary nature of the defect. They have overcome this problem by selecting the suitable burst on the bases of frequency matching and amplitude [8]. Sawalhi et al. [9] have proposed autoregressive inverse filtration combined with autocorrelation function to estimate the spall size in the bearing. To deal with the weak response of the rolling element entry into the defect pre-processing algorithm using autoregressive inverse filtration is used. Despite the high capability of these techniques in identifying and measuring the local defect, these techniques were not attempted to study the effect variable loading conditions. The major remonstrance with these techniques is their incapability to deal with the non-localized characteristics. Some authors have used statistical parameters to study the effect of non-localized characteristics such as the effectiveness of the equipment and to present the overall health of the rotating element [9]. Aye [10] investigated the sensitivity of contact-type accelerometer and non-contact-type laser vibrometer by the use of statistical parameters. He found that in the case of defect, laser vibrometer signal has given significantly higher statistical values than the accelerometer signal, thus making laser vibrometer more suitable to defect faults [10]. Almeida and

Almeida [11] carried out statistical analysis on two different levels of spread defects at different speeds. They also found that for the spread defects crest factor and kurtosis have not significantly changed because for such defects signal becomes more random and hence shows less variation with these parameters [11]. Dolenc et al. [12] carried out statistical analysis of the bearing fault for both simulated and experimental signals. They concluded that in comparison to other conventional parameters, the Jensen Renyi divergence shows monotonic behavior once the fault occurs [12].

Loading has a great influence on bearing life [13, 14] and on defect propagation. In the current work, effect of loading on defect signature was studied by using different statistical parameters. Complete analysis based on most commonly used statistical parameters along with Shannon entropy was presented for two different sizes of defect widths on the outer race of taper roller bearing and for three different loading conditions. The trend for all the parameters was observed with increase in loading, and in support of this trend, mathematical model analysis and single burst analysis were presented with valid arguments.

2 Theoretical Background

2.1 Statistical Parameters

Various statistical parameters such as root mean square "RMS" (measures the power contents), standard deviation "σ" (measures the dispersion of data from its mean value) [15], skewness (measure of lack of symmetry), kurtosis (measure of impulsiveness), and Shannon entropy "SE" were calculated for recorded vibration signal. All these values are expected to increase in the case of roughness on the surface of the defect [16].

SE in general measures the randomness by using logarithmic scale, which yields a higher value for even small irregularity on the surface. This parameter has a vast use in many fields [17–19] and many more to study defect characteristics. Mathematically for a random signal X with N outcomes $X_0, X_1, X_2, \ldots, X_{N-1}$ $x_0, x_1, x_2, \ldots, x_{N-1}$ and r_i as incident rate can be expressed by Eq. (1) [18]:

$$S(X) = \log_2 N - \frac{1}{N} \sum_{i=0}^{N-1} r_\mathrm{i} \log_2 r_\mathrm{i} \tag{1}$$

2.2 Fast Fourier Transform (FFT)

Fast Fourier transform (FFT) converts a time-domain signal into frequency components by breaking the signal into sinusoidal components [20]. The basic equation of FFT for a continuous-time signal $x(t)$ is given by Eq. (2):

$$X(f) = \int_{-\infty}^{+\infty} x(t) \cdot \mathrm{e}^{-i2\pi f t} \mathrm{d}t \tag{2}$$

here, $X(f)$ is Fourier transform and f represents global frequency and t denotes the time. The signal can then be analyzed for the strong frequency content present in the signal, which is not easy to be detected from the raw signal.

3 Experimental Setup

Customized bearing test rig was used to carry out the experimentation. The main shaft of the bearing was driven by an AC current motor of 0.75 kW capacity. A set of two taper roller bearings (Make: NBC, Model: 30205) were used to support the rotating shaft as shown in Fig. 1. One end of the shaft was attached with stepper pulley which is capable of rotating the shaft at speeds of 2050 rpm approximately and at the other end of shaft provision of loading is provided.

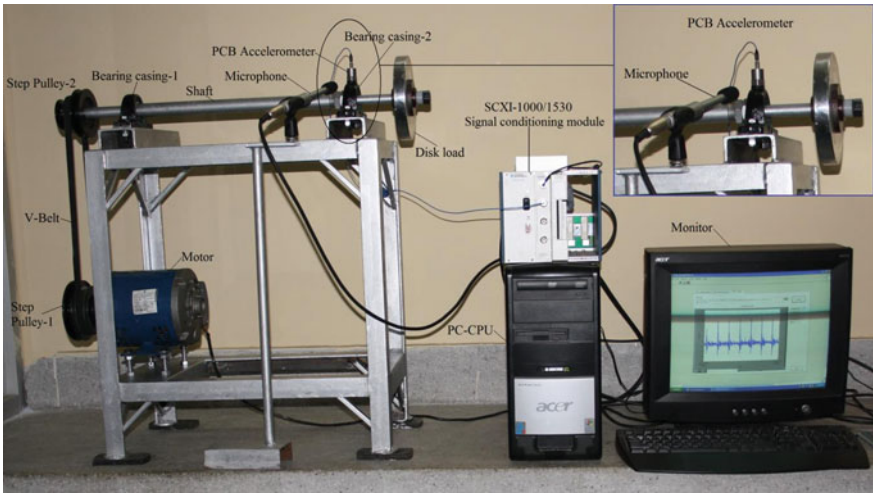

Fig. 1 Bearing test rig. Inset shows the enlarged view of accelerometer at the bearing casing 2

Optical tachometer was used to measure the speed of the shaft during each experiment. Provision of replacing healthy and faulty bearing was provided in the bearing casing 2. An uniaxial accelerometer was placed on the top of bearing casing 2 to acquire vertical acceleration. A PC-based data acquisition system was used to acquire and record vibration data from the bearing casing 2. The recorded signal later processed in the MATLAB environment.

In the present study, two different sizes of axial groove defects present on the outer race of taper roller bearing were selected for the purpose of analysis. The defects were introduced through laser engraving technique and measured for their width as 0.5776 mm (defect 1) and 1.7266 mm (defect 2) through image examination. The enlarged views of these defects are shown in Figs. 2 and 3.

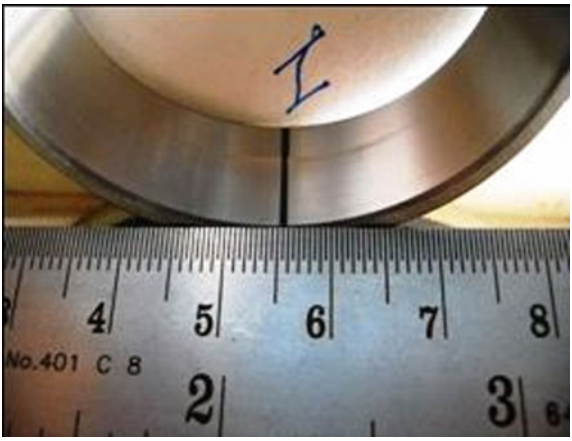

Fig. 2 Taper roller outer race defect of width 0.5776 mm

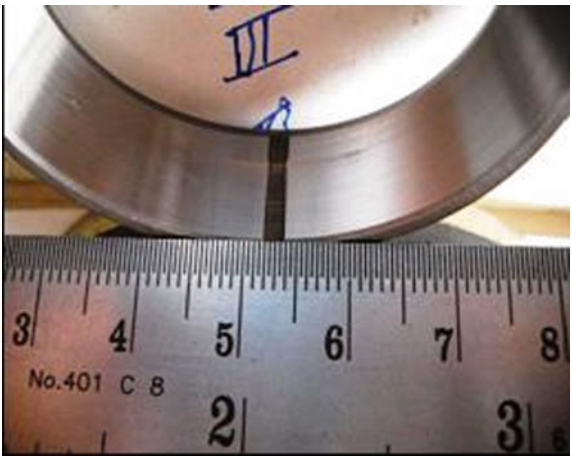

Fig. 3 Taper roller outer race defect of width 1.7266 mm

4 Result and Discussion

The analysis was carried out on the vibration signal for the aforementioned defect widths at 2050 RPM with three different lading conditions (without load, 2 kg load and 4 kg load). A typical raw signal for defect 1 at 2050 rpm and having 2 kg load is shown in Fig. 4. FFT for the same signal was drawn and shown in Fig. 5, where harmonics of 243 Hz frequency indicates the presence of outer race defect for the following specifications [21].

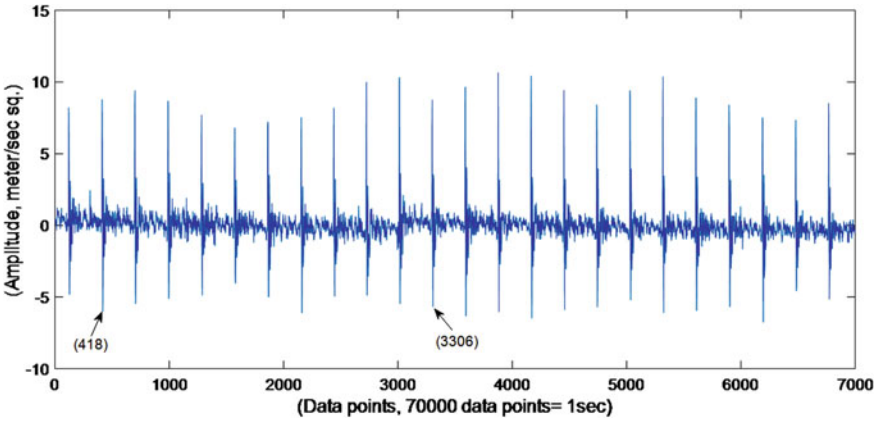

Fig. 4 Raw vibration signal for outer race defect width of 0.5776 mm at 2050 rpm shaft speed and 2 kg external load

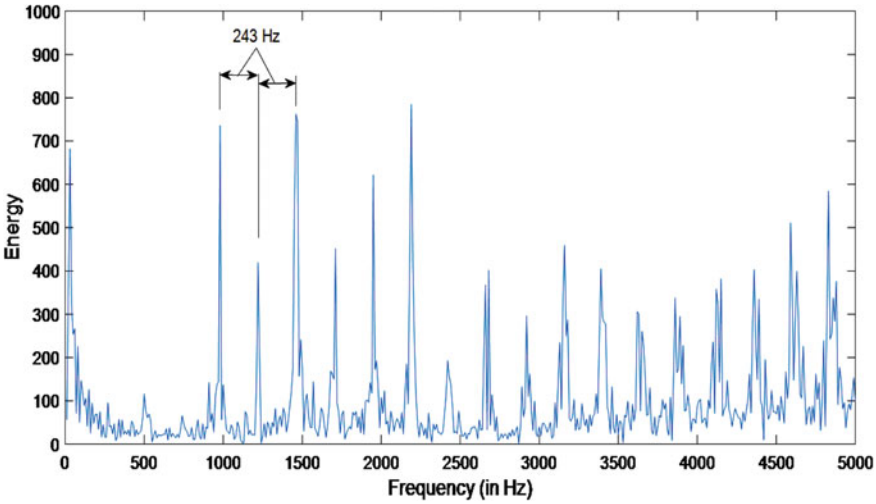

Fig. 5 FFT of raw acoustic signal shown in Fig. 4

Average pitch circle diameter = 38.30 mm
Average roller diameter = 6.05 mm
Number of rollers = 17
Pressure angle = 00
Inner race speed = 2050 RPM.

In the cases of other defects at different loading conditions, similar trend for the raw signal and FFT graphs was observed.

The parameters used prominently in the field of condition monitoring such as RMS, σ, skewness, kurtosis, and SE were used for analyzing the signals of healthy and defective bearings at different loading conditions. Different plots for RMS, σ, skewness, kurtosis, and SE for all the cases are shown in Fig. 6. To maintain the uniformity among parameters, all the negative skewness values were taken as positive while drawing the plots. This is because only higher numerical value of skewness

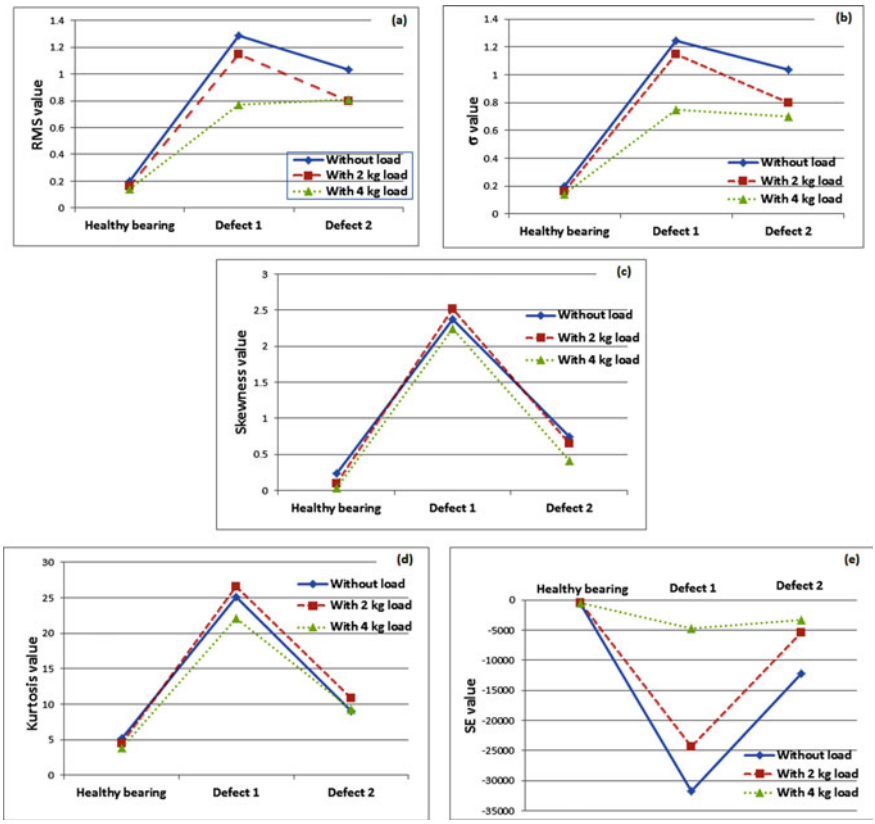

Fig. 6 Different statistical parameters plotted for healthy bearing, bearing having defect 1, and bearing having defect 2 at different loading conditions for raw vibration signal. **a** RMS, **b** σ, **c** skewness, **d** kurtosis and **e** SE

is having the significance as the negative value for skewness only indicates that data is skewed to the left of the normal distribution curve. It can be observed that all the values responded significantly for the case of defective bearing compared with the healthy bearing. To check the effectiveness of responded parameters to the defect, percentage increase in value for the defective case compared healthy case is calculated and presented in Table 1 along with average percentage increase for all the loading conditions.

In the case of SE, average % increase is coming out to be maximum as 3634.2 for defect 1 whereas kurtosis has minimum as 119 for defect 2. In overall scenario, SE shows maximum variation for the signal having impulsive response due to defect characteristics.

In further extension of the analysis, it can be observed that with an increase in loading, only σ and SE have shown a downward trend for all the cases. The response of σ and SE with respect to loading for all the cases is plotted and shown in Fig. 7.

In terms of vibration analysis, with an increase in load of the rotating shaft isolation to the impulse vibration response increases which in equivalent system can be said as higher torsional damping to the defect signature [22]. The higher damping may try to stabilize the impulses generated from local defect in a quick succession that may have resulted in reducing the randomness of the signal. This may be the reason for the downward trend shown by σ (deviation from mean value) and SE (randomness) with increase in loading. To check the authenticity of the above argument, three different signals were generated in the MATLAB environment for damping factors 0.010, 0.015, and 0.020 with same initial amplitude as 10 units by using Eq. (3):

$$x(t) = \frac{X_0}{\sqrt{1-\xi^2}} \mathrm{e}^{-\xi\omega_n t} \sin\left(\sqrt{1-\xi^2}\omega_n t + \pi/2\right) \tag{3}$$

Here, $x(t)$ represents signal, X_0 as initial amplitude, ξ as damping factor, and ω_n as natural frequency. These three signals for damping factor 0.010, 0.015, and 0.020 are shown in Fig. 8.

The responded parameters (σ and SE) to the loading were calculated for three simulated signals having different damping characteristics and shown in Table 2. In the theoretical signal analysis, σ and SE were showing a similar trend as the value of both of these parameters increases with an increase in damping as in the case of experimental signal analysis. In further support to this, statistical parameters were calculated for a single burst originated from defect for different local defects. These bursts were originated when rolling element strikes with the defect and these are the major contributors to the high increment in the statistical parameters.

This analysis was providing the practical insight for the effect of loading on the signal burst characteristics. To avoid the amplitude ambiguity, almost same range bursts were selected for a particular defect at different loading conditions. Starting point of the single burst was selected just before the signature originates from roller entry into the defect and till the defect signature completely stabilizes. One typical single burst enlarged from vibration signal for defect width 0.5776 mm and 2 kg external loading is shown in Fig. 9. In the case of defect width 0.5776 mm, 100 data

Table 1 Effectiveness ratio (ER) measured for different responded statistical parameters in the case of defect 1 and defect 2 by the use of raw vibration signal at different loading conditions along with the averages for particular cases

Case	Defect 1			Defect 2		
Loading	Without load	With 2 kg load	With 4 kg load	Without load	With 2 kg load	With 4 kg load
% increase in RMS	548.9	625.3	437.5	422.4	401.7	463.4
Avg. value of % increase for RMS at particular defect	537.2			429.1		
% increase in σ	592.5	626.2	423.7	423.1	402.3	388.6
Avg. value of % increase for σ at particular defect	547.4			404.6		
% increase in skewness	920.9	2502	5573.9	220.7	565.3	953
Avg. value of % increase for skewness at particular defect	29,998.9			579.6		
% increase in kurtosis	385.5	491.9	468.8	75.3	141.7	140.2
Avg. value of % increase for kurtosis at particular defect	448.7			119		
% increase in SE	4965.9	4933.8	1003	1852.7	1010.4	651.4
Avg. value of % increase for SE at particular defect	3634.2			1171.5		

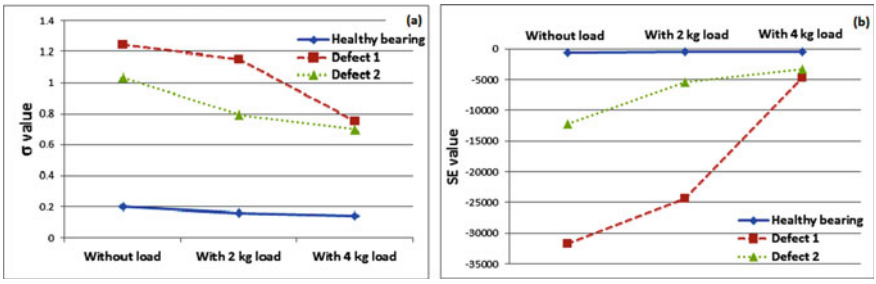

Fig. 7 Response of **a** σ, **b** SE to different loading conditions for the cases of healthy bearing, bearing having defect 1, and bearing having defect 2

points were considered and for defect width 1.7266 mm, 150 data points. The criteria for considering the number of data point were on the basis of burst stabilization.

The different statistical parameters were calculated and presented in Table 3 along with the range for the single burst at different loading conditions. In the case of single burst analysis, RMS, σ, and SE have shown the downward trend with an increase in load.

Finally, simple sensitivity index (SSI) [(valuemax − valuemin)/valuemax)] was calculated to check the sensitivity level of different parameters that have shown trend to the variable loading/damping. Parnell has proposed that SSI is equally good in calculating the sensitivity with the complex methods for a parameter toward the variation as a higher value of SSI yields better sensitivity [23]. The SSI for different parameters showing the downward trend with an increase in loading/damping has been calculated for full-length signal, theoretically constructed signal and single burst for a particular case and presented in Tables 4, 5, and 6, respectively. It can be observed from the tables that SE is more sensitive to the variable loading than any other responded parameters.

5 Conclusion

The statistical analysis holds good promise in the detection of outer race defect in taper roller bearing and to study the effect of variable loading conditions. In all the statistical parameters, Shannon entropy has shown maximum variation among all the statistical parameters measured in terms of percentage increase in value for both cases of defect in comparison to the healthy case. A downward trend was observed for standard deviation and Shannon entropy with an increase in loading for healthy and defective bearing when analysis was carried out with vibration signal. The main reason for this was derived from the mathematical model analysis which gives clear indication that with an increase in damping/isolation, a similar trend among parameters was observed as damping/isolation is undeviating related to loading. Single burst analysis reveals that after characteristics of impulse generated by defect

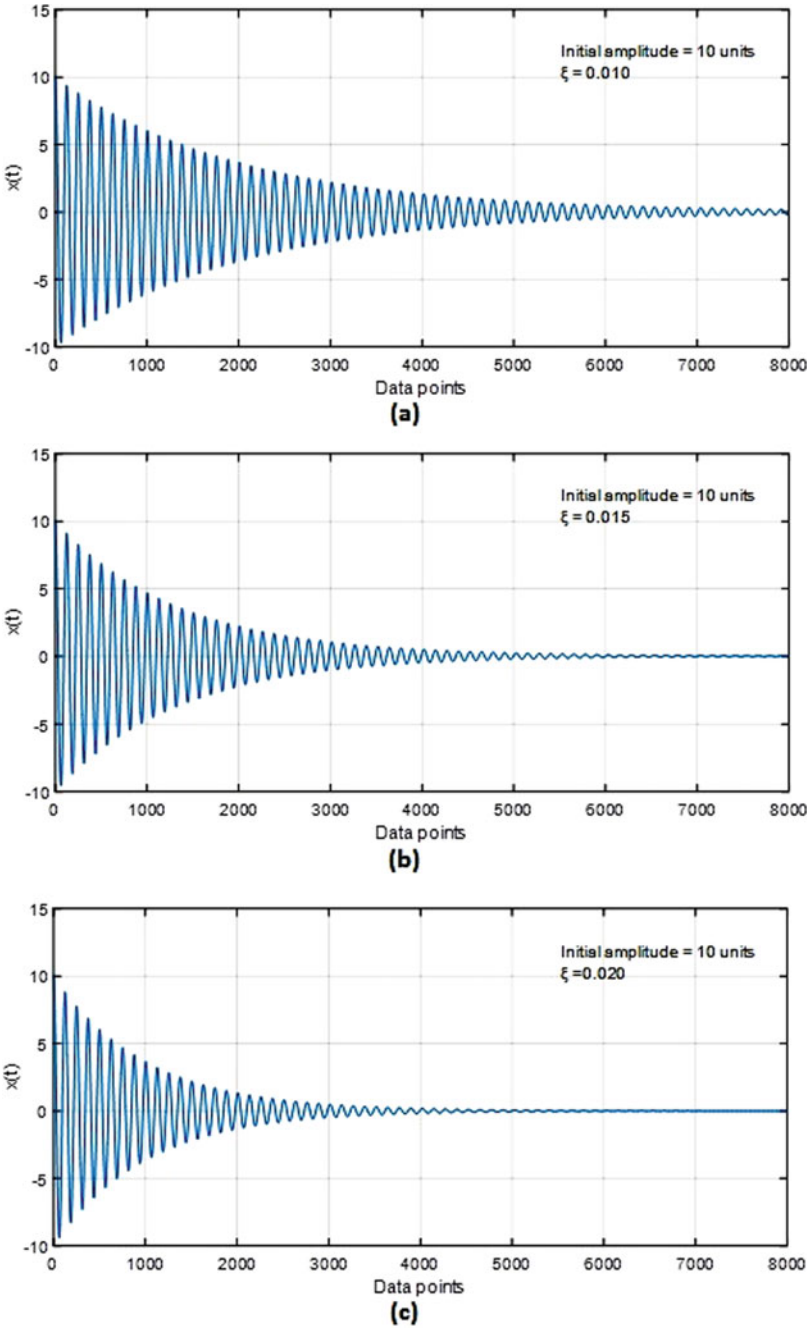

Fig. 8 Simulated signal with initial amplitude 10 units and damping factor **a** $\xi = 0.010$, **b** $\xi = 0.015$, **c** $\xi = 0.020$

Table 2 Responded parameters (σ and SE) calculated for theoretically constructed signals having different damping factor

Damping factor	σ	SE
$\xi = 0.010$	2.5011	−161,300
$\xi = 0.015$	2.0432	−107,600
$\xi = 0.020$	1.7702	−80,803

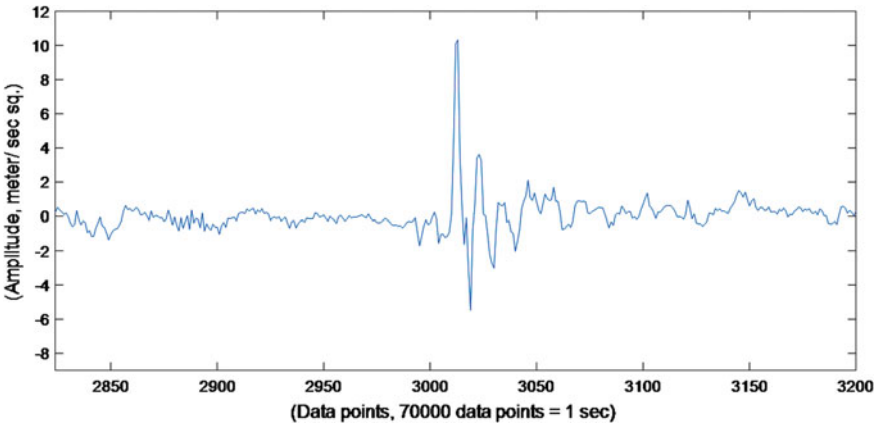

Fig. 9 A typical single burst enlarged from the original vibration signal shown in Fig. 4

Table 3 Statistical parameters measured from the single burst of raw vibration signal for the case of bearing having defect 1 and bearing having defect 2 at different loading conditions

Defect type	Loading	Range	RMS	σ	Skewness	Kurtosis	SE
Defect 1	Without load	15.3672	2.3178	2.3181	1.3110	8.6646	−1764.0
	With 2 kg load	15.6763	1.8770	1.8811	2.3755	15.5057	−1191.7
	With 4 kg load	15.6195	1.5044	1.4882	1.9492	11.5936	−532.9
Defect 2	Without load	8.031	1.8000	1.8060	0.4224	4.4047	−1087.9
	With 2 kg load	8.3851	1.2896	1.2939	0.2657	6.1705	−451.5
	With 4 kg load	8.6030	1.2377	1.1955	0.4536	6.1169	−374.3

were greatly influenced by an increase in loading as the values of root mean square, standard deviation, and Shannon entropy have decreased significantly. The simple sensitivity index was also calculated for parameters that have shown trend with an increase in loading for full-length signal and single burst, and in both the cases,

Table 4 Simple sensitivity index (SSI) measured for the different cases, where parameters have shown trend under variable loading for full-length signal

Case	SSI for σ	SSI for SE
Healthy bearing	0.2768	0.3115
Defect 1	0.3983	0.8500
Defect 2	0.3245	0.7351

Table 5 Simple sensitivity index (SSI) measured for σ and SE for theoretically constructed signal under different damping factors

Case	SSI for σ	SSI for SE
Theoretically constructed signal having different damping factors	0.2922	0.4990

Table 6 Simple sensitivity index (SSI) measured for the different cases, where parameters have shown trend under variable loading for single burst

Case	SSI for RMS	SSI for σ	SSI for SE
Defect 1	0.3509	0.3580	0.6984
Defect 2	0.3123	0.3380	0.6559

Shannon entropy has been found nearly double sensitive than other parameters for different cases of defect and hence recommended for dealing with loading conditions.

References

1. Hasib, A., Shlomi, K., Uri, B., Renata, K., & Moshe, T. (2019). Bearing fault detection and fault size estimation using fiber-optic sensor. *Mechanical System and Signal Processing, 120*(1), 392–407.
2. Bains, M., & Kumar, R. (2009). Detection of missing ball in bearing using decomposition of acoustic signal. *Asian Journal of Chemistry, 21*(10), 143–147.
3. Kumar, R., & Singh, M. (2013). Outer race defect width measurement in taper roller bearing using discrete wavelet transform of vibration signal. *Measurement, 46*(1), 537–545.
4. Gillich, G. R., Mituletu, I. C., Praisach, Z. I., Negru, I., & Tufoi, M. (2017). Method to enhance the frequency readability for detecting incipient structural damage. *Iranian Journal of Science and Technology, Transactions of Mechanical Engineering, 41*(3), 233–242.
5. He, Q., Li, P., & Kong, F. (2009). Rolling bearing localized defect evaluation by multiscale signature via empirical mode decomposition. *Journal of Vibration and Acoustics, 134*(6), 061013.
6. Yan, R., Gao, R. X., & Wang, C. (2009). Experimental evaluation of a unified time-scale-frequency technique for bearing defect feature extraction. *Journal of Vibration and Acoustics, 131*(4), 041012.
7. Zhu, D., Gao, Q., Sun, D., Lu, Y., & Peng, S. (2014). A detection method for bearing faults using null space pursuit and S transform. *Signal Processing*, *96*, 80–89.

8. Singh, M., Yadav, R. K., & Kumar, R. (2013). Discrete wavelet transform based measurement of inner race defect width in taper roller bearing. *MAPAN-Journal Metrology Society of India, 28*(1), 17–23.
9. Sawalhi, N., Wang, W., & Becker, A. (2017). Vibration signal processing for spall size estimation in rolling element bearings using autoregressive inverse filtration combined with bearing signal synchronous averaging. *Advances in Mechanical Engineering, 9*(5), 1–20.
10. Aye, S. A. (2011). Statistical approach for tapered bearing fault detection using different methods. In *Proceedings of the World Congress on Engineering* (Vol. III, pp. 2112–2115), July 6–8, London, U.K.
11. Almeida, F. R. V., & Almeida, M. T. (2005). Statistical analysis of vibration signals for condition monitoring of defects in rolling element bearings. In *Proceedings of the COBEM 2005: 18th International Congress of Mechanical Engineering* (pp. 678–685), November 6–11, Quro Preto, MG.
12. Dolenc, B., Boskoski, P., & Juricic, D. (2015). Change detection based on entropy indices with application to bearing faults. *IFAC-PapersOnLine, 48–21,* 1438–1443.
13. Jacobs, W., Boonen, R., Sas, P., & Moens, D. (2014). The effect of external dynamic loads on the lifetime of rolling element bearings: SEM analysis of raceway surface wear. In *International Conference on Noise and Vibration Engineering* (*ISMA 2014*) (pp. 405–414), September 15–17, Leuven, Belgium.
14. Fang, B., Zhang, J., Yan, K., Hong, J., & Wang, M. Y. (2019). A comprehensive study on the speed-varying stiffness of ball bearing under different load conditions. *Mechanism and Machine Theory, 136*(1), 1–13.
15. Jena, D. P., Singh, M., & Kumar, R. (2012). Radial ball bearing inner race defect width measurement using analytical wavelet transform of acoustic and vibration signal. *Measurement Science Review, 12*(4), 141–148.
16. Cambow, R., Singh, M., Bagha, A. K., & Singh, H. (2018). To compare the effect of different level of self-lubrication for bearings using statistical analysis of vibration signal. *Materials Today: Proceedings, 5*((14) Part 2), 28364–28373.
17. Lin, T. K., & Liang, J. C. (2015). Application of multi-scale (cross-) sample entropy for structural health monitoring. *Smart Materials and Structures, 24*(8), 085003.
18. Cabal-Yepez, E., Romero-Troncoso, R. J., Garcia-Perez, A., Osornio-Rios, R. A., & Alvarez-Salas, R. (2011). Multiple fault detection through information entropy analysis in ASD-fed induction motors. In *Proceedings of the 8th IEEE Symposium on Diagnostics for Electrical Machines, Power Electronics & Drives* (pp. 391–396), September, Bologna, Italy.
19. Bafroui, H. H., & Ohadi, A. (2014). Application of wavelet energy and Shannon entropy for feature extraction in gearbox fault detection under varying speed conditions. *Neurocomputing, 133,* 437–445.
20. Stein, E., & Weiss, G. (1971). *Introduction to Fourier analysis on Euclidean spaces*. Princeton: Princeton University Press.
21. Taylor, J. I. (2003). *The vibration analysis handbook: A practical guide for solving rotating machinery problems* (2nd ed., pp. 167–173). Int Press Publication.
22. Theodossiades, S., Gnanakumarr, M., Rahnejat, H., & Kelly, P. (2006). Effect of a dual-mass flywheel on the impact-induced noise in vehicular powertrain systems. *Proceedings of the Institution of Mechanical Engineers, Part D: Journal of Automobile Engineering*, *220*(6), 747–761.
23. Parnell, D. J. (1997). Sensitivity analysis of normative economic models: Theoretical framework and practical strategies. *Agricultural Economics, 16*(2), 139–152.

Vibration Analysis of Carbon Fiber and Glass Fiber Composite Beam

Ajay Kumar Kaviti and Amit Kumar Thakur

Abstract Composite materials are widely considered nowadays for several kinds of structural applications. In the analysis of the beam, particularly for a composite using experimental or numerical method, it is quite challenging in comparison with the regular conventional materials. Hence, in the present work, carbon fiber and glass fiber beam are considered for vibration analysis of composite beam. In the numerical modeling, three aspect ratios (i.e., L/H) in the range of 100–150 are considered with multilevel orientations (i.e., $[0/0]_3$, $[45/90]_3$, $[90/0]_3$ $[0/0]_4$, $[45/90]_4$, $[90/0]_4$). Two boundary conditions (cantilever, simply supported) are considered for the beams. From the numerical analysis, it is observed that glass fiber composite beams have a higher natural frequency in comparison to carbon fiber composite beam.

Keywords Composite material · Carbon fiber · Glass fiber · Aspect ratio

1 Introduction

Mainly, beams are of two kinds taking into consideration of shear deformation, thickness, and length of the beam. Those are Euler–Bernoulli beam and Timoshenko beam. Both types of beams have been exhaustively used in different load conditions. Osama and Mahmoud [1] used the energy approach to evaluate the effect of orientation of fibers in predicting the natural frequency of laminated composite beams. Murat and Omar [2] used the Euler–Bernoulli beam theory to predict the natural frequency of laminated beam under free vibration condition. In addition, they have developed the numerical model to predict natural frequency of composites under various boundary conditions for different aspect ratios.

Mohammed [3] considered the carbon glass hybrid composite beam for evaluating the natural frequency under free vibration condition. Avcar [4] considered aluminum

A. K. Kaviti
Department of Mechanical Engineering, VNRVJIET, Hyderabad, India

A. K. Thakur (✉)
Department of Mechanical Engineering, Lovely Professional University, Phagwara, Punjab, India
e-mail: amit.25010@lpu.co.in

© Springer Nature Singapore Pte Ltd. 2021

C. Prakash et al. (eds.), *Advances in Metrology and Measurement of Engineering Surfaces* , Lecture Notes in Mechanical Engineering,
https://doi.org/10.1007/978-981-15-5151-2_21

beams for predicting the natural frequency under free vibration condition through analytical method. Different boundary conditions were considered to estimate its effect on natural frequency. These analytical results are further verified with numerical results attained from the commercial finite element analysis software ANSYS. They find the close agreement of analytical results with numerical results. Wang et al. [5] analyzed the functional graded materials under different boundary conditions. Power law is considered for variation of material properties along the length and thickness. Natural frequencies are measured under free vibration condition. Simsek et al. [6] used the functionally graded materials for simply supported beam under uniformly distributed load. In their work also, power law is considered for variation of material properties along the thickness. Pradhan and Chakraverty [7] used the classical beam theory (CBT) to examine the functionally graded material (FGM). They have considered the different boundary conditions to measure the natural frequency of beam under free vibration condition. They concluded that FSD results are more accurate in comparison to classical beam theory. Dawe [8] considered a Timoshenko beam for vibration analysis. Quadratic element is considered for analysis of the beam. Two degrees of freedom (lateral deflection and the cross-sectional rotation) are assigned at each node. Natural frequency of beam under varying boundary conditions studied using quintic polynomial function.

Huang et al. [9] used inversion vibration technique to solve the cutting tool problems as a model of forced vibration. Della and Shu [10] compared the analytical solution of free vibration and compared with experimental results with various boundary conditions. Callioglu and Atlihan [11] investigated the effect of ply angles and boundary conditions with the variation of length-to-thickness ratio. Hence, in the present work, carbon fiber and glass fiber beam are considered for vibration analysis of composite beam. In the numerical modeling, three aspect ratios (i.e., L/H) in the range of 100–150 are considered with multilevel orientations (i.e., $[0/0]_3$, $[45/90]_3$, $[90/0]_3$ $[0/0]_4$, $[45/90]_4$, $[90/0]_4$). Three boundary conditions (cantilever, simply supported) are considered for the beams. From the numerical analysis, it is observed that glass fiber composite beams have a higher natural frequency in comparison to carbon fiber composite beam.

2 Finite Element Modeling of Composite Beam Materials

A rectangular beam is first modeled in ANSYS part modeler as per the specific orientation and dimension as shown in Fig. 1. Material properties used in the simulation are shown in Tables 1 and 2. The above properties of the carbon and glass are used as input for the engineering materials module in ANSYS. The same beam is imported and opened in ANSYS modal analysis module where various problem conditions are set. The beam is meshed using tetrahedron mesh of element of size, not more than 0.1 mm was assigned as shown in Fig. 2. The properties regarding the layers and orientation are assigned in the same module under layered section option as shown in Fig. 3.

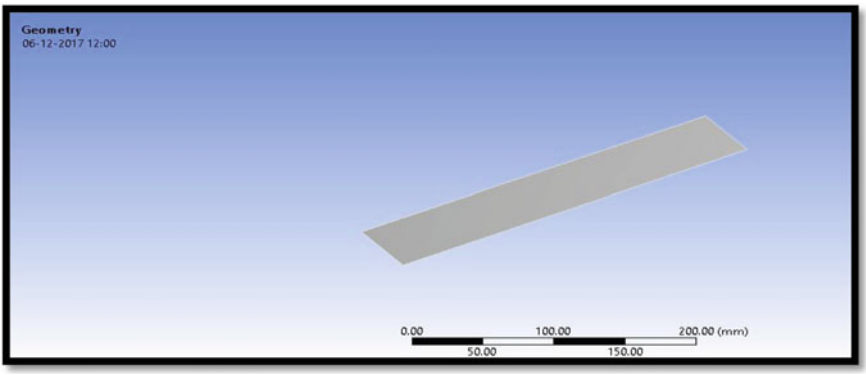

Fig. 1 Geometry creation of composite beam

Table 1 Properties of carbon fiber composite laminate

Density	2.1 gm/cc		
Young's modulus	$Ex = 100$ GPa	$Ey = 10$ GPa	$Ez = 10$ GPa
Poisson's ratio	$\mu xy = 0.286$	$\mu yz = 0.188$	$\mu zx = 0188$
Shear modulus	$Gxy = 4.89$ GPa	$Gyz = 4.3$ GPa	$Gzx = 4.3$ GPa

Table 2 Properties of glass fiber composite laminate

Density	2.54 gm/cc		
Young's modulus	$Ex = 53$ GPa	$Ey = 8$ GPa	$Ez = 8$ GPa
Poisson's ratio	$\mu xy = 0.23$	$\mu yz = 0.21$	$\mu zx = 0.21$
Shear modulus	$Gxy = 4.89$ GPa	$Gyz = 4.3$ GPa	$Gzx = 4.3$ GPa

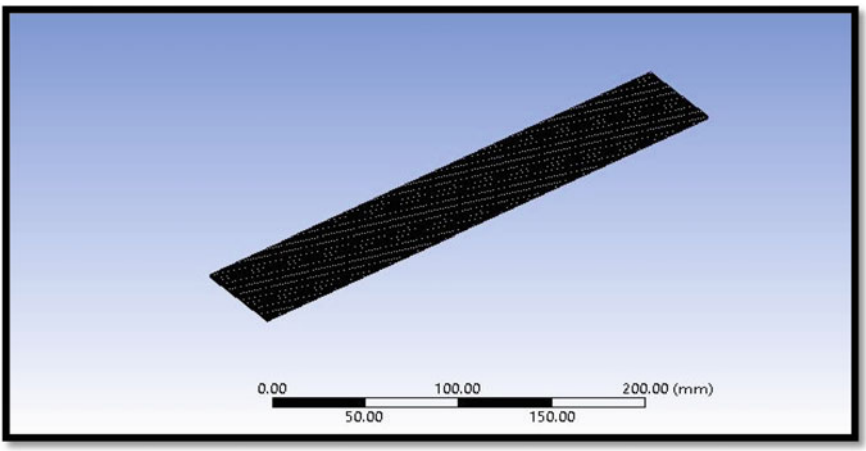

Fig. 2 Meshed composite beam

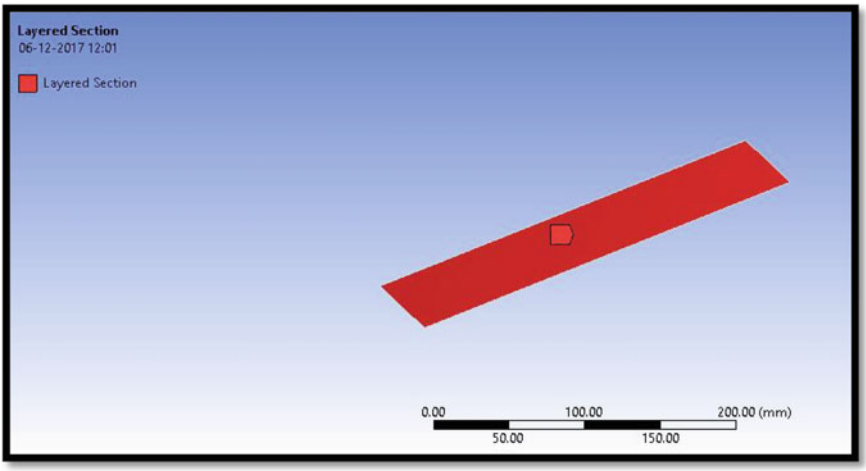

Fig. 3 Layer section of composite beam

3 Results and Discussion

3.1 Modal Analysis for Carbon Fiber with Respect to Length-to-Height Ratio

Figure 4 shows the relation between frequency and length-to-height ratio of the carbon fiber composite for various settings. Three orientation settings $[0/0]_3$, $[45/90]_3$, $[90/0]_3$ $[0/0]_4$, $[45/90]_4$, $[90/0]_4$ for simply supported beam and three orientation settings $[0/0]_3$, $[45/90]_3$, $[90/0]_3$ $[0/0]_4$, $[45/90]_4$, $[90/0]_4$ for cantilever beam are considered and are shown in the same graph. Here, for simply supported beam settings,

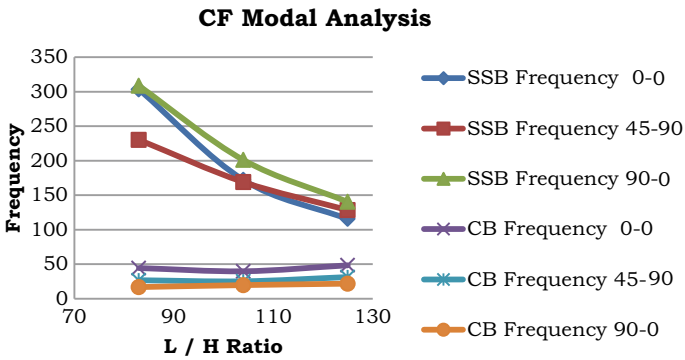

Fig. 4 Variation in frequency of carbon fiber cantilever beam and simply supported beam w.r.t. L/H ratio

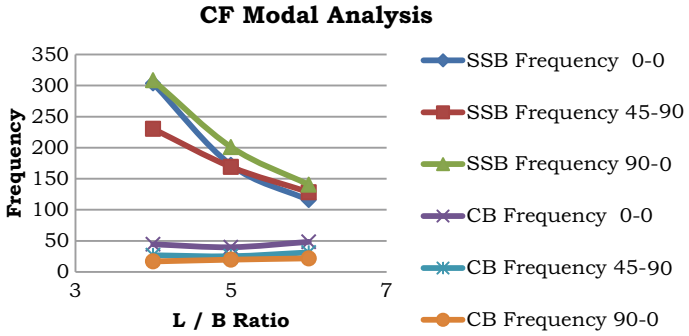

Fig. 5 Variation in frequency of carbon fiber cantilever beam and simply supported beam L/B ratio

the frequency seems to decrease as the L/H ratio increases, whereas for cantilever beam, the frequency is slightly increasing as L/H ratio increases.

3.2 Modal Analysis for Carbon Fiber with Respect to Length-to-Breadth Ratio

Figure 5 shows the relation between frequency and length-to-breadth ratio of the carbon fiber composite for various settings. Three orientation settings $[0/0]_3$, $[45/90]_3$, $[90/0]_3$ $[0/0]_4$, $[45/90]_4$, $[90/0]_4$ for simply supported beam and three orientation settings $[0/0]_3$, $[45/90]_3$, $[90/0]_3$ $[0/0]_4$, $[45/90]_4$, $[90/0]_4$ for cantilever beam are considered and are shown in the same graph. Here, for simply supported beam settings, the frequency seems to decrease as the L/B ratio increases, whereas for cantilever beam, the frequency is slightly increasing as L/B ratio increases.

3.3 Modal Analysis for Glass Fiber with Respect to Length-to-Height Ratio

Figure 6 shows the relation between frequency and length-to-height ratio of the glass fiber composite for various settings. Three orientation settings $[0/0]_3$, $[45/90]_3$, $[90/0]_3$ $[0/0]_4$, $[45/90]_4$, $[90/0]_4$ for simply supported beam and three orientation settings $[0/0]_3$, $[45/90]_3$, $[90/0]_3$ $[0/0]_4$, $[45/90]_4$, $[90/0]_4$ for cantilever beam are considered and are shown in the same graph. Here, for simply supported beam settings, the frequency seems to decrease as the L/H ratio increases. Also, for cantilever beam, frequency is slightly decreasing as L/H ratio increases.

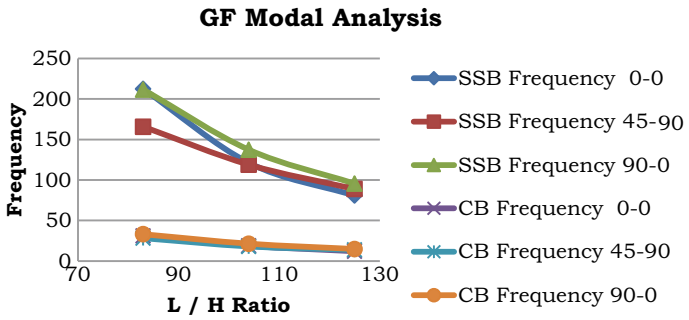

Fig. 6 Variation in frequency of glass fiber cantilever beam and simply supported beam L/H ratio

3.4 Modal Analysis for Glass Fiber with Respect to Length-to-Breadth Ratio

Figure 7 shows the relation between frequency and length-to-breadth ratio of the glass fiber composite for various settings. Three orientation settings $[0/0]_3$, $[45/90]_3$, $[90/0]_3$ $[0/0]_4$, $[45/90]_4$, $[90/0]_4$ for simply supported beam and three orientation settings $[0/0]_3$, $[45/90]_3$, $[90/0]_3$ $[0/0]_4$, $[45/90]_4$, $[90/0]_4$ for cantilever beam are considered and are shown in the same graph. Here, for simply supported beam settings, the frequency seems to decrease as the L/B ratio increases. Also, for cantilever beam, frequency is slightly decreasing as L/B ratio increases.

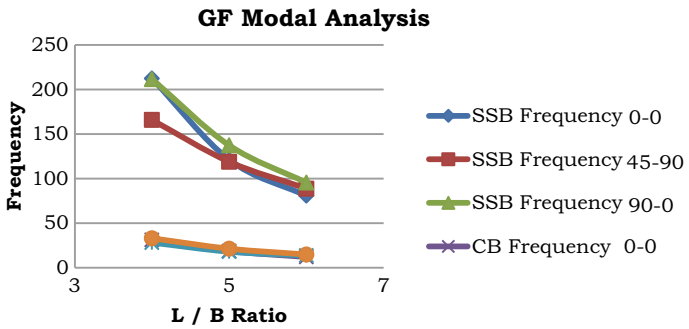

Fig. 7 Variation in frequency of glass fiber cantilever beam and simply supported beam L/B ratio

4 Conclusions

Modal analysis of carbon fiber and glass fiber composite beams with length-to-height ratio and length-to-breadth ratio is considered in this study under simply supported and cantilever boundary conditions. The following conclusions are drawn.

From the results, it is clear that aspect ratio (L/H ratio) is inversely proportional to frequency response of the material, i.e., as the ratio of length increases, the frequency of the beam decreases. This phenomenon is observed in both carbon fiber and glass fiber composite beams. Fibers with zero orientation observed with the highest frequency at lower aspect ratios and cross-orientation conditions have less frequency. In overall, glass fiber has a higher frequency than carbon fiber which indicates that stiffness material influences the frequency.

Acknowledgements Authors are thankful to VNR VignanaJyothi Institute of Engineering and Technology for providing the facilities to carry out the research work.

References

1. Osama, M., & Mahmoud, M. (2017). Vibration analysis of laminated beams. *International Journal of Engineering Research and Advanced Technology, 7,* 2454–6135.
2. Murat, B., & Omer, G. (2014). Free vibration analysis of a laminated composite beam with various boundary conditions. *International Journal of Automotive and Mechanical Engineering, 9,* 1734–1746.
3. Mohammed, A. M. (2013). Vibration analysis of hybrid laminated composite beam. *Al-Rafadain Engineering Journal, 21*, 1–13.
4. Avcar, M. (2014). Vibration of beams considering geometric, characteristics and boundary conditions. *International Journal of Mechanics and Applications, 4,* 94–100.
5. Wang, Z.-h., Wang, X.-h., Xu, G.-d., Cheng, S., & Zeng, T. (2016). Free vibration of two-directional functionally graded beams. *Composite Structures, 135*, 191–198.
6. Mesut, S. (2010). Non-linear analysis of a FG Timoshenko beam under action of a moving harmonic load. *Composite Structures, 92,* 102532–102546.
7. Pradhan, K. K., & Chakraverty, S. (2013). Free vibration of Euler and Timoshenko functionally graded beams by Rayleigh-Ritz method. *Composites Part B: Engineering, 51,* 51–59.
8. Dawe, D. J. (2014). A finite element for the vibration analysis of Timoshenko beams. *Journal of Sound and Vibration, 60*, 11–20.
9. Huang, C.-H., Shih, C.-C., & Kim, S. (2009). An inverse vibration in estimating the temporal-dependent external forces. *Applied Mathematical Modelling, 33,* 2683–2698.
10. Della, C. N., & Shu, D. (2005). Vibration of composite beams with over lapping delaminations. *European Journal of Mechanics-A/Solids, 24*(3), 491–503.
11. Callioglu, H., & Atlihan, G. (2011). Vibration analysis of delaminated composite beams. *Indian Journal of Engineering & Materials Sciences, 18,* 7–14.

Analysis of Transient Thermal Temperature Distribution Over Service Life of Taper Roller Bearing Using FEA

Rajeev Kumar, Manpreet Singh, Jujhar Singh, and Siddique Khan

Abstract Single row taper roller bearings are basically designed to withstand the radial load, axial load, and torque which results in generation of contact stresses. Generation of contact stresses will take place due to high speeds and heavy loads on bearing that can lead to failure of machine. Bearing life is limited by some of the common phenomena like wearing, smearing, flaking, etc. Bearing life can be enhanced by proper lubrication which separates roller with inner and outer rings. As prediction and validation of contact stresses experimentally is an arduous task, many researchers calculate theoretical method for approximate distribution of contact stresses on bearing race. Some of the methods are numerical method, finite element analysis (FEA) software, traditional method, and Hertz contact stress theory. In this paper, temperature behavior distribution in the bearing, contact stress, deformation of bearing rollers, and heat flux is analyzed by FEA tool. Inner race bearing surface and ball surface contact in bearings can cause an increase in temperature which may result in evaporation of lubricant due to improper heat dissipation and effect the service life of the bearing FEA results is compared with results obtained by Hertz theory to inspect the feasibility of bearing problem and its life. It is found that temperature distribution is 55 °C (maximum) at the inner ring, von Mises stress is 220.23 MPa, and heat flux is 0.61399 W/mm^2, whereas result obtained by Hertz theory is 195.2821 MPa. Compariosn of FEA and analytical result, the error is found to be 12.77% analysis of increase in temperature through FEA is a useful tool for estimating the service life of bearings.

Keywords Contact stresses · Heat flux · FEA

R. Kumar (✉) · M. Singh · S. Khan
Department of Mechanical Engineering, Lovely Professional University, Phagwara, India
e-mail: rajeev.14584@lpu.co.in

R. Kumar
Inder Kumar Gujral Punjab Technical University, Kapurthala, India

J. Singh
Department of Mechanical Engineering, Inder Kumar Gujral Punjab Technical University, Kapurthala, India

© Springer Nature Singapore Pte Ltd. 2021

C. Prakash et al. (eds.), *Advances in Metrology and Measurement of Engineering Surfaces* , Lecture Notes in Mechanical Engineering,
https://doi.org/10.1007/978-981-15-5151-2_22

1 Introduction

A bearing is a machine element to support another moving machine element which allows a relative motion between the contact surfaces during the operation and prevents wear and heat generation at the contact area or point which can be reduced by using the proper lubricant.

The rolling contact bearing is the most crucial component in any rotating machinery. They are supported load during rotary motion. According to surveys, bearing fault is one of the predominant causes for the failure of mechanical drives [1]. Therefore, detection and prognostic of the bearing are important. Taper roller bearings are designed to sustain the axial load and radial load. In this bearing, the rings and the rollers are at an angle (tapered) in the shape of cones to simultaneously support axial and radial loads. The taper roller bearing has the following component: inner ring, outer ring, and roller assembly. Lubrication is a process by which the friction and wear rate between the two moving components or elements can be reduced by using suitable lubricant which also helps in heat dissipation process [2]. Proper lubrication can prevent the corrosion and helps for long service life of bearing.

Desirable properties of lubricants used in the rolling element bearings are:

- Maintain a stable viscosity over a wide-ranging temperature.
- It should have high film strength, and it can support loads.
- The melting point of lubrication is high so that it protects two parts at a high temperature [3].
- It should be non-corrosive.
- It offers a layer against contaminant and moisture.

There are three types of lubrication liquid lubrication, semi-solid lubrication, and solid lubrication, and widely used two lubrications from the 1990s are oil and grease. As bearing contacts can get exploited after continues applications of loads on bearing which results in generation of highly localized pressures and stresses, it needs a good quality of lubrication to avoid contacts from stress concentration and results in improved service life of bearings [4]. Stress concentration can be caused by various reasons like surface roughness, particle denting, etc. and can lead to crack initiation [5] due to developed lubricant film at the dent or other related surfaces. Elasto-hydro-dynamic lubrication (EHL) film [6, 7] plays an important for improving service life of bearings because it is directly connected to lubrication factor which is further connected to micro-EHL pressures and stresses existing in an EHL contact produced by surface roughness and quality of lubrication. Wearing is occurred due to abrasive particles and vibration. It causes due to ineffective seals, improper lubricant, loose fit, and contamination by the foreign particle. Service life of bearing can be increased by using the proper amount of lubrication, maintaining workplace clean, and providing vibration absorb damping base. Smearing means when two deficiently lubricant surfaces slide against each other under load or by the contamination of debris between roller and rings, it causes roughening of surface which can be prevented by improving bearing clearance, sealing, and lubricant film

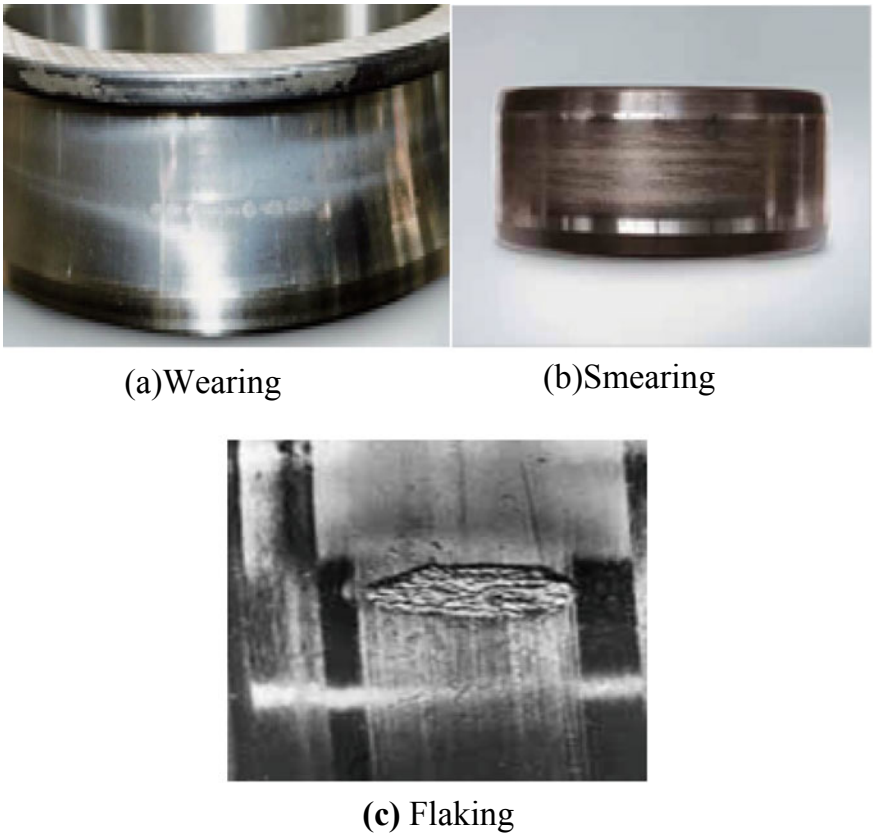

Fig. 1 Typical photograph of (NBC: 30205) defects in bearing [8]

ability. Flaking occurred because of shear stress [3] below the load capacity of the surface. After sometimes, stresses developed cracks which expand gradually up to the end of the surface. Rollers and balls are passing over these cracks, and material removed gradually from the surface are called flaking. Causes of flaking are poor lubrication [7], excessive load, and misalignment in the shaft (Fig. 1).

2 Methodology

Research methodology is the organized, theoretic concept of the approaches applied to a field of the study. It involves concept like a theoretical model, phases, and qualitative and quantitative methods. As an alternative, it gives the theoretical concept for the understanding which method is to be used. The flowchart of research methodology is shown in Fig. 2.

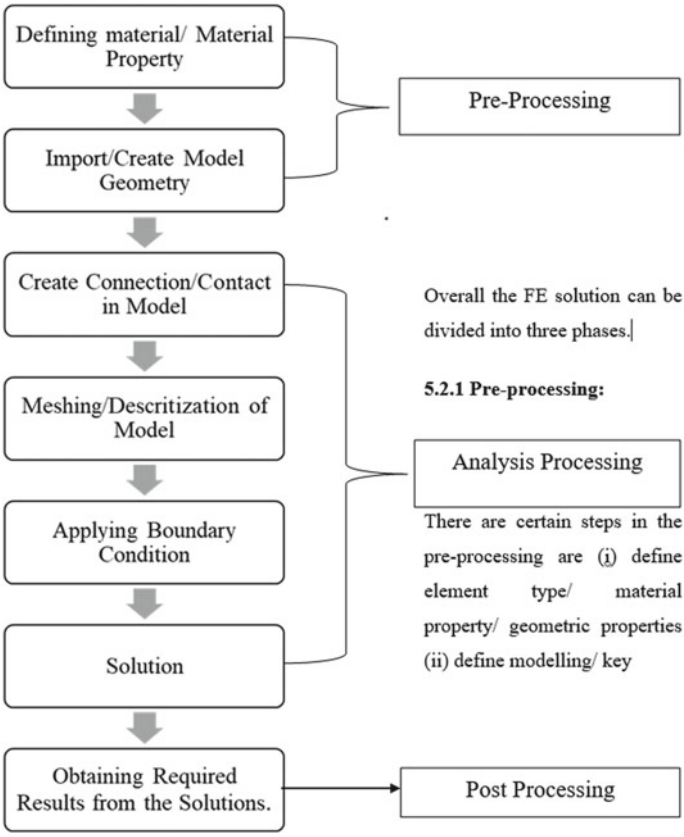

Fig. 2 Methodology flowchart

2.1 Geometry Definition

Geometry is the main part of any analysis. In geometry data, main focus is on the shape, size, and dimension. With a help of this data, we must create a 3D model. Existing dimensions of single row taper roller bearing 30205 are shown in Fig. 3.

2.2 Material Definition

Bearing model is made from the chromium steel AISI 52100. Meshing is defined as the process of discretization of whole components into small parts or elements so that we can uniformly distribute the load or any other loads [9, 10]. Meshing is one of the most critical features of engineering field. ANSYS provides many options for

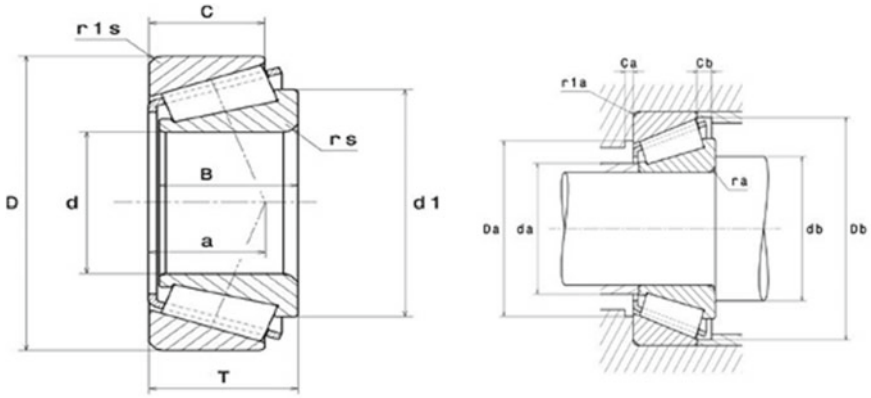

Fig. 3 Dimensions of bearing 30205

mesh generation according to shape and requirements of accuracy. Meshed model of taper roller bearing is shown in Fig. 4 (Tables 1 and 2).

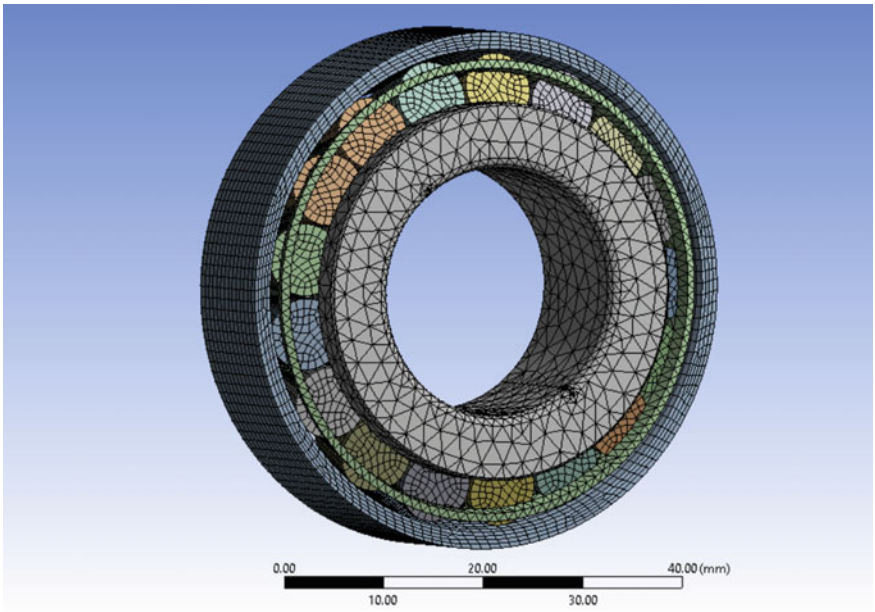

Fig. 4 Meshed roller bearing

Table 1 Chromium-steel physical properties of AISI 52100

Physical Properties	Metric	Imperial
Density	7.81 g/c	0.282 lb/in^3
Melting point	1424 °C	2595 °F
Modulus of elasticity	210 GPa	30,500 ksi
Bulk modulus	160 GPa	23,200 ksi
Poisson's ratio	0.30	0.30
Fracture toughness	15.4–18.7 MPa m½	14.0–17.0 ksi m½½
Shear modulus	80 GPa	11,600 ksi

Table 2 Chromium-steel thermal Properties of AISI 52100

Thermal Properties	Metric	Imperial
Specific heat capacity	0.475 J/g °C	0.114 BTU/lb °F
Thermal conductivity	46.6 W/m k	323 BTU in/h ft^2 °F
CTE, Liner	11.9 µm/m °C	6.61 µin/in °F

3 Result and Discussion

FEA solution includes the details of analysis setting; i.e., number of steps, initial time step, and maximum time steps are 20, 20, and 72000 s. After the analysis, results can be interpreted in many ways, results in temperature distribution, total heat flux, thermal error, and behavior for selected bearing material. From the Fig. 5, it can be

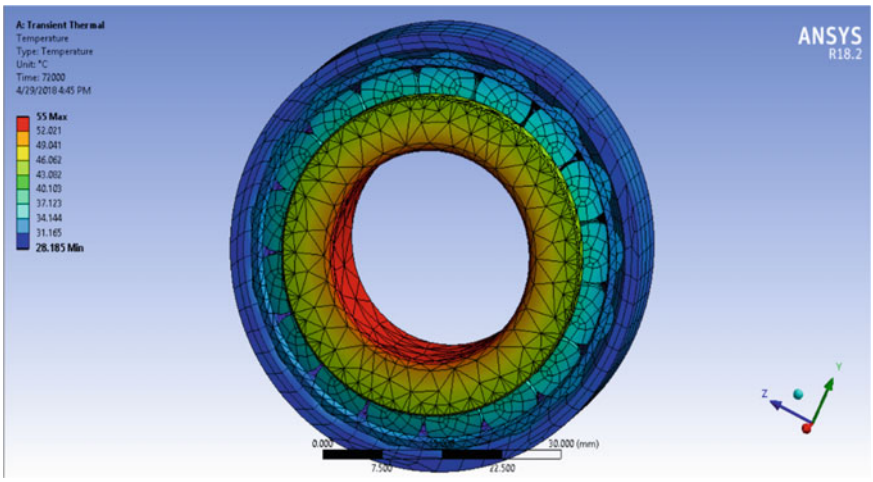

Fig. 5 Temperature distribution in Bearing

seen that maximum temperature is developed in the inner ring or raceway and rollers. Maximum temperature is arising up to 55 °C at an ambient temperature condition which is 25 °C. Outer ring temperature is approximately 25–30 °C. Total heat flux in bearing is shown in Fig. 6. Here, for the contact stress, outer ring is fixed. The force or load is applied radially on the inner ring of bearing, i.e., 300 N. For rotational speed, rotational velocity 2050 RPM must be applied by using joint load condition.

Equivalent stress 220 MPa is produced on the bearing. The maximum total deformation is 0.8 mm. The changing temperature loads with respect to time is given in Table 3. After the analysis of bearing, the result obtained from FEA is presented in Table 4. Von Mises stress obtained by FEA is shown in Fig. 7. To show the temperature distribution on different parts of assembly like on inner ring, as bearing

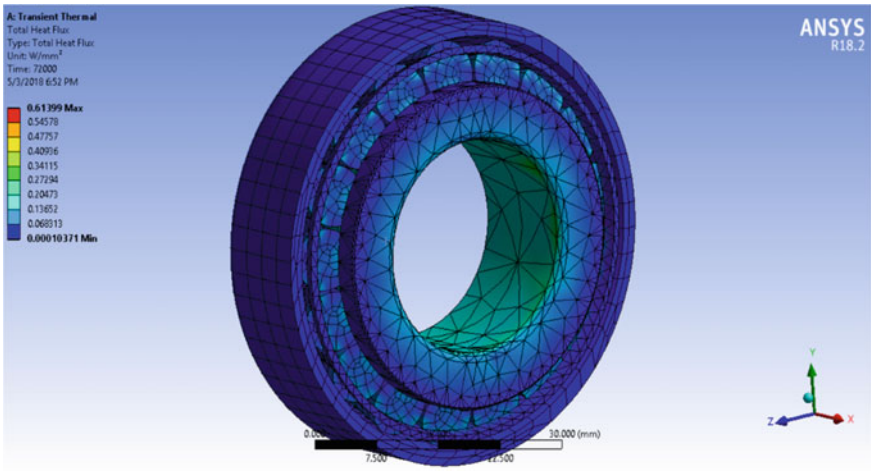

Fig. 6 Total heat flux in bearings

Table 3 Transient thermal temperature distribution results of taper roller bearing (NBC:30205) after 20 h

S. No.	Time (s)	Temperature (°C)
1	1	25
2	7200	32
3	14,400	35
4	21,600	37.5
5	28,800	40
6	36,000	42
7	43,200	45
8	50,400	47.502
9	57,600	50.001
10	64,800	52.501
11	72,000	55

Table 4 Results of transient thermal analysis of the taper roller bearing (NBC:30205)

S. No.	Parameter	Value
1	Total temperature of bearing (°C)	55
2	Temperature of rollers(°C)	48.918
3	Temperature of cone(°C)	33.839
4	Total heat flux (W/mm^2)	0.614

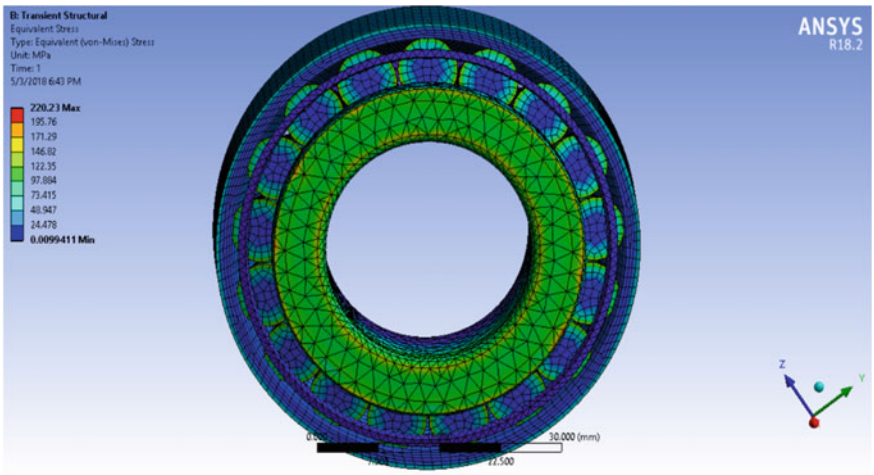

Fig. 7 Equivalent (Von Mises) stress

service life is an important parameter to consider, the bearing is tested under working conditions approximately for 20 h to determine the rate of temperature change and maximum temperature. This data can be used for improving heat flux or reducing contact stress by applying proper lubrication.

Finally, the equivalent stress and total deformation of bearing using FEA are calculated and demonstrates in Table 5, The effects of transient coupled field analysis report of the taper roller bearing the stress found from the transient thermal and structure are beneath of ultimate stress and yield stress (Figs. 8 and 9).

Stresses are induced when a load is applied to two solid bodies. Hertz developed one theory for calculating the contact stresses between two surfaces and resulting in the stress and compression developed in the body [11, 12]. This theory was derived for the non-conforming surface, and mating parts have a point or line contact. This

Table 5 Results of transient coupled field analysis of taper roller bearing (NBC:30205)

S. No.	Types of Stress	Value Obtained
1	Equivalent stress (MPa)	220.23
2	Total deformation (mm)	0.8

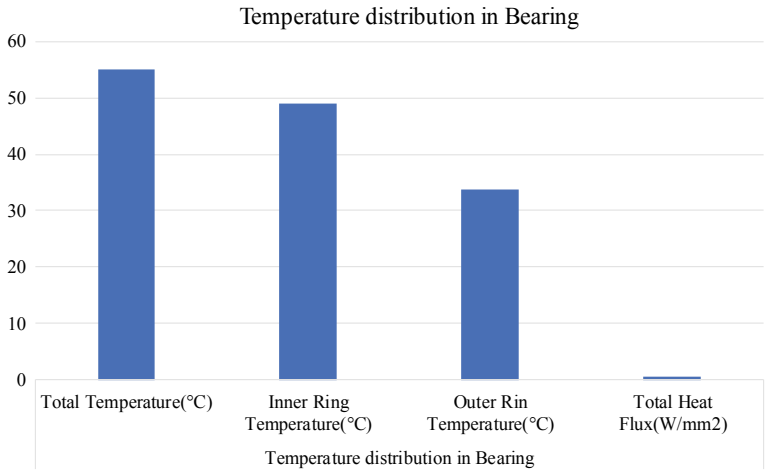

Fig. 8 Transient thermal temperature distribution of Taper roller bearing (NBC:30205)

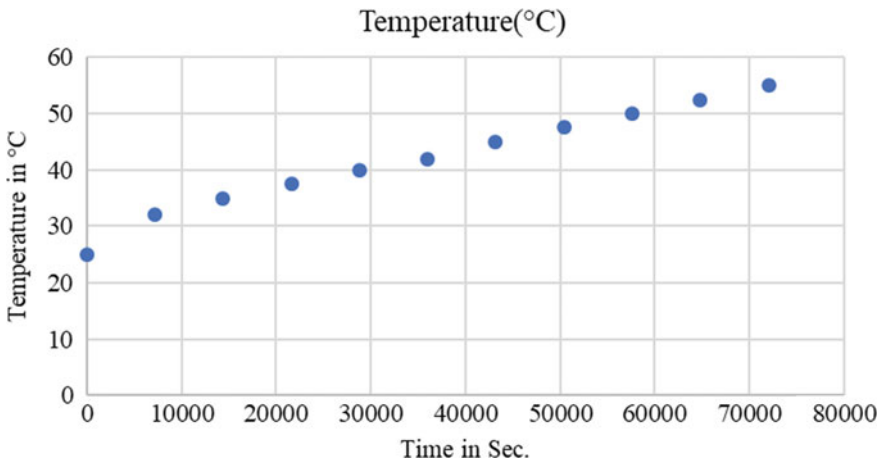

Fig. 9 Transient thermal temperature distribution results of Taper roller bearing (NBC:30205) after 20 h

mechanics is only applied when the two bodies are in contact with each other; otherwise, this phenomenon has not been applicable. Tapered roller bearings are used as mechanical apparatus in most self-moving machines, and they withstand on the time-varying loads. It is defined the influence of the preload for taper roller bearing to avoid a different type of failure like pitting and fatigue failure. The aim is to get the homogeneous flow of contact pressure on the inside and outside of the bearing. The researchers focused on the Hertzian contact pressure of pure geometries [13–17]. The contact stress is very important to evaluate because there is a different type of

Table 6 Input data of taper roller bearing (NBC:30205) for calculation

Inner ring diameter d_1 (mm)	25
Outer ring diameter d_2 (mm)	7.22
Force F (N)	300
Length of roller L (mm)	10
Poisson's ratio (ν)	0.30
Modulus of elasticity (MPa)	203,300

failure occur when there are contact friction between two bodies. The main cause of contact stress is a failure due to pitting, cracks, and flaking on the material surface.

Assumptions for Hertzian contact problems are:

- The strains are small as well as within the elastic limit
- Non-conforming and continuous surfaces
- The object surfaces are in frictionless contact.

Data for the calculation of contact Hertz stress is given in Table 6.

3.1 Calculation of Hertz Contact Stress [18, 19]

For calculation of Hertz contact stress, first we have to find the contact width (B),

$$\text{Contact width } B = \sqrt{\frac{2F}{\pi} \times \frac{d_1 \times d_2}{d_1 + d_2} \times \left(\frac{1 - v^2}{E_1} \times \frac{1 - v^2}{E_2}\right)}$$

$$B = 0.0978686\,\text{mm}$$

Later, after finding contact width, Hertz contact stress can be determined,

$$\text{Contact Hertz stress } P = \frac{2F}{\pi B L}$$

$$P = 195.2821\,\text{MPa}$$

So, finally the contact stress using hertz theory is found out to be 195.2821 MPa.

4 Conclusion

Accurate bearing service life prediction is one of the most critical effective condition-based maintenance for reducing overall maintenance cost and improving reliability. In this work, an effort is made to characterize and classify taper roller bearing temperature of different classes depending on their vibration features. In this paper, FEA

Table 7 Taper roller baring (NBC:30205) Comparison of both results

Load (N)	Theoretical value of contact Stress (MPa)	FEA Results of contact stress (MPa)	Percentage error (%)	Total deformation (mm)
300	195.2825388	220.23	12.77	0.8

is used to detect the bearing defect because even one percent of bearing defect may lead to sudden failure of machine. The main motive behind the present work is to assess the temperature distribution or behavior in the bearing and to find the failure rate due to overheating and stresses. In bearings, there is continuous contact of metals which causes inside temperature to exceed their limit and results in bearing failure. If there is no proper system for heat dissipation, failure will take place due to evaporation of lubricant because of excessive increment in temperature due to friction, and it also degrades the material. An FEA method is proposed for achieving more accurate thermal distribution over different elements of the bearing to estimate the service life. Condition monitoring is proposed as a best new feature to improve the results. For the validation purpose, the condition monitoring data collected from bearings are used. From the experiment, it was concluded that the proposed method can produce satisfactory estimated life prediction results.

Transient thermal analysis results are obtained from a taper roller bearing; the temperature varying (25–55 °C) range is obtained with respect to 20 h, whereas maximum temperature of rollers is 49 °C. FEA results are compared with theoretical values and found to be approximately same as shown in Table 7; besides, the maximum value of stress, temperature, total heat flux, and displacement are well within safe limits.

References

1. Deshpande, A. S., & Chandra Kishen, J. M. (2010). Fatigue crack propagation in rocker and roller-rocker bearings of railway steel bridges. *Engineering Fracture Mechanics, 77*(9), 1454–1466.
2. Koike, H., Santos, E. C., Kida, K., Honda, T., & Rozwadowska, J. (2011). Effect of repeated induction heating on fatigue crack propagation in SAE 52100 bearing steel. *Advanced Materials Research, 217,* 1266–1271.
3. Yan, K., Wang, N., Zhai, Q., Zhu, Y., Zhang, J., & Niu, Q. (2015). Theoretical and experimental investigation on the thermal characteristics of double-row tapered roller bearings of high speed locomotive. *International Journal of Heat and Mass Transfer, 84,* 1119–1130.
4. Brezeanu, L. C. (2014). Contact stresses: analysis by finite element method (FEM). *Procedia Technology, 12,* 401–410.
5. Kumar, R., Singh, G., Singh, M., Singh, J. (2017). Detection of crack Initiation in the ball bearing using FFT analysis. *International Journal of Mechanical Engineering and Technology, 8*(7), 1376–1382.
6. Crabtree, C. J. (2010). *Survey of commercially available condition monitoring system for wind turbines*. Technical Report, Durham University, School Of Engineering and Computing Science (2010).

7. Amarnath, A. M., & Kankar, P. K. (2014). Failure analysis of a grease-lubricated cylindrical roller bearing. *Procedia Technology, 14*, 59–66.
8. Hua, L., Deng, S., Han, X., & Huang, S. (2013). Effect of material defects on crack 43 initiation under rolling contact fatigue in a bearing ring. *Tribology International, 66,* 315–323.
9. Tarawneh, C. M., Cole, K. D., Wilson, B. M., & Alnaimat, F. (2008). Experiments and models for the thermal response of railroad tapered-roller bearings. *International Journal of Heat and Mass Transfer, 51*(25), 5794–5803.
10. Demirhan, N., & Kanber, B. (2008). Stress and displacement distributions on cylindrical roller bearing rings using FEM. *Mechanics Based Design of Structures and Machines, 36*(1), 86–102.
11. KayalI, Y., Ucun, I., & Aslantaş, K. (2009). Contact fatigue failure of a tapered roller bearing used in a lorry wheel. *Journal of Failure Analysis and Prevention, 9*(3), 288–294.
12. Tang, Z., & Sun, J. (2011). The contact analysis for deep groove ball bearing based on ANSYS. *Procedia Engineering, 23,* 423–428.
13. Rabold, F., & Kuna, M. (2014). Automated finite element simulation of fatigue crack growth in three-dimensional structures with the software system ProCrack. *Procedia Materials Science, 3*, 1099–1104.
14. Wang, Z. W., Meng, L. Q., Hao, W. S., & Zhang, E. (2010). Fesability analysis of solving contact Problem of roller bearing by finite element method. *Advanced Materials Research, 145,* 68–72.
15. Yongqi, Z., Qingchang, T., Kuo, Z., & Jiangang, L. (2012). Analysis of stress and strain of the rolling bearing by FEA method. *Physics Procedia, 24,* 19–24.
16. Pipaniya, S., Lodwal, A., & Vishwavidyalaya, A. (2014). Contact stress analysis of deep groove ball Bearing 6210 using Hertzian contact theory. *International Journal of Innovative Research in Engineering & Science, 7*(3), 8–16.
17. Puneethkumar, M. V., & Sunil, S. (2014). Analysis of contact pressure distribution of the straight and crowning profiles of tapered roller. *International Journal of Mechanical Engineering and Robotics Research, 3*(4), 483–492.
18. Purushothaman, P., & Thankachan, P. (2014). Hertz Contact Stress Analysis and Validation. *International Journal for Research in Applied Science & Engineering Technology (IJRASET), 2,* 531–538.
19. Gonzalez-Perez, I., Iserte, J. L., & Fuentes, A. (2011). Implementation of Hertz theory and validation of a finite element model for stress analysis of gear drives with localized bearing contact. *Mechanism and Machine Theory, 46*(6), 765–783.

Incipient Fault Detection in Roller Bearing Using Ultrasonic Diagnostic Technique

Shashikant Pandey, P. Sateesh Kumar, M. Amarnath, Teki Tanay Kumar, and Paladugu Rakesh

Abstract Rolling element bearings are extensively used in machinery to transmit rolling/sliding motion. These machine elements are prone to get damaged due to an increase in friction, which causes the heat generation and gradual wear on rolling contact surfaces of the bearing. Bearing failure leads to an unexpected shutdown of machinery. Therefore, many condition monitoring methods have been developed to predict bearing faults. The ultrasonic flaw detection method is one of the promising techniques to detect bearing faults. This paper describes the application of ultrasonic to detect incipient faults developed in the roller bearing subjected to fatigue load cycles. Results highlighted the suitability of the ultrasonic method to identify the incipient faults that appeared on the rolling contact surfaces.

Keywords Roller bearings · Ultrasonic waves · Wear · Lubrication

Nomenclature

H	Echo height ratio
h	Height of the second peak
h_0	Height of the first peak
R	Reflection coefficient
R_x	Effective radius
T	Signal transmitted through the materials
z_1 and z_2	Acoustic impedance of the media

S. Pandey (✉) · P. Sateesh Kumar · M. Amarnath · T. T. Kumar · P. Rakesh
Tribology and Machine Dynamics Laboratory, Department of Mechanical Engineering, PDPM Indian Institute of Information Technology, Design and Manufacturing, Jabalpur 482005, India
e-mail: pandey11211010@gmail.com

© Springer Nature Singapore Pte Ltd. 2021

C. Prakash et al. (eds.), *Advances in Metrology and Measurement of Engineering Surfaces* , Lecture Notes in Mechanical Engineering,
https://doi.org/10.1007/978-981-15-5151-2_23

1 Introduction

Rolling bearings are extensively used in high speed, heavily loaded rotating machinery, for example, aircraft engines, gas turbines, rolling mills, etc. Grease is the most commonly used lubricant, which reduces friction and wears, remove heat, and flushes wear particles in machine elements viz. gears, cams, ball/roller bearings. The life of the bearing is affected by various operating conditions such as load, speed and lubricant film thickness, etc. Variations in operating conditions result from a transition in lubrication regimes, thereby causing wear propagation on rolling contact surfaces of bearings [1].

Life prediction of a rolling element bearing is essential to prevent unexpected machinery shutdown. Various condition monitoring techniques have been developed by the researchers to predict bearing faults, which include vibration, sound, oil/grease degradation, and ultrasonic analysis methods. Wear is a phenomenon that occurs when moving surfaces interact with each other and material is released from the contacting surfaces; this released material is called wear particle. Wear occurs in a machine, or a component is mainly due to wear mechanisms such as abrasion, erosion, adhesion, surface fatigue, etc. All these mechanisms result in a gradual removal of material from the bearing surfaces and often develop in the presence of a lubricant [2–4].

Ultrasonic technique gaining its importance as a condition monitoring technique to identify the defects/flaws in the structures and machine elements. Figure 1 depicts the mechanism of ultrasound waves incident and transmits through the material; a part of the ultrasound wave is reflected inside the material. To ascertain the reflection coefficient R, the abundancy of the reflected wave and the underlying wave is looked at. The reflection coefficient R depends on the interface material's acoustic befuddle and determined by condition (1) [4].

$$R = \frac{Z_1 - Z_2}{Z_1 + Z_2} \tag{1}$$

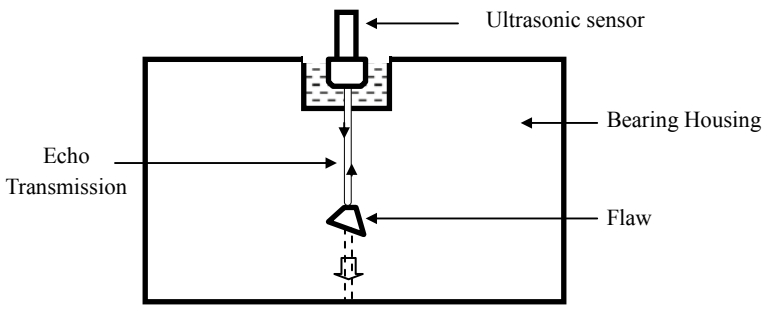

Fig. 1 Echo height ratio [4]

The acoustic impedance of media is Z_1 and Z_2 respectively. The part of the incident signal T, which is transmitted through the materials is calculated by using the following equation

$$T = 1 - R \tag{2}$$

For the ultrasound to occurr on a multi-layered framework, the sign transmitted or reflected is the superposition of the outcome of the use of conditions (1) and (2). The underlying reflected reverberation tallness (h) shifts its trademark, which relies upon the mounting of the test, the impact of dispersion and the dissipating of the acoustic wave during engendering. To beat these impacts, the contact condition is surveyed by the proportion of reverberation stature ($h/h0$) in which the two surfaces are consummately isolated.

Detection of damage in the structure is carried out by considering the echo height ratio, which is given by the following equation:

$$H = \{(1 - h/h_0) \times 100)\} \tag{3}$$

where h and h_0 are the height of the second peak and height of the first peak respectively.

The ultrasonic pulse waves with wave frequency ranging from 0.1–15 MHz are transmitted into a material to detect flaws. The transducer probe is mounted on the surface of the test specimen, which in turn is coupled to test objects with the help of lubricant oil, which acts as a coupling to avoid air gap. The piezoelectric component in the transducer energized by the very short electrical release transmits an ultrasonic heartbeat, again it gets the sign, in this way making it waver, again it receives the signal, thus causing it to oscillate. This leads to the generation of the short electric pulse, which is used to detect flaws in the specimen. The transducer used is a transceiver that transmits and receives ultrasonic waves. Caretta et al. [4] used an ultrasound technique to analyze the roll stress and deformation in the cold rolling process carried out on a metallic sheet. The outcomes were contrasted and numerical recreation. Creators have featured the conceivable outcomes of deciding the mean spiral worry of a roller by figuring an adjustment in the hour of trip of a reflected ultrasonic wave from the outside of a roller plant.

Kasolang et al. [5] used an ultrasonic flaw detection technique to investigate the performance of journal bearing operated under hydrodynamic lubrication. Authors have determined minimum film thickness and defects developed on the bearing contact surfaces. Wan et al. [6] conducted experiments to measure the oil film thickness between rolling surfaces of ball bearing contacts using the ultrasonic reflection method. The authors observed that there was a relatively low resolution, which resulted in the perturbations. However, the central film thickness measurement was well agreed with the established models.

Kai et al. [7] performed experiments to measure oil film thickness by using an ultrasound sensor in sliding contact bearings. The two reflected echoes from the substrate–babbitt interface and babbitt-lubricant interface were overlapped, which

resulted in film thickness values. The Gaussian reverberation and desire boost (EM) calculation are utilized by the creators to separate and secluded reverberation reflected from the oil film thickness layers.

The results provided a true film thickness values from the sliding contact bearings. Takeuchi [8] used ultrasonic technology to measure the indentation size in the ball bearing by considering three indexes, such as the fluctuation ratio, the intensity of impact and the change of gradient in echo height ratio. Authors have highlighted the possibilities to obtain a reliable estimate of the width of the shallow indentation, which minimizes the pitting damage on bearing contact surfaces.

In recent years, there are various methods and techniques to detect the faults in the bearing; they can be broadly classified as by vibration measurements, measuring the running temperature and wear debris measurement. In this present work, ultrasound acoustic energy in the form of waves with frequencies higher than 20 kHz is used for echo height analysis of the roller bearing elements. This data can be used to find the health condition of the bearing. This is a nondestructive method of online inspection of the fault developed in the roller bearings elements.

2 Experimental Procedure

Figure 2 shows the square outline of the exploratory arrangement utilized for the examination. It consists of a 5 HP three-phase induction motor used to drive the shaft through direct three-jaw coupling. The speed of the ac motor was controlled by using a variable frequency drive. The shaft was supported by the support bearing and test bearing, as shown in Fig. 2. A rectangular opening was machined on the test bearing lodging to mount the ultrasonic sensor. The load-bearing was placed nearer to the test bearing, and 1 kN load is applied on the load-bearing with the help of the wire rope mechanism. The reaction force act on the test bearing as shown in Fig. 2. Einstein TFT II ultrasonic flaw detector was used to acquire the ultrasonic

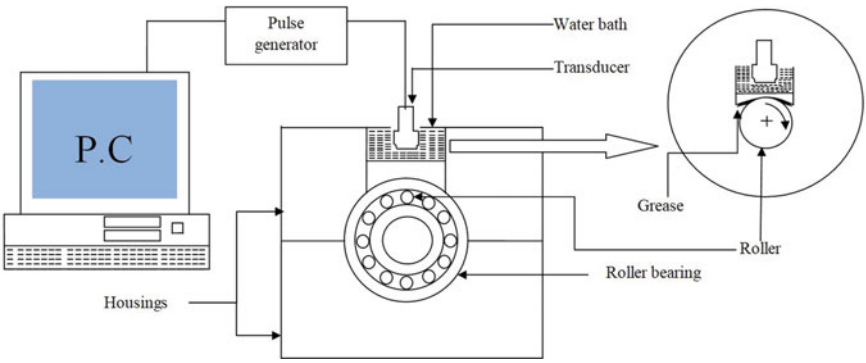

Fig. 2 Block diagram of the experimental test rig

Table 1 Bearing dimensions

Bearing model	NJ307ECP (mm)
Bearing outer raceway	80
Bearing inner raceway	35
Ball diameter	12

signals from the test bearing and stored on the personal computer. The experiment was conducted 8 h a day. The first 100 h the test rig was allowed in the running wear period, then test bearing was cleaned and mount again. The wear propagation on the rolling contact surfaces was studied with the help of a USB microscope with high resolution. The surface examination of wear and ultrasonic testing were carried out in every 300 h. The geometry of the bearing SKF NJ307 ECP is given in Table 1.

During the experiment, water is used as coupler so that sound can quickly propagate inside the bearing and loss of sound can be minimized. Every measurement of ultrasonic eco pulse was repeated three times and the maximum wear area on the rolling surfaces is presented in the result.

3 Results and Discussions

The fatigue test experiments were carried out for 800 h; the test bearing was dismantled at a regular interval of 300 h to observe the development of surface fatigue wear on the inner race of the bearing. Figure 3a–d shows the micrograph of the inner race of roller bearing surface after 300, 600 and 800 h. Figure 3a represents bearing surface after run-in wear where no significant wear is visible. With an increase in the fatigue load cycles, micro pitting wear appears on the bearing surface due to cyclic loading. Figure 3b represents the micrograph of the inner race after 300 h, significant micro pitting wear and small scratches are visible on the surface of the inner race. Figure 3c depicts the surface condition on the inner race after 600 h. An increase in the size of pitting and various micro pitting wear are visible in the micrograph.

As the operating time increases, the lubricant loses its lubrication properties viz cooling, viscosity which accelerates the formation of various wear mechanisms on the bearing contact surfaces. Wear particles and contamination also affect the lubrication in the bearing contact surfaces in increased operating time ultimately the lubricant film between the two contact surfaces get reduced and load is supported directly by the contact surfaces of the bearing which results in the abrasive wear and severe scuffing are formed on the rolling contact surfaces. A gradual increase in the wear can be observed in this condition. With continuous operation of roller bearing, fatigue wear mechanism defect pitting on the bearing surfaces are converted into spalling. Figure 3d shows the condition of the bearing after 800 h, sever scuffing and spalling can be observed on the inner race surfaces, which confirms degradation of the rolling contact surfaces operating under constant load and speed.

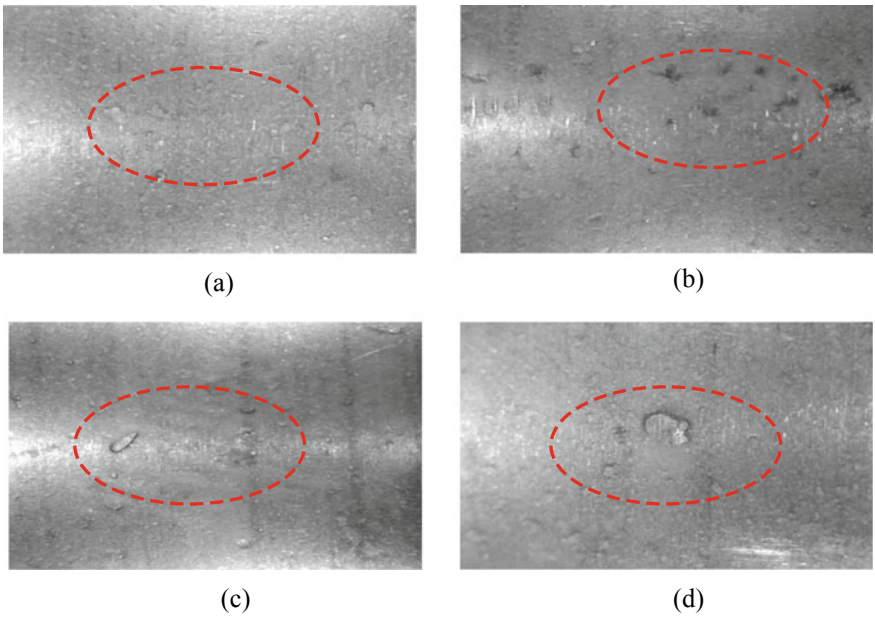

Fig. 3 Wear propagation on the inner rolling surface of roller bearing; **a** after 100 h, **b** after 300 h, **c** after 600 h, **d** after 800 h

The ultrasonic transducer is mounted in the lubricant jacket of the test bearing housing. The ultrasonic signal generator enabled the sensor to transmit and receive the ultrasonic waves. These signals acquired at a regular interval of 300 h, the diagnostic feature used to detect the bearing fault is the echo height ratio (H). The signal contains several peaks out of which the first two peaks highlight the bearing fault-related information. The first two peaks heights are denoted by $h0$, and h, respectively, the values of H after every regular interval are taken into consideration to evaluate the fault development in roller bearing. The values of echo height ratio obtained within the range of 0–1, the ultrasonic signals acquired from the bearing housing are shown in Fig. 4a–c. The x-axis indicates range that covers housing and bearing components and the Y-axis provides echo height. There is an increase in the amplitudes of the second peak h, due to a rise in surface fatigue wear and reduction in the film thickness between the contact surfaces of roller bearing. The value of pulse height after 300 h is 0.22, which increases to 0.4 after 600 h of operation. As the film thickness decreases, the reflected ultrasound to the receiver of an ultrasound sensor gets increased, which causes an increase in the reflected sound energy. The value of the second pulse eco height after 900 h is 0.7, which confirms a further rise in the surface wear, as shown in Fig. 4.

Figure 5 shows the variation of echo height ratio versus operating time as a function of operating time. As discussed in Fig. 4 same trends in the increase in the difference

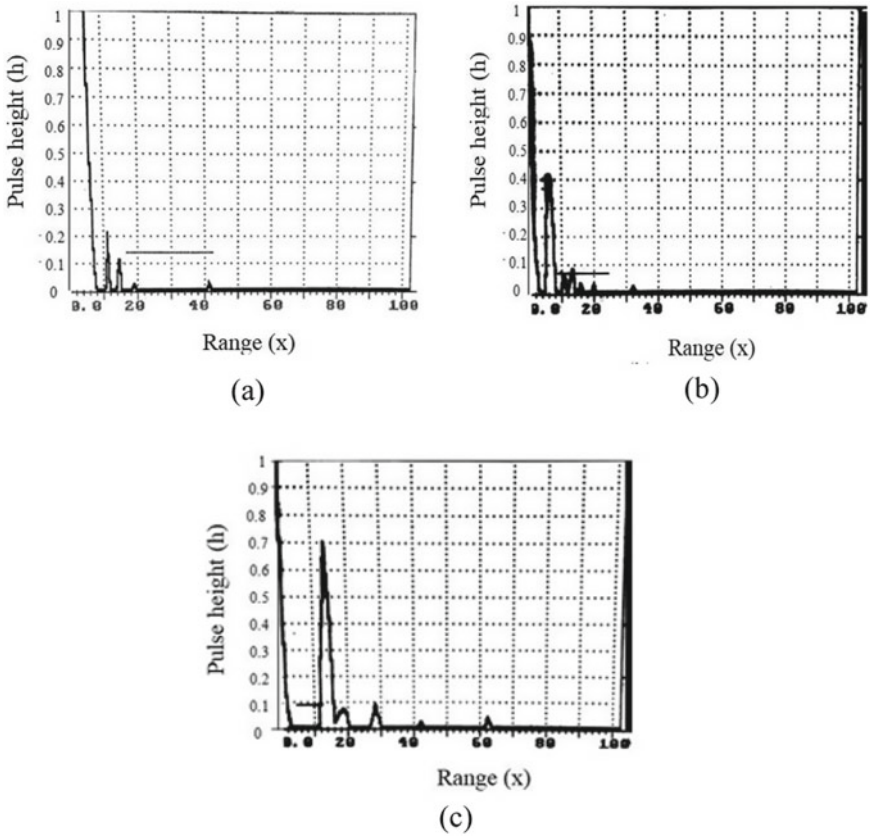

Fig. 4 Characteristic pulse-echo signals; a 0 and 300 h, **b** 300 and 600 h, **c** 600 and 800 h

in echo height ratio can also be observed in Fig. 5. The change of echo height ratio increases with an increase in the wear propagation on the rolling contact surfaces.

4 Summary and Conclusions

In the present work, experiments were conducted to detect surface fatigue wear developed on roller bearing contact surfaces. The results from experimental investigations give the following findings.

1. The amplitude levels of ultrasonic signals showed an increase in the trend, thereby causing a gradual decrease in the echo height ratio values, which indicated the fault propagation on the inner race due to fatigue load cycles.
2. The wear images obtained after every 300 h indicate micro pitting and pits developed on the inner race.

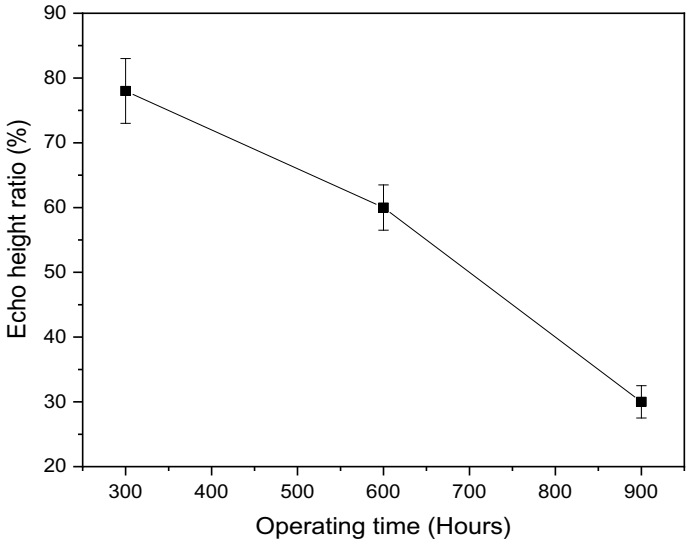

Fig. 5 Variation of echo height ratio versus operating time

3. Extended load cycles resulted into increase in the size of pits and spalls on bearing contact surfaces.

The results obtained from experimental studies suggest that ultrasound transducer can successfully be used for condition monitoring of the rolling element bearing and provide a good correlation between an increase in echo height ratio and bearing wear on the rolling contact surfaces. In the future, authors suggest to compare and combine the ultrasonic method with the other condition monitoring techniques viz. vibration, sound, wear particle analysis and lubricant degradation analysis to enhance the robustness on the condition monitoring of roller bearing system.

References

1. Taylor, P., Farhana, N., Yusof, M., & Ripin, Z. M. (2014). Analysis of surface parameters and vibration of roller bearing analysis of surface parameters and vibration of roller bearing. *Tribology Transactions, 57*(4), 37–41.
2. Peng Z., Kirk T. B., Xu Z. L. (2006). The development of three-dimensional imaging techniques of wear particle analysis. *Wear, 203–204*, 418–424.
3. Nayak, A., Kankar, P. K., Jain, N., & Jain, P. K. (2018). Force and vibration correlation analysis in the self-adjusting file during root canalshaping: An in-vitro study. *Journal of Dental Sciences, 13,* 184–189.
4. Carretta, Y., Hunter, A. K., Boman, J. P., Legrand, N., & Laugier, M. (2017). Ultrasonic roll bite measurements in cold rolling—Roll stress and deformation. *Journal of Materials Processing Technology, 249,* 1–13.

5. Kasolang, S., Ahmed, D. I., Dwyer-Joyce, R. S., & Yousif, B. F. (2013). Performance analysis of journal bearings using ultrasonic reflection. *Tribology International, 64,* 78–84.
6. Wan, I. M. K., Gasni, D., & Joyce, D. (2012). Profiling a ball bearing oil film with ultrasonic reflection. *Tribology Transactions, 55*(4), 409–421.
7. Kai, Z., Qingfeng, M., Tao, G., & Nan, W. (2015). Ultrasonic measurement of lubricant film thickness in sliding Bearings with overlapped echoes. *Tribology International, 88,* 89–94.
8. Takeuchi, A. (2012). An attempt to evaluate insufficient supply of oil in ball bearing with ultrasonic technique. *Materials Transactions, 53*(2), 250–255.

Comparative Analysis of Imaging and Novel Markerless Approach for Measurement of Postural Parameters in Dental Seating Tasks

Vibha Bhatia, Jagjit Singh Randhawa, Ashish Jain, and Vishakha Grover

Abstract Postural inaccuracies in persistent dental tasks indicated an upsurge in the prevalence of musculoskeletal disorders in dentists. The study assessed the angle parameters related to the bodily movement of upper arm (UA), lower arm (LA), wrist (W), neck (N), and trunk (T) using self-developed markerless Kinect V2 system and conventional imaging technique. Ten dentists were monitored with both techniques while performing real-time dental procedure. The agreement between the techniques was assessed using Bland–Altman at 95% bias, Pearson and concordance correlation coefficients ($r1$ and $r2$), mean difference, and percentage error. For conclusive agreement analysis, contingency coefficient (C), proportion agreement index (Po), Cohen's kappa (k), and Mann–Whitney at 95% confidence interval were evaluated. Data from both techniques possessed strong correlations ($r1$ and $r2 > 0.90$). Cohen's kappa (0.67) at standard Landis and Koch scale showed good agreement in RULA data. Postural analysis of slow-motion tasks like dentistry using Kinect V2 system proved as unobtrusive and efficient. This may be used by dentists to have periodic postural check.

Keywords Dentists · Musculoskeletal disorders · Ergonomics · Real-time assessment · Kinect V2

V. Bhatia (✉)
Industrial and Product Design(CoE), Department of Production & Industrial Engineering, Punjab Engineering College (Deemed to be University), Chandigarh, India
e-mail: vibhabhatia.phdidp17@pec.edu.in

J. S. Randhawa
Department of Production & Industrial Engineering, Punjab Engineering College (Deemed to be University), Chandigarh, India

A. Jain · V. Grover
Dr. Harvansh Singh Judge Institute of Dental Sciences and Hospitals, Panjab University, Chandigarh, India

© Springer Nature Singapore Pte Ltd. 2021

C. Prakash et al. (eds.), *Advances in Metrology and Measurement of Engineering Surfaces* , Lecture Notes in Mechanical Engineering,
https://doi.org/10.1007/978-981-15-5151-2_24

1 Introduction

Despite all measures taken worldwide for improvement of work environments, leading economies are facing consequences of occupational hazards. According to American Working Conditions Survey [1] and European Working Conditions Survey [2], 40.5% and 44% of workers were exposed to tiring postures, respectively, whereas 75% and 62% of workers were susceptible to repetitive arm and hand motions. All MSDs instigated or induced by work performances are concluded as WMSDs [3]. WMSDs are a serious global concern and prevalent among both developing and developed nations. In developing nations, compromising work environments have led to an alarming rise in WMSDs [4, 5].

Various studies documented in the literature worldwide have reported a high incidence of MSDs among the dental practitioners [6–14]. The dental profession demands precision, good visual acuity, psychomotor skills, depth perception, manual dexterity, and concentration accompanied with narrow work area (oral cavity of the patient), resulting in inflexible awkward postures for a longer duration during dental task [14, 15]. Even adoption of an optimal sitting posture, due to the little movement of joints static contraction, is there in more than 50% of body muscles. Static posture behavior makes dentists prone to MSDs like tendinitis, tenosynovitis, synovitis, and bursitis [15, 16]. Lower back problems are prevalent among dentists worldwide accompanied by problems in neck, shoulders, hand, and wrist; more than one-third required medical treatment for MSDs [17–19].

Movement- and posture-related data of worker is prerequisite to evaluate the vulnerability to risk factors for MSDs with the subsequent aim of ergonomic intervention [20]. Subjected to variation in the mensuration method, varieties of tools are available and are categorized as (1) self reporting, (2) direct measurements, and (3) observational [21, 22]. Mostly self-administered questionnaires, checklists, interviews, and rating scales were used in various studies investigating the prevalence of WMSDs in dentists [10, 12, 13, 23–30] and usually lead to biased results [31, 32]. Delfa et al. and Blanc et al. have used direct methods to analyze postural and biomechanical data in dentistry by making use of wearable sensors like goniometers, EMG electrodes, or markers for motion capturing in simulated dental environments [33, 34]. In actual dental work, direct methods may be difficult to implement as wearable devices usually cause discomfort and affect postural activity. The mass adoption of direct methods becomes inappropriate due to intrusive, expensive, and time-consuming nature of sensors involved [35, 36]. Also, the high contrast stickers used in marker technology may fall off during actual work [37, 38]. In dental ergonomics area, studies have been done using ergonomic evaluation by observational methods like RULA and REBA. These methods involve the judgment of bodily angles using images and video frames and thus require expert opinion for correct estimation of angles [39].

To rule out the drawbacks of above methods, elbow, shoulder, and wrist joint data from a field survey of videos during shoulder abduction in 2D was automatically picked up by using a graphic algorithm which controlled error within 12° [40]. However, to obtain body joint data in 3D, in 2013, skeletal tracking system using Kinect

V1 was integrated into the RULA method for 3D motion analysis [41], DHM Jack tool, and Task Analysis toolkit module [42]. Choppin et al., discussed the accuracy of Kinect, the maximum error, proportional error, median RMSE, and systematic bias were reported as 58.2°, 1.15°, 12.6°, and 4.38°, respectively, using IPIsoft algorithm and 63.1°, 1.19°, 13.8°, and 3.16°, respectively, using NITE algorithm [43]. Kinect sensors being fully automatic, cheap, portable, non-intrusive, markerless and high frame rate technology justifies its robust applications and studies, covering health care, robotics, physical therapy, performing arts, natural user interface, virtual reality, fall detection, and 3D reconstruction [44]. K2RULA a semi-automatic software was developed which is capable of detecting awkward postures in real time using Kinect V2 [45]. Kinect V2 according to its specifications and studies conducted outperformed Kinect V1 being able to detect 25 body joints, robust to both natural or unnatural light sources and more accurate to human body skeletal tracking [46, 47]. A marker-based study using Kinect V2 as a computational tool was conducted by Weidemann et al.; upper body joint angle inclinations were highly accurate(deviation less than 7.2°) with lower accuracy in neck angle ($-31° \pm 9.1°$) and upper body rotation across a longitudinal axis ($24.0° \pm 3.5°$) [48]. The real-time feedback was developed by Chika Edith Mgbemena et al. which can inform the workers to change the instantaneous awkward sitting posture [49]. Yusuf et al. had captured static (lateral hand lift) and dynamic (lower arm) movement using Kinect V2 sensor, with the respective error rate of 2% and 5% [50]. The above studies establish the possibility of Kinect V2's use in real-time application tasks and a promising tool for postural analysis.

Dental practitioners all over the world being susceptible to WMSDs need to assess their postures while working. During long-duration dental tasks, it becomes difficult to analyze the posture of the dentist and the presence of ergonomist cannot be avoided. The real-time postural evaluation of dentists, which may eliminate the need of ergonomists is a serious challenge till date. Also, ISO standard 1128-3:2007(E) can be considered as the basis to establish the workplace environment. The steady system for any workstation can be developed using depth sensors which can monitor body joint angles of a worker for an early check of exposure to WMSDs. The current study aims at examining the use of Microsoft Kinect V2 sensor in capturing the real-time postural data in dental practitioners during their practice hours. The study focuses on (1) examining the body joint angle data of dentist acquired by Kinect V2 while doing the actual dental task and its comparison with the data collected through conventional imaging technique. (2) Calculation and comparison of final RULA score from body joint data collected from both Kinect V2 sensor and imaging techniques.

Dental practitioners all over the world being susceptible to WMSDs need to assess their postures while working. During long-duration dental tasks, it becomes difficult to analyze the posture of the dentist and the presence of ergonomist cannot be avoided. The real-time postural evaluation of dentists, which may eliminate the need of ergonomists is a serious challenge till date. Also, ISO standard 1128-3:2007(E) can be considered as the basis to establish the workplace environment. The steady system for any workstation can be developed using depth sensors which can monitor

body joint angles of a worker for an early check of exposure to WMSDs. The current study aims at examining the use of Microsoft Kinect V2 sensor in capturing the real-time postural data in dental practitioners during their practice hours. The study focuses on (1) examining the body joint angle data of dentist acquired by Kinect V2 while doing the actual dental task and its comparison with the data collected through conventional imaging technique. (2) Calculation and comparison of final RULA score from body joint data collected from both Kinect V2 sensor and imaging techniques.

2 Methods

2.1 Subjects

Dental practitioners and hygienists were enlisted from the regional dental institute. Subjects having any prior history of WMSDs, injuries in hands, wrists, arms, neck, back, and shoulder were excluded from the study. Ethical permission for the study was taken from Panjab University's Ethics Committee. Ten professional dental workers (6 males and 4 females) and their patients voluntarily signed the written informed consent form for participation in study, with the disclosure for needful use of procedural photographs concealing their facial identity. To maintain the consistency of data, all the participants were checked for their dominant hand as the right hand and dental scaling with manual tools as the performing job. Participants were explained the study protocol and purpose in advance. The subjects had mean age, height, and weight of 29 ± 4 years, 162 cm, and 67 ± 9 kgs, respectively. All the dentists performed the sitting dental job for more than 15 h a week.

2.2 System Overview

The automatic data capturing software was developed using Microsoft Kinect V2 for windows, PC with windows 8.1,64 bit,8 gbRAM, Intel core i5 processor @2.2GHz. The C# (.NET framework) and Microsoft Kinect for windows SDK2.0 were used as the programming platform to capture 3D depth image and skeletal joint coordinate data. High-quality videography still camera (SONY, HDR-XR550) was used to capture image streams simultaneously while capturing depth image data. The sampling frequency of both Kinect V2 and still camera was 30 fps.

2.3 Experimental Design

2.3.1 Data Collection

The postural data was collected from a typical dental workstation which included modern Pelton and Crane chair arrangement. The current study involved manual dental scaling task, and for achieving the current objective of capturing better body joint data (with least occlusion), the adjustment with hanging ultrasound cleaning appliance and nozzles were kept at a distant position from Kinect's proximity. No other modification was made for the current study in dental hospital's workstation. Dentists performed the dental cleaning task in both standing and sitting postures as per their preference. The dentists who performed the job while sitting used dental stool with backrest. The Kinect sensor was placed radially in between standard 8–9'o clock position of dental chair setup at a distance of 3.5 m from chair center and at a 1.2 m height from the ground using a tripod. The tilt angle of Kinect was kept zero as the optical axis of the sensor was parallel to the ground. The high-quality videography camera was placed at the nearest possible proximity of Kinect sensor at approximately the same position and direction. The digital clock was kept within the camera frame in a fashion that it does not disturb the dentist. To avoid the inessential body skeleton tracking of a patient's body, the patient was asked to lie on the dental chair before the Kinect is switched on because Kinect sensor considers patient and dental chair as merged bodies or unity is unable to generate automated patient's virtual skeleton. Dentists were instructed to stand still for once in front of Kinect for 3–4 s just before initiating the scaling task to allow Kinect to detect human body joint coordinates. The data was collected continuously for 5 min, while each dentist performed real-time dental scaling task, sitting between standard 9–11'o clock dental chair position as illustrated in Fig. 1. Both Kinect and videography camera were simultaneously initiated, and more accurate data synchronization was obtained by using digital and stop watches. The flowchart shows the procedure followed in the present study in Fig. 2. The typical RGB image perspective while recording data for the study from the Kinect and videography camera orientation is shown in Fig. 3.

2.3.2 Data Processing and Analysis

The body skeletal information is transformed into a large set of features which were fed into a software program created in Visual Studio. The recorded coordinate joint data was used to create vectors, and subsequent computation was done to calculate final angle values. C# program computed the five prime body angles(dependent variables) present at the right shoulder, right elbow, right wrist, neck, and trunk joints and were represented as angles related to UA, LA, W, N, and T (shown in Fig. 1) (Table 1).

The angle values corresponding to thirty relevant image frames from each cycle of dental scaling work were extracted. RULA method was applied for all the right side

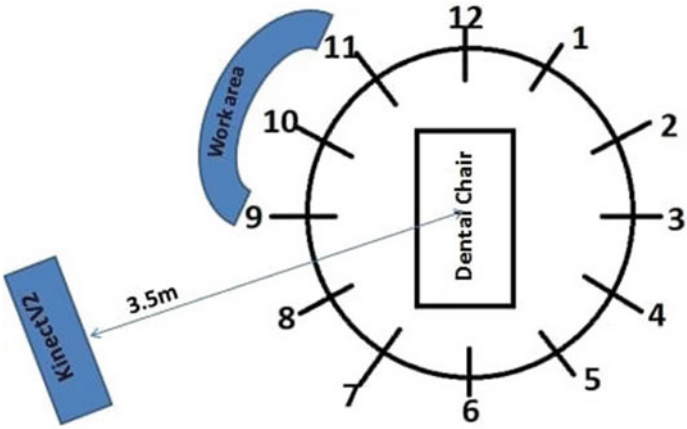

Fig. 1 Kinect positioning and sitting orientation of dental practitioner based on standard dental clock positions

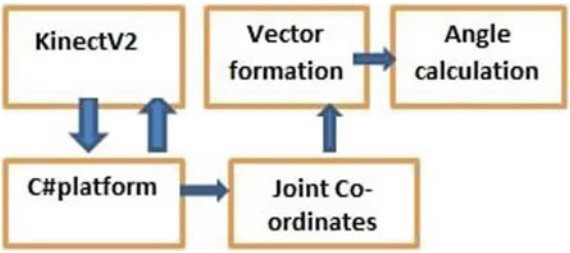

Fig. 2 Data acquisition and calculation of postural parameters

physiological features for both Kinect and image readings. Relevant values from both Kinect and conventional readings were considered after removing outlier values.

Following hypothesis were selected to assess the agreement between the results of Kinect and conventional imaging technique. Hypothesis 1: Kinect V2 data values are in agreement with data collected with the conventional method. Hypothesis 2: Final RULA score calculated using Kinect V2 data is in agreement with the RULA score calculated using conventional techniques.

To evaluate agreement among Kinect and conventional imaging technique, Bland–Altman mean difference (bias) and 95% limit of agreement(LoA) defined as bias ± 1.96SD were plotted. Mean, mean difference, and standard deviation(SD) of mean difference values from both techniques related to each body angle parameter were recorded. To assess the strength of association among angle parameters recorded using both Kinect and conventional imaging techniques, Pearson correlation coefficient ($r1$) was evaluated and corresponding p-values were assessed to know the probability of occurrence of results. Also, to evaluate the level of agreement or disagreement among angle parameters recorded using both techniques, concordance

Fig. 3 RGB image frame while data recording

correlation coefficients ($r2$) were evaluated. Percentage errors (PE) were evaluated to assess the percentage of differences between angle values for all body joints derived from both techniques.

For more concrete and conclusive agreement analysis between two sets of calculated RULA values(Kinect and imaging), nonparametric statistical tests were performed. Differences in medians of RULA scores between two techniques were assessed using Mann–Whitney U test at 95% confidence interval to test the null hypothesis: No significant difference exists in the RULA values between Kinect and imaging technique. To assess the strength of association among both systems based on final RULA scores, contingency coefficient (C) was evaluated using two-dimensional contingency tables. Proportion agreement index (P_O) was calculated to check the proportion of cases for which RULA scores for both techniques agree. For the sample to sample inter-rater agreement, Cohen's kappa coefficient (k) [51] was calculated as a quality index, using ordinal RULA scores for both recording techniques.

Table 1 Anatomical movements and corresponding joint angles. Angle at—upper arm (UA) corresponding to right shoulder flexion/extension, lower arm (LA) corresponding to right elbow flexion/extension, right wrist (W) flexion/extension, neck and trunk (TA) flexion/extension

Joint	Movement type	Image	Angle details	
Right shoulder	(UA)flexion/extension		Between plane formed by joints 4, 5, 16 and vector formed by joints 5, 7	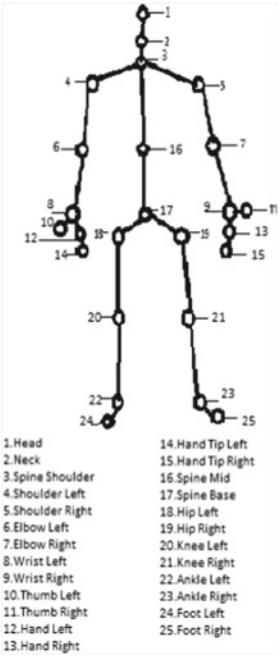
Right elbow	(LA)flexion/extension		Between vector formed by 5, 7 and vector formed by 7, 9	
Right wrist	(W)flexion/extension		Between vector formed by 7, 9 and 9, 13	
Neck	Neck(N) Flexion/extension		Between vector formed by 2, 3 and vector formed by 1, 2	
Trunk	(T)Flexion/extension		Between plane formed by 17, 18, 19 and plane formed by 3, 18, 19	

3 Results

Table 2 summarizes the values of mean (±SD), Bland–Altman mean difference with 95% limits of agreement, percentage errors, Pearson correlation coefficient, and concordance correlation coefficient from body joint angle data using Kinect and imaging techniques.

Table 2 Mean (±SD) values corresponding to Kinect and imaging, mean difference (°), percentage error (PE), Pearson correlation coefficient ($r1$), concordance correlation coefficient ($r2$), and 95% limits of agreement for body joint angle data from Bland–Altman plot

Body joints	Kinect (°) Mean (±SD)	Image (°) Mean (±SD)	$r1$ (298)	p-value	$r2$ (298) at 95% CI	Mean diff (°)	95% LOA	[a]PE (%)
UA	28.68 (±19.38)	28.98 (±18.86)	0.991	<0.001	0.9903 (0.9879–0.9922)	−0.2992	−0.5998 to 0.0015	10.17
LA	85.74 (±32.41)	85.97 (±31.05)	0.997	<0.001	0.9957 (0.9947–0.9965)	−0.2259	−0.5580 to 0.1061	3.00
W	150.26 (±20.84)	153.10 (±7.18)	0.939	<0.001	0.9111 (0.8927–0.9266)	−2.8401	−3.7013 to − 1.9788	3.53
N	17.64 (±7.53)	18.19 (±7.59)	0.951	<0.001	0.9484 (0.9357–0.9856)	0.5493	−0.8186 to − 0.2800	11.85
T	76.12 (±5.92)	76.77 (±5.65)	0.914	<0.001	0.9075 (0.8856–0.9254)	−0.6477	0.9218 to − 0.3736	2.45

[a]The formula used for calculating percentage error = {100 * [∑|(Mean Kinect Values-Mean Imaging Values)/Mean Kinect Values|])/Total number of image frames evaluated

The graphs in Fig. 4a–e illustrates the scatter plots of each respective body joint angles data using Kinect–conventional methods (the differences along the vertical axis against the mean values along the horizontal axis). Mean difference or bias and 95% LoA values are represented as horizontal lines on each graph. Bland–Altman test indicated that the data points were evenly and closely distributed across the horizontal bias line. In most of the body angles, more than 95% of the method difference values were spotted within the defined LoA range except in W, which showed the less agreement between the methods in calculating W data. Also, comparatively higher bias value (systematic error = −2.84) recorded in the case of W indicated the systematic difference in results produced by the two methods. Wide LoA in W plot suggested the possible inaccuracy of results with one of the technique. Overestimation of joint angle values was recorded with Kinect in the case of W; observation of the graph suggested the higher existence of data points above the bias line. In case of LA proportional bias was observed, as Kinect underestimated the LA angle values when mean angle values were low and vice versa.

Body angle data (for LA, UA, W, N and T) from Kinect and imaging techniques resulted in optimally high Pearson's ($r1(298) \geq 0.90, p < 0.001$) and concordance correlation coefficients ($r2(298) \geq 0.90$), indicating the significant positive correlation between both techniques.

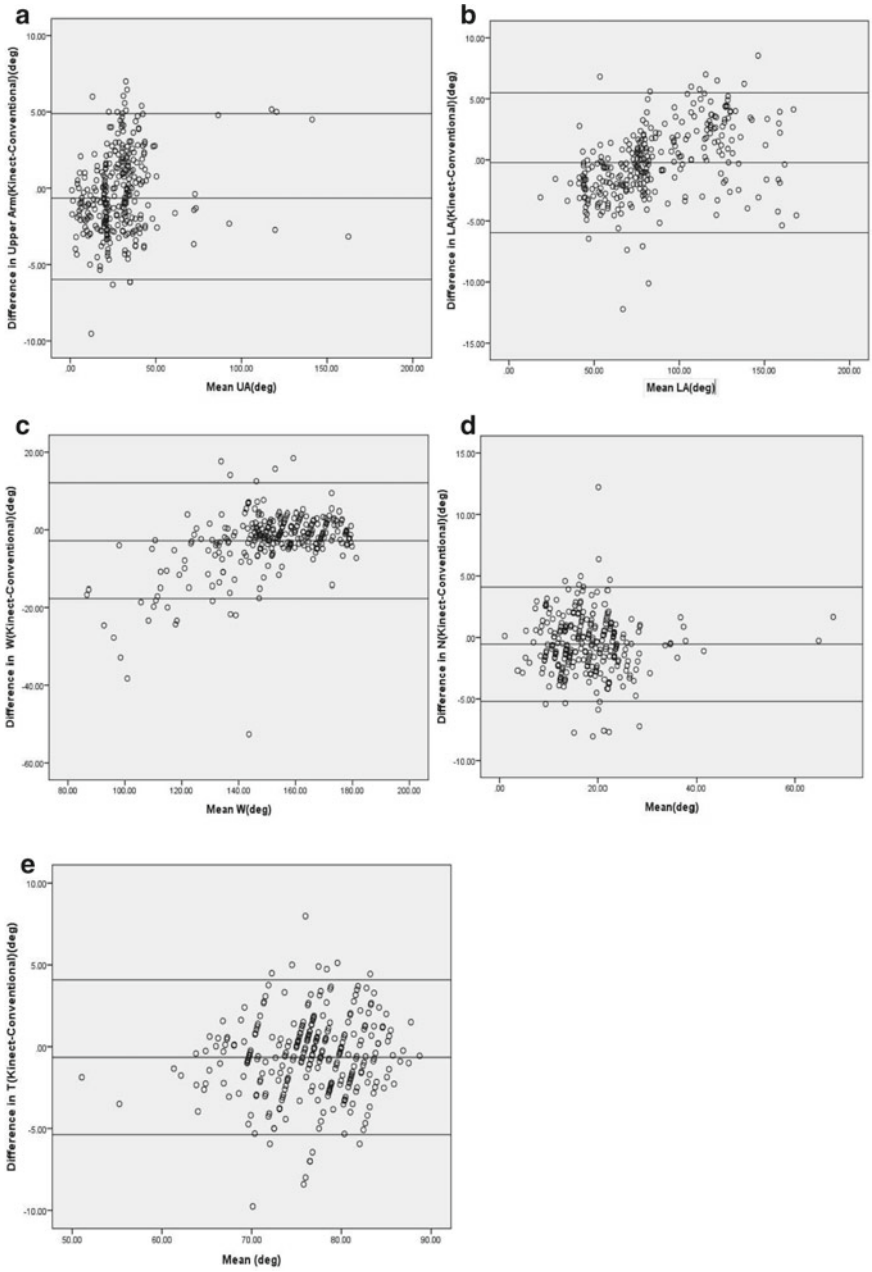

Fig. 4 Bland–Altman plot with limits of agreement for postural parameters (The difference of angle reading between two techniques (Kinect–conventional imaging) is plotted on the y-axis and the mean value using both techniques on the x-axis

Table 3 Z value(Mann–Whitney test at 95% confidence interval), Contingency coefficient (C), proportion agreement index (P_0), Cohen's kappa coefficient (k) for the sample to sample inter-rater agreement and agreement level at Landis and Koch scale for RULA scores evaluated from angle data of both techniques (Kinect-Imaging)

Z value (Mann–Whitney Test)	p value	C	P_0	Cohen's kappa (k)	Landis and Koch scale agreement
−1.893	0.058	0.757	0.74	0.67	Good agreement

For LA, correlation coefficients had highest values ($r1(298) = 0.997$, $p < 0.001$) and ($r2(298) = 0.995$) with lowest PE (3%) and mean difference (0.225°) values, inferring more association and lower differences among Kinect and imaging technique, therefore indicating the closeness in values obtained from both techniques.

For UA and N, correlation coefficient values were optimally higher ($r1(298) = 0.991$, $p < 0.001$), ($r2(298) = 0.0.990$) and ($r1(298) = 0.951$, $p < 0.001$), ($r2(298) = 0.948$) with relatively higher PE values (10.75% and 11.85%), showing Kinect data values have a good association with conventional values but with more error differences in the values.

The concrete agreement analysis between two sets of calculated RULA values (Kinect and imaging) is summarized in Table 3. The results of the Mann–Whitney test conducted came out to be statistically non-significant ($z = -1.893$, $p > 0.05$). Therefore, Mann–Whitney U test results directed to accept the null hypothesis, inferring the similarity in the RULA scores from both techniques. The value of contingency coefficient ($C = 0.757$) shows the existence of fairly high association among the two RULA score groups. Proportion agreement index ($P_o = 0.74$) indicated that 74% of the total RULA values from both techniques had an agreement. Consistency among RULA values from both Kinect and imaging technique was assessed by calculating Cohen's kappa index, $k = 0.67$ ($p < 0.0.001$), 95% CI (0.504, 0.848). The value of the kappa index was evaluated on Landis and Koch's scale resulting in "good" agreement among both the techniques. The above results concluded the validity of Hypothesis 2: Final RULA score calculated using Kinect V2 is in agreement with the RULA score calculated using conventional techniques.

The cross-validation of results obtained from Kinect V2 and conventional technique pointed out that the values derived from Kinect V2 were close to those derived using conventional techniques.

4 Discussion

In this section, the results reported in the current study are discussed and bring light to some limitations.

4.1 Main Contributions

The present study aimed at better understanding the body kinematics of dentist while doing the dental procedure and examining the feasibility of Kinect V2 in real-time postural analysis for slow-motion tasks. To the author's knowledge, this investigation was the first effort to use Kinect as a markerless technique to assess the dental practice ergonomically. In the current study, considerable validity of recorded spatial parameters was observed between the values of joint angle data from markerless and imaging technique.

There lies an anomaly in accuracy of data collection using imaging method while capturing orientations which require depth information (like in W) in 2D. Also, the overestimation of W angle joint data in Bland–Altman plots suggested the possible problem in the accuracy of one of the techniques. The presence of occlusions while capturing the wrist data in certain postures using Kinect might also be the responsible factor for inaccuracies. During the dental procedure, it was observed that 90% of the time hand palm was dorsiflexed which made it cumbersome to capture joint data associated with W accurately. In general, considering joint angle data except for W, no over- or underestimation of data points was observed. This may be supported by the fact that the optical axis of the Kinect sensor was kept parallel to the ground. This is in contrast with the study where overestimated body angle data was obtained [52], which may be due to the adjustment of the Kinect's tilt angle to capture the body joint skeleton. Non-homogeneity of Kinect data in measurement error within measurement volume was reported in a separate study backing up the fact that measurement errors along with all the three coordinate axis of the Kinect may be responsible for the results with proportional error [53].

As noticed, the values of correlation coefficients for body joint angle data from Kinect and imaging technique ranged on the higher side (near to value 1) unlike the study by other authors where values of correlation coefficients ranged from 0.04 to 0.77 (Pfister et al. [54]). This may be due to the less dynamic nature of dental work procedure if compared with the highly dynamic tasks which involve walking and jogging.

In the present study, the PE values for N and UA ranged on the higher side (10.75–11.85%). Apart from recorded flexion and extension movements in N and UA, the co-existence of other anatomical movements (lateral flexion or torsion in neck and abduction or adduction in the upper arm) in certain postures may be responsible for large deviation of Kinect values from the imaging values.

The Kinect method has proved its potential for the precise spatial data recording of non-static tasks. In the current study, spatial joint angle parameters involving slow-motion dynamic dental task had an overall PE (2.45–11.85%) comparable with an overall PE (4.02–7.73%) from spatial gait parameters in another study [55], which involved the walking trials by backpack carrying school children. Conventional imaging technique was considered as the gold standard for both the current study and the study involving walking trials.

The value of the contingency coefficient (*C*) in the current study is lesser than the value obtained in an investigation by other authors (Manghisi et al. [45]); the plausible influential factor may be the real-time data collection in the present case study. The authors of the current study suspected the presence of occluded data while doing real-time ergonomic assessment as the deterministic aspect for resulted good agreement level (and not excellent agreement) value of Cohen's kappa at standard Landis and Koch scale.

It appeared from the results of the current study that Kinect V2 may be considered for its use in detecting optimally correct body angles at least in less dynamically active but dexterity demanding dental procedure tasks. Further, the body angles may provide information about awkward postures in real time, and in the long run, it may be useful to prevent MSDs in dentists. The current study illuminates the idea of developing real-time posture correction feedback system, is operationally compliant with the dentists use, and may reduce the need of ergonomics expert in the routine

postural assessment. In dental studies, ergonomic aspects related to dentistry are taught theoretically in coursework, but currently there is no assessment tool to examine the postural correctness in amateur dentists like students and interns. Therefore, a warning-cum-posture assessment system may be developed to be served as a teaching aid in dental colleges, with the aim of forging young dentists habitual to recommended working postures.

4.2 Limitations

Due to methodological standardization and some acceptable shortcomings of Kinect device, results in the current study were constrained. The study was conducted in the controlled lightening environment where no other human or any extra object intervention was allowed in between the Kinect and the dentist him/herself which may have avoided further occlusions in the data. Further dentists and patients were made to follow the protocol of the study so as to be able to capture the data in a standardized format which may be difficult to follow while routine dental procedures. Without disturbing the code of conduct of dentists, the readings were taken while dentists were in their normal daily wear and laboratory coats, which may have recorded some errors in angle calculation as Kinect scans whole body surface for joint positioning. The role of working positions and isometric spinal loads in determining spine kinematics was not taken into consideration. The data recorded in the current study did not contain any overhead or extremely awkward dentist's postures, so appropriate prevalidation of Kinect is necessary for such data collection.

5 Conclusion

In this paper, the study related to the use of Kinect V2 sensor in detecting postural data in the actual dental procedure and the variation in its results from conventional imaging methods were discussed. Considering dental work postural variation as non-frequent and non-quick, the proposed system seemed to be an effective option in the case of slow-motion real-time task assessment. Kinect data collection and assessment appeared to be quick and easier than conventional methods. Despite the reported limitations, the results of the present study are promising enough to validate the Kinect method as a viable option for ergonomic evaluation of dental workstations. Hence, keeping a check on the postural inaccuracies in dentists during work using the user-friendly and contemporary Kinect device, the long-term effect on the biomechanical aspects can be restrained.

Acknowledgements This study was funded by Centre of Excellence in Industrial & Product Design, Punjab Engineering College, Chandigarh, India, under National Project Implementation Unit scheme with grant number AC/TEQIP-III/MHRD/2017. The authors wish to thank the dental practitioners who volunteered and participated in the study.

Declaration of Interest Statement The authors have no conflict of interest regarding the publication of this manuscript.

References

1. Maestas, N., Mullen, K. J., Powell, D., Wachter, T. V., & Wenger, J. B. (2015). Working conditions in The United States: Results of 2015 American working conditions. United States.
2. Eurofound. (2016). *Sixth European working conditions survey—Overview report*. Luxembourg: Publications Office of the European Union.
3. Luttmann, A., Jäger, M., Griefahn, B., Caffier, G., Liebers, F., & Steinberg, U. (2003). Protecting workers health series No. 5. Preventing Musculoskeletal Disorders in Workplace. Retrieved from https://www.who.int/occupational_health/publications/en/oehmsd3.pdf.
4. Kumar, M. W., Kumar, R. A., Gnanaraj, D. (2012). RULA analysis of workers assembly workstation. Humanizing work and work environment. Ergo: Safety for All, pp. 290–295.
5. Jafry, T., & O'Neill, D. H. (2000). The application of ergonomics in rural development: A review. *Applied Ergonomics, 31,* 263–268.
6. Puriene, A., Janulyte, A., Musteikyte, M., & Bendinskaite, R. (2007). General health of dentists. Literature review. *Stomatologija, Baltic Dental and Maxillofacial Journal, 9*, 10–20.
7. Gandavad, A., Ramsay, J. R. E., & Burke, F. J. T. (2007). Assessment of dental student posture in two seating conditions using RULA methodology—A Pilot Study. *British Dental Journal, 203*, 601–605.
8. Chaikumarn, M. (2005). Differences in dentists' working postures when adopting proprioceptive derivation vs. conventional concept. *International Journal of Occupational Safety and Ergonomics (JOSE), 11*, 441–449.
9. Leggat, P. A., Kedjarune, U., & Smith, D. R. (2007). Occupational health problems in modern dentistry: A review. *Industrial Health*, 611–621.
10. Garcia, P., Pinelli, C., Derceli, J., & Campos, J. (2015). Musculoskeletal disorders in upper limbs in dental students: Exposure level to risk factors. *Brazilian Journal of Oral Sciences, 11*(2), 148–153.

11. Gupta, S. (2011). Ergonomic applications to dental practice. *Indian Journal of Dental Research, 22,* 816–822.
12. Newell, T. M., Kumar, S. (2004). Prevalence of musculoskeletal disorders among orthodontists in Alberta. *International Journal of Industrial Ergonomics, 33*(2), 99–107.
13. Pargali, N., & Jowkar, N. (2010). Prevalence of musculoskeletal pain among dentists in Shiraz, Southern Iran. *International Journal of Occupational and Environmental Medicine, 1*(2), 69–74.
14. Finsen, L., Christensen, H., & Bakke, M. (1998). Musculoskeletal disorders among dentists and variation in dental work. *Applied Ergonomics, 29*(2), 119–125.
15. Durgha, K. (2014). Sakthi, Occupational hazards and its impact on quality of life of dentists. *IOSR Journal of Dental and Medical Sciences, 13*(7), 53–56.
16. Carvalho, M. V., Cavalcanti, F. I., Miranda, H. F., Soriano, E. (2006). Partial rupture of supraspinous tendon in a dentist: A case report. FIEP Bulletin, 76–131.
17. Doorn, J. W. (1995). Low back disability among self-employed dentists, veterinarians, physicians and physicaltherapists in The Netherlands. *Acta Orthopaedica Scandinavica, 263,* 1–64.
18. Ylipää, V., Arnetz, B., & Preber, H. (1999). Predictors of good general health, well-being, and musculoskeletal disorders in Swedish dental hygienists. *Acta Odontologica Scandinavica, 57,* 277–282.
19. Dong, H., Loomer, P., Barr, A. (2007). The effect of tool handle shape on hand muscle load and pinch force in a simulated dental scaling task. *Applied Ergonomics, 38*, 525–531.
20. Viera, E. R., Kumar, S. (2004). Working Postures: a literature review. *Journal of Occupational Rehabilitation, 14*(2),143–159.
21. David, G. C. (2005). Ergonomic methods for assessing exposure to risk factors for work-related musculoskeletal disorders. *Occupational Medicine, 55*(3), 190–199.
22. Li, G., & Buckle, P. (1999). Current techniques for assessing physical exposure to workrelated musculoskeletal risks, with emphasis on posture-based methods. *Ergonomics, 42*(5), 674–694.
23. Aljanakh, M., Shaikh, S., Siddiqui, A. A., Mansour, M. A., & Hassane, S. S. (2015). Prevalence of musculoskeletal disorders among dentists in the Ha'il Region of Saudi Arabia. *Annals of Saudi Medicine, 35*(6), 456–461.
24. Decharat, S., Phethuayluk, P., Maneelok, S. (2016). Prevalence of musculoskeletal symptoms among Dental health workers, Southern Thailand. *Advances in Preventive Medicine*, 5494821.
25. Muralidharan, D., Fareed, N., Shanthi, M. (2013). Musculoskeletal disorders among dental practitioners: does it affect practice? *Epidemiology Research International*, 716897(2013).
26. Kalappa, S., & Raghavendra, S. (2017). A study on the influence of ergonomics on the prevalence of chronic pain disorders among dentists. *International Surgery Journal, 4*(12), 3873–3878.
27. Atri, M., & Nagraj, A. (2014). Identifying musculoskeletal disorders amongst dentists—The need for the hour. *International Journal of Medical Science and Public Health, 3,* 730–734.
28. Moodley, R., & Naidoo, S. (20015). The prevalence of musculoskeletal disorders among dentists in KwaZulu-Natal. *South African Dental Journal, 70*(3), 98–103.
29. Mendegeri, V., Ramdurg, P., Kambale, S., & Gajapurad. (2014). Prevalence of musculoskeletal disorders among dentists: A Pilot study. *Indian Journal of Dental Sciences, 5*(6), 16–20.
30. Moosavia, S., Desaia, R., Hallaj, S., Sundaramb, K. K., & Hegdec, V. S. (2015). Ergonomic analysis to study the intensity of MSDs among practicing Indian dentists. In *Procedia Manufacturing 3, 6th International Conference on Applied Human Factors and Ergonomics (AHFE 2015) and the Affiliated Conferences* (Vol. 5, No. 6, pp. 5419–5426).
31. Burdorf, A., & Laan, J. (1991). Comparison of methods for the assessment of postural load on the back. *Scandinavian Journal of Work, Environment & Health, 17,* 425–429.
32. Wiktorin, C., Karlqvist, L., & Winkel, J. (1993). Validity of self-reports exposures to work postures and manual material handling. *Scandinavian Journal of Work, Environment & Health, 19*, 208–214.
33. Delfa, N. J. L., Grondin, D. E., Cox, J., Potvin, J. R., & Howarth, S. J. (2017). The biomechanical demands of manual scaling on the shoulders & neck of dental hygienists. *Ergonomics, 60*(1), 127–137.

34. Blanc, D., Farre, P., & Hamel, O. (2014). Variability of musculoskeletal Strain on dentists: An Electromyographic and goniometric study. *International Journal of Occupational Safety and Ergonomics, 20*(2), 295–307.
35. Kowalski, K., Rhodes, R., Naylor, P.-J., Tuokko, H., & MacDonald, S. (2012). Direct and indirect measurement of physical activity in older adults: A systematic review of literature. *International Journal of Behavioral Nutrition and Physical Activity, 9*(1), 148.
36. Xu, X., Gorry, M. R. W., Chou, L., Lin, J., & Chang, C. (2015). Accuracy of Microsoft Kinect for measuring gait parameters during treadmill walking. *Gait Posture, 42*,145–151.
37. Bhagwat, S., Hegde, S., & Mandke, L. (2015). Prevalence of musculoskeletal disorders among Indian dentists: A pilot survey with assessment by rapid entire body assessment. *World Journal of Dentistry, 6*(1), 39–44.
38. Kriangkrai, R., Sirimala, N., Nathamtong, S., Wintsch, S., Choden, K., & Taechasubamorn, P. (2016). Self-reported prevalence and risk factors of musculoskeletal pain in Thai dental students. *International Dental Journal of Students Research, 4*(3), 116–122.
39. McAtamney, L., & Corlett, E. N. (1993). RULA: A survey methods for the investigation of work-related upper limb disorders. *Applied Ergonomics, 24*(2), 91–99.
40. Bruno, J. L., Li, Z., Trudeau, M., Raina, S. M., & Dennerlein, J. T. (2012). A single video camera postural assessment system to measure rotation of the shoulder during computer use. *Journal of Applied Biomechanics, 28*, 343–348.
41. Haggag, H., Hossny, M., Nahavandi, S., & Creighton, D. (2013). Real time ergonomic assessment for assembly operations using kinect. In: *Computer Modelling Simulation (UKSim),UKSim 15th International Conference* (pp. 495–500).
42. Siemens. (2013). Jack and process simulate human. http://www.plm.automation.siemens.com/en_gb/products/tecnomatix/manufacturing-simulation/humanergonomics/jack.shtml.
43. Choppin, S., Lane, B., & Wheat, J. (2014). The accuracy of the Microsoft Kinect in joint angle measurement. *Sports Technology, 7*(1–2), 98–105.
44. Lun, R., & Wenbig, Z. (2015). A survey of applications and human motion recognition with Microsoft Kinect. *Electrical Engineering & Computer Science Faculty Publications*, 408.
45. Manghisi, V. M., Uva, A. E., Fiorentino, M., Bevilacqua, V., Trotta, G. F., & Monno, G. (2017). Real time RULA assessment using Kinect v2 sensor 2017. *Applied Ergonomics, 65,* 481–491.
46. Wang, Q., Kurillo, G., Ofli, F., & Bajcsy, R. (2015). Evaluation of pose tracking accuracy in the first and second generation of Microsoft Kinect. In *Health-Care Informatics (ICHI, 2015 International Conference)* (pp. 380–389). IEEE.
47. Zennaro, S., Munaro, M., Milani, S., Zanuttigh, P., Bernardi, A., Ghidoni, S., & Menegatti, E. (2015). Performance evaluation of 1st and 2nd generation Kinect for multimedia applications. In *Multimedia Expo (ICME), 2015 IEEE International Conference* (pp. 1–6). IEEE.
48. Wiedemann, L., Planinc, R., Nemec, I., & Kampel, M. (2015). Performance evaluation of joint angles obtained by KinectV2. In: *Technologies Active-Assisted Living (TechAAL), IET International Conference* (pp. 380–389). IET.
49. Mgbemena, C. E., Oyekan, J., Hutabarat, W., Xu, Y., & Tiwari, A. (2017). Design and implementation of ergonomic risk assessment feedback system for improved work posture assessment. *Theoretical Issues in Ergonomics Science, 19*(4), 431–455.
50. Yusuf, K. M. S. T., Nazri, A. F. A., Mustapha, G., & Mahmud, J. (2015). Analysis of static and dynamic motion accuracy for Kinect-virtual Sensei system. *Journal of Engineering and Applied Sciences, 10*(17), 7328–7335.
51. Fleis, J. L., Levin, B., & Paik, M. C. (2004). The measurement of interrater agreement. In *Statistical methods rates proportions* (pp. 598–626). Wiley. Retrieved from https://onlinelibrary.wiley.com/doi/abs/10.1002/0471445428.ch18.
52. Bhatia, V., Kalra, P., & Randhawa, J. S. (2010). Upper body postural analysis in sitting workplace environment using Microsoft Kinect V2 Sensor. In *Proceedings of ICoRD 2019 Volume 2. Research into Design for a Connected World* (pp. 575–586).
53. Dutta, T. (2012). Evaluation of the Kinect sensor for 3-D kinematic measurement in the workplace. *Applied Ergonomics, 43*, 645–649.

54. Pfister, A., West, A. M., Bronner, S., & Noah, J. A. (2014). Comparative abilities of Microsoft Kinect and Vicon 3D motion capture for gait analysis. *Journal of Medical Engineering & Technology, 38*, 274–280.
55. Gupta, I., Kalra, P., & Iqbal, R. (2017). Gait parameters in school going children using a marker-less approach. *Current Science, 111*(10), 1668–1675.